

A Doppler Lidar system with preview control for wind turbine load mitigation

Zur Erlangung des akademischen Grades eines

DOKTOR-INGENIEURS (Dr.-Ing.)

von der Fakultät für
Elektrotechnik und Informationstechnik
am Karlsruher Institut für Technologie (KIT)
genehmigte

DISSERTATION

von

M.Eng. Leilei Shinohara

geb. am 17.03.1982 in Shandong (China)

Tag der mündlichen Prüfung:

04.12.2014

Hauptreferent: Prof. Dr. rer. nat. Wilhelm Stork

Korreferent: Prof. Dr. Carlo L. Bottasso

Karlsruhe, den November 4, 2014



Dieses Werk ist lizenziert unter einer Creative Commons Namensnennung –
Weitergabe unter gleichen Bedingungen 3.0 Deutschland Lizenz
(CC BY-SA 3.0 DE): <http://creativecommons.org/licenses/by-sa/3.0/de/>
DOI 10.5445/IR/1000048736

A Doppler Lidar system with preview control for wind turbine load mitigation

1. Auflage: November 2014

©2014 Leilei Shinohara

Dedicated to my beloved wife and son ...

Preface

This dissertation was prepared at the department Electrical Engineering and Information Technology (ETIT), the Karlsruhe Institute of Technology (KIT) in partial fulfilment of the requirements for acquiring the PhD degree in engineering. The work was carried out in the period October 2009 - November 2014. The supervisors were Professor Dr. rer. nat. Wilhelm Stork (ETIT, KIT) and Professor Dr. Carlo L. Bottasso (ME, TU Munich).

The presented results in this dissertation were based on the pre-research project of "Laser Doppler remote wind sensing for offshore wind turbine" supported by Karlsruhe School of Optics and Photonics (KSOP) and the research project "Laser-Doppler Windprofilmessung zur aktiven Lastregelung von Windkraftanlagen und zur Standortexploration (LAWAL)" financially supported by the Federal Ministry for the Environment, Nature Conservation, Building and Nuclear Safety (BMU), later transferred to the Federal Ministry for Economic Affairs and Energy (BMWi).

Part of the materials in this dissertation are published on the following journals and conferences ([SBH⁺12], [SATF⁺14], [BSFS14], [SBB⁺13], [SBF⁺14a], [SBF⁺14b], [SBH⁺12], [STB⁺14], [SXBS14]).

In this dissertation, I divided into four parts:

Part I: Background information and knowledges gives an introduction, theoretical background and the state of the art technologies which are given in the presented work. The works in this part are not my original but based on paper researches.

Part II: The cost efficient Doppler wind Lidar system is my first original work in this dissertation. In this part I show the development of the cost efficient Doppler wind Lidar system. I start with the requirement analysis, then follow with the Lidar simulator development, and end with the experimental realizations in compare with the calculation and simulation result to show the feasibility with the present new approach.

Part III: The "industry-friendly" Lidar assisted active pitch control design is my second contribution in this dissertation. In which I developed a "industry-friendly" design of model predictive controller. In this chapter I describe the wind turbine system modelling, controller design and the simulation evaluation.

Part IV: Discussion and conclusions includes the discussion about the results and a summery conclusion for the presented concept.

Karlsruhe, on November 4, 2014
M.Eng.Leilei Shinohara

Acknowledgement

I would like to express my special appreciation and thanks to my supervisor Professor Dr. rer. nat. Wilhelm Stork for his encouraging and motivating me to my research work and for allowing me to grow as a research scientist. I have been amazingly fortunate to have an advisor who gave me freedom to explore on my own and at the same time helped me to overcome many crisis situations. Your advice on both research as well as on my career have been priceless. I would also like to thank my co-supervisor Prof. Dr. Carlo L. Bottasso from Technical University of Munich for encouraging and advising me on the wind turbine pitch control design part to accomplish the unique dissertation. Then, I would like to thank to the committee members, Prof. Dr.-Ing. Gert Trommer, Prof. Dr. rer.nat. Uli Lemmer, Prof. Dr.-Ing. John Jelonnek for serving as my committee members even at hardship. I also want to thank you for letting my defence be an enjoyable moment, and for your brilliant comments and suggestions.

I am also grateful to the Institute of Information Processing Technology (ITIV) and the Department of Electrical Engineering and Information Technology (ETIT) for providing me a great research environment among students, faculty, and administrative staff. Furthermore, I would like to thank Karlsruhe School of Optics and Photonics for the financial support during my work, and the Federal Ministry for the Environment, Nature Conservation, Building and Nuclear Safety (BMU), the Federal Ministry of Education and Research (BMBF), and the Federal Ministry for Economic Affairs and Energy (BMWi) for the financial support on the research projects I have worked on. I would like to give special thanks to Denica Angelova-Jackstadt, Ingrid Hauck, Werner Fasel, and Alfred Schyma.

I would like to express my profound and hearty thanks to my colleagues Thorsten Beuth, Harsha Umesh Babu, Nico Heussner, Siegwart Bogatscher, Kai Worms, Svetlana Danilova, Markus Butzbach, and Andre Malz from ITIV for having a great discussion during the work. I would also like to thank the project members, Dr. Andreas Streck and Maik Fox from ELOVIS, and Oliver Becker from Vensys to have a very helpful discussion through the project progress.

I acknowledge Prof. Masayuki Fujita and Dr. Takeshi Hatanaka from Tokyo Institute of Technology for encouraging me the novel pitch controller design. I would also like to thank Eric Simley from University of Colorado Boulder for the discussion and helping on the Lidar system simulator for control simulations. Furthermore, I would like to appreciate and thank to Fiona Dunne from University of Colorado Boulder, Na Wang from National Renewable Energy Laboratory (NREL), David Schlipf from the University of Stuttgart, and Carlo E.D. Riboldi from Polytechnic University of Milan for their help on the discussion of different wind turbine pitch control design and applications. I also thank Mr. Samuel DAVOUST from Avent Lidar technology for providing the technical information of Wind iris.

A special thanks to my family. Words cannot express how grateful I am to my mother-in-law, father-in-law, my mother, and father for all of the sacrifices that you have made on my behalf. Your help to take care of my son sustained me thus far. I would also like to thank

all of my friends who supported me in writing, and intended me to strive towards my goal. At the end I would like express appreciation to my beloved wife Lifang who spent sleepless nights with and was always my support in the moments when there was no one to answer my queries. I would like to express gratitude and regretful to my son Maki Lawrence for not being a competent father during the period of dissertation writings.

Karlsruhe, in December 2014
Leilei Shinohara

Zusammenfassung

Aufgrund der steigenden Energieverbrauch und drängenden sozialen Erwartungen, wird die Windenergie vor vielen Herausforderungen in der Entwicklung und Anwendung. Heutzutage werden Windkraftanlagen werden immer größer und in schwer zugänglichen Lokationen aufgestellt wie Offshore. Solche Lokationen verursacht ein Overhead-Kosten, nicht nur durch unregelmäßige Wartung, sondern auch die hohe Erreichbarkeit Kosten. Die modernen großen Windkraftanlagen unterliegen größeren Windgeschwindigkeit Turbulenzen und ertragen starke Drehmomentschwankungen. Die Motivation der vorliegenden Arbeit ist auf die Gestaltung eines kosteneffizienten Systems Lösung durchgeführt, um die Windenergiekosten durch Verringerung der dynamischen Belastungen auf einer Windkraftanlage zu verringern. Fig.1 veranschaulicht die allgemeine Vorstellung von dem vorliegenden Konzept.

Bisher werden die industriellen Windkraftanlage Pitch-Regler auf den Feedback-Methoden, die die Generatordrehzahl Fehler in den Regelkreis zu füttern, um die Blattsteigungswinkel regulieren basiert. Allerdings haben diese Methoden Einschränkungen auf den großen Windkraftanlagen. Den letzten Jahren die Lidar unterstützte Steuerungstechnologien, wie Feedforwarder-Kontrolle und Model Predictive Control, sind oft für Forschung und Entwicklung eingesetzt. Diese Methoden verwenden Wind Lidar-Systeme, um im Vorfeld das oberstromigen Windfeld aus einzelnen Punkt oder vielfache Distanzen, zu messen und prognostizieren.

Doppler Wind Lidar ist ein Fernerkundungstechnik, die als genaue und zuverlässige Methode zur Messung der Windgeschwindigkeiten von zehn meter bis kilometer bewährt hat. Es funktioniert nach dem Prinzip der Messung vom Doppler-Verschiebungsfrequenz des Rückstreulicht durch atmosphärischen Aerosolen und Molekülen zum Erhalt der Windgeschwindigkeit. Die Anwendung Lidare zur Steuerung von Windkraftanlagen als ein oberstromiges Windgeschwindigkeitsmesswerkzeug wurde zuerst im Jahre 1989 vorgehabt. Jedoch wegen der hohen Kosten, eine dauerhafte oder kontinuierliche Verwendung eines solchen Systems für einen Windkraftanlage - Steuerungsanwendung ist es trivial. Daher wird eine kosteneffiziente Entwicklung für Windkraftanlagen wichtig.

Die vorliegende Arbeit konzentrierte sich auf die Gestaltung eines kosteneffizienten Lidar-System zusammen mit einer Preview-Kontrolle basiert auf Lidar für die aktiven Windkraftanlage Pitchsystem. Im Rahmen dieser Arbeit, unter der oben genannten Motivation, werden das Lidar-System-Design und prädiktive Pitch Controller Design beide zur Berücksichtigung konzentriert. Der Teil des Lidar-System-Designs ist durch die Einführung eines breiten Spektrums Halbleiterlaser mit einer relativ kürzeren Kohärenzlänge einzigartig. Der prädiktive Pitch Controller Design konzentriert auf die Entwicklung eines Industriefreundliche Konzept durch die Einführung der fortschrittlichen modellprädiktive Controller in den konventionellen PI Regelkreis, ohne der Zerstörung der Original-Controller.

Modernste Doppler Wind Lidar-Systeme verwenden häufig Faserlaser mit langer Kohärenzlänge (km). Normalerweise werden die Breitbandlaser nicht in einem kohärenten Doppler-Lidar-System verwendet, aufgrund des hohen Phasenrauschen. Doch solche Laser kosten



Fig. 1.: Sketch of the general idea of Lidar assisted wind turbine pitch control system (Background picture source: Microsoft office template)

weniger als 1/5 mit Faserlaser. Dieser Ansatz basiert auf der früheren Forschung der Verwendung eines super kontinuierlichen Lasers auf einem kohärenten optischen Frequenzbereich bezogenes Tomographiesystem für die Papierherstellung entwickelt. Es kann den Erfolg in zwei Aspekten zu erreichen: 1. Laserquellenkosten reduziert; 2. die Kohärenzlänge des Lasers eingesetzt, um eine konstante Sondenlänge zu definieren.

Für solche Lidar-Systemgestaltung, eine systematische Berücksichtigung sowohl von dem Sensor Design und der Anforderung von der Pitch - Kontrolle analysiert und diskutiert. Dann wird ein Simulator zur Simulation verschiedener Teile der Lidar-Komponenten ausgelegt ist. Der Simulator hat zwei verschiedene Formen; eine statische Simulation führen eine Berechnung der Empfangsleistung und System Signal-Rausch-Verhältnis. Diese Simulation berechnet die Rückstreuung für jedes Teilchen und fasst die einzelnen Rückstreuung, die Lidar-Signal ohne die Bewegung von Teilchen und Laufzeit von Lasern zu bilden. Eine dynamische Simulation ist eine modifizierte Feuilette Modell, das die Atmosphäre in kleine Elemente Scheiben schneiden. Innerhalb der einzelnen Elemente, sofern die optischen Eigenschaften und die Bewegungsgeschwindigkeit des Aerosols gleich sind. Durch Ausbreitung des Laserstrahls auf jeder Atmosphäre Scheiben werden die Rückstreusignalsignals mit Zeitverzögerungen erzeugt. Mit diesem Modell kann eine Time-Domain-Full-System Simulation einfach verarbeitet werden. Schließlich, um das Lidar-System zu entwickeln, ein schrittweise experimenteller Realisierungsprozess wird durchgeführt. Verschiedene Freiraum-Versuchseinrichtungen sind für die Bewertung des neuen Konzepts entworfen und Anhaftungen. Fig.2 veranschaulicht das Konzept der kurzen Kohärenzlänge Laser-Doppler-Wind-Lidar.

Unterdessen, um diese Lidar-Systeme anzuwenden, wird ein branchenfreundlicher Pitch-Control-Ansatz nämlich 2-DOF RHC / FB Steuerung ausgelegt. Das Konzept ist ähnlich wie bei einem Standard-2-DOF FF / FB-Controller, aber wird der FF Begriff mit einem optimalen Steuerungsverfahren entwickelt, die zurückweichenden Horizont Steuerung (RHC), um das System Constrains in dem Reglerentwurf bringen zu können.

In der vorliegenden Arbeit wird die entworfen Controller auf einem linea reduzierte Modell einer Windkraftanlage, die aufgerufen wird Nominalmodell . Die nominale Modell

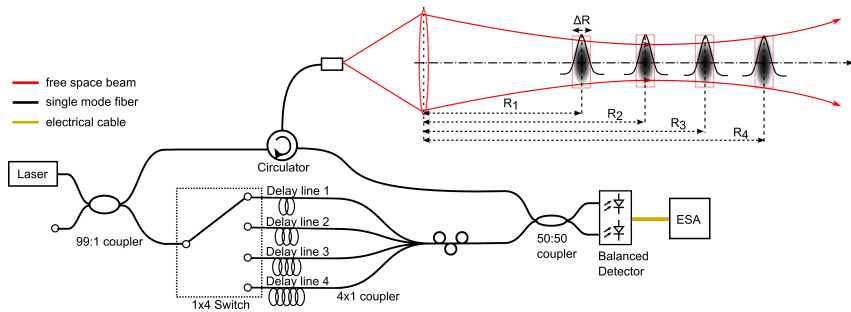


Fig. 2.: Illustration of CW Lidar concept with range independent probe length

beinhaltet die Aerodynamik Teilmodelle, elasticdynamics Struktur Teilmodelle und Servodynamik Teilmodelle. Andere Struktur Teilmodelle können frei kombiniert werden, je nach dem Ziel der Kontrollen. Hier, in dieser Arbeit, ist die Steuerung vor allem auf einem zwei-Freiheitsgrad Strukturmodell, nämlich Rotordrehung und Turm Vorwärts-Rückwärts-Biegefreiheitsgrad.

Die entworfene Steuerung erzeugt die Pitch Befehle mit der RHC Verfahren aus den Lidar Vorschau Windmessungen und fügt zu der ursprünglichen Regelkreis ohne ändern der Original-Controller. Selbst die prädiktive Steuerung nicht richtig funktioniert, das ursprüngliche Rückkopplungssteuerungscontroller kann immer noch die Steuerung des Systems stabilisieren. Fig.3 veranschaulicht das Konzept der Steuerung ausgelegt.

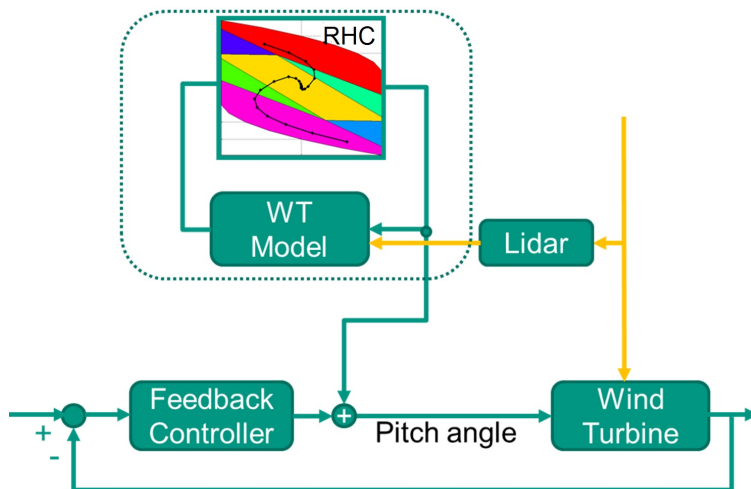


Fig. 3.: 2DOF RHC/FB preview control for wind turbine active pitch system

Abstract

Due to the increase of energy consumption and pressing social expectations, wind energy faces many challenges in development and application. Nowadays wind turbines become larger and larger and they are set up in difficult to access locations such as offshore. Such locations bring an overhead in costs caused not only by irregular maintenance but also expenses due to hard accessibility. Large modern wind turbines are subject to wider wind speed turbulence and endure strong torque fluctuations. Research and development in wind industries are focused on reduction of wind turbine loads and maximization of wind energy capture in order to reduce the overall cost of wind energy.

The motivation of the present work is carried on design of a cost efficient system solution to reduce the cost of wind energy by mitigation of the dynamic loads on a wind turbine system. Fig.4 illustrates the general idea of the present concept.



Fig. 4.: Sketch of the general idea of Lidar assisted wind turbine pitch control system (Background picture source: Microsoft office template)

So far, the industrial wind turbine pitch controls are based on the Feedback (FB) methods which feed the generator speed error into the control loop to regulate the blade pitch angles. However, these methods have limitations in the large wind turbine applications due to their slow reaction on load reductions which are caused by the inhomogeneous wind field. Recent years the Lidar assisted control technologies, such as Feedforward (FF) control and model predictive control, have often been used for research and development. These methods use wind Lidar systems to measure beforehand and predict the upstream wind field from a single or multiple distances.

Doppler wind Lidar is a remote sensing technique which has been proven as an accurate, reliable method for measuring wind velocities from couple ten meters to couple kilometers. It works on the principle of measuring the Doppler shift frequency of backscattering light due to atmospheric aerosols and molecules for obtaining the wind speed. The application of Lidars for control of wind turbines as an upstream wind speed measurement tool was

first proposed in 1989. However due to the high prices of Lidar system, for a permanent or continuous use of such system on a wind turbine control application, it is difficult. Therefore, the development of a cost efficient system for wind turbines becomes important.

Within this work, under the aforementioned motivation, the Lidar system and predictive pitch controller design are both focused under the consideration for the researches. The part of Lidar system design is unique on introducing a broad spectrum semiconductor laser with a relatively shorter coherence length. The predictive pitch controller design is focused on developing of an "industry-friendly" concept by introducing the advanced model predictive controller into the conventional Proportional-Integral-Derivative (PI(D)) feedback control loop without destroying the original controller.

State of the art Doppler wind Lidar systems commonly use fiber lasers with couple kilometres coherence length. Normally, the broad spectrum lasers are not used in a coherent Doppler Lidar system, due to the high phase noise. However, such lasers cost less than 1/5 in compare with fiber lasers. This approach is developed based on the previous research of using a super continue laser on a frequency domain optical coherent tomography system for paper production applications. This approach can achieve two aspects: 1. the price of laser source can be reduced; 2. the coherence length of laser can be used to define a constant probe length.

For designing of such Lidar systems, a systematic consideration both from the sensor design point of view and the requirement from the pitch control point of view are analyzed and discussed. Then, a simulator to model different parts of the Lidar components is designed. The simulator has two different forms; a static simulation perform a calculation of receiving power and system signal to noise ration. This simulation calculates the back-scattering for each particle and sums up the individual backscattering to form the Lidar signal without considering the movement of particles and propagation time of lasers. A dynamic simulation is a modified Feuillette model which slices the atmosphere into small elements. Within each elements, assuming the optical properties and the moving speed of aerosols are the same. By propagating the laser beam to each atmosphere slices, the back-scattering signals with time delays are generated. With this model, a time domain full system simulation can be easily processed. Finally, a step wise experimental realization process is performed. Various free space experimental setups are designed and buildup for the evaluation of the new approach. Fig.5 illustrates the concept of the short coherence length laser Doppler wind Lidar.

Meanwhile, to apply such Lidar system, an industry friendly pitch control approach namely 2-DOF RHC/FB control is designed. The concept is similar to a standard 2-DOF FF/FB controller, but the FF term is designed with an optimal control method, the receding horizon control (RHC), in order to be able take system constrains into the controller design.

In the presented work, the designed controller is based on a linearised reduced model of a wind turbine which is called nominal model. The nominal model includes the aerodynamics submodels, elasticdynamics structure submodels, and servo dynamics submodels. Different structure submodels can be freely combined depending on the objective of controls. Here, in this thesis, the controller is mainly focused on a 2 degree of freedom structure model, namely rotor rotation and tower fore-aft bending degree of freedom.

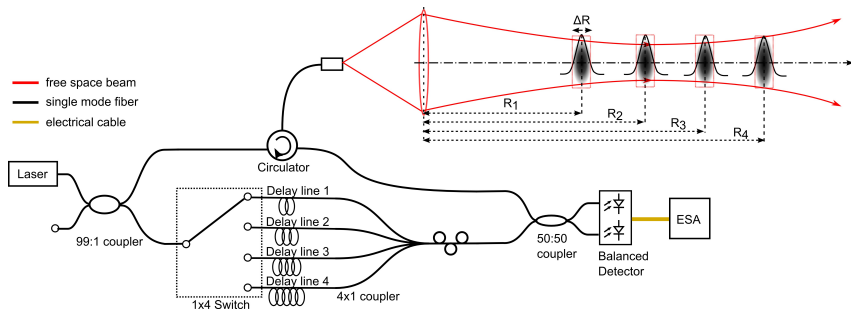


Fig. 5.: Illustration of CW Lidar concept with range independent probe length

The designed control creates the pitch commands with the RHC method from the Lidar preview wind measurements and adds to the original feedback control loop without modify the original controller. Therefore, even the predictive controller does not work properly, the original feedback controller still can control the system to be stable. Fig.6 illustrates the concept of the designed controller.

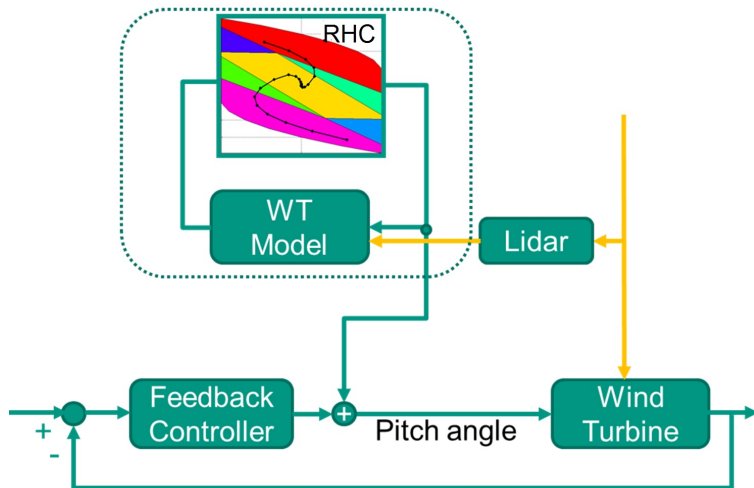


Fig. 6.: 2DOF RHC/FB preview control for wind turbine active pitch system

Contents

I	Background information and knowledges	1
1	Introduction	3
1.1	Overview	3
1.2	Description of wind turbine systems	5
1.3	Contributions and approach of the present work	7
1.3.1	Approach of the present work	8
1.3.2	Outline of this thesis	9
2	Background knowledge	11
2.1	Background of wind energy	11
2.1.1	Working principles of wind turbines	13
2.1.2	Classification of wind energy systems	15
2.2	Working principle of Doppler wind Lidar	18
2.2.1	Lidar equation	19
2.2.2	Coherent detection	21
2.2.3	Balanced detection	25
2.3	Background knowledge of wind field	26
2.3.1	Surface boundary layer wind share	27
2.3.2	Gust wind field	28
2.3.3	Turbulence wind field	29
2.3.4	Wind speed changes on the induction zone	29
2.3.5	Blade effective wind speed	30
2.4	Summary	31
3	State of the art	33
3.1	Overview of wind sensing technologies for wind energy	33
3.1.1	Mechanical anemometers	33
3.1.2	Ultrasonic wind sensors	33
3.1.3	Wind Lidar	35
3.2	Commercial Lidars for wind energy applications	35
3.2.1	Leosphere WindCube Lidar system	35
3.2.2	Avent Wind iris Lidar system	42
3.2.3	ZephIR wind Lidar system	46
3.2.4	Windar Photonics Wind Eye	52
3.2.5	Summary	54
3.2.6	Other commercial Lidar systems	56

3.3	Doppler wind Lidar on researches	57
3.3.1	A comparison of the Different Lidar system	60
3.4	Wind turbine control system	61
3.4.1	Standard industrial feedback control	62
3.4.2	2-DOF Feedforward/Feedback control	63
3.4.3	Model predictive control	65
3.5	Summary and conclusion	66
II	The cost efficient Doppler wind Lidar system	69
4	System design architecture and requirement analysis	71
4.1	Design concept	71
4.1.1	Coherence length of lasers	71
4.1.2	Concept of a broad spectrum laser Lidar design	74
4.1.3	Probe length of the new concept	74
4.2	System requirement analysis	75
4.2.1	Measurement distance	75
4.2.2	The trade-off of probe length	80
4.2.3	Single or multiple distance measurements	80
4.2.4	Scan scenarios	82
4.2.5	Components specification analysis	83
4.3	Laser safe operation consideration	85
4.4	Summary and conclusion	85
5	Simulation of the Doppler wind Lidar	87
5.1	Atmospheric scattering simulation	88
5.2	Modelling of lasers	90
5.2.1	Gaussian shape laser beam	90
5.2.2	Spectrum of Laser	91
5.3	Sending and receiving optics	92
5.3.1	A simplified spatial collection efficiency model	93
5.3.2	SCE model with a Gaussian field	96
5.3.3	SCE model for an off-axis case	96
5.3.4	Simulation of range reduction factor	97
5.4	Full system simulation	98
5.4.1	Simplified cylindrical coordination concept	98
5.4.2	The modified Feuillete model	98
5.4.3	Full simulation results	100
5.4.4	Simulation results with the dynamical simulation	101
5.5	Summary and conclusion	103
6	Experimental realization of the Doppler Lidar feasibility	105
6.1	Wind tunnel design for wind flow measurements	105
6.2	Laser transmitter	106
6.2.1	Evaluation of laser coherence length	106
6.2.2	Evaluation of the laser diode intensity noise	107

6.3	Sending and receiving optics design	110
6.3.1	Bi-static system with single photo detector	110
6.3.2	Bi-static configuration with balanced photo detector	111
6.3.3	Monostatic configuration with 50:50 BS as a combiner	112
6.3.4	Monostatic configuration with off-axis parabolic mirror	112
6.4	Variable length reference beam design	114
6.5	Summary and conclusion	117
III	The “industry-friendly” Lidar assisted active pitch control design	119
7	Wind turbine modelling	121
7.1	FAST wind turbine model	122
7.2	Aerodynamics model	123
7.2.1	Linearisation of the aerodynamics model	124
7.3	Wind turbine Servo-Elastic structure model	125
7.3.1	Dynamic model of rotor	126
7.3.2	Dynamic model of generator	126
7.3.3	Tower first order fore-aft model	127
7.3.4	Drive-train model	129
7.4	Wind turbine actuator model	131
7.4.1	Generator torque actuator model	131
7.4.2	Pitch actuator model	131
7.4.3	Dynamic wind model	132
7.5	The combined reduced DOF numerical model of wind turbine	133
7.5.1	The nonlinear nominative model	133
7.5.2	Linear numerical model	134
7.5.3	Piecewise Linear (Affine) model	137
7.6	Wind filed modelling	138
7.6.1	Lidar measurement simulation	139
7.7	Summary and conclusion	141
8	Active pitch control system design	143
8.1	Benchmark control system design	144
8.1.1	Collective pitch feedback control	144
8.1.2	Full-state feedback LQR controller	148
8.1.3	A comparison of LQR control with PI Feedback baseline control	151
8.1.4	2-DOF Feedforward/Feedback Control	153
8.2	Design of the 2-DOF RHC/FB controller	153
8.2.1	Controller structure	153
8.2.2	Receding horizons	154
8.2.3	Prediction model	154
8.2.4	Cost function	154
8.2.5	Solving the MPC optimization problem	155
8.3	Controller verification	157
8.3.1	Fatigue and extreme loads	157
8.3.2	The simplest 1-state pitch controller	158

8.3.3	2-DOF RHC/FB control	160
8.3.4	Simulation with a step changes wind profile	161
8.3.5	Simulation with a deterministic gust wind profile	163
8.4	Simulation results with the non-linear FAST turbine model	166
8.4.1	Simulation results with a deterministic gust wind model	166
8.4.2	Simulation results with a normal turbulent wind model (NTM)	167
8.4.3	Simulation result with a hub height wind measurement only Lidar	170
8.5	Summary and conclusion	170
9	Discussion and conclusion	175
9.1	Contributions of the presented work	175
9.2	Conclusion and discussions	176
9.3	Future works	181
A	Information for wind turbine modelling	187
A.1	Aerodynamics of wind turbine	187
A.2	Properties of NREL 5-MW reference wind turbine	189
A.3	Linear models of wind turbines	192
A.3.1	2-DOF linear model with tower Fore-Aft DOF	192
A.3.2	2-DOF linear model with drivetrain and rotor DOFs	195
A.3.3	3DOF linear model with tower fore-aft, drivetrain and rotor DOFs	199
A.3.4	Linear 4DOF model by adding collective pitch flapwise DOF	204
B	Design of the RHC controller	211
B.1	Linear RHC controller design	211
C	Evaluation of the laser noise	215
D	Atmospheric scattering theory	217
D.1	Rayleigh scattering (Molecular)	217
D.2	Mie scattering (Aerosol)	217
D.3	Aerosol parameters	218
Indexes		221
List of Figures	221
List of Tables	226
List of Symbols and Abbreviations	229
References		237
Supervised Student Research		249
Publications included in this Dissertation		251

Part I.

Background information and knowledges

1. Introduction

Nowadays the modern wind turbines are designed to work in varies conditions. Especially due to the high demands on wind in the future energy market, research and development of offshore wind are becoming more and more important. Fig.1.1 illustrates the environmental challenges that large offshore turbines need to face during their operations [46]. The non-uniform wind is one of the main sources which causes the loads and failures. The objective of the presented work is to develop a system to identify the non-uniform wind field and reducing of the loads which are caused by such wind.

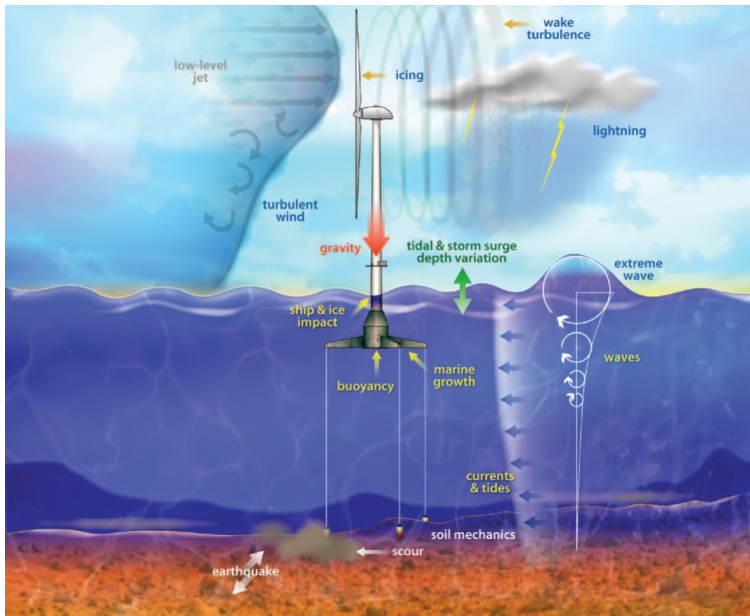


Fig. 1.1.: Illustration of environmental challenges for the modern offshore wind turbines [46]

1.1. Overview

The history of wind power can be tracked back to 3000 years ago. Back there wind was only used for providing mechanical power, such as to pump water. The wind turbines used for electricity generation purpose, which is called Wind energy conversion system (WECS), was first developed in the early 20th century. However, due to the unstable wind power, WECS were not recognized as a reliable and consistent power source. After the first oil

price shock in 1970s, the electricity generation from wind became more popular. With the next two decades of technological development and progress, wind turbine becomes one of the most important sustainable energy resources [1]. In 1985, WECS with 50 kW rated power and 15 m diameter was standard. But 20 years later the 5 MW wind turbine with 126 m diameter is commercialized. Nowadays the largest offshore WECS has 8 MW rated power and 164 m diameter. Furthermore, the research project "Upwind" demonstrates that a 20 MW wind turbine design with 250m rotor diameter is feasible (Fig.1.2) [7]. Until now

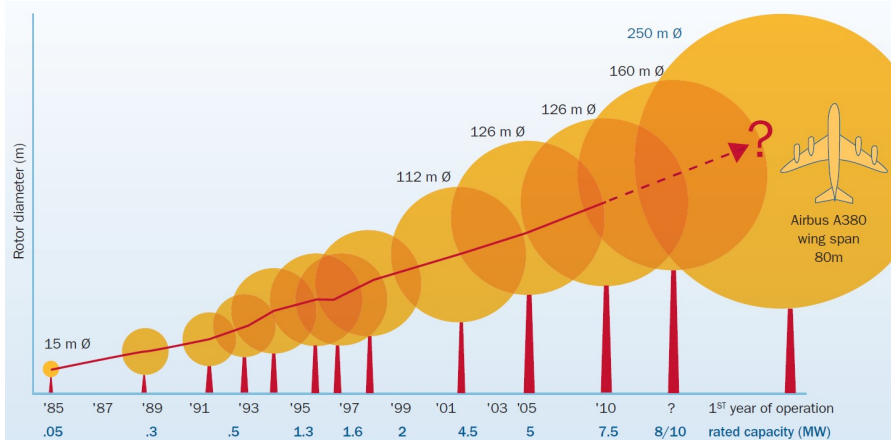


Fig. 1.2.: The growth of wind turbine in size [7]

only few offshore wind power plants have been installed due to the unknown lifetime of mechanical parts of the large offshore machines. Problems are caused by the high and complex loads on the turbines blades, internal mechanics, and towers by the wind speeds fluctuations, for example. These changes excite large transient forces due to rotor thrust and torque which place a heavy load on turbines. In order to reduce the loads to improve the reliability, advanced blades pitch control technology depending on the wind speed could greatly enhance the lifetime expectation. To develop such techniques, a full wind behaviour of shear and turbulence measurements and preview need to be taken into account.

So far, the industrial wind turbine pitch controllers which based on the FB methods use the generator speed information to control the blade pitch angles. This methods have limitations on the large wind turbine applications. Recent years the studies of Lidar assisted control technologies, such as FF control and Model Predictive Control (MPC), have often been used for research and developments [185]. These methods use wind Light Detection And Ranging (Lidar) systems to measure and predict the upstream wind field. The Two Degree of Freedom (2-DOF) FF/FB controller is one of the most used Lidar assisted control methods. FF controllers use an inversion model of wind turbine for predicting the future pitch angles based on the wind measurement data from a Lidar system. Meanwhile, the FB controller deals with the unpredicted factors [54,158]. However, the design of FF controller has limitation to deal with the system constrains which are very important in a real system. The MPC method based on optimal control strategy has the benefits to over cover this

issue by considering the system constraints. Recently, some researches have been applied MPC into wind turbine control and proof their benefits on reducing the fatigue loads and increasing the power capturing [76]. Nevertheless, all these methods require a wind measurement system for wind preview.

Lidar is a remote sensing technique for measuring properties of a distant target, such as distance or speed. Wind Lidar based on coherent Doppler Lidar (CDL) techniques have been proven as accurate, reliable remote sensing for wind velocities since 1970s [57,83]. CDL works on the principle of measuring the Doppler shift frequency of backscattering light due to atmospheric aerosols and molecules for obtaining the wind speed. The application of CDL for control of wind turbines as an upstream wind speed measurement tool was first proposed in 1989 [178]. In 2004, British government establishment QinetiQ patented a system for control of wind turbines, which sits in the hub of the wind turbines with the beam directing to the rotation axis of the rotor [72]. However such Lidar system based on a $1.5 \mu\text{m}$ fiber laser with a maximum measurement distance of 400 m currently sells for a price of ca.135,000Euro with the lifetime of about 5 years [187]. For a permanent or continuous use of this system on a wind turbine, the price is too high, thus only pilot projects and wind field measurements are performed. Therefore, the development of a cost efficient system for wind turbines becomes important.

1.2. Description of wind turbine systems

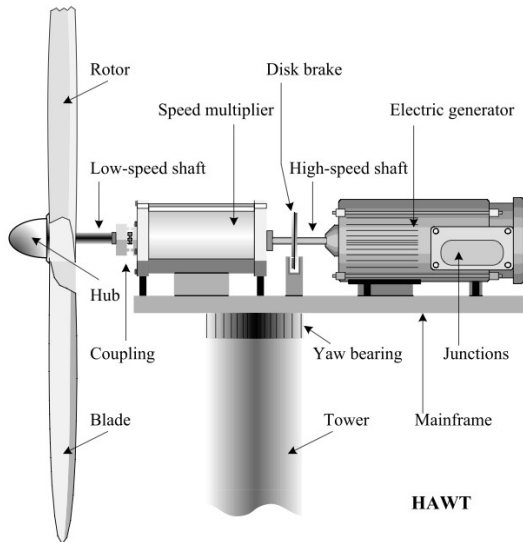


Fig. 1.3: Main components of a standard HAWT system [23]

A standard Horizontal axis wind turbine (HAWT) system has five different subsystems as shown in Figure 1.3. The aerodynamics subsystem consists of turbine rotor, blades, and hub to support the blades. A drive train subsystem includes a low speed shaft to

connect the rotor, a speed multiplier (gear box) to transfer the low speed rotation to a high speed in order to drive the generator, and a high speed shaft to connect the generator. The Permanent magnet direct-drive (PMDD) wind turbines connect the rotor directly to the generator without speed multiplier. The electromagnetic subsystem is the generator to convert the mechanical rotation energy into electrical energy. The electric subsystem is the electric systems for connecting to grid. The tower subsystem consists of the tower to support all the other parts, and a yaw system to direct the rotor perpendicular to the wind direction for maximizing the energy capture.

The WECS is designed to convert the wind energy into electricity. As shown on Fig.1.2, modern wind turbines have a rotor span diameter of more than 150 meters. The non-uniform wind distribution on this huge span area creates mechanical loads on different parts of the wind turbine systems. The mechanical loads applied into a wind turbine system consist of static and steady loads from the mean wind speed; cyclic loads from vertical and horizontal wind shares, system yaw errors and motions, and blades gravities; stochastic loads due to the wind turbulence; resonance induced loads due to the excitations at near the designed natural frequency of the structure dynamics [169]. The cyclic and stochastic loads can be grouped as fatigue loads which lead to fatigue damages, due to the fluctuating winds applied to wind turbines. The fatigue loads affect the lifetime which can be expressed with the Cyclic Stress to Number to Failure (S-N) curve (Figure.1.4). Commercial WECS are normally designed for 20 ~ 30 years lifetime.

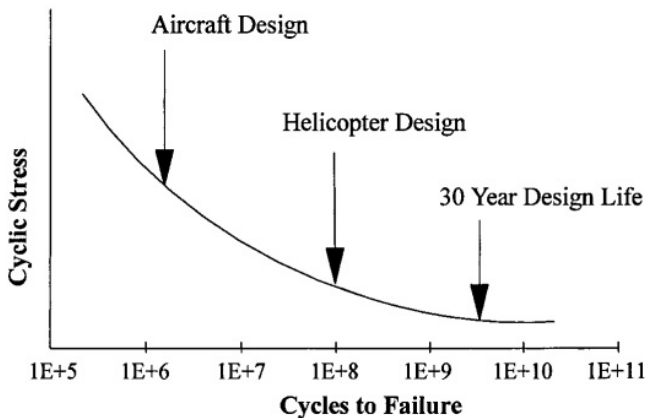


Fig. 1.4: Schematic S-N diagram for various fatigue critical structures [169]

The failures and damages on the drive-train (gearbox and generators) and blades were big problems for an operational wind turbines which are major parts of the cost of wind turbine components as shown on Fig.1.5. Thereby, the 30% failures rate of drive-train and blades are responsible for the 60% cost of the entire wind turbines. Fig.1.6 illustrates examples of the failure on a drive-train system of wind turbine.

It is extremely important to design the system structure to fulfil the long lifetime requirement. Furthermore, when scaling up the size of the wind turbine, due to the higher loads amplitude, the mass of rotor and tower growth with cubic order of the rotor size (Fig.1.7 and 1.8). However, the power extracted from air only increases with square of the rotor size

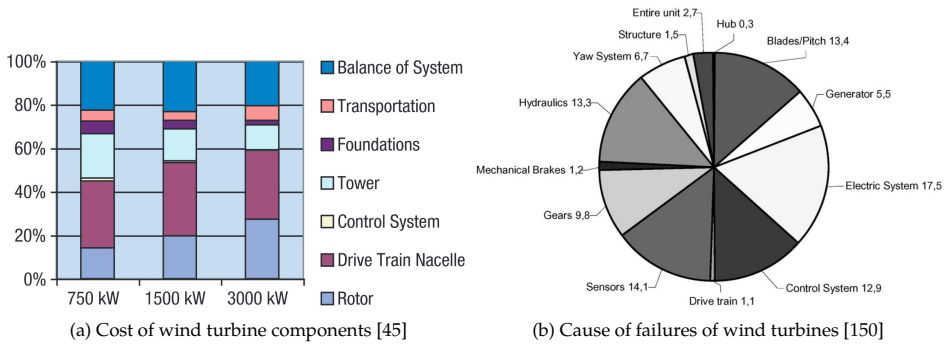


Fig. 1.5.: Cost breakdown of a wind turbine and their failures rates



(a) Damages on the gearbox bearing (Source: NOAA) (b) Generator failure by over speed (Source: BBC)

Fig. 1.6.: Damages and failure examples on the drive-train of a wind turbine

as described with Eq.(2.5). Therefore, up-scaling the wind turbine leads to a significant increase of mass, which directly corresponds the increasing of material cost of the turbine construction.

1.3. Contributions and approach of the present work

Lidar wind remote sensing and the control of wind turbine based on Lidar preview measurement are state of the art technologies. However, the high cost of Lidar system limited their application on the commercial wind turbine. The presented work focused on two parts: the developing of a cost efficient Lidar system and the development of a preview control for the active wind turbine pitch system. The Lidar system design part is unique by introducing a broad spectrum semiconductor laser with a relative shorter coherence length. The predictive pitch controller design part is focused on developing of an industry-friend

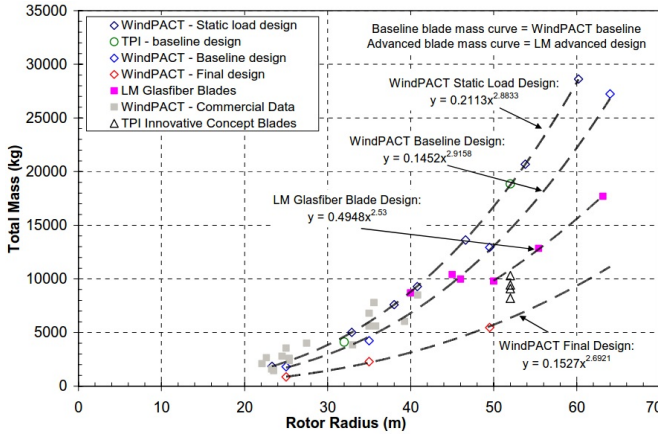


Fig. 1.7: Tower mass scaling with swept area of rotor [52]

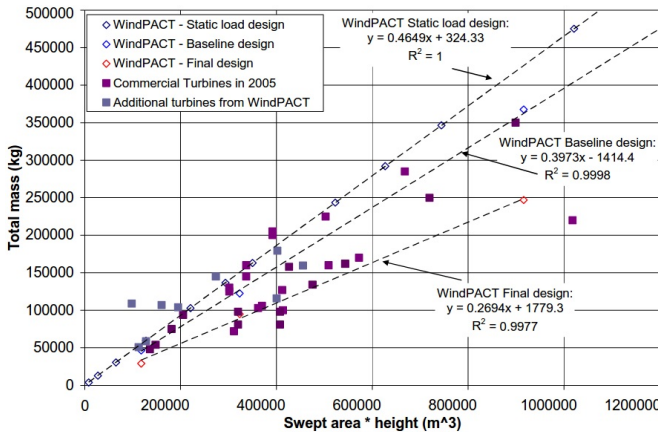


Fig. 1.8: Blades mass scaling with swept area of rotor [52]

concept by introducing the advanced model predictive controller into the conventional PI feedback controller without destroy the original controller.

1.3.1. Approach of the present work

State of the art Doppler wind Lidar systems commonly use fiber lasers with couple kilometres coherence length. Normally, the broad spectrum lasers are not used in a coherent Doppler Lidar system, due to the high phase noise. However, such lasers cost much less than the fiber lasers. The presented approach is developed based on the previous research of using a super continuum laser on a frequency domain Optical Coherence Tomography (OCT) system for paper production applications [24]. With this approach, the price of laser source can be dramatically reduced, on the other hand, the coherence length of laser can be used to define a constant probe length on a CW Doppler Lidar system.

For designing of such Lidar systems, first of all, a systematic consideration both from the sensor design structure point of view and the requirement from the pitch control point of view are analysed and discussed. Then, a simulator to simulate different parts of the Lidar components is designed. The simulator consists two different parts; a static simulation perform a calculation of receiving power and system signal to noise ration. This simulation calculates the back-scattering for each particle and sums up the individual back-scattering to form the Lidar signal without considering the movement of particles and propagation time of lasers. A dynamic simulation is a modified Feuillette model which slices the atmosphere into small elements. Within each elements, assuming the optical properties and the moving speed of aerosols are the same. By propagating the laser beam to each atmosphere slices, the back-scattering signals with time delays are generated. With this model, a time domain full system simulation can be processed.

Finally to design the Lidar system, a step wise experimental realization process is performed. Within this process, various free space experimental setups are designed and build up to evaluate different parts.

Meanwhile, to apply such Lidar system into applications, an industry friendly pitch control approach named 2-DOF Receding Horizon/Feedback Control (2-DOF RHC/FB) control is designed. This approach is based on the research by T. Hatanaka et.al. [73] for controlling of an electrodynamic shaker. The design concept is similar to the standard 2-DOF Feedforward/Feedback (2-DOF FF/FB) controller, where the FF term is designed with an optimal predictive control approach Receding horizon control (RHC) to take system constrains into the controller design.

The designed controller creates the pitch commands with the RHC method based on the Lidar preview wind measurements and adds to the original FB control loop without modify the original controller. Therefore, even the predictive controller is not working proper, the original PI(D) FB controller still can control the system to be stable. Figure 1.9 illustrates the general idea of the present concept.

1.3.2. Outline of this thesis

As briefly discussed on this chapter, under the long term motivation of reducing the cost of wind energy. A cost efficient engineering solution to extend the lifetime of wind turbine, reducing the fatigue and extreme loads of wind turbine system is developed.

Chapter 2 to 3 describe the background and theories of this work. The main working contents in this thesis can be divided into two major parts: Part II, includes chapter 4 to chapter 6, describes the design of the cost efficient Lidar system based on a broad spectrum diode laser. Chapter 4 describes the design structure and system requirements. Chapter 5 shows the simulation of the Doppler Lidar system for assisting of the Lidar system design. Chapter 6 illustrates the experimental realization process of evaluation the feasibility of the cost efficient Doppler wind Lidar system.

Part III is the development of the 2-DOF RHC/FB controller, a control method combines the RHC for predictively generating the pitch commands based on the Lidar preview measurement and a FB controller to deal with the unpredictable and unmeasurable disturbances.



Fig. 1.9.: Sketch of the general idea of Lidar assisted wind turbine pitch control system (Background picture source: Microsoft office template)

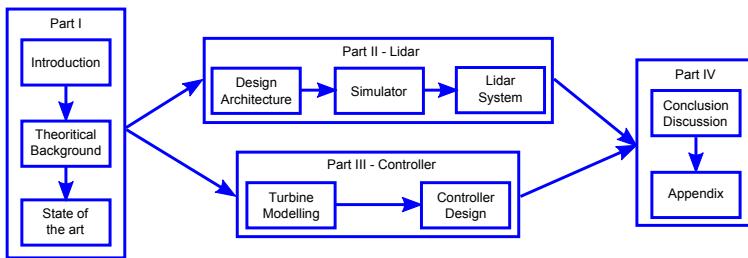


Fig. 1.10.: Sketch diagram of the thesis structure

Chapter 7 describes the modelling of a wind turbine, chapter 8 shows the design of the collective pitch controller based on a linearised model. Chapter 9 concludes the thesis and discusses the problems and topics.

2. Background knowledge of wind energy

Due to the increasing of overall energy consumption and pressing social expectations, wind energy is facing many challenges in development and applications. Nowadays larger wind turbines, are set up in difficult to access locations such as offshore. Such locations bring an overhead in Operations and Maintenance (O&M) costs caused not only by irregular maintenance but also the high accessibility expenses. In this chapter, the background knowledge of wind energy and the theory basis of Doppler wind Lidar system are presented.

2.1. Background of wind energy

The worldwide energy consumption is growing at a rate of around 2.5% each year. As shown in Fig.2.1, the major energy resource is coming from fossil fuel (coal, oil, and nature gas) [21]. However, fossil fuel is the main source of greenhouse gases emission as well. In 2010 the European Union (EU) has set up a goal to reduce the greenhouse gases emission by 20% in 2020 and for a long term target of 80% to 95% cut until 2050 [33].

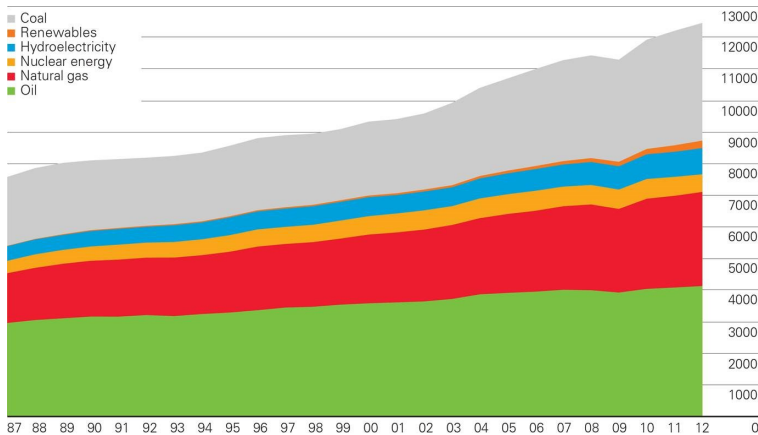


Fig. 2.1.: Primary energy world consumption Million tones oil equivalent [21]

Nuclear power plants are another major power resource for electricity generations. However, their safety issues, especially after the Chernobyl accident in Ukraine in 1986 and the 2011 Japan Fukushima disaster, the public fear of nuclear disaster is becoming a strong obstruction of their growth. According a survey in 2007, 71% of the EU citizens supported wind energy, while coal was supported by 26% and nuclear by only 20% [49]. As an example,

after the Fukushima disaster, large anti-nuclear protests occurred in Germany which lead to the nuclear power plants phase out by 2022 [100].

Under the pressure of reducing the share of fossil fuel and nuclear in the future energy scenario, a big chance comes to the renewable energy. Although, the renewable energy only takes a small part in the energy productions, they are still the fastest growing sources in the last decade. According to an International Energy Agency (IEA) report at 2013, from 2006 to 2012 renewable energy increased 1330 TWh. Furthermore, until 2018 it is expected to increase another 1990 TWh to reach 25% of total global gross power generation and become the second largest electricity generation resource [84].

Wind and photovoltaic (PV) are the major renewable sources which drive the fast growth. Wind energy increased the capacity from 6.1 GW in 1996 to 318.1 GW in 2013 which means an annual growth rate of 26% Fig.2.2 [66]. A totally 117.3 GW wind power has been installed until 2013 in EU. In a normal wind condition around 257 TWh electricity can be produced to cover around 8% of overall EU electricity consumption [142]. Furthermore, until 2020 a 230 GW total wind power installation is estimated by European Wind Energy Association (EWEA) to cover 15-17% EU electricity consumption. This share is expected to rise up to 28.5% in 2030 (totally 400 GW wind power installation, 150 GW of which should be offshore) [51]. Then, in 2050 the total cumulative wind power targets to 785 GW for a 50% share of overall electricity capacity, more than half of this capacity should be offshore [50]. Therefore, offshore wind powers are going to provide a major part of the future electric generation.

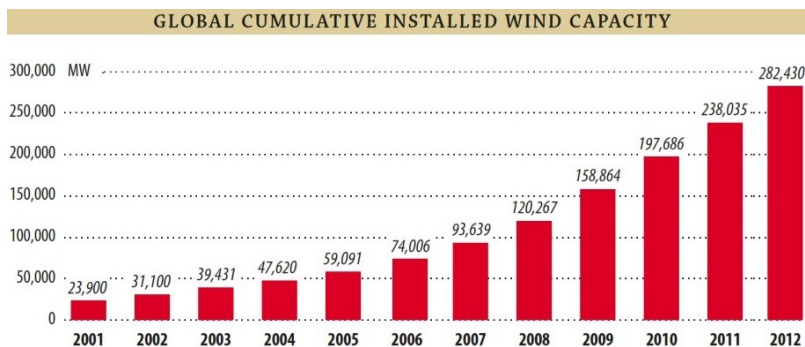


Fig. 2.2.: Global cumulative installed wind capacity 2001-2012 [66]

To fulfil this significant growth, development on new technologies and up-scaling of wind turbines to reduce the Levelized cost of energy (LCOE) becomes most important. The study report from Fraunhofer ISE shows the LCOE of onshore wind power has a compatible price level compared to fossil fuel power plants (ca. 0.045 to 0.107 Euro/kWh). However, the offshore wind energy still has potential to lower down their price (Fig.2.3) [107].

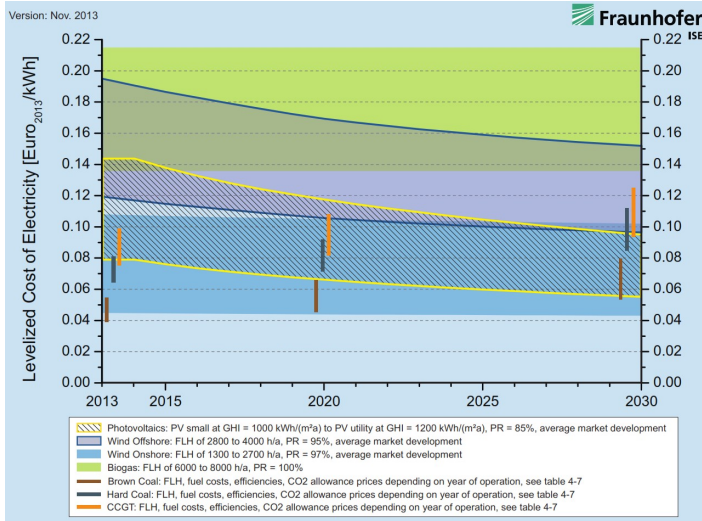


Fig. 2.3.: A prediction of the LCOE of different renewable energy technologies and conventional power plants in Germany by 2030 [107]

2.1.1. Working principles of wind turbines

The work principle of HAWT can be described with the stream tube concept (Fig.2.4) and the blade element theory [59]. The simplest model of wind turbine is actuator disc model by replacing the turbine with a circular disc. This model with stream tube theory explains energy extraction process as given with Eq.(2.1). The air stream flow with a velocity U_∞ , air density ρ , area of the cross-section A_∞ , passes through the disc. When the energy is extracted, wind speed slows down but only the mass of air which passed through the rotor disc is affected. As shown in Fig.2.4, a boundary surface is used to show the affected air mass and this boundary surface can be extended to form a stream-tube. If no air exchange across the boundary, the mass flow rate of the air along the stream-tube will be the same for all positions. The kinetic energy of the air in the stream-tube decreased. Therefore, the air slows down and the cross-sectional area will expand to accommodate the slow air [23].

$$\rho A_\infty U_\infty = \rho A_D U_D = \rho A_W U_W \quad (2.1)$$

here, A_D , U_D denotes the cross-sectional area and velocity at the disc position, A_W refers in the far wake position. The actuator disc induces a velocity variation which must be superimposed on the free stream velocity. Define the variation of velocity as $(-a_{\text{Ind}} U_\infty)$, where a_{Ind} is axial flow induction factor, leads to wind flow velocity at disc U_D and far wake position U_W to be described with Eq.(2.2).

$$U_D = U_\infty(1 - a_{\text{Ind}}), U_W = U_\infty(1 - 2a_{\text{Ind}}) \quad (2.2)$$

The force on the air becomes

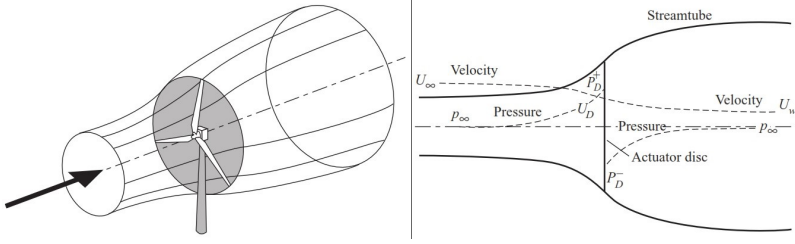


Fig. 2.4.: Illustration of the actuator disc model and stream tube theory [59]

$$T = (P_D^+ - P_D^-)A_D = 2\rho A_D U_\infty^2 a_{\text{Ind}}(1 - a_{\text{Ind}}) \quad (2.3)$$

The power extracted from the air by the rotor disk is given as Eq.(2.4).

$$P_{\text{Rtr}} = T U_D = 2\rho A_D U_\infty^3 a_{\text{Ind}}(1 - a_{\text{Ind}})^2 \quad (2.4)$$

The power of the air flow P_{Air} with a constant wind speed U_∞ is given as Eq.(2.5).

$$P_{\text{Air}} = \frac{d}{dt}(E_{\text{Air}}) = \frac{d}{dt}\left(\frac{1}{2}m_{\text{Air}}U_\infty^2\right) = \frac{1}{2}\rho A_D U_\infty^3 \quad (2.5)$$

Where, E_{Air} is the energy of the air flow, m_{Air} is the air mass of the flow. The power coefficient C_p of wind turbine is given by the power captured with the rotor disk P_{Rtr} (Eq.(2.4)) divide by the power available in the air flow P_{Air} [59].

$$C_p = \frac{P_{\text{Rtr}}}{P_{\text{air}}} = \frac{2\rho A_D U_\infty^3 a_{\text{Ind}}(1 - a_{\text{Ind}})^2}{0.5 \cdot \rho A_D U_\infty^3} = 4a_{\text{Ind}}(1 - a_{\text{Ind}})^2 \quad (2.6)$$

The maximum power efficiency is given as $C_p = 16/27 \approx 59.3\%$ (when $a_{\text{Ind}} = 1/3$) which is known as Lanchester-Betz limit [11, 12]. C_p is a nonlinear function of the turbine Tip Speed Ratio (TSR), λ_{TSR} , (Eq.(2.7)) and blade pitch angle β_{Pitch} .

$$\lambda_{\text{TSR}} = \frac{\omega_{\text{Rtr}} \cdot R_{\text{Rtr}}}{U_{\text{wind}}} \quad (2.7)$$

here, ω_{Rtr} is the rotor rotational speed, U_{wind} is the wind speed, R_{Rtr} is the radius of the rotor. Blade element model describes the forces, torque and captured power produced by the airflow on a blade to explain the aerodynamics phenomena such as stall and aerodynamic loads. Fig.2.5 illustrates the forces on a transverse cut of blade elements. The relative moving speed of the blade element and air flow is U_{rel} , which is the composition of the upstream wind speed U and the tangential blade element speed Ω_{tr} . The airflow passes the rotor which creates a pressure difference around the blade element. Therefore, a force

perpendicular to the air flow direction, lift force f_L , is created. Meanwhile, in the flow direction a drag force f_D is established as Eq.(2.8b) [59].

$$f_L = 0.5 \cdot \rho c V_{rel}^2 C_L(\alpha) \quad (2.8a)$$

$$f_D = 0.5 \cdot \rho c V_{rel}^2 C_D(\alpha) \quad (2.8b)$$

here C_L and C_D are the lift and drag coefficients, c is the chord length of blade element, α_{inc} is the incidence angle (angle between the flow and chord) $\alpha_{inc} = \phi - \beta_{Pitch}$. ϕ is the angle between the flow direction and rotor plane, β_{Pitch} is the blade pitch angle which is defined as the angle between the chord and the rotor plane. The lift and drag force can be resolved into axial thrust force f_T perpendicular to the rotor plane and tangential forces f_R along with the rotor plane which develops the rotational torque τ_{Rtr} .

$$f_T = 0.5 \cdot \rho c U_{rel}^2 (C_L(\phi - \beta) \cos(\phi) + C_D(\phi - \beta) \sin(\phi)) \quad (2.9a)$$

$$\tau_r = 0.5 \cdot \rho c V_{rel}^2 r (C_L(\phi - \beta) \sin(\phi) + C_D(\phi - \beta) \cos(\phi)) \quad (2.9b)$$

Fig.2.5 shows that the lift force develops useful torques while the drag force opposes it. Therefore, a higher C_L/C_D ratio has high conversion efficiency.

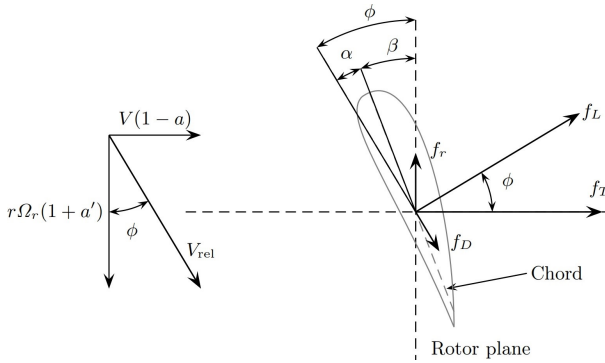


Fig. 2.5: Illustration of the forces on a wind turbine blade element [59]

2.1.2. Classification of wind energy systems

HAWT can be classified according to speed and power control ability, leading to wind turbine classes differentiated by the generating system (speed control) and the method employed for limiting the aerodynamic efficiency (power control). The speed-control criterion leads to two types of HAWT: fixed-speed and variable-speed, while the power control ability divides HAWT into two fixed-pitch and variable-pitch. Therefore, HAWT can be classified into four categories.

1. Fixed-Speed (FS) - Fixed-Pitch (FP) HAWT
2. FS - Variable-Pitch (VP) HAWT

3. Variable-Speed (VS) - FP HAWT

4. VS - VP HAWT

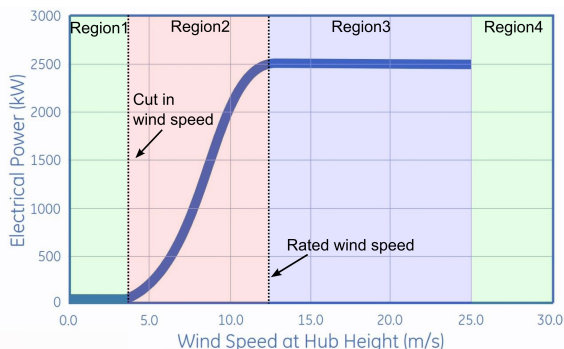


Fig. 2.6: Power curve of a commercial wind turbine "GE TC3 2.5-103" rated power of 2.5MW, and its operation ratios for different wind speeds [44]

The operation of WECS can be divided into 4 regions depending on the wind speed (Fig.2.6). Under the cut-in wind speed, the generator is not connected to the grid, therefore no power is produced in Region 1. When the wind speed increases, the generator is connected to start producing electricity (Region 2). In this region the generator speed is under the rated speed, the control objective is to extract as much power as possible from the wind flow. The fixed pitch operation is commonly used. When the wind speed increases above rated, the generator produces at nominal power (Region 3). The wind speed is high therefore the control is to keep the generation power on the rated value to avoid overloading. In this region a variable pitch system control the pitch angle in order to keep the optimal rotor speed to get a stable working condition to reduce the mechanical loads on turbines. When the wind speed is above the cut-off speed (Region 4), the generator is disconnected and the turbine is stopped in the strong wind condition.

2.1.2.1. Fixed-Speed (FS) HAWT system

FS-HAWT systems are the pioneers on wind turbine industry. They use induction generators, such as Squirrel-Cage Induction Generators (SCIG), to directly connect to grid, giving them an almost constant rotor speed stuck to the grid frequency, regardless of the wind speed. Since the FS-FP systems do not require additional dynamical pitch system, they are simple and low cost. Therefore, before 1990s FS-FP HAWT has been the dominant configuration. However, since no active control can be done to alleviate the mechanical loads and improve power conversion quality, the conversion efficiency is far from optimal [13]. FS-FP HAWT systems are normally using the stall effect to regulate the power at region 3.

Fig.2.7 illustrates the stall effect on an airfoil blade. When the flow attacks at a small angle (Fig.2.7 left), the boundary layers developed on the upper and lower surfaces of the airfoil do not separate, no wake occurs. While increasing the incident angle leads to flow separation (Fig.2.7 right), wake occurs and lift decreases. The (passive) stall controlled HAWT have the blade aerodynamics designed as stall occurring at the rated wind speed. When the speed increases over rated, the blades start to stall, then the lift force drops and the drag increases

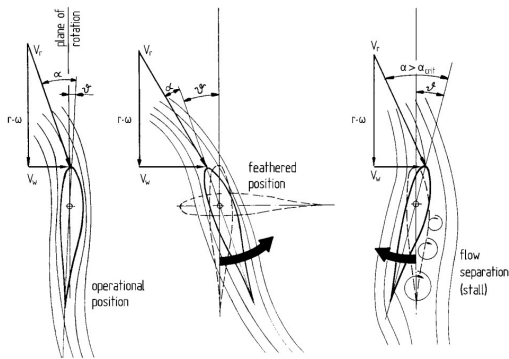


Fig. 2.7: Illustration of stall and feather effect for different incident angle to the blade [59]

to reduce the rotor torque. Stall controls were widely used by some manufactures until 1990s for FS-HAWT with power below 1.5 MW [143]. However, aerodynamic performance of stall controlled HAWT is not optimum, because the blade design needs to consider the stall effects. Therefore, this technique is not state of the art anymore.

The variable pitch system has been developed and employed commercially for the medium to high power HAWT systems. Under the rated wind speed in region 2, turbine operates with a FP system to allow max power capture. In above rated wind speed (region 3), the power is limited by controlling the pitch angle. Two power control methods are commonly used: pitch-to-feather which is conventionally referred as pitch angle control and pitch-to-stall which is also named active stall control. Within the pitch-to-feather methods, the controller regulates the pitch angle to adjust the lift force in order to keep the torque in the rotor plane constant. In contrast, within the pitch-to-stall methods, the controller adjusts the pitch angle to reinforce stalls which decrease lift whereas increase drag to keep the force in the rotor plane constant [187]. Since the FS-HAWT generator almost rotates in a constant speed, the maximum power conversion only can be attainable at a single wind speed. Therefore, the energy conversion efficiency is low, and the wind fluctuation directly leads to unstable output power for grid which causes disturbances to power system.

2.1.2.2. Variable-Speed (VS) HAWT system

VS-HAWT systems are the most common WECS currently. The decoupling between generator system and grid make them more flexible in terms of control and optimal operation.

Doubly fed induction generator (DFIG) based WECS with a high-speed generator is the industry standard since 1990s. It uses electrically excited copper windings on both rotor and stator to create magnetic fields. When the rotor spins, interaction between these magnetic fields generates electricity. The rotor is controlled by the power converter to keep the generator synchronized with the grid while rotor speed is varies. The stator is directly connected to the grid and feed the electricity to the grid without losses. Only little part of the energy is lost through the power converter.

permanent magnet synchronized generator (PMSG) are often used with VS-HAWT systems as well. PMSG works at low speed and convert full power directly to output. Between the grid and generator, a full power converter is used. In low speed region, since PMSG does not need a current injection, it provides higher efficiency than DFIG.

Furthermore, the high controllability offered by the VS operation is a powerful advantage in achieving higher wind energy penetration levels. The VS operation allows the rotational speed of the wind turbine to be continuously adapted (accelerated or decelerated) in such a manner that the wind turbine operates constantly at its highest level of aerodynamic efficiency. While FS-HAWT are designed to achieve maximum efficiency at one wind speed, VS-HAWT achieve maximum efficiency over a wide range of wind speeds. Furthermore, VS operation allows the use of advanced control methods to reduce mechanical stress, acoustical noise, and increase power capture [23, 166].

2.2. Working principle of Doppler wind Lidar

Coherent Doppler wind Lidar systems work on the principle of measuring the Doppler frequency due to the movement of atmospheric aerosols and molecules for obtaining the wind velocity. A laser beam is projected into the atmosphere where aerosols and molecules scatter the laser beam. The backscattered laser is Doppler shifted in frequency by an amount proportional to the Line-of-Sight (LOS) velocity of the aerosols and molecules. By collecting the scattering light and analysing the Doppler frequency, the LOS wind speed is estimated.

Fig.2.8 shows a bistatic Lidar concept, where a transmitter is placed an angle ϕ_{TR} with the receiver. The transmitter has a light frequency ν_{Inc} , assuming the wind flow has an angle of ϕ_x with transmitter and ϕ_r with receiver. The scattering light is shifted to the frequency of $\nu_p = \nu_x + (V/\lambda) \cos \phi_x$, and light received at receiver obtains a frequency of $\nu_t = \nu_p + (V/\lambda) \cos \phi_r$. The Doppler frequency shift caused by wind flow is $\nu_{Dopp} = \nu_r - \nu_x = \frac{V}{\lambda} (\cos \phi_x + \cos \phi_r)$ [62]. If the system is monostatic ($\phi_x = \phi_r = \phi_{TR}$), the Doppler frequency shift is $\nu_{Dopp} = \frac{2V}{\lambda} \cos \phi_{TR}$.

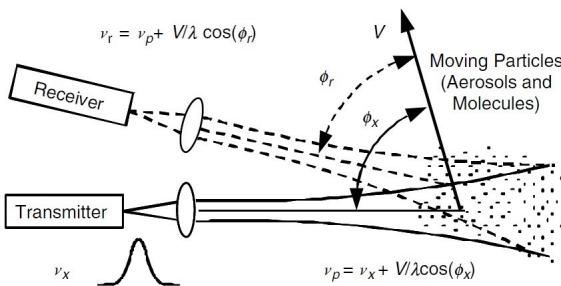


Fig. 2.8: A bistatic wind Lidar concept [62]

2.2.1. Lidar equation

Fig.2.9 illustrates the measurement geometry of a standard pulsed Lidar system. A laser pulse is transmitted into the atmosphere with a length of τ_{pulse} which gives a probe length of $\Delta R = c\tau/2$. Assuming the transmitted laser power P_L , due to the extinction during atmospheric transmission, the power reached at probe volume is becoming $P_{\text{inc}} = P_L \cdot T(\lambda, R)$, where $T(\lambda, R)$ is transmission term which is given as

$$T(\lambda, R) = \exp \left[- \int_0^R \alpha(\lambda, r) dr \right] \quad (2.10a)$$

$$\alpha(\lambda, R) = \sum_j N_j(R) \delta_{j, \text{ext}}(\lambda) \quad (2.10b)$$

Where α_{ext} is extinction coefficient, σ_{ext} is the particle extinction cross section which

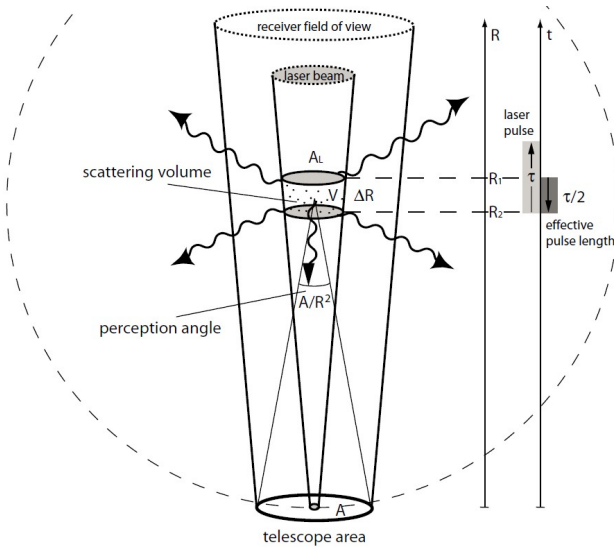


Fig. 2.9: Illustration of the Lidar system geometry [126]

includes scattering σ_{sca} and absorption σ_{abs} , $N_j(R)$ is particle concentration in the probe volume at distance R , where j denotes different type of particles. For a short range Lidar system, the absorption loss can be ignored, therefore, $T(\lambda, R) = 1$. Assuming that the backscattering coefficient is $\beta_\pi = \beta_{\text{mol}}(\lambda, R) + \beta_{\text{aer}}(\lambda, R)$ which includes the backscattering from molecular β_{mol} and aerosol β_{aer} , the backscattering power in the probe volume is given as $P_{\text{sca}} = P_{\text{inc}} \cdot \beta(\lambda, R) \cdot \Delta R$, where back scattering coefficient β_π is given as

$$\beta(\lambda, R) = \sum_j N_j(R) \frac{ds_{j, \text{sca}}(\pi, \lambda)}{d\Omega} \quad (2.11)$$

Here σ_{abs} is the scattering cross-section, $\frac{d\sigma_{\text{sca}}(\pi, \lambda)}{d\Omega}$ illustrates differential backscattering cross section with incident light wavelength λ_0 . Varies researcher used different aerosol backscatter coefficient, details data value can be found from Table.2.1. The backscattering coefficient at different height can be expressed as

$$\beta(z) = \beta_0 \exp(\gamma z). \quad (2.12)$$

Assuming backscattering light from probe volume can be fully collected by receiver. The received power at telescope is $P_{\text{rec}} = P_{\text{sca}} \frac{A_{\text{L}}}{R^2}$. Let the collection and system efficiency are η_{coll} , η_{sys} , the detected Lidar signal power is given as Lidar equation, Eq.(2.13) [126].

$$P_{\text{rec}}(\lambda, R) = P_{\text{L}} \cdot [\beta(\lambda, R) \cdot \Delta R] \cdot \frac{A_{\text{L}}}{R^2} \cdot \eta_{\text{coll}}(R) \cdot \eta_{\text{sys}}(\lambda) \quad (2.13)$$

Where, P_{rec} is the detector receiving power from distance R with laser wave length of λ_0 . P_{L} describes the transmitted laser power, β_{π} is the backscattering efficient together with the scattering volume ΔR , $[\beta(\lambda, R) \cdot \Delta R]$ shows the probability of the light being scattered by the objects. $[\frac{A}{R^2} \eta_{\text{coll}}(R)]$ describes the range dependent collection efficiency, A is the effective area of the receiver aperture, η_{coll} is the collection efficient. η_{sys} describes general system losses, e.g. reflection from the surface of optical components.

Table 2.1.: Summary of backscattering coefficient values [118]

Authors	Measured β at wavelength ($\text{m}^{-1}\text{sr}^{-1}$)	β scaled to $1.55\mu\text{m}$ ($\text{m}^{-1}\text{sr}^{-1}$)	Note
Gras and Jones [65]	$10^{-10} \sim 10^{-8}$ @ $10.6\mu\text{m}$	$5 \times 10^{-9} \sim 5 \times 10^{-7}$	$< 2\text{km}$
Bibro et.al. [14]	$10^{-10} \sim 10^{-5}$ @ $10.6\mu\text{m}$	$5 \times 10^{-9} \sim 5 \times 10^{-4}$	
Tothornel and Jones [151]	$10^{-8} \sim 10^{-7}$ Summer $10^{-9} \sim 10^{-8}$ Winter @ $10.6\mu\text{m}$	$5 \times 10^{-7} \sim 5 \times 10^{-6}$ $5 \times 10^{-8} \sim 5 \times 10^{-7}$	Sea level values
Post [144]	$2 \times 10^{-10} \sim 2 \times 10^{-8}$ @ $10.6\mu\text{m}$	$2 \times 10^{-8} \sim 1 \times 10^{-6}$	4km altitude
Hawley et.al. [74]	2×10^{-6} @ $1.06\mu\text{m}$ 2×10^{-9} Modeled	1×10^{-7} 1×10^{-10}	Sea level 15km altitude
Targ et.al. [170], Post et al. [145], Menzies et.al. [122], Kent et al. [104]	1.28×10^{-6} @ $2.09\mu\text{m}$ (Modeled) 5.12×10^{-8} @ $10.59\mu\text{m}$ (measured)	2.4×10^{-6}	
Kane et.al. [102]	10^{-9} @ $1.06\mu\text{m}$ Mod- eled	5×10^{-10}	Very clean air
Menzies [121]	6×10^{-8} @ $0.5\mu\text{m}$ 2×10^{-10} @ $9.25\mu\text{m}$	7×10^{-9}	5 km altitude

2.2.2. Coherent detection

Coherent detection (Heterodyne/Homodyne detection) is a method which was originally developed in the field of radio waves and microwaves. There, a weak signal of interest is mixed with a stronger reference in a nonlinear device such as a rectifier, and the resulting mixing product is then detected, often after filtering out the original frequency. The beat frequency is the sum or difference of the signal and reference frequencies [136]. Fig.2.10 shows a sketch of a modified Mach-Zehnder interferometer for coherent detection.

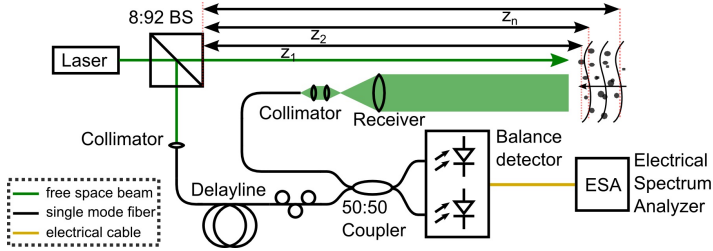


Fig. 2.10.: A modified Mach-Zehnder interferometer for coherence detection

The reference beam can be expressed in complex electrical wave form as

$$E_{\text{ref}} = A_{\text{ref}} \cdot \exp(-j \cdot 2\pi \cdot (\nu_{\text{ref}}\tau + z_{\text{ref}}/\lambda)) \quad (2.14)$$

Here A_{ref} is electrical field amplitude, ν_{ref} and λ_0 are light frequency and wavelength, z_{ref} is optical path distance of the reference beam. The backscattering signals from each aerosols can be described in complex wave form as

$$E_s(i) = A_s(i) \cdot \exp(-j2\pi \cdot (\nu_s\tau + 2z_i/\lambda)) \quad (2.15)$$

Aerosols are located at different location z_i (Fig.2.11), then the signal collected by detector

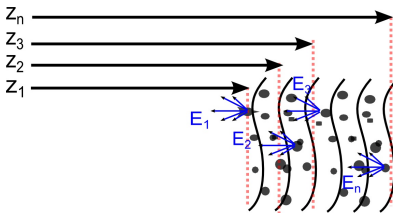


Fig. 2.11: Model of the backscattering from different particles

is the integral over all backscattering signal from each particles.

$$E_s = \sum_{i=0}^N A_s(i) \exp(-j2\pi \cdot (\nu_s\tau + 2z_i/\lambda)) \quad (2.16)$$

Therefore, the mixed electrical field at detector is given as

$$E_{\text{out}} = A_{\text{ref}} \cdot \exp\left(-j2\pi\left(\nu_{\text{ref}}t + \frac{z_{\text{ref}}}{\lambda}\right)\right) + \sum_{i=0}^N A_s(i) \cdot \exp\left(-j2\pi\left(\nu_s t + 2z_i/\lambda\right)\right) \quad (2.17)$$

The detector has a cut-off frequency typically less than GHz which is not fast enough to respond the light frequency. Therefore, the light frequency is detected as DC. The optical power is proportional to the irradiance of electrical wave which is given as Eq.(2.18) [88].

$$\begin{aligned} P_{\text{out}} &= \left\langle \left| A_{\text{ref}} \exp\left(-j2\pi\left(\nu_{\text{ref}}t + \frac{z_{\text{ref}}}{\lambda}\right)\right) + \sum_{i=0}^N A_s(i) \exp\left(-j2\pi\left(\nu_s t + \frac{z_i}{\lambda}\right)\right) \right|^2 \right\rangle \\ &= \frac{1}{2}(P_{\text{ref}} + P_{s1} + P_{s2} + \dots), \quad [\text{DC Terms}] \\ &+ \sum_{i=0}^N \gamma(z_i - z_{\text{ref}}) \sqrt{P_{\text{ref}} P_{s_i}} \exp\left(-j(\nu_{s_i} - \nu_{\text{ref}})t + \frac{2\pi}{\lambda}(z_i - z_{\text{ref}})\right), \quad [\text{Cross correlation}] \\ &+ \sum_{i=0}^N \gamma(z_i - z_j) \sqrt{P_{s_j} P_{s_i}} \exp\left(\frac{2\pi}{\lambda}(z_i - z_j)\right), \quad [\text{Auto correlation}] \end{aligned} \quad (2.18)$$

The output power at the detector can be separated into three parts:

- 1) The DC term, $\frac{1}{2}(P_{\text{ref}} + P_{s1} + P_{s2} + \dots)$, has a higher frequency than the cut off frequency of detector. Therefore, it results as the mean of light power on detector.
- 2) The cross correlation term, which is the desired component on the coherent Doppler Lidar, carries the Doppler frequency $\nu_{\text{Dopp}} = \nu_i - \nu_{\text{ref}}$. When mixing the backscattering light in the detector, phase noises are added into the detection due to the random position of particles carrying different light path distances to the detector.
- 3) An auto correlation term represents the interference occurring between the scatterings from different particles, which causes the speckle effects.

The photo current i_{det} , produced by the photo detector from the optical power is

$$i_{\text{det}}(t) = \frac{e\eta_{\text{quan}}}{h\nu} \cdot P_{\text{out}}(t) \quad (2.19)$$

Where, $e = 1.6 \times 10^{-19}$ is electron charge, η is quantum efficiency of detector, h is Planck's constant, ν is optical frequency. Thus, the detector photo current is

$$\begin{aligned} i_{\text{det}} &= \frac{e\eta_{\text{quan}}}{2h\nu} \left\{ \sum_i (P_{s_i} + P_{\text{ref}}) + \sum_{i=0}^N \gamma(\Delta z_i) \sqrt{P_{\text{ref}} \cdot P_{s_i}} \cdot \exp\left(-j\nu_{\text{Dopp}}t + \frac{2\pi}{\lambda}\Delta z_i\right) \right. \\ &\quad \left. + \sum_{i,j=0}^N \gamma(\Delta z_{i,j}) \sqrt{P_{s_j} \cdot P_{s_i}} \cdot \exp\left(\frac{2\pi}{\lambda}\Delta z_{i,j}\right) \right\} = i_{\text{DC}} + i_{\text{Dopp}} + i_{\text{Noise}} \end{aligned} \quad (2.20)$$

Therefore, the DC current and Doppler frequency term can be written as

$$i_{\text{DC}} = \frac{e\eta_{\text{quan}}}{2h\nu} \left(\sum_i P_{si} + P_{\text{ref}} \right) \quad (2.21a)$$

$$i_{\text{Dopp}} = \frac{e\eta_{\text{quan}}}{2h\nu} \sum_i \sqrt{P_{si} \cdot P_{\text{ref}}} \cdot \exp \left(-j2\pi\nu_{\text{Dopp}}t + \phi_{\text{Dopp},i} \right) \quad (2.21b)$$

$$i_{\text{Noise}} = \frac{e\eta_{\text{quan}}}{h\nu} \sum_{i,j=0}^N \gamma \left(\Delta z_{i,j} \right) \sqrt{P_{sj} \cdot P_{si}} \exp \left(\frac{2\pi}{\lambda} \Delta z_{i,j} \right) \quad (2.21c)$$

With coherence detection, $P_{\text{ref}} \gg P_s$, therefore,

$$\begin{aligned} i_{\text{Dopp}} &= \frac{2\sqrt{P_s \cdot P_{\text{ref}}}}{P_s + P_{\text{ref}}} \cdot i_{\text{DC}} \cdot \exp \left(-j2\pi\nu_{\text{Dopp}}t + \phi_{\text{Dopp}} \right) \\ &= 2\sqrt{P_{\text{ref}}/P_s} \cdot i_{\text{DC}} \cdot \exp \left(-j2\pi\nu_{\text{Dopp}}t + \phi_{\text{Dopp}} \right) \end{aligned} \quad (2.22)$$

The mean-square photo detector current is given by

$$\langle i_{\text{Dopp}}^2 \rangle = 2 \frac{P_s}{P_{\text{ref}}} i_{\text{DC}}^2 \quad (2.23)$$

2.2.2.1. Noise sources

Noise in a Lidar system can be divided into "thermal noise, intensity noise, and shot noise".

Thermal noise is generated by thermal agitation of the charge electrons within an electrical conductor. It occurs regardless of the applied voltage because the charge carriers vibrate as a result of temperature. This vibration is dependent upon temperature. Thermal noises are random in nature and not possible to predict. It can be represented as

$$\langle i_{\text{tn}}^2 \rangle = \frac{4kT}{R_{\text{Load}}} B \quad (2.24)$$

where, $k = 1.38 \times 10^{-23}$ J/K is the Boltzmann constant, T is the temperature, B is the bandwidth, and R_{Load} is the load register of photo detector.

Intensity noise is the optical power fluctuations from laser source which is commonly specified as the Relative intensity noise (RIN). Optical power of lasers is given as $P(t) = \bar{P} + \delta P(t)$. RIN is given by $\delta P(t)$ divided by the average power which can be statistically described with Rower spectral density (PSD).

$$\text{RIN}(\nu) = \frac{2}{\bar{P}} \int_{-\infty}^{+\infty} \langle \delta P(t) \delta P(t + \tau) \rangle \exp(j2\pi\nu\tau) d\tau \quad (2.25)$$

which depends on the noise frequency f . It can be calculated as Fourier transform of the auto-correlation of the power fluctuations. The units of RIN is Hz^{-1} or dBc/Hz . PSD may also be integrated over an interval over the noise frequencies $[f_1, f_2]$ to obtain a root mean square value [136]. The RIN on a coherent Lidar system is mainly from reference beam. Low intensity noise lasers have $-120\text{dBc}/\text{Hz}@1\text{MHz}$ and $> 5\text{MHz}$ with shot noise limited. The RIN current of a receiver can be described as Eq.(2.26) [101].

$$\langle i_{\text{RIN}}^2 \rangle = 10^{\frac{\text{RIN}}{10}} \cdot \langle i_{\text{DC}}^2 \rangle B \quad (2.26)$$

Shot noises are quantum-limited intensity noises, related to the discreteness of photons and electrons. Photons are emitted by sources randomly, the amount is not constant but with statistical fluctuations. Originally, it was interpreted as arising from random occurrence of photon absorption events in a photo detector [136]. It does not depend on the quality of detectors and is unavoidable. The mean squared shot noise response is given by

$$\langle i_{\text{sn}}^2 \rangle = 2ei_{\text{DC}}B \quad (2.27)$$

2.2.2.2. Carrier to noise ratio

Taking all noises into account, the overall Carrier to noise ratio (CNR) can be written as

$$\text{CNR} = \frac{\langle i_{\text{Dopp}}^2 \rangle}{\langle i_{\text{tn}}^2 \rangle + \langle i_{\text{RIN}}^2 \rangle + \langle i_{\text{sn}}^2 \rangle} = \frac{2P_s/P_{\text{ref}} \langle i_{\text{DC}}^2 \rangle}{(4kT/R_{\text{PD}} + 10^{\text{RIN}/10} \cdot \langle i_{\text{DC}}^2 \rangle + 2ei_{\text{DC}}) B} \quad (2.28)$$

Normally, since reference power is set much higher than signal power, $P_{\text{ref}} \gg P_s$, in optical coherent detection, we can ignore the signal power from i_{DC} [186].

$$i_{\text{DC}} = \frac{e\eta_{\text{quan}}P_{\text{ref}}}{2h\nu} = \frac{R_{\text{diode}} \cdot P_{\text{ref}}}{2} = i_{\text{ref}} \quad (2.29)$$

The CNR is given as Eq.(2.30).

$$\text{CNR} = \frac{2P_L\beta\Delta R A_L (T(\lambda, R))^2 \eta_{\text{coll}}\eta_{\text{sys}}\eta_{\text{quan}}^2}{R^2 \left(\frac{4kT}{P_{\text{ref}}R_{\text{PD}}} \left(\frac{2h\nu}{e} \right)^2 + 10^{\text{RIN}/10} \eta_{\text{quan}}^2 P_{\text{ref}} + 4\eta_{\text{quan}}h\nu \right) B} \quad (2.30)$$

Therefore, increasing P_{ref} leads to an increase of system RIN but a decrease of thermo noise. Overall there is an optimal reference beam power $P_{\text{ref}}|_{\text{Opt}}$ makes a maximum CNR of the system by minimizing the denominator of Eq.(2.30) .

$$P_{\text{ref}}|_{\text{Opt}} = \sqrt{\frac{kT}{R_{\text{PD}}}} \left(\frac{4h\nu}{e\eta_{\text{quan}}} \right) 10^{-\frac{\text{RIN}}{20}} \quad (2.31)$$

Fig.2.12 illustrates the plot of CNR depending on reference beam powers.

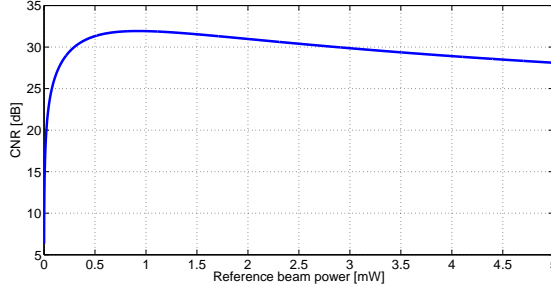


Fig. 2.12.: CNR plot for a coherent Doppler Lidar with $P_L = 1\text{W}$, $\beta = 10^{-7} \text{ m}^{-1}\text{sr}^{-1}$, $R = 100 \text{ m}$, $\Delta R = 10 \text{ m}$, $\eta_{\text{coll}} = \eta_{\text{sys}} = \eta_{\text{quan}} = 80\%$, $T = 300 \text{ K}$, $\text{RIN} = -150 \text{ dB/Hz}$

2.2.3. Balanced detection

In a coherent Lidar system, reference beam power is chosen to be very strong (ca. milliwatt) in comparing with backscattering signals (ca. picowatt). The strong reference brings high RIN into detection. Therefore, a balanced detection method is used to suppress the DC components and maximize the signal photo-current [105]. By using a 3dB optical coupler, a 180° phase shift is added between the two outputs [42]. Fig.2.13 shows the concept of balanced detection. The mixture electrical fields of signal and reference beam at two outputs from the splitter are

$$E_1 = \frac{1}{\sqrt{2}}(E_s + E_{\text{ref}}), \quad E_2 = \frac{1}{\sqrt{2}}(E_s - E_{\text{ref}}) \quad (2.32)$$

Then the photon current after the two detectors are

$$i_1 = \frac{1}{4} \frac{e\eta_{\text{quan}}}{h\nu} (P_s + P_{\text{ref}}) + \frac{e\eta_{\text{quan}}}{2h\nu} \sqrt{P_s \cdot P_{\text{ref}}} \cdot \exp(-j2\pi\phi_{\text{Dopp}}t + \phi_{\text{Dopp}}) \quad (2.33a)$$

$$i_2 = \frac{1}{4} \frac{e\eta_{\text{quan}}}{h\nu} (P_s + P_{\text{ref}}) - \frac{e\eta_{\text{quan}}}{2h\nu} \sqrt{P_s \cdot P_{\text{ref}}} \cdot \exp(-j2\pi\phi_{\text{Dopp}}t + \phi_{\text{Dopp}}) \quad (2.33b)$$

Assuming the two detectors have the same performance, the differential photon current output is then given by

$$i_{\text{IF}} = i_1 - i_2 = \frac{e\eta_{\text{quan}}}{h\nu} \sqrt{P_s \cdot P_{\text{ref}}} \cdot \exp(-j2\pi\phi_{\text{Dopp}}t + \phi_{\text{Dopp}}) \quad (2.34)$$

2. Background knowledge

The two outputs on balance detection are from the same source, the RIN from reference beam are common on both ports which can be canceled. Then the CNR is given as

$$\text{CNR} = P_L \cdot \beta \cdot \Delta R \cdot A_L \cdot (T(\lambda, R))^2 \cdot \eta_{\text{coll}} \cdot \eta_{\text{sys}} \cdot \eta_{\text{quan}} / 2R^2 h\nu B \quad (2.35)$$

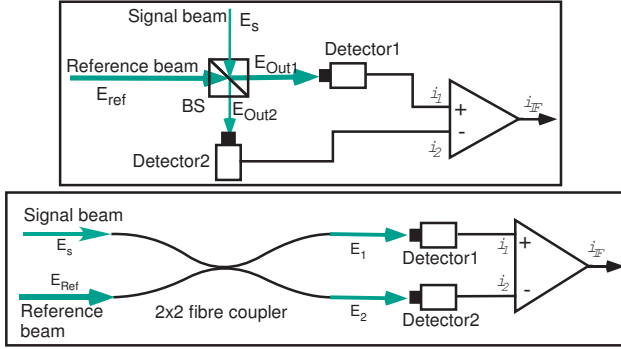


Fig. 2.13: Configuration of the balanced coherent detection

With balanced detection, RIN is canceled but increasing the reference beam power cannot make the CNR better. Since the intermediate signal power and shot noise are equally increased. On a real balanced detector, it is not possible to subtract the entire DC component. The performance of a balanced detector is measured by the parameter Common-Mode Rejection Ratio (CMRR), which describes how much of the DC signal power will appear in the output (Eq.(2.37)), where V_{CM} is the common mode voltage which is the DC output, V_{BAL} is the AC carrier voltage which carries the beat frequency signal.

$$\text{CMRR [dB]} = 20 \log_{10} (V_{\text{CM}} / V_{\text{BAL}}) \quad (2.36)$$

$$P_{\text{out}} = \frac{1}{2} \cdot \frac{P_s + P_{\text{ref}}}{10^{\frac{\text{CMRR}}{20}}} + \sqrt{P_s \cdot P_{\text{ref}}} \cdot \exp(-j2\pi\nu_{\text{Dopp}}t + \phi_{\text{Dopp}}) \quad (2.37)$$

Rewrite the CNR based on the reduced common mode intensity noise, we get

$$\text{CNR} = \frac{2P_L \cdot \beta \cdot \Delta R \cdot A_L \cdot (T(\lambda, R))^2 \cdot \eta_{\text{coll}} \cdot \eta_{\text{sys}} \cdot \eta_{\text{quan}}}{R^2 \left(10^{\frac{2 \cdot \text{RIN} - \text{CMRR}}{20}} P_{\text{ref}} \cdot \eta_{\text{quan}} + 4h\nu \right) B} \quad (2.38)$$

2.3. Background knowledge of wind field

Wind field is the three-dimensional spatial pattern of winds, wind velocity, rate of wind velocity and gradient changes. Knowledge of wind field is generally implicitly assumed in energy harvesting research on the Atmospheric boundary layer (ABL) which is the lower part of the atmosphere, where the atmospheric variables change from their free

atmosphere characteristics to the surface values. Researches on the wind field for wind energy applications focused on different aspects, such as low level wind shear, wind gust, turbulent wind, low level jet, wind model on induction zone and wake zone of wind turbine.

2.3.1. Surface boundary layer wind share

Wind field is modeled as a function of boundary layer height (BLH) in the lower ABL, Surface Boundary Layer (SBL). The height has a strong impact on wind speed and directions. The vertical wind shear distribution in speed is given as a logarithmic profile [140].

$$u = \frac{u_*}{K} \left[\ln \left(\frac{z}{z_0} \right) - \psi_m \right] \quad (2.39)$$

Where ψ_m is the extension of wind profile which is account for atmospheric stability, $\psi_m = -4.7z/L$, where L is Obukhov length which can be estimated as

$$L = -\frac{u_*^3 T}{Kg w' \Theta'_v} \quad (2.40)$$

Where T is the mean temperature and $\overline{w' \Theta'_v}$ it the kinematic virtual heat flux. For unstable atmospheric condition, the wind profile extension is then given as

$$\psi_m = \frac{3}{2} \ln \left(\frac{1+x+x^2}{3} \right) - \sqrt{3} \arctan \left(\frac{2x+1}{\sqrt{3}} \right) + \frac{p}{\sqrt{3}} \quad (2.41)$$

with $x = (1 - 12 \frac{z}{L})^{1/3}$. To simplify, a power law model is used for vertical wind shear.

$$u = u_r (z/h_r)^a \quad (2.42)$$

Where u_{ref} and h_{ref} are reference wind speed and height, a is power law coefficient.

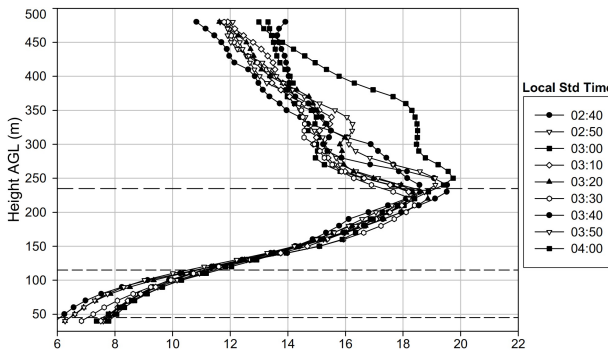


Fig. 2.14: Logarithmic wind shares [120]

2.3.2. Gust wind field

Wind gust is an extreme wind event which can lead to very large loads causing fatigue, automatic shut-downs or even damage to turbines. Gust wind field is represented as

$$w = w_0 + \sum_{n=1}^N a_n \sin(\Omega_n s + \phi_n) \quad (2.43)$$

here α is the motion along the path, ϕ_n is the random process, the coefficient a_n defines the power spectral density. The frozen Dryden turbulence model and von Karman model are the most common used model for gust wind. With the frozen Dryden turbulence model, the gust wind power spectral density is defined as Eq.(2.44) [112].

$$\Phi_{u_g}(\Omega_{sf}) = \sigma_u^2 \frac{2L_u}{\pi} \frac{1}{1 + (L_u \Omega)^2} \quad (2.44)$$

here u_g is the gust longitudinal linear velocity, α_u is the turbulence intensity, L_u is the turbulence scale length, and Ω_{sf} is the spatial frequency. The PSD of the longitudinal linear velocity component for a von Karman model is defined as

$$\Phi_{u_g}(\Omega) = s_u^2 \frac{2L_u}{p} \frac{1}{(1 + (1.339L_u \Omega)^2)^{\frac{5}{6}}} \quad (2.45)$$

IEC standard defined the Extreme operating gust (EOG) as

$$V_{gust} = \text{Min} \left\{ 1.35(V_{e1} - V_{hub}); 3.3 \left(\frac{s_u}{1 + 0.1 \frac{D}{\Lambda_1}} \right) \right\} \quad (2.46)$$

Where $s_u = I_{ref} (0.75V_{hub} + b)$ is the turbulence standard deviation, with $b = 5.6$ m/s, I_{ref} is the expected value of the turbulence intensity at 15 m/s, the value is defined by the wind turbine classification parameters (Table.2.2). Where A, B, and C designate the category for higher, medium, and lower turbulence characteristics [85]. Fig.2.15 show an example of the EOG for $V_{hub} = 18$ m/s, $D = 42$ m, Class IA wind turbine.

Table 2.2.: Parameters for wind turbine classes

Wind turbine class		I	II	III
V_{ref}	[m/s]	50	42.5	37.5
A	I_{ref}	0.16		
B	I_{ref}	0.14		
C	I_{ref}	0.12		

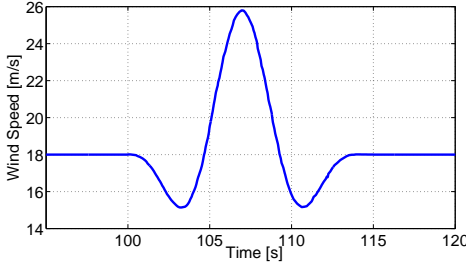


Fig. 2.15: An example of EOG 1 Year gust wind profile (Based on IEC standard)

2.3.3. Turbulence wind field

The turbulent wind means random variations in the wind velocity. Normally in wind energy applications, according the IEC61400-1 standard, this is measured within 10 min averages. Assuming the height invariant turbulence standard deviation for the longitudinal and vertical wind are s_u, s_v , then the power spectral densities S_u and S_v are given as

$$S_u(f) = 0.05\sigma_u^2(\Lambda_1/u_{hub})^{-\frac{2}{3}}f^{\frac{5}{3}}, S_v(f) = \frac{4}{3}S_u(f) \quad (2.47)$$

Where $\Lambda_1 = \begin{cases} 0.7H_{hub} & H_{hub} \leq 60 \text{ m} \\ 42 \text{ m} & H_{hub} \geq 60 \text{ m} \end{cases}$ is longitudinal turbulence scale parameter at hub height H_{hub} . The turbulent wind in longitudinal and vertical can be written as

$$u(t) = \bar{u} + u'(t), \quad v(t) = \bar{v} + v'(t) \quad (2.48)$$

where, \bar{u} and \bar{v} are the mean velocities, $\bar{u} = \int_t^{t+T} u(t)dt$, $u'(t) = \bar{u} - u(t)$ is the turbulent fluctuation. Then, the Turbulence Intensity (TI) is given as

$$TI = \frac{u_{rms}}{\bar{u}} \quad (2.49)$$

Where u_{rms} is the root mean square of the turbulence fluctuation, $u_{rms} = \sqrt{\overline{u'(t)^2}}$.

2.3.4. Wind speed changes on the induction zone

Based on the stream tube theory, due to the wind energy evaluation by wind turbine, wind speed changes in the upstream induction zone. When the Lidar measurement data is coming from a fixed location, this wind evaluation effect has impact on the Lidar measurement distance. Fig.2.16 shows the wind speed changes inside of the induction zone based on a simulation with a large eddy simulation (LES) by the Computational Fluid Dynamics (CFD) software Simulator for Wind Farm Applications (SOWFA) from National renewable energy laboratory (NREL). The simulation results show that the wind speed changes are rather nonlinearly depends on the initial wind speed and distance to the wind turbine.

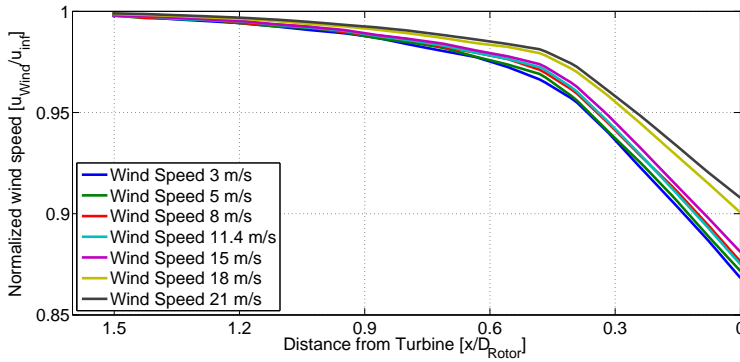


Fig. 2.16.: Wind speed changes in upstream induction zone at different distance and initial wind speed based on the 5MW NREL reference turbine with 126m diameter

2.3.5. Blade effective wind speed

To estimate the effective wind speed disturbances on the rotor blades from variable time delays is interest for turbine pitch control applications. However, the Blade Effective Wind Speed (BEWS) is not able to be measured directly. It needs to be estimated based on the Lidar measurement and turbine working conditions. There are different ways to estimate BEWS. The power balanced estimator based on solving the wind power equation is explained in [82]. A Disturbance accommodating control (DAC) method uses a disturbance estimator to estimate the unobservable system states from the full states wind turbine model [94]. Unknown input observer (UIO) method is designed to account for estimating the uncertainties in the aerodynamic model and wind speed [133]. An Immersion and invariance (I&I) estimator using the rotor dynamic is implemented for BEWS estimation [135]. The Extended Kalman filter (EKF) estimator based on the state space model is described by T.Knudsen [106]. Inspired by the state estimation and combined with tracking control to achieve disturbance estimation, a Kalman filter based estimator is explained by K.Z. Ostergaard [134] and applied by E. Simley [159] and D. Schlipf [154]. Further details of different methods are summarized by M. Soltani [165].

For the purpose of turbine control, BEWS experienced by the rotor disk is calculated by integrating the wind speeds across the entire rotor disk with the formula (Eq.(2.50)) [48].

$$u_{\text{BEWS}} = \left(\frac{\int_0^{2p} \int_0^R u^3(r, \phi) C_P(r) r dr d\phi}{\int_0^{2p} \int_0^R C_P(r) r dr d\phi} \right)^{\frac{1}{3}} \quad (2.50)$$

Where $C_P(r)$ is the radially dependent power coefficient, R is the rotor radius. u_{BEWS} is the uniform wind speed that would produce the same power as the actual distribution of wind speeds across the rotor disk. Here only the u component of wind speed is considered, since when the turbine is operating in above rated wind speeds, variations in the u component have a greater effect than variations in the v and w components. E. Simley et.al. uses a

coherence function, $\gamma_{w_i w_m}^2(f)$ (Eq.(2.51)), between the true wind disturbance and the Lidar measurement to describe the Lidar measurement performance (Fig.2.17) [48].

$$\gamma_{w_i w_m}^2(f) = \frac{|S_{w_i w_m}(f)|^2}{S_{w_i w_i}(f) \cdot S_{w_m w_m}(f)} \quad (2.51)$$

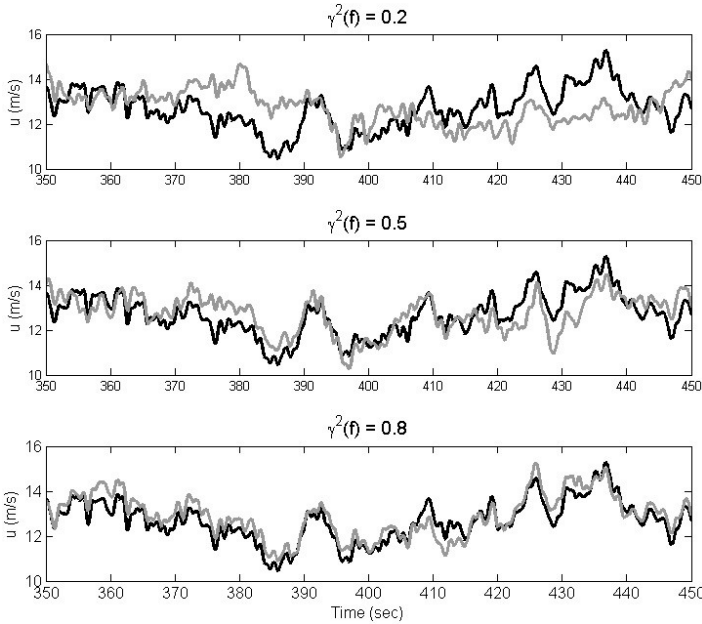


Fig. 2.17.: An example of coherence function of measured wind and BEW speed for low coherence (up) to high coherence (down) [47]

2.4. Summary

In this chapter, background information of wind energy market and the current situation are briefly introduced to show the necessary of this work. Following with the introduction of the theoretical background knowledge of the horizontal axis wind turbine systems to show how the wind turbine works. Furthermore, the background knowledge of coherent Doppler wind Lidar systems have been discussed. The Lidar equation describes the power received on the detector. This equation is used to estimate the receiving power on detectors for defining the system design parameters.

The coherent detection methods are commonly used for the Doppler Lidar system to demodulate the low frequency Doppler signal. By applying a strong reference beam with

the coherent detection, the weak backscattering signal can be amplified to the level that a standard photo detector can be used to detect. However, the strong reference power brings intensity noise into detection. By introducing balanced detection, the intensity noise can be removed completely or reduced.

The theoretical background discussed in this chapter is the basis of this thesis, and going to be used in the following chapters.

3. State of the art

3.1. Overview of wind sensing technologies for wind energy

The modern wind turbines need accurate wind measurement and prediction not only for the control purpose, but also for assessment of site development and planning of the wind farm. There are lots of techniques available for onsite wind resource measurement. The point measurement sensors such as cup and sonic anemometers are the industry standards. The short to medium range remote sensing techniques, such as Sound detection and ranging (Sodar) and Lidar systems, are starting to be applied for wind energy industry.

3.1.1. Mechanical anemometers

The cup anemometers are the most common used wind measurement instrument because of the simplicity and reliability. It was invented by the Irish astronomer T.R. Robinson in 1846 [123, 137]. It works on the different aerodynamic forces from the convex and concave surfaces. Assuming the wind speed u , the rotation speed S , the cup arm length r , then, the equation of the cup anemometer motion can be written as Eq.(3.1) [109].

$$I \frac{dS}{dt} = M = \frac{1}{2} \rho A r \left[C_+ (u - rS)^2 - C_- (u + rS)^2 \right] \quad (3.1)$$

I is the moment of inertia, M is the torque, ρ is the air density, A is the area of the cup, C_+ and C_- are the drag coefficient. The cup anemometer can be theoretically determined as

$$u = \left(\frac{1 + \sqrt{C_-/C_+}}{1 - \sqrt{C_-/C_+}} \right) rS = A_r S \quad (3.2)$$

here A_r is the calibration constant. The cup anemometer factor K can be defined as the ratio between the wind speed u and the rotation speed rS .

$$K = \frac{u}{rS} = \left(\frac{1 + \sqrt{C_-/C_+}}{1 - \sqrt{C_-/C_+}} \right) \quad (3.3)$$

3.1.2. Ultrasonic wind sensors

In 1944, Carrier and Carlson first time described the theoretical background of the sonic anemometers "true air speed indicator" [30]. By using two microphones placed upwind and downwind from a sound source, wind velocity was obtained by measuring the phase difference [148]. Fig.3.1 shows a 3D ultrasonic anemometer from Gill which contains 3 pairs

of transmitter and receiver (left) and the working principle with one pair of transmitter and receiver which placed in a distance of l . t_{12} and t_{21} are the transition time from transceiver to receiver. Therefore, for an uniform and stationary wind flow, wind speed can be calculated by time of flight difference between t_{12} and t_{21} [39].

$$u_M = \frac{l}{2} \left(\frac{1}{t_{21}} - \frac{1}{t_{12}} \right) \quad (3.4)$$

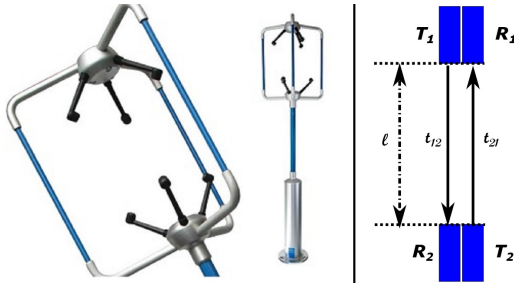


Fig. 3.1: A 3D Gill ultrasonic anemometer (left) and its working principle (right) (Source: Gill)

Both the cup and ultrasonic anemometers are point measurement techniques. In order to measure the wind field over a volume, multiple equipments are necessary. Doppler Sodar system is a remote sensing device using sound for probing the wind field in a volume. It sends a sound wave with a certain frequency into the atmosphere, where the sound wave is scattered due to the turbulence of atmosphere caused by temperature and humidity fluctuations and gradients as well as wind shares. These turbulence are moving along with wind flow, which creates the Doppler effects on the scattered sound wave.

Since the Doppler shift of the carrier frequency only occurs in the direction of the beam, to determine the vector wind field three independent beams are required. Vertical component w can be measured by directing the beam straight up, the horizontal components require a tilt angle of θ_x and θ_y for determine the two horizontal components u and v [6].

$$w = \frac{-\Delta f \cdot S}{f_0}, u = \frac{-\Delta f \cdot S}{2f_0 \sin \theta_x} - \frac{w}{\tan \theta_x}, v = \frac{-\Delta f \cdot S}{2f_0 \sin \theta_y} - \frac{w}{\tan \theta_y} \quad (3.5)$$

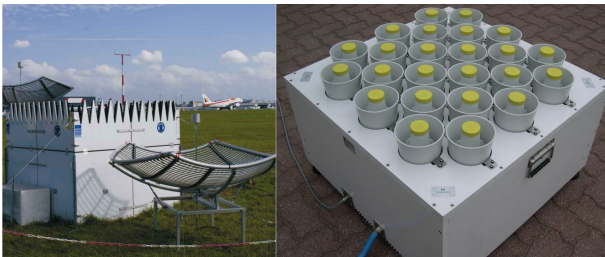


Fig. 3.2: A Sodar system (left), and the antenna array of the Sodar system (right) (Source: Metek)

Table 3.1.: A comparison of Sodar and Lidar system during 2007-2009 [32]

Sodar	ZephIR Lidar
Decreasing data availability with height	High data availability until 150m
Good data availability for low wind	Low data availability for winds < 4 m/s
Low data availability for winds > 20 m/s	High data availability for wind > 20 m/s
Careful post-processing needed	Little post-processing needed
Careful use of absolute values	Absolute values seem OK?
High vertical resolution (10m)	Only five height levels
Fast GSM download	Slow (expensive) GSM download
Moderate transport and installation	Relatively easy transport and installation
High energy consumption	Moderate energy consumption
Sound emission	No sound emission
Moderates costs	High costs

3.1.3. Wind Lidar

Similar to the Doppler Sodar system, wind Lidar system uses the Doppler effect from the back scattered light wave instead of sound wave by aerosols which are moving along the wind flow. Lidar systems are new commercial wind field meteorology technique, which is commercialized in the last two decades after the quick growth of telecommunication lasers and components. Comparing with the Sodar systems and all the other state of the art wind profiling technology, their high price limited the applications. Rene Cattin et. al. compared the Sodar and Lidar (ZephIR) with the data collected through the measurement campaigns with both Lidar and Sodar system during 2007-2009 (Table.3.1) [32].

3.2. Commercial Lidars for wind energy applications

Several commercial Lidar systems are developed mainly for meteorology purpose, such as Halo Photonics, Mitsubishi Electronics, Lockheed Martin. In the last decade, French company Leosphere, which focused on pulsed Lidar systems (WindCube and Wind iris), and British company ZephIR (established from UK government Research & Development company QinetiQ at 2003), which focused on a Continue wave (CW) Lidar system, are the main market player on wind energy applications. However, all those Lidar systems are offered at a high price (more than 135,000 Euro). Most recently, the Windar Photonics released a Lidar product "wind eye" with a price of 22,000 Euro. In this section, these four major commercial Lidar is explained in detail.

3.2.1. Leosphere WindCube Lidar system

WindCube (Figure 3.3) is one the most popular Lidar systems for wind energy applications. It is developed by Leosphere and ONERA (the French Aerospace Lab). It uses a pulsed

Table 3.2.: The four major commercial Lidar systems for wind energy applications

	Pulsed	CW
Ground based	WindCube	ZephIR
Nacelle mounted	Wind iris	WindEye

Lidar technology, in which laser pulses are sent to the atmosphere and scattered back by the aerosols. Table.3.3 shows the main specifications of WindCube.



Fig. 3.3: WindCube pulse Lidar system, V1 and V2 (Source: Leosphere)

3.2.1.1. Structure of the WindCube Lidar system

Fig.3.4 illustrates the general concept of WindCube Lidar, which contains the following parts: transmitter, receiver, detector, and signal processing units [26].

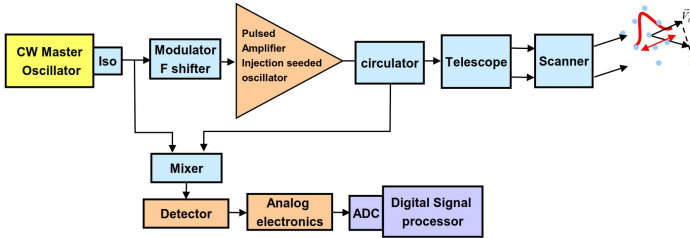


Fig. 3.4.: Block diagram of the WindCube pulse Lidar system structure [26]

The transmitter unit includes seed laser, pulse amplifier, and frequency shifter. The seed laser is a CW laser source which is also called Master Oscillator (MO) for the Master oscillator power amplifier (MOPA). The seed laser defines most important parameters for the Lidar performance, such as wavelength, coherence length (linewidth), intensity noise, and polarization states. Choice of the laser sources need to consider of the laser eye safety operation, atmospheric propagation, signal to noise ratio, and the cost. Fig.3.5 shows the atmospheric propagation and eye safety operation effect for different wavelengths. WindCube Lidar uses the Erbium-Ytterbium lasers with wavelength of $1.54\mu\text{m}$ to ensure

Table 3.3.: Specification of WindCube Lidar system

Transmitter		Erbium-Ytterbium laser
Wavelength	μm	1.54
Repetition rate	kHz	10
Pulse energy	μJ	10
Pulse length	ns	200
Range (min, max)	m	40, 200
Speed range	m/s	0 to +60
Speed accuracy	m/s	0.1
Data accumulation time	s	0.5
Data output frequency	Hz	1
Number of measurement heights		12
Sampling range resolution	m	20
Scanning cone angle		30°
Azimuth–elevation scanning accuracy		1.5°
Price	Euro	V1 Ca. 150,000 Euro V2 Ca. 135,000 Euro

a high energy allowance and better transmission efficiency in atmosphere [27]. The laser linewidth is another important parameter for the Doppler Lidar applications that an ultra-narrow linewidth (ca. 10 kHz) is commonly used to ensure a low phase noise during a long distance measurement. The frequency shifter is used to shift the reference beam to a certain frequency offset, in order to allow the system to detect both negative and positive frequency shifts. Normally an Acousto-Optic Modulator (AOM) is used.

The receiver unit includes a circulator, a telescope, and a scanner. The circulator is used to transmit the laser pulse to the telescope and direct the back scattering light into the detection unit. For the coherent Lidar, a polarizer is commonly used by the circulator to assure a good performance [27].

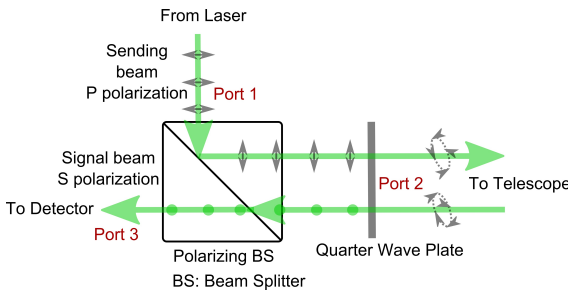


Fig. 3.5: A circulator setup by using of polarization concept

Fig.3.5 shows the work principle of a circulator based on polarization concept. It includes a polarization beam splitter to transmit the S polarization and reflect the P polarization, and a quarter wave plate to change the linear polarization to a circular polarization. A good

circulator needs to have good transmission efficiency from port 1 to 2 and isolation from port 1 to 3. Telescope is used to focus the transmission laser beam into a certain distance and receive the back scattering light from interesting area. Basically a bigger telescope collects more light and increases the spatial resolution. However, the atmospheric turbulence create wave distortion which decreases the coherence detection efficiency. To keep this distortion negligible, the telescope aperture needs to be smaller than the coherence diameter:

$$d_0 = 0.37\lambda^{1.2} \left(C_n^2 \cdot Z \right)^{-0.6} \quad (3.6)$$

Where C_n^2 is the index structure constant; λ is wavelength; Z is the distance.

Lidar systems measure the LOS wind speed. In order to obtain the full wind vector, measurements from different directions are necessary. The scanner is used to direct the beam into different directions. There are different type of scanners, Mitsubishi Lidar system moves the entire telescope [4]. Optical Air Data Systems (OADS), LLC. Vindicator and Wind Eye system uses multiple telescopes to obtain different measurement directions without using any mechanical scanner systems. WindCube V1 uses a rotation prism to direct the beam into four directions, the WindCube scanning Lidar 200S uses a dual flat scanning mirror to scan a hemispherical field.

The detector unit includes a mixer to mix the scattering signal beam with the reference beam, and a photo detector to detect the light signal. Doppler Lidar can use a double edge filter to achieve a direct detection concept [119] or more commonly format a coherent detection concept. Basic principle of coherent detection is by mixing the Doppler shifted signal beam with the original laser beam to demodulate the beat frequency. To ensure good coherent detection efficiency, the amplitude and phase between the signals and reference beam need to be perfect matched; the polarization state must be the same; and the temporal coherence is optimum. The heterodyne efficiency of a perfect Doppler Lidar system with a circular aperture and Gaussian beam is limited to 40% by spatial coherence [58].

The signal processing unit includes a signal pre-processing analogue electronics unit, an Analogue to Digital Converter (ADC) and a Digital Signal Processing (DSP) unit. The analogue signal is preprocessed to reduce the noise and ensure a good signal condition. The ADC digitizes the acquired signal for DSP unit. WindCube uses the maximum likelihood estimator (MLE) method, which is based on the likelihood of Fourier transform of the signal, to process the noisy spectral signal.

3.2.1.2. Wind vector reconstruction

To reconstruct a wind vector from a Lidar system which only measures the LOS speed, multiple beams to measure the three components at the same location are necessary. However, with a single compact Lidar system, it is difficult. WindScanner project uses three ZephIR or WindCube Lidars to simultaneously measure the wind speed at the same location [125].

Fig.3.6 shows the operation of the WindCube for retrieving the wind speed components. WindCube sequentially scans the space with 5 lines of sight in four different directions, North, East, South, West, and Center. The LOS wind speed are marked as $Vr0$, $Vr90$, $Vr180$,

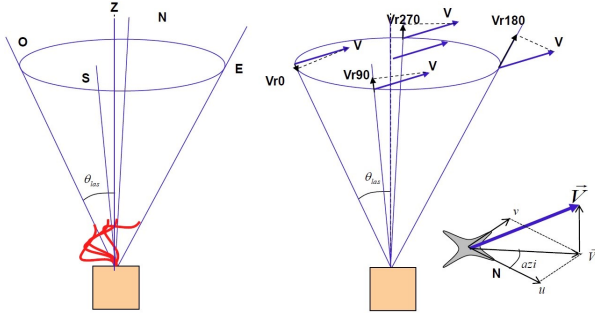


Fig. 3.6: Sketch of the operation of WindCube for retrieving wind speed [27]

$Vr270$, and Vrz respectively. To reconstruct the wind field, assuming at the same horizontal plane the vector wind speeds are the same at the five different measurement points and within the measurement time frame. Then, the North-South component u and East-West component v can be written as Eq.(3.7).

$$u = \frac{Vr0 - Vr180}{2 \sin \theta_{las}}, v = \frac{Vr90 - Vr270}{2 \sin \theta_{las}} \quad (3.7)$$

where, θ_{las} is the scanning cone angle. Vertical component can be direct measured from the center beam, and calculated from the other four components.

$$w = \frac{Vr0 + Vr90 + Vr180 + Vr270}{4 \cos \theta_{las}} \quad (3.8)$$

Therefore, the horizontal velocity Vh and azimuth angle Azi become

$$Vh = \sqrt{u^2 + v^2}, Azi = \text{atan} \frac{v}{u} \quad (3.9)$$

The 3D vector wind velocity and 2D horizontal vector wind velocity are

$$\vec{V} = \vec{u} + \vec{v} + \vec{w}, \vec{Vh} = \vec{u} + \vec{v} \quad (3.10)$$

3.2.1.3. Performance analysis

CNR is one of the most important factors to measure the performance of a Lidar system which is given as the ratio of signal and noise power. For a pulsed coherent Lidar system, CNR is given as Eq.(3.11) [113].

$$\text{CNR} = \frac{R_{PD}^2 \cdot \eta_{Lidar} \cdot c \cdot \beta \cdot E_l \cdot A_r e^{-2\alpha Z} \cdot t \cdot P_{LO}}{Z^2 \left(2eR_{PD}P_{LO} + \frac{4k_b T}{R_L} + RIN(f) P_{LO}^2 \right)} \quad (3.11)$$

here R_{PD} is the responsibility of the photo diode, η_{Lidar} is the Lidar efficiency which includes the system transmission (η_T) and heterodyne efficiency (η_H), c is the speed of light, β_π is the atmospheric backscattering coefficient, E_L is the energy of the laser pulse, A_{Rec} is the area of receiver telescope, α_{ext} is the atmospheric extinction ratio, Z is the distance, τ_{Pulse} is the pulse length, P_{ref} is the reference beam power, e is the elementary charge $e = 1.6 \times 10^{-19} C$, k_b is the Boltzmann's constant $k_b = 1.38 \times 10^{-23} J/K$, T is the temperature, R_L is the transmittance of the photo detector, $RIN(f)$ is the relative intensity noise from the reference beam.

Spatial resolution is limited by the pulse duration. Fig.3.7 describes the propagation of a laser pulse into atmosphere in spatial and time domain with an analysis window of τ_m . The measured velocity at distance Z becomes

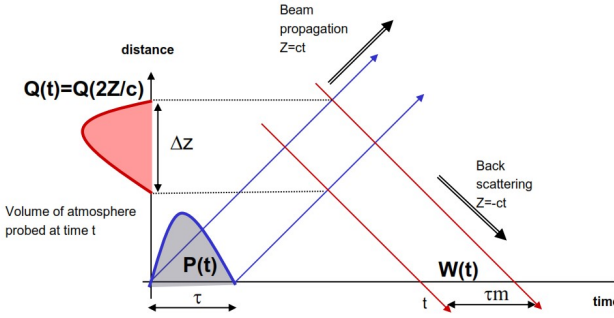


Fig. 3.7: Propagation of a laser pulse τ and the receiving of backscattering light with a time gate τ_m [27]

$$V_d(Z) = \int_{-\infty}^{\infty} RWF(R)V_r(R)dR \quad (3.12)$$

here $V_r(R)$ is the velocity at close points with distance R to the measurement point, $RWF(R)$ is the Range weighting function (RWF) which is given as an analytical equation. Assuming laser pulse is Gaussian with $FWHM = \tau$, range gate measurement time window τ_m is flat, sending and receiving system is collimated [163].

$$RWF(Z) = \frac{1}{\tau_m} c \left[\operatorname{erf} \left(\frac{4\sqrt{\ln 2}}{c\tau} (Z - Z_0) + \frac{\sqrt{\ln 2}}{\tau} \right) - \operatorname{erf} \left(\frac{4\sqrt{\ln 2}}{c\tau} (Z - Z_0) - \frac{\sqrt{\ln 2}}{\tau} \right) \right] \quad (3.13)$$

here c is the speed of light in air, $\operatorname{erf}(x) = \frac{2}{\sqrt{\pi}} \int_0^x \exp(-t^2)dt$ is the error function. range resolution is defined as the Full Width at Half Maximum (FWHM) of the RWF function which is expressed as Eq.(3.14).

$$\Delta z = \frac{\tau_m c}{2 \cdot \operatorname{erf} \left(\sqrt{\ln 2} \tau_m / t \right)} \quad (3.14)$$

Furthermore, focusing the beam into the detection area leads a better resolution. A general description of the RWF can be describes with Eq.(3.15) [113].

$$RWF(Z) = \eta_{foc}(Z) \cdot (Pulse\ FFT_{window})(Z) \quad (3.15)$$

here $\eta_{foc}(Z) = \left(1 + Z^2 \left[\frac{1}{Z} - \frac{1}{Z_{foc}}\right]\right)^{-1}$ is the focusing efficiency.

The Pulse Reputation Frequency (PRF) is another important parameter of the transmitter. In a pulse Lidar system, the maximum PRF is defined by the maximum measurement range, since the time between the pulses ($1/PRF$) must be longer than the round trip time of pulse flight over maximum measurement range Z_{max} , $PRF_{max} = c/(2Z_{max})$. WindCube choses PRF=10 kHz, which equivalent to a maximum range of 15 km.

Velocity resolution is depending on the bandwidth of the Doppler spectrum which is broadened by atmospheric parameters, such as the wind field homogeneity within the detection range, and Lidar parameters, such as the pulse duration and numbers of spectra average. The scanning cone angle θ_{las} is a trade-off between Lidar velocity resolution and atmosphere homogeneity. Smaller θ_{las} leads better wind homogeneity but worse in projection of the wind vector. The cone angle between 15 and 30 shows good stability in the horizontal wind speed retrieval [16]. With the Cramer Rao lower bound (CRLB), the minimum velocity resolution can be written as

$$sv_{CRLB} = \frac{\sqrt{2}\lambda}{2\tau} \frac{\sqrt{1 + CNR}}{\sqrt{N} \cdot CNR} \quad (3.16)$$

here, N is the numbers of spectra average. Fig.3.8 shows the LOS velocity resolution as a function of CNR and number of spectra average N based on CRLB.

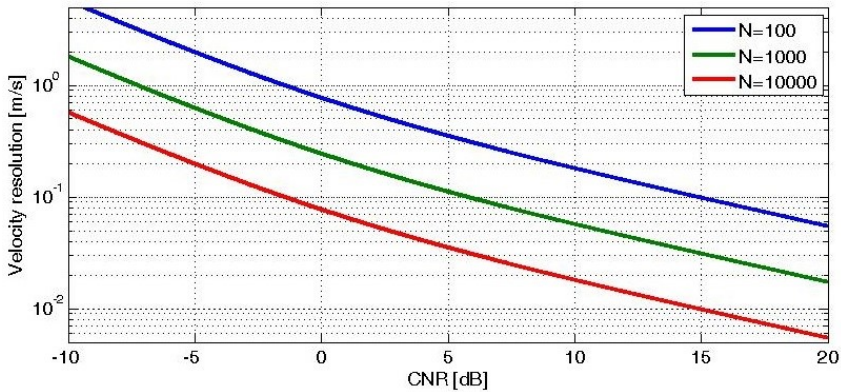


Fig. 3.8.: LOS velocity resolution for different CNR and average number N

Table 3.4.: Specification data of Wind iris Lidar system

Transmitter		Fiber pulsed laser
Wavelength	μm	1.54
Repetition rate	kHz	10
Pulse energy	μJ	10
Pulse length	ns	200
Range (min, max)	m	40 ~ 200 or 80 ~ 400
Speed range	m/s	-10 ~ +40
Speed accuracy	m/s	0.1
Accumulation time	s	0.5
Data output frequency	Hz	1 ~ 4 or 1 ~ 2
Number of measurement heights		10
Sampling range resolution	m	30 or 60
Scanning cone angle		Half angle 15°
Leveling accuracy		$\pm 0.05^\circ$
Price	Euro	Ca. 135,000

3.2.2. Avent Wind iris Lidar system

Avent Lidar Technology is a French company formed in 2009 as a joint investment of Leosphere and Renewable NRG Systems. They are focused on developing and manufacturing turbine mounted Lidar systems "Wind iris" (Fig.3.2.2) for extending the reliability and optimization of the performance of wind turbines and farms. The technologies of Wind iris are similar to WindCube. Table.3.4 gives the main specification of Wind iris.



Fig. 3.9: Wind iris turbine mounted Lidar system (Source: Avent Lidar Technology)

3.2.2.1. Structure of the Avent Wind iris Lidar system

Wind iris composites two parts, an optical head which can be mounted on a nacelle top contains two telescopes for measuring at two directions with an angle of 30°. The processing unit, which contains laser transmitters, detectors, and other optoelectronic components, can be set inside of the nacelle. In between they are connected with an interface cable.

The optical head unit contains two telescopes and a polarizer (Fig.3.10). Wind iris uses a polarizer, polarization Beam Splitter (BS), to switch the measurement directions as shown on Fig.3.4. Such non-mechanical method with polarization is used on OADS Vindicator Lidar system and Windar Photonics Wind Eye as well. The polarizer reflects the S-Polarization light and transmits the P-Polarization light. When sending an S-Polarization laser, the polarizer reflects the beam into the telescope 1 to measure the LOS1 wind speed. When the polarization switching changes the polarization to P, polarizer transmits the beam into telescope 2 to measure the LOS2 wind speed. The angle between direction LOS1 and LOS2 is 30° . Both the telescopes are weakly focused the laser beam into 300 m distance.

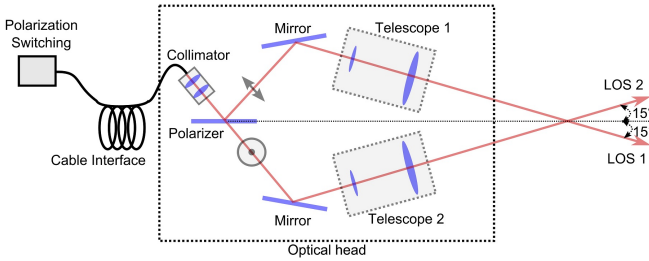


Fig. 3.10: Optical head structure of the Wind iris 2 beam Lidar system (estimated)

Data processing unit contains the electrical components, such as laser source, detector, data processing and control units. Wind iris uses the same laser as WindCube (An Erbium-Ytterbium laser with $1.54 \mu\text{m}$, 10 kHz repetition rate, and $10 \mu\text{J}$ pulse energy). Pulse length is 200 ns for the 200 m range configuration and 400 ns for the 400 m range configuration. The depth resolution is then depending on the pulse length which is calculated as the same as WindCube system with Eq.(3.14).

3.2.2.2. Wind field reconstruction

Fig.3.11 illustrates the wind speed and direction calculation of the two beams Lidar system. Where α_{Lidar} is half angle between the two directions (for Wind iris, $\alpha_{\text{Lidar}} = 15^\circ$), γ_{Yaw} is the yaw direction or the turbine, U_l is the LOS wind speed from the left beam, U_r is the LOS wind speed from the right beam, U_{wind} is the longitudinal wind speed [179].

$$U_l = U_{\text{Wind}} \times \cos(\alpha_{\text{Lidar}} - \gamma_{\text{Yaw}}), U_r = U_{\text{Wind}} \times \cos(\alpha_{\text{Lidar}} + \gamma_{\text{Yaw}}) \quad (3.17)$$

Therefore,

$$\gamma_{\text{Yaw}} = \tan^{-1} \frac{f - 1}{\tan \alpha_{\text{Lidar}}(f + 1)}, \text{ with } f = \frac{U_r}{U_l} \quad (3.18a)$$

$$u = \frac{U_r + U_l}{2 \cos \alpha_{\text{Lidar}}}, v = \frac{U_r - U_l}{2 \sin \alpha_{\text{Lidar}}} \quad (3.18b)$$

$$U_{\text{Wind}} = \frac{1}{2} \sqrt{\left(\frac{U_r + U_l}{\cos \alpha_{\text{Lidar}}} \right)^2 + \left(\frac{U_r - U_l}{\sin \alpha_{\text{Lidar}}} \right)^2} \quad (3.18c)$$

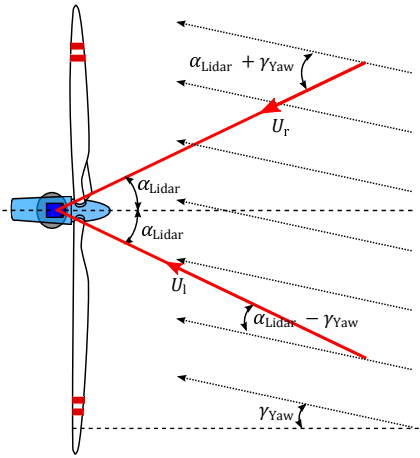


Fig. 3.11: Illustration of wind speed and direction calculation with a yaw angle γ_{Yaw}

3.2.2.3. Performance analysis

Wind iris is designed for operation on the top of a wind turbine’s nacelle. The wind vector measurement accuracy is depending on the individual LOS wind speed measurement uncertainty and the calibration of tilting and rolling of Lidar beams. Fig.3.12 shows the beams with a tilted angle β and rolled angle f to the beam plane (AB-AC) [36].

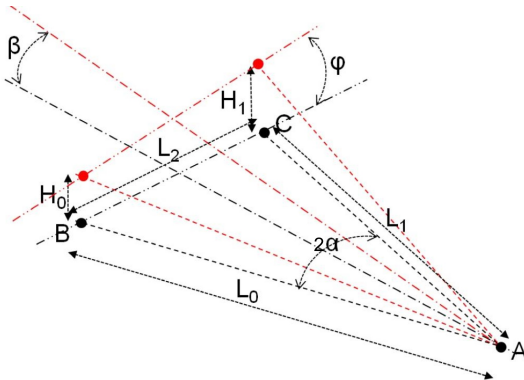


Fig. 3.12: Illustration of a tilted (β) and rolled (φ) Lidar beam with wind iris [36]

The height H_0 at the measurement point B and H_1 at the measurement point C are given by

$$H_0 = L_0 \cos \alpha \sin \beta - L_0 \sin \alpha \sin \gamma, H_1 = L_1 \cos \alpha \sin \beta + L_1 \sin \alpha \sin \gamma \quad (3.19)$$

Where, L_0, L_1 are LOS measurement distances of the two beams. L_2 is the distance between the two points. α is the half opening angle of the two Lidar beams. Therefore,

$$\sin \beta = \frac{H_0 + H_1}{2\cos \alpha}, \sin \gamma = \frac{H_1 - H_0}{2\sin \alpha}, \cos 2\alpha = \frac{L_0^2 + L_1^2 - L_2^2}{2L_0L_1} \quad (3.20)$$

Uncertainty from the calibration

Wind speed measurement uncertainty from Lidar calibration during the setup is well documented by M.Courtney [36]. On another study by Dr.Wagner et.al., calibration uncertainty is documented as $d_{\text{cal}} = 0.1$ m/s (Fig.3.13) [180].

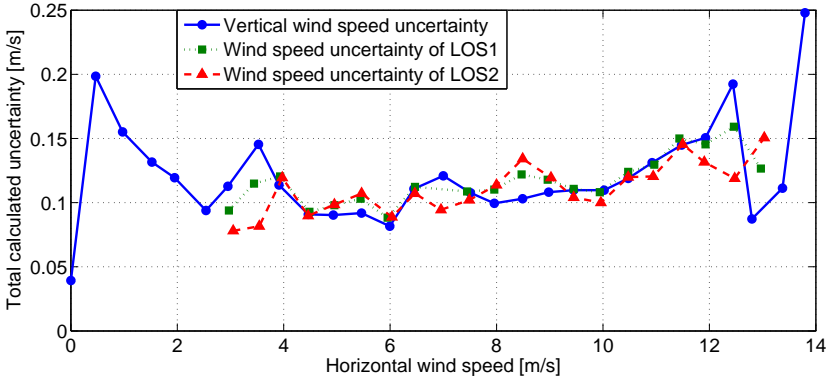


Fig. 3.13.: Wind speed measurement uncertainty from calibrations for each LOS, and horizontal wind speed uncertainty (Blue) (Graph regenerated with data from [180])

The tilt angle uncertainty

Assuming uncertainty of Lidar tilt angle during calibration is $\Delta\beta_L$ and uncertainty of turbine tilt angle during calibration is $\Delta\beta_T$, let measurement range $L_0 = L_1 = L$, therefore, the height error on measurement position is given as

$$\Delta H = L\cos \alpha \sin(\Delta\beta_L + \Delta\beta_T) \quad (3.21)$$

With a strong wind shear characteristics with a power law profile $\alpha_{\text{shear}} = 0.2$ with the mean wind speed of $v = 8$ m/s, the measurement uncertainty is then given as

$$d_{\text{tilt}} = \frac{1}{\sqrt{3}} \left(\left(\frac{H_{\text{hub}} + \Delta H}{H_{\text{hub}}} \right)^{0.2} - 1 \right) v \quad (3.22)$$

Where H_{hub} is the hub height, assuming $H_{\text{hub}} = 80$ m, for measuring at a distance of $L = 200$ m, $a = 15^\circ$, $\Delta\beta_L = 0.1^\circ$, $\Delta\beta_T = 0.2^\circ$. Therefore, the height uncertainty $\Delta H = 1.01$ m. The wind speed measurement uncertainty $d_{\text{tilt}} = 0.012$ m/s.

Non-uniform airflow in the probe volume

The measurement uncertainty from non-uniform airflow is caused by random variations of the radial wind velocity component (U_{LOS}) and the random location of aerosols. The return signal is produced by the backscattering from individual random particles. Based on the Kolmogorov spectrum theory of turbulence, Frehlich studied those effects and found that uncertainty of the ensemble averaged wind speed estimations can be expressed as $\Delta Z/L_0$, a function of probe length ΔZ and the Kolmogorov turbulence outer scale L_0 [56,60]. When $\Delta Z/L_0 < 0.1$ (reported by Banakh et.al [8]), the average wind speed error is estimated to be $d_{Airflow} \cong 2 \sim 3\% \approx 0.2$ m/s. This uncertainty can be reduced to 1% on offshore [180].

To deliver overall Lidar measurement uncertainty, a root sum square method is used. Assuming wind speed U is a function of several variables, x_1, \dots, x_n with uncertainty of dx_1, \dots, dx_n , therefore, overall uncertainty can be calculated as Eq.(3.23) [173].

$$\delta U = \sqrt{\left(\frac{\partial U}{\partial x_1} \delta x_1\right)^2 + \dots + \left(\frac{\partial U}{\partial x_n} \delta x_n\right)^2} \quad (3.23)$$

Assuming wind measurement is linearly depend on all of the variables, and all the components of uncertainty can be treated as separate sources, then, overall Lidar uncertainty is given as Eq.(3.24) [86].

$$\delta U_{Lidar} = \sqrt{(\delta_{cal})^2 + (\delta_{tilt})^2 + (\delta_{Airflow})^2} \approx 0.22 \text{ m/s} \quad (3.24)$$

3.2.3. ZephIR wind Lidar system



Fig. 3.14: The ZephIR Doppler wind Lidar [70]

ZephIR Lidar was first introduced in 2003 by QinetiQ which was initially deployed on the nacelle of a turbine for the first time to remotely measure the upstream wind speed at 200m in front of turbine blades (Fig.3.14 top left) [70]. Based on this success, a prototype

of ground based scanning Lidar is launched immediately (Fig. 3.14 top middle). In 2005, the ground based Lidar was commercially available at a price of 135,000 Euro (Fig.3.14 top right). The two bottom pictures of Fig.3.14 show the 2nd generation "ZephIR 300" and the dual mode Lidar "ZephIR DM". Table.3.5 gives the specification and main parameters.

Table 3.5.: Specification of ZephIR Lidar

Transmitter		Erbium doped DFB fiber laser
Wavelength	μm	1.575
Laser power (average)	W	1
Pulse energy	μJ	10
Pulse length	μs	10
Pulse repetition frequency	kHz	100
Range (min, max)	m	10, 200
Range resolution	m	±0.07 @10m, ±7.7 @200m
Min/max wind speed	m/s	2/70
Accuracy	m/s	±0.1
Receiver telescope aperture	mm	70
Prices	Euro	Ca. 135,000

3.2.3.1. Structure of the ZephIR Lidar system

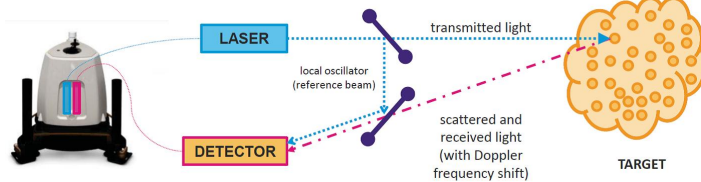


Fig. 3.15.: A bistatic Lidar system to explain the work principle [162]

Fig.3.15 shows the concept of ZephIR Lidar. It is using a CW laser source as transmitter. Particularly, an ultra-low phase noise seed laser with extremely narrow linewidth is used for seeding the fiber amplifier. It is a Distributed Feedback (DFB) fiber laser with 1565 nm wavelength which is made from a linear fiber Bragg grating to ensure a narrow linewidth (\sim kHz) operation. ZephIR Lidar is using an Erbium Doped Fiber Amplifier (EDFA) direct amplify the seed laser without any pulsation process and without the AOM to preshift the frequency. Therefore, ZephIR Lidar cannot distinguish the wind direction from the measurement data.

Transmission and receiving unit

Unlike the pulse Lidar system using the time of flight to distinguish the return signal from different measurement distances, the CW Lidar cannot tell from which distance the

scattering signal received. Assuming that the received energy is only or mostly coming from the focused volume which depends on the depth of focus of the transmission and receiver optics. Fig. 3.16 shows the difference of the CW Lidar and pulsed Lidar in terms of the optical system design of transmitter and receiver: CW Lidar focuses to the detection volume sharply to determine the measurement volume, while pulsed Lidars are rather using a collimated optics setup to softly focus to the center of maximum detection range.

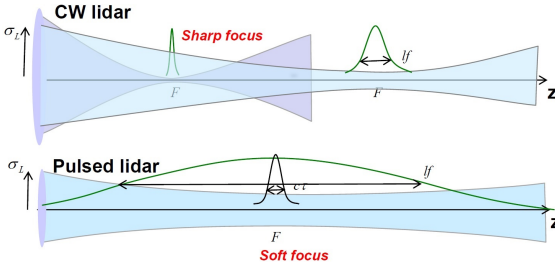


Fig. 3.16: Transmission and receiving optics design of a CW and Pulsed Lidar [162]

When measuring different distances, ZephIR Lidar first focuses to one distance, then shifting the focus to the next (Fig.3.17). Measuring each distance takes around 3 seconds. In total, 5 different distances can be measured.

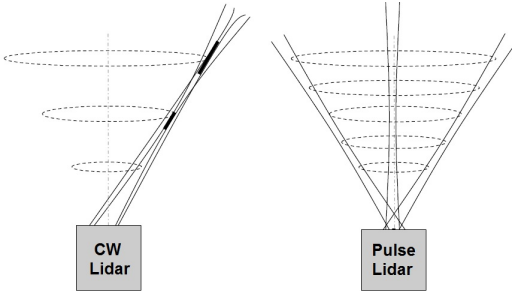


Fig. 3.17: Illustration of CW and pulse Lidar measuring at different heights [162]

For a monostatic Lidar, the total power received at detector is proportional to the contribution of the focused beam at distance R .

$$S_T \propto \int_{-\infty}^{\infty} S(R)dR \tag{3.25}$$

Where, $S(R) = \frac{\Gamma/p}{\Delta^2 + \Gamma^2}$ is a Lorentzian function describing the contribution of the focused beam, Δ is the distance from the focus point along the optical axis, $\Gamma = \lambda R^2 / A_{Tel}$ is FWHM of the collection power weighting factor, λ is wavelength of laser, R is focus range, A_{Tel} is effective beam area at the position of telescope lens [71, 162]. Fig.3.18 shows the collection power weighting factor plot (left), the probe length and volume (right) at different focused height R . Therefore, for a shorter distance the resolution is very small (less than 30 m under 130 m range). However, it cannot focus beam to a long distance (over 300 m). Since the system losses range resolution ability at long distance.

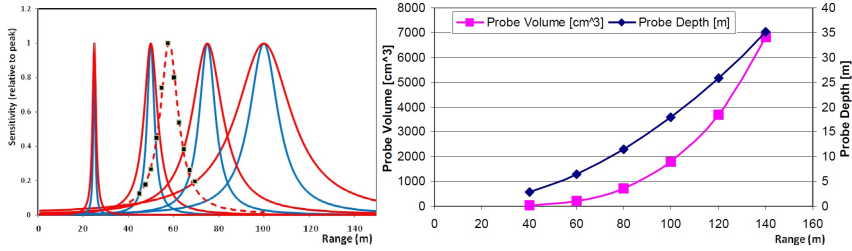


Fig. 3.18.: (Left) Calculated signal collection efficiency when focused different ranges with beam waist diameter at the lens position of (red) $A=20\text{mm}$, (blue) $A=28\text{mm}$, the black squares points are calibration measurement at distance of 68m . (Right) probe length and probe volume at different range [162]

The scanning unit of ZephIR Lidar uses a conical scan mechanism that the beam rotates to scan in a cone by a rotating mirror with a 30° scan angle. The mirror rotates in 1 Revolutions per seconds (RPS), which create 50 measurement points in one rotation. After it finishes three scan circles in each distance, the system mechanically adjust the focal distance to the next distance. The refocus of laser takes around 1 second. Standard ZephIR measures 5 different heights and one unfocused height for cloud detection. Therefore, to finish one full space wind profiling, ZephIR Lidar needs at least 24 seconds.

The detection unit uses the coherence detection to detect the Doppler shift frequency. However, the ZephIR Lidar does not preshift an offset frequency, therefore, it is not possible to determine the shift direction of the radial velocities. A wind direction sensor is mounted on the system to sense the wind direction. Furthermore, due to the laser RIN and other lower frequency noises, the measurement of low wind speed is not accurate [37].

Signal processing unit includes an ADC with a sampling frequency of 100 MHz, a hardware low-pass filter with cut-off frequency of 50 MHz to eliminate aliasing problems, and a Field Programmable Gate Array (FPGA) for Fast Fourier Transform (FFT) to analyze the spectrum. With the 50 MHz cut-off frequency, the maximum detectable LOS wind speed is around 38.8 m/s with the 1550 nm laser. ZephIR uses 512 points DFT to calculate the spectrum and output to 256 spectral points with 200 kHz bin width which corresponds to 0.15 m/s LOS wind speed. Each DFT uses $5\text{ }\mu\text{s}$ data, then 4000 spectrum are averaged to increase the Signal to noise ratio (SNR). The processing time at each point is around 20 ms which results a 50 Hz measurement rates.

3.2.3.2. Wind field reconstruction

Assuming the wind speed the probe volume is the same. By the conical scan, the LOS wind speed becomes a function of the scan angle as shown in Fig.3.19.

$$\langle U_{\text{LOS}} \rangle = |a \cdot \cos(f - b) + c| \quad (3.26)$$

Where, f is the scanning *Azi* angle, parameters a , b , and c are the coefficient obtained by applying a nonlinear least-square fitting for up to 150 LOS wind speed data sets. ZephIR Lidar uses a polar plot, the "Figure of eight" (Fig.3.19 right), to provide the information at a glance of the speed, direction, and vertical wind component. The wind speed can be determined by substitution in Eq.(3.27) [162].

$$u_{\text{Wind}} = \frac{a}{\sin \theta}, \quad w_{\text{Wind}} = \frac{c}{\cos \theta}, \quad \text{Azi} = b, \text{ or } b \pm 180^\circ \quad (3.27)$$

here u_{Wind} and w_{Wind} are horizontal and vertical wind speed, *Azi* is the direction. Since the LOS wind speed does not distinguish the up or down shift of the Doppler frequency, there are two equally valid solutions separated by 180° for the coefficient b . The system chooses the value which is closed to the measured wind direction from the direction sensor.

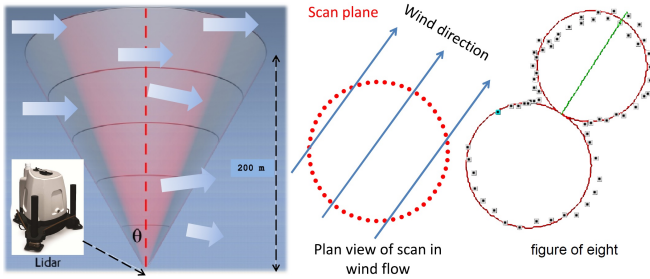


Fig. 3.19.: Illustration of the conical scan of ZephIR Lidar system and the Velocity-Azimuth Display (VAD) data visualization of the LOS wind speed [162]

3.2.3.3. Performance analysis

Backscattering light power is direct proportional to the SNR which is given as the sensitivity of the ZephIR Lidar system as [80].

$$\text{SNR} = P_L \frac{\pi \eta \beta_\pi \lambda}{B h \nu (1 + N_D(\nu) + \text{RIN}(\nu))} \quad (3.28)$$

here P_L is the laser power, η_{Lidar} is the system efficiency, β_π is backscattering coefficient, λ_0 is the laser wavelength, B is the signal bandwidth, $h\nu$ is the light quantum energy ($h\nu = 1.3e - 19\text{J}$), $N_D(\nu)$ is the dark noise and $\text{RIN}(\nu)$ is the laser RIN. The receiving power is proportional to the probe volume and solid angle. With ZephIR Lidar, the probe length is proportional to R^2 and inverse proportional to the area of aperture A . Meanwhile, the solid angle is inverse proportional to R^2 and proportional to the aperture area A . Therefore, the ZephIR Lidar SNR is independent of the focus range R and aperture A . Based on the following parameters, $\text{SNR} = 0.1$, $\eta \sim 0.3$, $P_T = 1\text{W}$, $\lambda = 1.565\mu\text{m}$, $B \sim 1\text{MHz}$, the minimum detectability of the β_π calculated as $\beta_\pi|_{\text{Min}} = 8 \times 10^{-9} \text{m}^{-1} \text{sr}^{-1}$.

3.2.3.4. System measurement uncertainties

The measurement uncertainty limited the performance of a Lidar system. As mentioned above, the vector wind speed is estimated via the curve fitting of VAD data. The LOS wind speed is calculated with $V_{LOS} = \frac{2}{\lambda} v_{Dopp}$ over a probe volume. The MTC final progress report by renewable energy research laboratory has well documented the factors that limiting the measurement uncertainty of ZephIR [91]. In this session those factors are summarized based on this report.

Uncertainty from mean Doppler frequency

ZephIR Lidar estimates the averaged LOS wind speed through the whole probe volume $V_{LOS} = \frac{\lambda}{2} \overline{v_{Dopp}}$, $\overline{v_{Dopp}}$ is the mean Doppler frequency through the probe volume. Therefore, uncertainties from the mean value estimation brings error to the measurement accuracy over the probe length ΔZ . It can be described as Eq.(3.29) [8].

$$\delta_v^2 = 0.26 \frac{\sigma_{LOS}^2 \lambda}{t_0 (\Delta Z \epsilon_T)^{1/3}} \quad (3.29)$$

here σ_{LOS}^2 is the variance of LOS wind speed, λ_0 is the laser wavelength, t_0 is the integration time, ΔZ is the probe length, ϵ_T is the rate of turbulent energy dissipation. Accordingly, with $t_0 = 20$ ms, at 100 meters height, probe length $\Delta Z = 18$ m, standard deviation of a 3 m/s average wind speed is $\delta_{LOS} = 0.018$ m/s, assuming the turbulent energy dissipation rate $\epsilon_T = 10^{-2} \text{ m}^2/\text{s}^3$, the uncertainty from mean Doppler frequency is $\delta_{Dopp} \cong 0.2\%$.

The range accuracy

ZephIR Lidar probes the atmosphere by adjusting the internal optics with uncertainties. These uncertainties leads to a wind speed estimation error, which is defined as

$$\delta_{Range} = \frac{c \delta_v}{4 \Delta v \cdot v_{mod}} \quad (3.30)$$

here c is the speed of light, σ_v is standard deviation of the measured frequency. Δv and v_{mod} are the modulation parameters which are assumed to be 1 kHz and 1.3 GHz for ZephIR Lidar [103]. Karlsson et.al. documented the range accuracy of the ZephIR Lidar system to be approximately 6 m. Therefore, with a strong wind shear ($\alpha_{shear}=0.2$), the measurement uncertainty at 100 ± 6 m is 0.09 m/s in an 8 m/s average wind speed. Therefore, the wind speed measurement uncertainty from the range accuracy is $\delta_{Range} \cong 1.2\%$.

Non-uniform airflow in the probe volume

When $\Delta Z/L_0 < 0.1$, the average wind speed error from the non-uniform airflow in the probe volume is estimated to be $\delta_{Airflow} \cong 5\%$ [91].

Velocity estimation uncertainty is coming from the error in Doppler spectrum estimation. Lidar CNR can be improved by averaging the spectrum. ZephIR Lidar averages 4000 spectrum to get the output. Error from the spectrum estimation is given as

$$\epsilon_s = \sqrt{(A - 1) + A/m} \quad (3.31)$$

Where m is the number of single spectra measured during the integral time, A is the spatial resolution, where A tends to unity for longer probe length. For long range measurement, the spectrum estimation uncertainty reduces with the square root of m . which means that by averaging 4000 spectra, the relative error associated to each measurement is $\sqrt{1/4000} = 1.58\%$. This error is further averaged by 105 times (the effective LOS data in 3 s). Hence, the velocity estimation uncertainty is approximated as $\delta_{esti} \cong 0.2\%$.

Error from nonlinear least squares data fit

Estimation the coefficients of the LOS speed to azimuth angle data with Eq.(3.32) leads the error of wind vector.

$$\langle V_{LOS} \rangle = |a \cdot \cos(f - b) + c| \quad (3.32)$$

The curve fitting algorithm is a regression analysis that the error in the estimated best-fit parameters cannot be avoided. The estimated standard error during the process is given as

$$\hat{\delta} = \sqrt{\frac{\sum \hat{u}_i^2}{n - 2}} \quad (3.33)$$

Where, \hat{u}_i is the estimated error, n is the number of data point, in the case of ZephIR Lidar, $n=105$ in each 3 second measurement period. Jaynes et.al used a simulation approach to randomly generate the Lidar data for the nonlinear least square fitting process, and found the error during the wind speed parameter extraction process is $\delta_{fit} \cong 0.1\%$ [91].

Improper instrument setup

An improper instrument setup leads a non-horizontal probe volume which causes the scan points at different levels. Assuming the Lidar measurement range is 100 m, 1° instrument setup error corresponds to 2.02 m of overall altitude divergence. This uncertainty corresponds to a measurement uncertainty of 0.03m/s in an 8 m/s average wind with a strong wind shear ($\alpha_{shear} = 0.2$). Thus, the uncertainty from improper instrument setup is

$$\delta_{setup} = 0.4\% \quad (3.34)$$

Assuming all the components of uncertainty can be treated as separate sources. The overall uncertainty can be describe with Eq.(3.35) [86, 180].

$$\delta U_{Lidar} = \sqrt{(\delta_{Dopp})^2 + (\delta_{BS})^2 + (\delta_{Flow})^2 + (\delta_{esti})^2 + (\delta_{fit})^2 + (\delta_{setup})^2} \approx 5.2\% \quad (3.35)$$

3.2.4. Windar Photonics Wind Eye

The Windar Photonics Lidar system (Fig.3.20) replaced the high cost fiber laser source with a low cost semiconductor laser which breaks down the market price into an affordable region. As a wind turbine nacelle mounted system, Wind Eye has similar design as Wind iris. It equipped two fixed telescopes to measure at two directions with an angle of 60° .



Fig. 3.20: Windar Photonics WindEye Lidar (Source: Widar Photonics)

Table 3.6.: Specification of Windar Photonics WindEye Lidar (Source: Widar Photonics)

Transmitter		CW Semiconductor Laser (MOPA-SL)
Wavelength	μm	1.55
Laser power	mW	~ 600
Range		Fixed 70m (LOS), 60m (Horizontal)
Wind speed range	m/s	2 \sim 30
Wind speed accuracy	m/s	0.2
Wind direction range		$-30^\circ \sim +30^\circ$
Wind direction accuracy		$\sim 1^\circ$
Probe length	m	9.5 (LOS)
Data output rate	Hz	1
Prices	Euro	Ca. 22,000

3.2.4.1. Structure of the WindEye Lidar system

Fig.3.21 shows the design of WindEye Lidar, which is similar to the Avent Wind Iris Lidar: it consists an optical head and a processing unit, in between they are connected with an interface cable. Both are using two fixed telescope and one non-mechanical direction switch for the two directional measurements. A liquid crystal switch for switching between S and P polarization is used together with a polarization BS to change the directions. OCS is the optical circulator/switch, Photo detector/diode (PD) is the photo detector, Contr is the controller for OCS liquid crystal switch, FPGA denotes the field-programmable gate array, PSU is the power supply unit, LOS1 and LOS2 mean the LOS direction 1 and 2 [161].

The optical head unit contains two telescopes, a polarizing beam splitter, a liquid crystal polarization switch, and a photo detector. Two telescopes are directed with angles of 30° from the center. The two beams are focused into 70m distance with a probe length of 9.5m along the LOS. The probe length of a CW Lidar system can be calculated as

$$L_{\text{Probe}} = 2\lambda R^2 / \pi(D_{\text{Rec}}/2)^2 \quad (3.36)$$

The diameter of telescope, D_{Rec} , can be calculated as $D_{\text{Rec}} = 2R\sqrt{2\lambda/\pi L_{\text{Probe}}} = 45\text{mm}$.

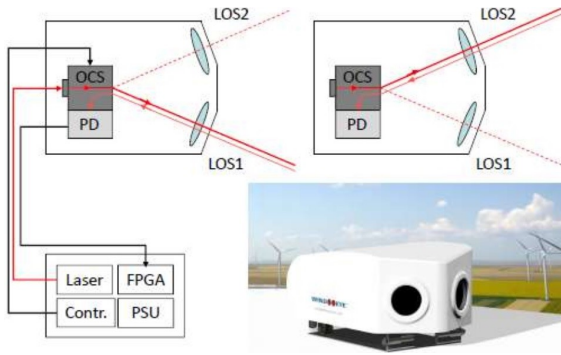


Fig. 3.21: System structure of WindEye Lidar [161]

Processing unit of wind Eye Lidar contains the electronics parts of the system, such as the power supply unit, control and signal processing unit, as well as the laser source. Wind Eye is using a novel CW Semiconductor Laser (SL) in combination with a semiconductor power amplifier (MOPA-SL) [138, 161]. The MOPA-SL is a fiber pigtailed butterfly laser module with a wavelength of 1550 nm, optical power output from the fiber over 500 mW, and ultra-narrow linewidth (ca.200 kHz) single mode operation, and low RIN.

3.2.4.2. Wind field reconstruction

Reconstructing the wind field is the same as the Wind iris which is shown on Fig.3.11 where the measured LOS wind speeds can be described as a function of the yaw angle γ_{Yaw} .

$$U_l = U_{Wind} \times \cos(\alpha_{Lidar} - \gamma_{Yaw}), U_r = U_{Wind} \times \cos(\alpha_{Lidar} + \gamma_{Yaw}) \quad (3.37)$$

where,

$$\gamma_{Yaw} = \tan^{-1} \frac{f - 1}{\tan \alpha_{Lidar}(f + 1)}, f = \frac{U_r}{U_l}, u = \frac{U_r + U_l}{2\cos \alpha_{Lidar}}, v = \frac{U_r - U_l}{2\sin \alpha_{Lidar}} \quad (3.38a)$$

$$U_{Wind} = \frac{1}{2} \sqrt{\left(\frac{U_r + U_l}{\cos \alpha_{Lidar}}\right)^2 + \left(\frac{U_r - U_l}{\sin \alpha_{Lidar}}\right)^2} \quad (3.38b)$$

3.2.5. Summary

Various commercial Lidar products are on the market recent years, here in this section the four major products focused on the wind energy applications have been shown in details. These four products can represent most of the commercial Lidar techniques. Table.3.7 shows the summary of those four major commercial Lidar system specifications.

Table 3.7.: A comparison of the parameters of different Lidar system

Lidar Products	WindCube	Wind iris	ZephIR	WindEye
Type	Ground	Nacelle	Ground	Nacelle
Transmitter	Pulsed	Pulsed	CW	CW
Wavelength	1.54 μm	1.54	1.565	1.55
Average (Peak) power	0.2 (5) W	0.2 (5)	1	~ 0.6
Repetition rate	20 kHz	20 or 10	100	NA
Pulse energy	10 μJ	10 or 20	10	NA
Pulse length	200 ns	200 or 400	10 [μs]	NA
Beam configuration	5 beams	2 beams	VAD	2 beams
Range (min, max)	40~200 m	40 \sim 200 or 80 \sim 400	11 \sim 200	70 (LOS)
Speed range	0 \sim +60 m/s	-10 \sim +40	+2 \sim +70	+2 \sim +30
Speed accuracy	0.1 m/s	0.1	0.1	0.2
Data output frequency	1 Hz	1 \sim 4 or 1 \sim 2	1/3	1
Number of ranges	12	10	5	1
Range resolution	20 m	30 or 60		9.5 (LOS)
Scanning cone angle	30°	30°	30°	60°
Price	Euro 135,000	135,000	115,000	22,000

3.2.6. Other commercial Lidar systems

Sgurr Energy Galion Lidar, Halo Photonics "Stream line" series Lidar system, Mitsubishi Electronics Lidar, Lockheed Martin WindTracer are mainly for wind meteorology purpose.

Galion Lidar was launched in 2008 by the British renewable energy consultancy Sgurr Energy, a member of the international energy services company Wood Group. The Galion Lidar is a pulsed Lidar system which has a range of 250m with the short range type G250 and a range of 4 km with the long range system G4000 (Fig.3.22). The long range type G4000 can probe 130 different ranges simultaneously with a resolution of 30m.



Fig. 3.22: Galion Lidar G250 and G4000 (Source: Sgurr Energy)

Halo Photonics Ltd. offers the pulsed Lidar system "Stream line" series (Fig.3.23). The short range system "Stream line pro-Lo" offers a 250m range. The standard version has a range of 3 km and optionally can be extend to 10 km. The system has a high temporal resolution up to 0.1s which allows measurements of the wind fluctuations as a measure of atmospheric turbulence. A unique scanning unit "all sky scanner" provides a 0.01° resolution full space scan feasibility for a 360 point VAD scanning. DBS wind profiles, staring and arbitrary scans can be achieved. System also provides a second receiver channel can be added to determine the depolarization ratio.

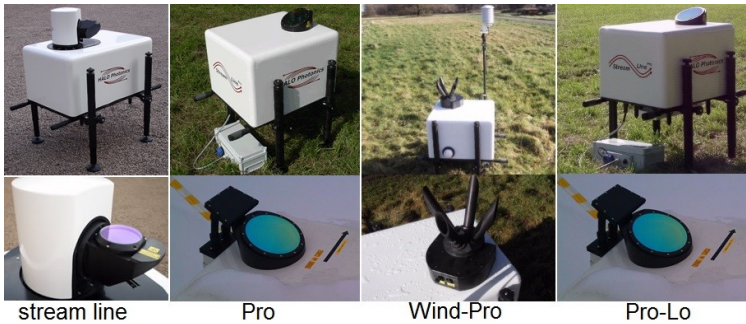


Fig. 3.23.: Halo Photonics Stream Line Lidar series, from left standard, Pro, Wind-Pro, and Pro-Lo, (down) scanning for each lineup (Source: Halo Photonics)

The Japanese company Mitsubishi Electric has been involved to develop an all-fiber CDL system since 2004. The first commercial all-fiber CDL system (LR-05FC series) has been manufactured in 2005 [4]. Today, Mitsubishi has 4 different products (Fig.3.24). The all fiber

compact Lidar standard system has a full scanning optical head with a 60 mm diameter telescope which can focus the beam into 100 m - 1 km without truncation. The system allocates a 1.54 μm MOPA laser system with selectable pulse duration of 200, 500, and 1000 ns which allows the range resolution of 30m, 75m, and 150m. Except the all fiber Lidar product, Mitsubishi also has a compact all in one system, Nacelle Lidar system with 9 telescopes which can simultaneously measure at 9 different points (Fig.3.25).



Fig. 3.24.: Mitsubishi Electric Lidar system lineups: from left) standard Compact Optical-fiber Doppler Lidar System, Compact Wind Lidar, Nacelle Lidar, and Large-scale Coherent Doppler Lidar System (Source: Mitsubishi)



Fig. 3.25.: Mitsubishi Nacelle Lidars (Source: Mitsubishi)

WindTracer Lidar is designed by US security and aerospace company Lockheed Martin (Fig.3.26). The earlier product is equipped a 2 μm laser, while current product uses a 1617nm laser with $300 \pm 150\text{ns}$ pulse length. WindTracer has a maximum range of 33 km with 100 m resolution. It equips a 12 cm aperture mirror scanner to perform a 360° azimuth angle and $-5^\circ \sim 185^\circ$ elevation angular range with 0.001° resolution. Main application area of WindTracer is on airport safety, wind resource assessment and meteorological researches.

3.3. Doppler wind Lidar on researches

In last decade due to the increasing of the demands on wind resource assessment and quick increasing of wind power installation, the research and development of accurate and low cost wind sensing systems are becoming more and more popular. In 2008, Liu et.al.



Fig. 3.26: WindTracer Lidar system (Source: Lockheed Martin)

published the development of a mobile Doppler wind Lidar for the measurement of sea surface wind by the Key Laboratory of Ocean Remote Sensing of Ministry of education of China in Ocean University of China [114]. The system is an incoherent Lidar system using an iodine filter based on single-edge technique to discriminate the Doppler frequency shift. Fig.3.27 shows the system on operation, and (right) shows the system design structure. Table 3.8 shows the specification parameters of the system. However, this system is not able to clear the laser safety during operation.

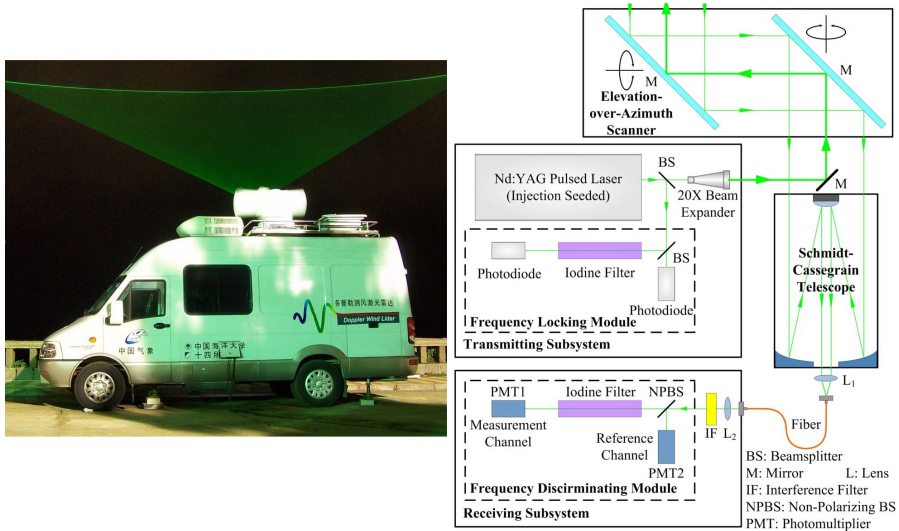


Fig. 3.27.: Incoherent Doppler wind Lidar system based on 532nm laser at Ocean University of China, (right) illustration of the system design [114]

Table 3.8.: Specification parameter of the Ocean University of China incoherent Lidar [114]

Transmitter		Diode-pumped Nd:YAG laser
Wavelength	nm	532
Repetition rate	kHz	2.8
Pulse energy	mJ	2.2
Pulse width	ns	30
Pulse laser linewidth	MHz	<35
Spectral purity		>99.9%
Far-field divergence	μrad	70
Beam pointing stability	μrad	<5
Telescope aperture	mm	305
Field of view	μrad	120
Interference filter bandwidth	nm	0.11
Interference filter transmission		76%
Sampling range resolution	m	10
scanning speed	$^\circ/\text{s}$	1 ~ 10
scanning accuracy	$^\circ$	0.1

The system uses an injection seeded Nd:YAG pulsed laser with 532nm and 2 mJ pulse energy. Part of the transmitting laser passes an iodine filter for frequency locking control to ensure a long term frequency stability. The receiving unit uses a direct detection method where part of the Doppler shifted scattering light passes into the MPT as a reference, where the other part passes through the iodine filter and is detected by the MPT to measure the Doppler frequency. Assuming the detection range is r , detected photon on the reference N_R and on the measurement channel N_M can be written as

$$N_R = k_R \left(\frac{\Delta R}{r^2} \right) [\beta_a + \beta_m] \exp \left(-2 \int dr [a_a(r') + a_m(r')] \right) \quad (3.39a)$$

$$N_M = k_M \left(\frac{\Delta R}{r^2} \right) [f_a \beta_a + f_m \beta_m] \exp \left(-2 \int dr [a_a(r') + a_m(r')] \right) \quad (3.39b)$$

Where ΔR is the probe range, β_a and β_m are the backscattering coefficient of aerosols and molecules, α_a and α_m are the extinction coefficient of aerosols and molecules, k_R and k_M are the system constant for the reference and measurement beam, f_a and f_m are the transmission factor of aerosol and molecule which are given as

$$f_a(\nu_D) = \int G(\nu - \nu_D) F(\nu) d\nu \quad (3.40a)$$

$$f_m(\nu_D, T, P) = \int \mathfrak{R}(\nu - \nu_D, T, P) F(\nu) d\nu \quad (3.40b)$$

Where, ν_{Dopp} is the Doppler frequency, $G(\nu - \nu_D)$ is the normalized laser line shape function with $\int G(\nu - \nu_D) d\nu = 1$, $F(\nu)$ is the iodine filter transmittance function, $\mathfrak{R}(\nu -$

v_D, T, P) is the normalized Cabannes function with $\int \mathfrak{R}(v - v_D, T, P)dv = 1$. Then the wind ratio is given as

$$R_w(v_D, R_b, T, P) = \frac{k_M}{k_R} f(v_D, R_b, T, P) \tag{3.41}$$

with

$$f(v_D, R_b, T, P) = \frac{f_a(v_D)R_b + f_m(v_D, T, P)}{R_b + 1} \tag{3.42a}$$

$$R_b(r) = \frac{\beta_a(r) + \beta_m(r)}{\beta_m(r)} = \frac{f_m N_R(r)}{N_M(r)} \tag{3.42b}$$

Therefore, the LOS wind can be written as

$$V_{LOS,i} = \frac{R_{w,i} - r_0}{r_0 S} \tag{3.43}$$

here r_0 is wind ratio when LOS speed is zero $V_{LOS} = 0$, $S = (1/r_0)(dR_w/dV_{LOS})$ defined as the fractional change in the wind ratio per unit LOS velocity.

Another interesting work is from the group at TU Hamburg-Harburg, for a CW synthetic low-coherence wind Lidar system. Fig.3.28 shows the design of the low coherence CW Lidar system [22]. The method described by this group basically is similar as my presented approach where a short coherent length laser is used along with a delayline to match the phase of the signal and reference beam to achieve the optical coherent detection. Their concept uses a so called synthetic broadband laser source which includes a single longitudinal and transverse mode laser diode with a linewidth of 100kHz, and an electro-optical phase modulator to broad the linewidth to 10 ~ 100MHz.

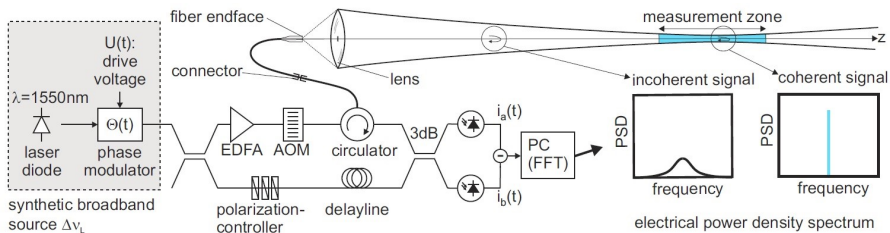


Fig. 3.28.: Design concept of low coherence CW-Lidar system TU-Hamburg-Harburg [22]

3.3.1. A comparison of the Different Lidar system

Table.3.9 illustrates the major differences of CW and pulsed Lidar based on UpWind project report [28]. CW Lidars have a variable range gate which is depending on measurement distances. The range depending gate means that system performance is varied at different

Table 3.9.: The main differences between CW and pulsed Lidar systems [28]

	CW Lidar	Pulsed Lidar
Velocity accuracy	Limited by coherence time of the atmosphere	Limited by the pulse duration
Range gate	Determined by focus increases as R^2	Constant, around $c\tau/2$
Number of range	Less than 10, sequentially addressed	Can be more than 100, simultaneously addressed limited by SNR at long range
SNR	Independed on measurement range	Linearly depended on measurement distance
Sensitivity to targets out of focus	High	No
Max range	Hundreds meters	Some kilometers
Laser power	Large average power	Limited average power (However high peak power)
Polarization	Not necessary	mandatory

measurement ranges but the received backscattering power remains the same. Pulsed system has a fixed probe length which is only depending on the pulsed length. With stronger pulse energy, the pulse Lidar can reach some kilometers measurement distance. This is also the reason that most Lidar products use the pulse system.

3.4. Wind turbine control system

Since 1990s, the pitch control, torque control, and power quality control of wind turbine systems have become industry standard. Generally, reducing the Cost of energy (COE) is the main purpose of the control system. The COE for a wind turbine system includes the capital cost and O&M cost. In order to reduce COE, maximum energy capture, lower mechanical loads to reduce the O&M cost and extend the lifetime, meanwhile get better power quality are the main objectives of the controls. As shown on Fig.2.6, the operation of wind turbine can be mainly divided into two regions, below and above the rated wind speed (since on region I and IV, the turbine is parked, they are not considered here). The control strategies are different in different regions: under rated speed, generator torque control provides the input to vary the rotor speed, and keeps the blade pitch angle and TSR to maximize the power capturing; in above rated conditions, the primary objective is to maintain a constant power output by keeping the generator torque constant with pitch control by varying the blade pitch angle to adjust the capturing wind energy. The active pitch control has been proved to be an efficient way to reduce fatigue load and increase the power captures [1]. Especially, since the rotor sizes increases, the effects from wind shear are getting stronger [7]. Therefore, to reduce not only the fatigue loads but also the extreme loads need more advanced pitch system as well as new designs of the blades and

using of new materials. In [168], a preview based control is presented to improve the blade load reduction via the blade pitch angle control which guarantees a hard upper bound on the flap wise bending moment. In [17], an extra input is added to the control system by using an accelerometer to measure the acceleration of the tower. This new measurement is used to calculate the extra pitch contribution to the original pitch which helps to damp the tower motion in the control system.

In this session, a brief overview of different wind turbine pitch control technologies are given.

3.4.1. Standard industrial feedback control

Most commercial wind turbines are using FB control for the active pitch system. FB control is a control mechanism that uses information from measurements to manipulate a variable to achieve the desired result. Most of the FB controllers are designed as straight forward PI(D) based Collective Pitch (CP) controllers, while the derivative term may be filtered to reduce the measurement noise errors from sensors. The PI(D) FB works as reducing the errors between the rated and actual rotor speed by controlling the pitch angles as shown in Fig.3.29 [181]. K_P , K_I , and K_D are the scheduled controller gain due to system nonlinearities. Then, the pitch control signals are given as the rates of angle changes or directly the pitch angle.

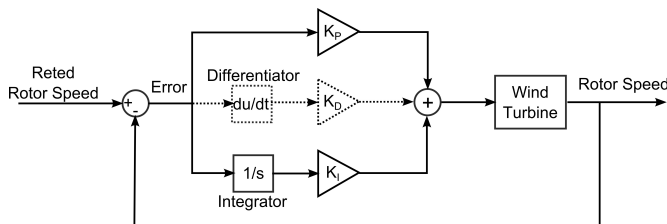


Fig. 3.29: A PI FB controller for wind turbine pitch system

Collective pitch control strategies are mostly common used in industry due to the easy implementation and the low LCOE for such systems. However, since the increasing of modern multi-megawatt wind turbine sizes, the wind fluctuations effect the torques more significantly. Furthermore, as wind turbine rotor moves through un-uniform wind field, blades experience periodic loading. The spectrum of this periodic loading has the most pronounced harmonic at the frequency of wind turbine rotational speed. Therefore, for reduction of periodic loading, Individual Pitch Control (IPC) system has also been evaluated successfully for mitigating such loads [7, 168]. In contrast to collective pitch control which adjusts the pitch of all rotor blades to the same angle at the same time, IPC dynamically adjusts the pitch angle of each rotor blade individually. The main benefit of IPC is the reduction of fatigue loads on the rotor blades and tower to increase the turbine lifetimes. The project Upwind mentioned a more advanced pitch system, changing the pitch of the tip more than the root could reduce more loads [7]. Adding flaps on the blades as on aircraft is also mentioned as an option for further load reduction. The 4.1MW offshore wind turbine from General Electric (GE) implemented the IPC in operations [182].

3.4.2. 2-DOF Feedforward/Feedback control

Sensitive to the disturbance is the principle limitation of FB control, since with FB there is a time delay on reacting of the disturbance. After a disturbance happen to the system which leads to an error, then FB controller starts to minimize the error. Therefore, the disturbance effects cannot be avoided (Fig.3.30). In contrast to FB control, FF control measures the disturbance and pre-calculates the output to cancel the disturbance therefore to avoid the error.

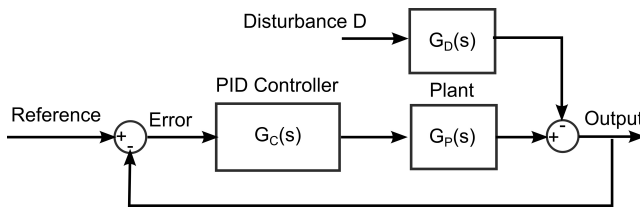


Fig. 3.30: General working principle of a feedback control

In order to optimize the control system, a so-called 2-DOF control strategy with the both advantages of FF and FB control is used. When a measurable disturbances effect the control system, the FF controller can determine the manipulated value to counteract the effect by applying the FF control directly into the target. Then, the unknown disturbances can be controlled by the FB controller part. In the case of wind turbine pitch control system, the wind turbulence as disturbance inputs can be measured by a Lidar system. This Lidar assisted control strategies are often used at researches recent years [54, 155]. Fig.3.31 shows this 2-DOF pitch control strategy with Lidar. The FF controller part gets the wind speed information via the Lidar measurement before it reaches the turbine and generates the required pitch angle to the turbine in advance. Meanwhile the FB controller mitigates the unpredictable rotor speeds error. Therefore, the load on turbine could be alleviated by the pre-emptive control of the turbine. Advantages of using Lidar have been investigated in different studies [54, 155, 158, 168, 181].

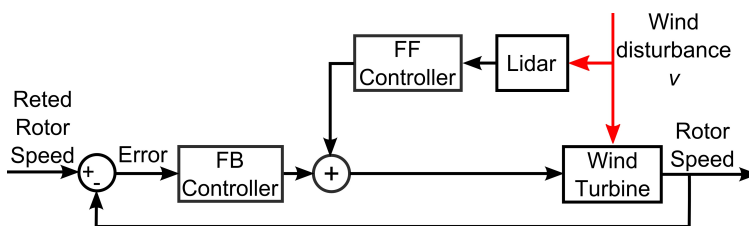


Fig. 3.31.: Combined FB and FF 2-DOF control for the wind turbine pitch system

Two designs of FF control are tested by N. Wang [181], an adaptive FF controller based on Filtered-X Recursive Least Square (FX-RLS) algorithm and a non-adaptive controller based on Zero-Phase-Error Tracking Control (ZPETC) technique. ZPETC is a model inverse FF design method. The linearised wind turbine model is designed around a specific operating point. Fig.3.32 shows the design of ZPETC method, where $P_{\Omega u}$ and $P_{\Omega \beta}$ are the open loop

turbine transfer functions from wind speed u and blade pitch angle β to rotor speed error Ω_e . Therefore, the rotor speed error is given as

$$\Omega_e = \frac{P_{\Omega\beta} \cdot FF \cdot u + P_{\Omega u} \cdot u}{1 - P_{\Omega\beta} \cdot FB} = 0 \quad (3.44)$$

Therefore, the FF controller gain is given as

$$FF = -P_{\Omega\beta}^{-1} \cdot P_{\Omega u} \quad (3.45)$$

However, if $P_{\Omega\beta}$ consists of non-minimum phase zeroes, then the FF controller is unstable. Therefore, ZPETC method is applied to avoid this situation [175]. Let's the transfer function model containing non-minimum phase zeros $P(q)$ be written as

$$P(q) = \frac{B^-(q)B^+(q)}{A(q)} \quad (3.46)$$

where $B^-(q)$ and $B^+(q)$ represent the uncancellable and cancellable portions. q is the forward shift operator which is given as $q \cdot u(t) = u(t + 1)$. Therefore, the model inverse FF controller based on ZPETC method is given as Eq.(3.47) [120].

$$FF_{ZPETC}(q) = \frac{B^-(q^{-1})A(q)}{B^-(1)^2B^+(q)} \quad (3.47)$$

Another FF controller design method is the adaptive FF algorithm with "FX-RLS" method

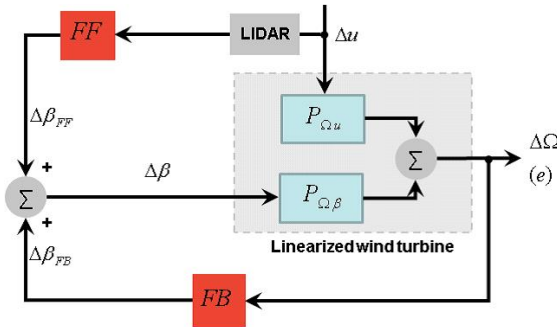


Fig. 3.32: A 2DOF pitch controller with FF term designed by ZPETC [181]

[181]. FX-RLS method is based on RLS adaptive filter algorithm which recursively finds the coefficients which minimize a weighted linear least squares cost function related to the input signals. With the help of Lidar data, the parameter of FF controller can be adjusted by the FX-RLS algorithm to provide load alleviation and rotor speed regulation. Fig.3.33 shows the design of a 2DOF controller where the FF term is designed by such FX-RLS algorithm, where the rotor speed error $e(n, \vec{\theta})$ is a function of discrete time step n and FF

controller parameters $\vec{\theta}$. $\widetilde{P}_{\Omega\beta}$ is the estimated transfer function of $P_{\Omega\beta}$, $\Delta x(n)$ is the Lidar measurement at time step n , $\Delta x'(n)$ is the filtered signal by the $\widetilde{P}_{\Omega\beta}$ which is estimated by a Finite Impulse Response (FIR) filter. Then the error function can be written as

$$e(n, \vec{\theta}) \approx \frac{g(n) + F(n, \vec{\theta}) \cdot \Delta x'(n)}{1 - P_{\Omega\beta} \cdot FB} \quad (3.48)$$

Therefore the RLS algorithm is minimizing the rotor speed error to determine the FF controller parameter. The cost function is given as

$$J = \min_{\vec{\theta}} \frac{1}{N} \sum_{n=1}^N e^2(n, \vec{\theta}) \quad (3.49)$$

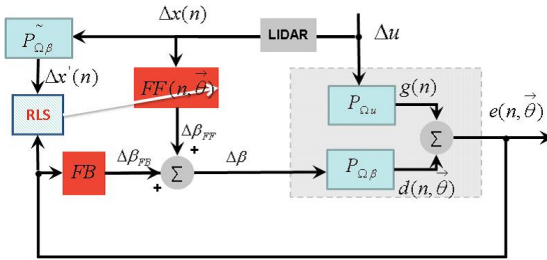


Fig. 3.33: A 2DOF control where FF term is designed by FX-RLS algorithm [181]

3.4.3. Model predictive control

FF and FB control algorithms are often used due to their simplicity and easy implementation. However, when system is getting complex, theoretical limitations restrict the control performance. Therefore, more advanced control methods, such as MPC, start to be more prevalent in research projects [40, 174]. MPC is an advanced control method that has been used in the process industries such as chemical plants and oil refineries since 1980s. Recent years it has started to be used in dynamics system control as well. Especially, the RHC method is approved to be advantageous for a short term planning of ongoing process control problems such as trajectory or reference signal planning for autonomous vehicles [38, 73] and dynamical system for reducing the load from torque fluctuations [174]. Qin and Badgwell reported over 5000 applications of MPC from 1980 to 2003 [146]. MPC controllers rely on the dynamic models of the process. The advantage of RHC is that it allows system at current time slot to be optimized, while keeping future time slots into account. This is achieved by optimizing a finite time horizon, but only implementing the current time slot. RHC has ability to anticipate future events and take control actions accordingly. Furthermore, MPC is an optimal control based method and capable to handle constraints. The MPC model is either obtained by mathematical equations or system responses from

step inputs. The complexity or order of model is usually lower than actual plant, only the significant states are modelled [76]. Fig.3.34 shows a traditional MPC design.

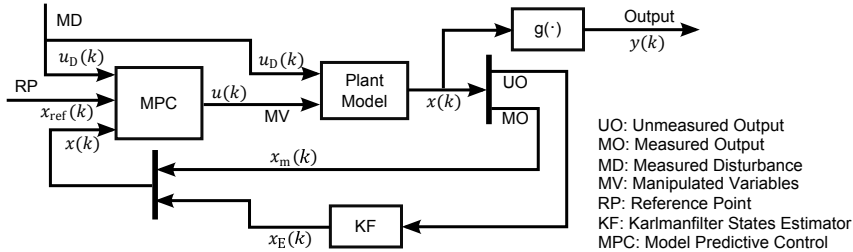


Fig. 3.34.: A full states feedback model predictive control block diagram

3.5. Summary and conclusion

Due to the worldwide energy transition, the needs for renewable energy, especially wind energy, are increasing dramatically in the last decades and expected to continue growing in the future. Under this background, mobile remote wind sensing devices for wind resource assessment and wind turbine aerodynamics studies accelerate the development of Doppler Lidar systems. However, most of the commercial systems are in a high price (> 125,000 Euro), which limited their applications. In Section 3.2, the four major commercial Lidars for wind energy applications were discussed. The ZephIR Lidar and WindCube are multiple purpose Lidar systems which are designed as a mobile device for carrying around for wind resource measurement instead of the unmovable measurement tower. Then, the nacelle Lidar system, Wind iris and Wind eye, are more focused on the wind direction measurement for the slow yaw error corrections.

Meanwhile, fast increasing of wind turbine scale strongly affects the system loads due to the wind shares and turbulence. The demands on more advanced control methods attract the interest of researchers. In the last decade, the studies on Lidar based preview control methods are becoming more prevalent. Such methods require a wind turbine head/nacelle mounted Lidar system for wind field prediction.

These demands lead to a new Lidar market, Nacelle Lidar. So far, the multiple purpose devices, ZephIR and WindCube, are the major devices which are applied on researches of Lidar based control applications and have been approved the benefits on reducing system loads and improving the power production. However, their high prices destined their application only on researches and pilot projects. The low cost Lidar, Wind eye, however can only measure single point in a short distance of 70 meters LOS. And it is more focused on yaw error correction and power curve estimation applications. Due to their slow update rate, and limitations on the flexibility of measurement positions, so far, no works of Lidar assisted preview control based on this kind of nacelle Lidar have been found.

Furthermore, an overview of the state of the art wind turbine pitch control systems have been briefly discussed. The commercial wind turbine systems are mostly equipped with

the conventional PI(D) Feedback collective pitch control. For better performances, some modern turbines use the gain scheduling approach to reduce the effect of nonlinearity. More advanced FB control approach, model based Linear-Quadratic Regulator (LQR), Linear-Quadratic-Gaussian (LQG), and DAC methods have shown their benefits on research projects as well. Section 8.1.2 shows a detail design and performance comparison of a full states FB LQR controller based on the work from Mr. C. Riboldi [149].

In summary, the states of the art Lidar systems are mostly multiple purpose systems which are not yet suitable for the preview pitch control applications for commercial wind turbines due to the economical reasons. So far there are lacks of research and development of a lower cost Lidar system for preview control applications.

Furthermore, from the wind turbine control system point of view. The Lidar assisted preview control approaches are popular in research since last couple years. Those approaches use the Lidar system to remotely measure the wind field in front of the turbines about couple ten to hundreds meters. Therefore, the measured wind field information are the short future wind fields which are going to attack the turbine rotors. With the time gap between the measurement and attacking, a predictively preparing of pitch actuation can be performed. These preview control methods include the FF control methods and MPC methods. The former methods have been tested on field and have been approved the advantages on reducing structure loads and increasing of power productions.

Part II.

The cost efficient Doppler wind Lidar system

4. System design architecture and requirement analysis

To overcome the deficiency of state of the arts Lidar systems, a new concept based on a short coherence length diode laser and multiple length fiber delay-lines is proposed. Then, based on the scenario of Lidar measurement for pitch control applications, requirements of the Lidar parameter are analysed. Part of the results on this chapter can be found on author's publication [SBH⁺12].

4.1. Design concept

Reducing the cost is most important for the research and development of a Lidar system for mass productions. Some concepts have been reported [22, 161], such as WindEye system uses a unique SL-MOPA laser module to reduce the cost. The concept of using a broad spectrum laser with fiber delay-lines to achieve the cost requirement is published on 2012 [SBH⁺12]. Comparing to state of the arts Lidar systems in which fiber lasers with couple kilo-meters coherence length are commonly used, semiconductor lasers has a relative shorter coherence length, in generally couple meters to hundred meters. Within a coherent Doppler wind Lidar system, such short coherent lasers are normally not used due to the high phase noises. Hereby, the presented approach is to introduce such low coherence length diode laser for a Doppler wind Lidar system.

The concept was developed based on our earlier research of using a super continues laser on a frequency domain OCT system for paper production applications (Fig.4.1) [24, 25]. In this system, a broad spectrum laser source with micrometers coherence length is used. By adjusting the reference mirror position, measurement can be achieved only when the light path difference between sample and reference beam is within the coherence length. Therefore, the coherence length of laser sources defines the depth resolution.

The broad spectrum diode lasers not only lower down the system cost but also benefit for selecting a stable probe length based on the coherence length of laser on a standard CW Lidar system with a range depended depth resolution. Losing the range resolution for long distance measurement is the deficiency of the standard CW Lidar system.

4.1.1. Coherence length of lasers

Laser coherence length relates to the interference phenomenon of a laser system. A coherent light means a fixed phase relationship between electric field at different locations or times. There are two different coherence: "spatial" and "temporal". Temporal coherence is the correlation between the electric fields at one location but different time. It is depended

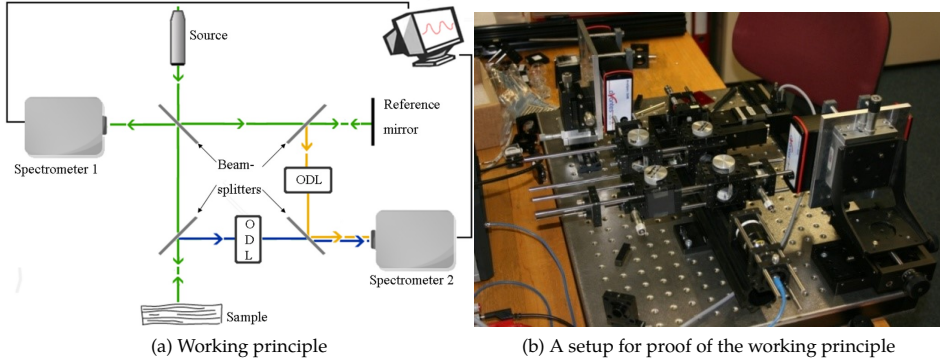


Fig. 4.1.: A modified OCT system setup for paper quality measurement [25]

on the source spectrum $S(\nu)$ which can be described with Eq.(4.1) as a function of the Lorentzian or Gaussian spectrum linewidth $\Delta\nu$ centered at ν [63, 183].

$$\int_{-\infty}^{\infty} S^{(0)}(\nu) d\nu = I_0 \quad (4.1)$$

where I_0 is the intensity of the light over all the spectrum, ν is the frequency. The intensity can be simplified to write as a squared law of the complex electrical field.

$$I(\nu) = |E(\nu)|^2 = E^*(\nu)E(\nu) \quad (4.2)$$

Assuming $E(t)$ is the Fourier transformation of $E(\nu)$, the intensity field can be written as

$$I(\nu) = |E(t)|^2 \int_{-\infty}^{\infty} g^{(1)}(\tau) e^{-j2\pi\nu\tau} d\tau \quad (4.3)$$

Where $g^{(1)}(\tau) = \frac{\langle E^*(t)E(t+\tau) \rangle}{\langle E(t) \rangle^2}$ is the first order correlation function of electrical field, which is also called coherence function $\gamma(\tau)$. It is obtained to describe the degree of coherence as a function of temporal distance z or the time delay $\tau = z/c$. Therefore, the intensity as a function of frequency is the Fourier transformation of the first order correlation function $g^{(1)}(\tau)$ which is known as the Wiener Khinchine theory [90]. The coherence function $\gamma(z)$ is

the inverse Fourier transform of the light source spectrum function $S(\nu)$ [64]. The spectrum function of Gaussian and Lorentzian shape spectrum beam are given as

$$\text{Gaussian : } \gamma(z) = \exp\left(-\frac{1}{\ln 2} \left(\frac{\pi z \Delta\nu_0}{2c}\right)^2\right) \xleftrightarrow{\mathcal{F}} S(\nu) = I_0 \exp\left(-4 \ln 2 \left[\frac{\nu - \nu_0}{\Delta\nu}\right]^2\right) \quad (4.4a)$$

$$\text{Lorentzian : } \gamma(z) = \exp\left(-\frac{\pi \Delta\nu_0}{c} |z|\right) \xleftrightarrow{\mathcal{F}} S(\nu) = I_0 \cdot \frac{\Delta\nu_0^2}{4(\nu - \nu_0)^2 + \Delta\nu_0^2} \quad (4.4b)$$

The coherence time, τ_c , describes the degree of first order temporal coherence via the time when coherence is lost. The coherence length l_c is the propagation length when coherence is lost. Normally, l_c and τ_c is defined as the full width at $1/e$ of its maximum value of $\gamma(z)$. Therefore, the coherence length l_c can be written as

$$\text{Gaussian : } l_c = \frac{2\sqrt{\ln 2} \cdot c}{\pi \Delta\nu_0} \quad (4.5a)$$

$$\text{Lorentzian : } l_c = \frac{c}{\pi \Delta\nu_0} \quad (4.5b)$$

Fig.4.2 shows the plot of a Gaussian and Lorentzian spectrum $S(\nu)$ (right) and its inverse Fourier transform of the coherence function $\gamma(z)$ (left) with a bandwidth $\Delta\nu_0$ of 10MHz centred at wavelength of 785nm. With the same spectrum linewidth (10MHz), the coherence function plot shows a longer coherence length with Gaussian shaped spectrum ($l_c \approx 30m$) comparing to the Lorentzian shaped spectrum ($l_c \approx 20m$).

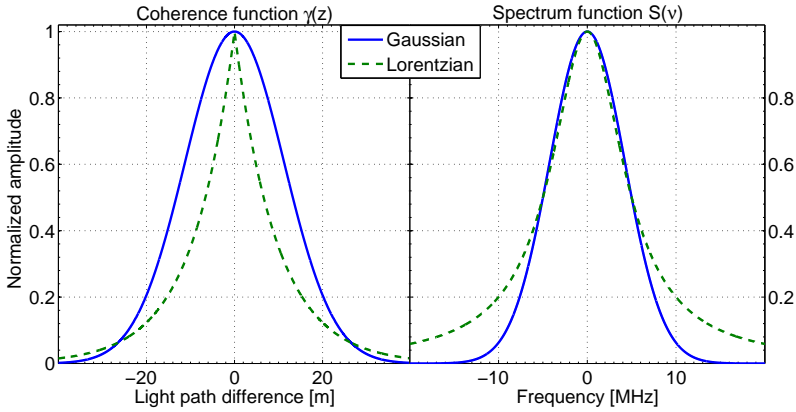


Fig. 4.2.: (Right) Laser spectrum $S(\nu)$ characterized by the central wavelength ν_0 and FWHM bandwidth $\Delta\nu_0 = 10\text{MHz}$, (left) inverse Fourier transform $\gamma(z)$ of coherence function $S(\nu)$

4.1.2. Concept of a broad spectrum laser Lidar design

A broad spectrum laser source means a shorter coherence length. The concept of using a broad spectrum laser source for Doppler Lidar system design is by selecting the laser source spectrum width or controlling the source spectrum width to choose the coherence length which defines the system probe length. Fig.4.3 illustrates the concept of using the coherence length of laser to design probe length and selecting measurement distance by matching the fiber delayline length. Therefore, the four different lengths of delay lines match the four different measurement distances.

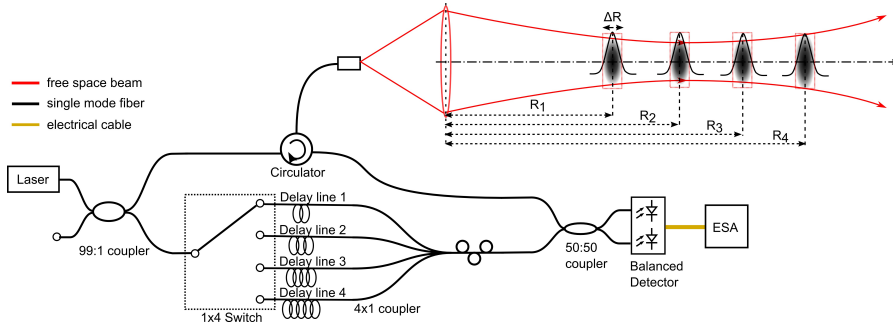


Fig. 4.3.: Illustration of CW Lidar concept with range independent probe length

4.1.3. Probe length of the new concept

Lidar system measures the scattering light along the laser passing through the air. In order to resolve in a spatial domain, CW Lidar focuses the beam to the measurement distance. The probe length of a CW Lidar system is defined by RWF which is depending on the focus of the system. Assuming a Gaussian laser beam, the receiving signal power is given as RWF (Eq.(4.6)).

$$RWF(z) = 1 / \left(1 + \left(\frac{\lambda(z - z_{Foc})}{pw_0^2} \right)^2 \right) \tag{4.6}$$

Where z_{Foc} is the focused distance of the telescope, w_0 is the beam waist radius at the focused position, for a Gaussian shape beam, it is

$$w_0 = \left(\frac{2\lambda}{p} \right) \left(\frac{z_0}{D_{Rec}} \right) \tag{4.7}$$

where D_{Rec} is the diameter of the receiver telescope. The coherence function of the laser source is given as $\gamma(\Delta z) = e^{-\frac{\pi\Delta\nu}{c}|\Delta z|}$ for a Lorentzian shape spectrum. Then, the coherence length (FWHM) is given as $\Delta R_{Lorentzian} = \frac{c}{\pi\Delta\nu}$, which is depending on the spectrum linewidth $\Delta\nu$. Therefore, the overall RWF of the new concept is then given as the convolution

of function $S(z - z_0)$ and $\gamma(\Delta z)$. Fig.4.4 shows a comparison of the RWF for the standard CW Lidar and the new concept with different laser linewidth. If the coherence length of laser is shorter than the system Rayleigh length, the probe length is mainly defined by its coherence length.

$$RWF_{\text{New}}(z) = \frac{1}{1 + \left(\frac{\lambda(z-z_0)}{\pi w_0^2}\right)^2} \exp\left(-\frac{\pi \Delta \nu_0}{c} \cdot 2 |z - z_{\text{range}}|\right) \quad (4.8)$$

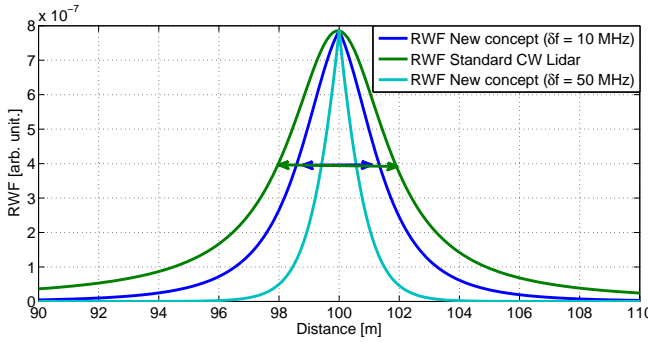


Fig. 4.4: Range weighting function as a function of distance

4.2. System requirement analysis

In order to develop the cost efficient Lidar system, the analysing process of minimum requirement is showing in this section. The analysing process divide into four different parts: measurement distance; probe volume; longitudinal and transverse scan scenario; and the components specifications.

4.2.1. Measurement distance

4.2.1.1. Impact on the receiving power

The power collected by receiver can be expressed by the Lidar equation (4.9) which is detailed explained at Section.2.9.

$$P_{\text{rec}}(R) = P_L \cdot \beta \cdot \Delta R \frac{A_L}{R^2} \cdot [T(R)]^2 \cdot \eta_{\text{coll}} \cdot \eta_{\text{sys}} \quad (4.9)$$

Assuming the collection efficiency η_{coll} is unchanged through the entire range, $\eta_{\text{coll}} = 1$, the system efficiency $\eta_{\text{sys}} = 0.5$. For the short range Doppler Lidar system ($< 200m$), the

transmission losses can be ignored ($T(R) = 1$). Fig.4.5 illustrates the receiving power of the backscattering light for different aerosol types and measurement distances. Consider a continental atmospheric condition, where most onshore wind turbine installed, the receiving power from 100 m distance is calculated less than 50 picowatt with a initial laser power of 500 mW. When consider the very clean air condition ($\beta = 1 \times 10^{-8} \text{sr}^{-1} \text{m}^{-1}$), the receiving power is lower down to couple ten femto-watt. Assuming CMRR=40dB, signal bandwidth $B=0.15\text{MHz}$. Fig.4.6 shows the calculated CNR at different distance for different aerosols. With 1000 spectrum averaging, in the very clean air conditions, 200 m is calculated as the theoretical detection limit.

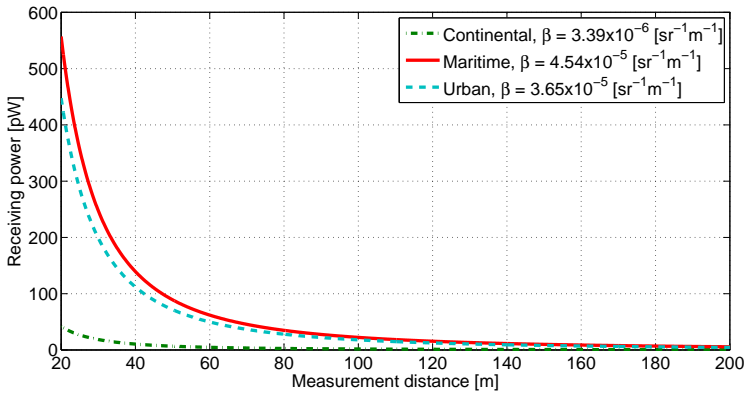


Fig. 4.5.: Calculated backscattering power at different distances for different aerosols

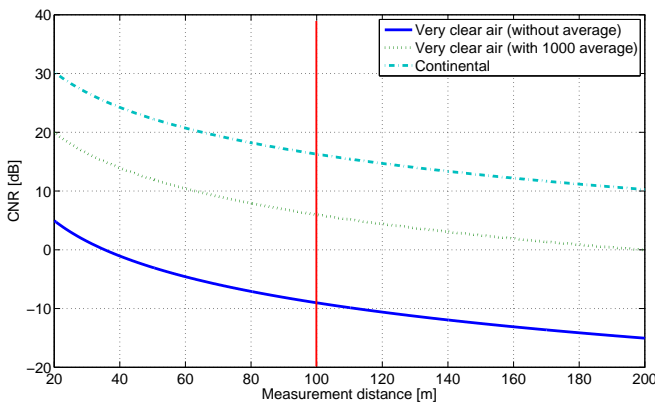


Fig. 4.6: CNR at different measurement distance and aerosols

4.2.1.2. Impact on induction zone wind speed changes

Based on the IEC standard 61400-12 "Power performance measurements of electricity producing wind turbines", the wind speed at $2.5D$, with D as the diameter of turbine rotor, does not show wind speed reducing impact. For the modern large scale wind turbine, $2.5D$ means a distance of 300 m. Furthermore, from the study by Simley et al., a measurement distance of $0.6D$ to $0.7D$ is suggested to be optimal for pitch control applications. While measuring closer to the turbine, measurements are more correlated with the true disturbances (Fig.4.7). Therefore, a closer measurement distance between 50-70 m is optimal.

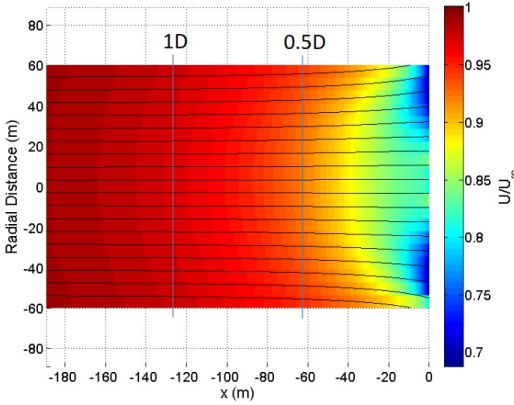


Fig. 4.7: A simulation result of wind turbulences within the induction zone [130]

4.2.1.3. Impacts on the measurement accuracy

Assuming the LOS wind speed measurement is accurate, the uncertainty of Lidar measurement is due to the tilt and roll of the system. Assuming uncertainty of Lidar tilt angle $\Delta\beta = 0.3^\circ$, roll angle $\Delta f = 0.1^\circ$, and measurement range L , the height error on measurement position is

$$\Delta H = L \tan \Delta\beta + 2L \tan \alpha \tan \Delta f \quad (4.10)$$

Where $\alpha = 15^\circ$ is half angle of the scanning or opening angle of the beams. With a power law wind shear profile $\alpha_{\text{shear}} = 0.2$ with the mean wind speed of $v = 8 \text{ m/s}$, the measurement uncertainty is then given as

$$d_{\text{tilt}} = \frac{1}{\sqrt{3}} \left(\left(1 + \frac{\Delta H}{H_{\text{hub}}} \right)^{0.2} - 1 \right) v \quad (4.11)$$

Where H_{hub} is the hub height $H_{\text{hub}} = 80 \text{ m}$. Fig.4.8 shows the measurement uncertainties with different measurement distance.

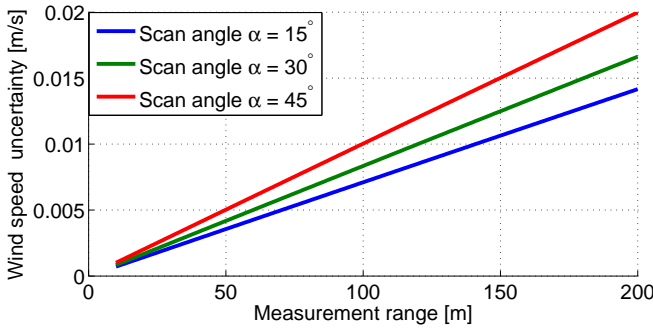


Fig. 4.8: Calculated wind speed measurement uncertainty from the tilt

4.2.1.4. Impacts of the preview time for the controller

Lidar system measures the wind speed in one or couple locations, for the wind turbine pitch control applications, the accurate estimation of transportation time for the measured wind field travelling to rotor blade is important for the control performance. For the design of predictive controller, preview time or steps are fixed. However the Lidar systems measure the wind speed in a fixed or couple fixed positions, therefore, different wind speed results different preview time. Assuming the measurement distance is Z_{range} , a mean wind speed \bar{U} , then the preview time is given as $T_p = Z_{range} / \bar{V}$. Due to wind turbulent structures, evolution, and speed changes caused by the induction zone, varies time delays occur during the process of control.

Fig.4.9 illustrates the delays during applying the control to blade pitch system. The main delays in a FF control are: phase delay by implementation of the control d_{FF} , delays due to the scan d_s , delays due to the low-pass filtering d_{LPF} , delay due to applying the pitch commands to drive the pitch d_{Pitch} , and delay due to the REWS estimation d_r .

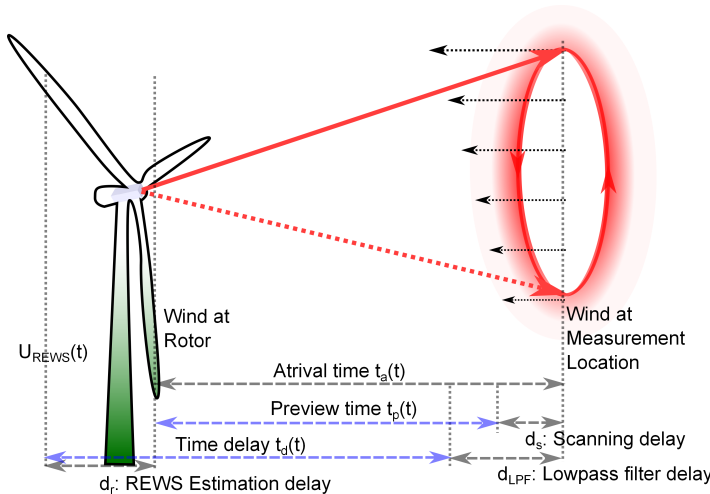


Fig. 4.9: Illustration of the time delay of measured wind speed

The phase delay applied on the idea FF control which is the phase between $T_{y\beta_{FF}}$ and $T_{y\omega_t}$, which means the blade pitch command taking longer to affect the output of interest than the wind disturbance. In application of FF control, when choosing the output y as the generator speed error, this delay results a range from 0.05 to 0.3 seconds depending on the average wind speed [47].

For the FF control, a prefilter H_{pre} is introduced to form the estimation ω_t based on the Lidar measurement ω_m . The prefilter output variable y is given as Eq.(4.12) [54].

$$y = T_{y\omega_t}(\omega_t - H_{pre}\omega_m) \quad (4.12)$$

The low-pass prefilter introduces delays. Better wind measurement quality needs less filtering and higher cut-off frequency therefore less delays. The time needed for the prefilter decreases with increasing wind speed. The prefilter delays in the range of 1.5 to 3 seconds. This filter processing time can be shorter when the measurements are more accurate.

In total due to the Lidar measurement data signal processing, additionally bring 2-5 s delay during the measured data transport to the rotor blades. This time delay leads to a wind field transportation distance about 10-50 m. Therefore, for a better control performance, a minimum measurement distance of 50 m is required. Fig.4.10 illustrates the wind speed weighting factor along the blade span which is calculated based on the BEWS function,

$$u_{BEWS} = \sqrt{\frac{\sum_{i=1}^N A_{Ann}(i)C_Q(i)r(i)u^2(i)}{\sum_{i=1}^N A_{Ann}(i)C_Q(i)r(i)}} \quad (4.13)$$

Where, $A_{Ann}(i)C_Q(i)r(i)$ denotes the weighting factor along the blade. Fig.4.10 shows that the wind applied on the blade at 50% ~ 95% (30 ~ 60m) position has most effects.

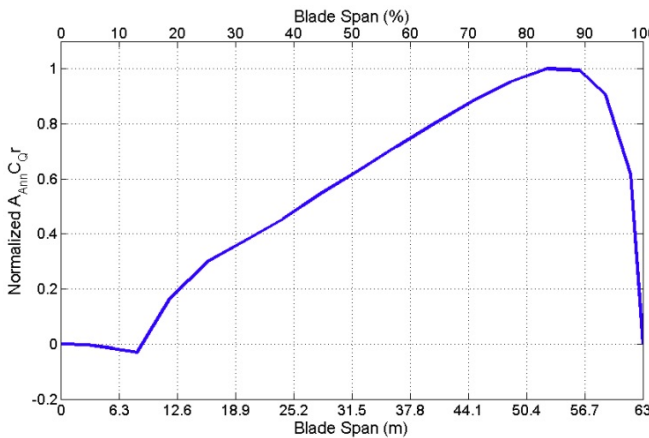


Fig. 4.10: Wind speed weighting factor along the blade span [47]

Fig.4.11 illustrates the single distance measurement scenario of the Lidar system. Considering a fixed two beam Lidar system (Fig.4.11 left), the best measurement distance is at

$0.6 \sim 0.7D$ which is around $70 \sim 90\text{m}$ ahead of the turbine rotor. With a 30° open angle (half), the measured wind speed on rotor blade is on the position $40 \sim 50\text{m}$. Therefore, the LOS distance is $80 \sim 100\text{m}$, the beam is focused on 90m distance. The single distance scan scenario (Fig.4.11 right) can be simply considered as rotate the fixed beam along with rotor rotation.

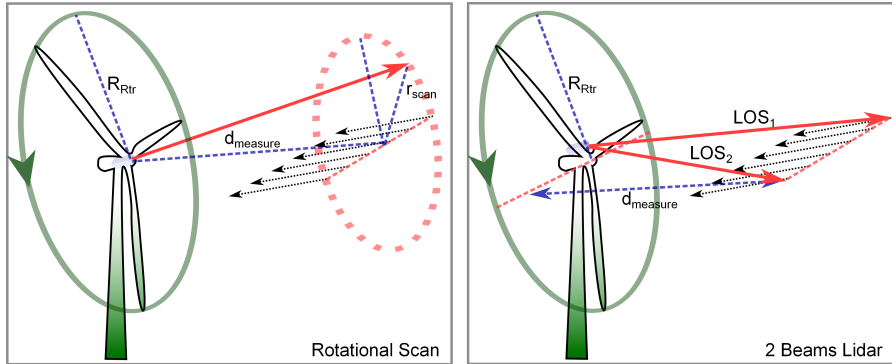


Fig. 4.11.: Single distance Lidar measurement scenario, (left) rotational scan along the rotor, (right) fixed 2-beams Lidar

4.2.2. The trade-off of probe length

The probe length defines the amount of aerosols contained in the probe volume. As mentioned on Section 3.2.2, $\beta(\lambda, R) = \sum_j N_j(R) \frac{ds_{j,sca}(\pi, \lambda)}{d\Omega}$, then the back scattering light power $P_{sca} = P_{inc} \cdot \beta(\lambda, R) \cdot \Delta R$. Assuming β_{π} is a constant, the backscattering power is proportional to probe length. Longer probe length brings higher backscattering power which directly leads to a better measurement qualities. However, Lidar measures the average wind speed through the entire probe volume, the long probe length leads to a low accuracy on the turbulence measurement. Fig.4.12 shows the Lidar measurement data with different probe lengths, (from top) the focal distance are 10m (probe length 15cm), 25m (probe length 1m), 50m (probe length 4m), 100m (probe length 15m), and 200m (probe length 60m). Therefore with couple meters spatial average, Lidar systems are able to measure good wind speed fluctuations. However Lidar measurement does not give a good measurement with more than 15m probe length.

4.2.3. Single or multiple distance measurements

Lidar system measures the wind speed in one or multiple distances, Fig.4.13 illustrates the WindCube measurements in five different distances. Assuming the wind field compo-

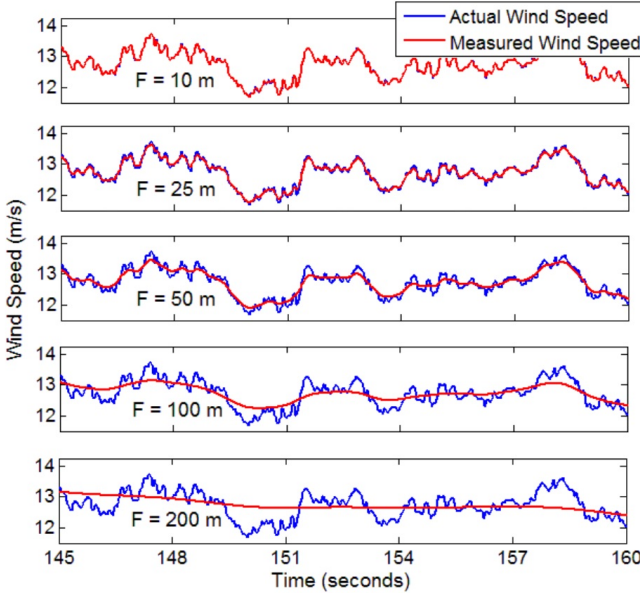


Fig. 4.12: Wind turbulence measurement (simulated) for different probe length with CW ZephIR Lidar [47]

nents v and w are zero, therefore, the LOS wind speed $v_{\text{los},i}$ of each measurement point $[x_i \ y_i \ z_i]^T$ is given as

$$v_{\text{los},i} = l_{x_i}u_i + l_{y_i}v_i + l_{z_i}w_i = l_{x_i}u_i \quad (4.14)$$

Therefore, the effective wind speed v_0 is given as

$$v_0(t) = \frac{1}{5} \sum_{i=1}^5 v_i(t - T_{\text{Preview},i}) \quad (4.15)$$

Where, $T_{\text{Preview},i}$ is the preview time at the range i . Multiple distance measurements are discussed by Dr. Schlipf [156], however, it leads to a longer delay on the scanning for a conventional CW Lidar system. Most important is that the simultaneous multiple measurements lead the complexity of Lidar systems. E. Simley et.al. proposed measurements at single distance but with three beams positioning at the same angles as the turbine blades [48]. However, this approach assumes that the Lidar measurement at each beam will perfectly reach the blades. In reality, since the wind speed is changing, this assumption is difficult.

From the controller design point of view, FF controller only need a single wind speed which is going to reach the rotor. However, MPC is able to consider a span of preview data during the prediction horizon, therefore, the Lidar system with simultaneous multiple range measurements is supposed to provide better performance for MPC controller (Fig.4.13).

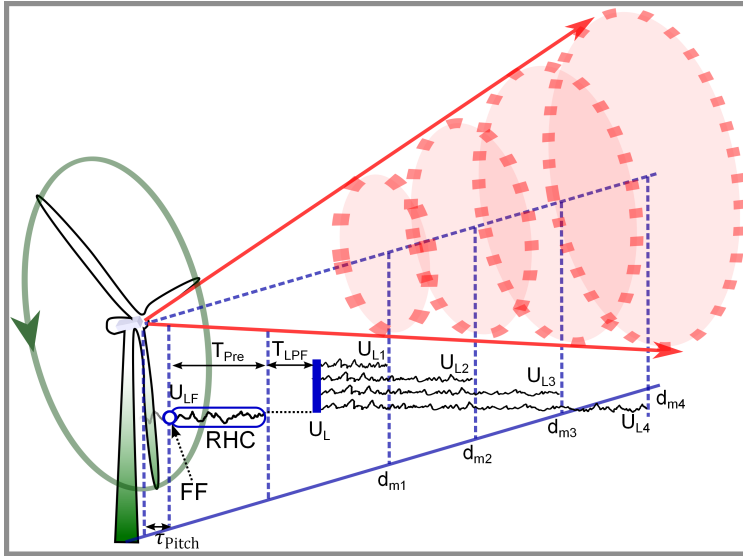


Fig. 4.13.: Multiple distance and position measurement scenario

4.2.4. Scan scenarios

Different scan scenario is aforementioned. Two beams Lidar is the simplest system and used by the Windar Photonics "WindEye" and Avent Lidar "Wind iris". Wind iris is approved its benefits by varies applications, such as pitch and yaw control to gain higher energy captions. The collective pitch control system regulates three pitch angles at the same rates depending on the BEWS over the entire rotor. Therefore, the two beam Lidar system for measuring the wind speeds at the hub height is good enough. However, modern wind turbines have a huge span area which covers the vertical height from couple ten to 200 m. The wind speeds vertical share changes as shown in Fig.4.15. Therefore, those speeds varies effect the rotor blades at different heights. For the collective pitch control, the Rotor Effective Wind Speed (REWS), which is the single wind speed representative of the whole wind speed profile in front of the wind turbine rotor in term of power production. It is defined as

$$U_{eq} = \left(\frac{1}{A} \int_{-R}^R u(z)^3 c(z) dz \right)^{1/3} \approx \left(\sum_{i=1}^N u_i^3 \frac{A_i}{A} \right)^{1/3} \quad (4.16)$$

For the collective pitch control system, the detailed 2D wind measurement for entire rotor span is not real necessary, since the collective pitch system only cares the REWS. However, for an individual pitch control system, only knowing the REWS is not benefiting. Therefore, a more precise 2D measurement is required.

As a summary, different scan scenario is depending on the applications. For the collective pitch control system, knowing the REWS is enough. However, a 2D scanning could benefit

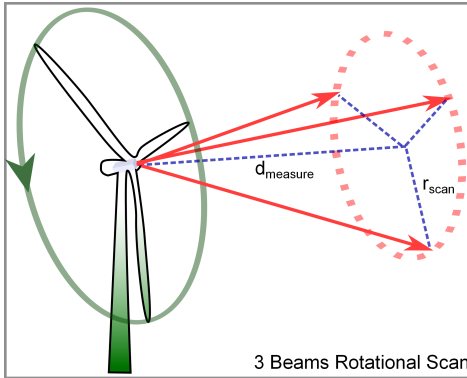


Fig. 4.14: Lidar system with three beam measurements at a fixed distance

to construct the REWS. Then, the independent pitch control requires the BEWS on each blade. Therefore, the detailed wind speed distribution on a full span area is needed.

4.2.5. Components specification analysis

Fig.4.3 illustrates the design of the broad spectrum laser Lidar system. It consists: a laser source, a coupler to divide the laser beam into 99% as transmission and 1% as the reference beam, a circulator to direct the beam into the telescope further to the atmosphere and redirect the signal beam into the detection unit, then a 1x4 switch and a 4x1 coupler for constructing a multiple length delay line concept, a 50:50 coupler to mix the signal and reference beam for the balanced detection, and an ESA for analysing the beat frequency signal. This section explains the requirement of the new concept analytically.

4.2.5.1. Laser sources

The main parameters for a laser source include the optical power, and spectrum linewidth. Optical power is defined by the design parameter of measurement distance, probe volume, and the design of receiving optics. And the spectrum linewidth restricts the probe volume.

First of all, the above mentioned probe length is required as less than 10 m for maintaining a good wind turbulence measurement. As mentioned by E. Simley, when considering the induction zone effects, for a FF controlled pitch system, a measurement distance at $0.6 \sim 0.7D$ ($ca.50 \sim 100m$) and scan radius of $0.7R$ ($ca.30 \sim 50m$) shows a good measurement quality. This equals to a LOS distance of $60 \sim 120m$. Therefore, a maximum 120 m measurement distance with 10 m probe depth and 1000 spectrum averages, the calculated minimum optical power can be calculated with the Eq.(4.17).

$$CNR \cdot \sqrt{N_{Avg}} = \frac{2P_L \cdot \beta \cdot \Delta R \cdot A_L \cdot (T(\lambda, R))^2 \cdot \eta_{coll} \cdot \eta_{sys} \cdot \eta_{quan}}{R^2 \left(10^{\frac{2 \cdot RIN - CMRR}{20}} P_{ref} \cdot \eta_{quan} + 4h\nu \right) B} \quad (4.17)$$

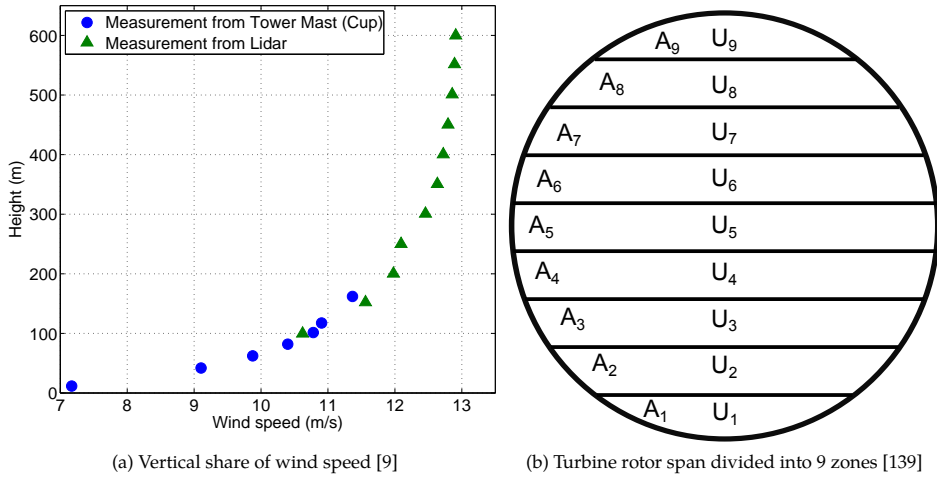


Fig. 4.15.: (Left) vertical share of wind speed, (right) wind turbine rotor span divided into 9 zones and effective wind speed in different zones

Therefore, the $P_{L,Min} = 0.6$ (W). Then, the spectrum linewidth is calculated as $l_c = c/\pi\Delta\nu_0$, which is result as $\Delta\nu_0 = 10$ (MHz).

4.2.5.2. Delay lines

The delay lines are used to match the phase of the signal beam and reference beam. The delay line fiber length is calculated as $l_{Delay} = 2z_{Ref}/n_{Fiber}$, where n_{Fiber} is the refractive index of the fiber core n_{Fiber} (1550nm) ≈ 1.468 , therefore, for measuring distances at 40, 60, 90, and 120 m, which corresponds the LOS distance of 45, 67, 100, 135 m. Therefore, this measurement distance required delay line lengths of 60 m, 90 m, 136 m, and 180 m.

4.2.5.3. Transmitter and receiver optics

The transmitter and receiver optics can be designed as a bistatic or monostatic, an unconfocal or confocal system. Detailed design is discussed on Chapter.6. Nevertheless, focusing the beam into a far distance required a minimum receiver diameter. As discussed on Section.3.2.1, to keep the wave distortion negligible to minimize the spatial coherence effect, a maximum telescope diameter is 120 mm for a measurement distance less than 150 m.

4.3. Laser safe operation consideration

To enable an easy access to the market, the system is aiming for the laser class 1 operation, therefore, the system assumes a pulse durations of $1 - 10\mu\text{s}$ at a wavelength of 1550nm . The choice of the wavelength is based on the increasing allowed emission power which comes with the inferred and the atmospheric transmission window in that region (Fig.4.16). This leads to the following laser safety restrictions: The Maximum Permissible Exposure (MPE) value is $1\text{J}/\text{cm}^2$ which results in an Accessible Emission Limit (AEL) of 8×10^{-3} for class 1 operation [87]. For repetitive pulse sources the correction factor C_5 has to be

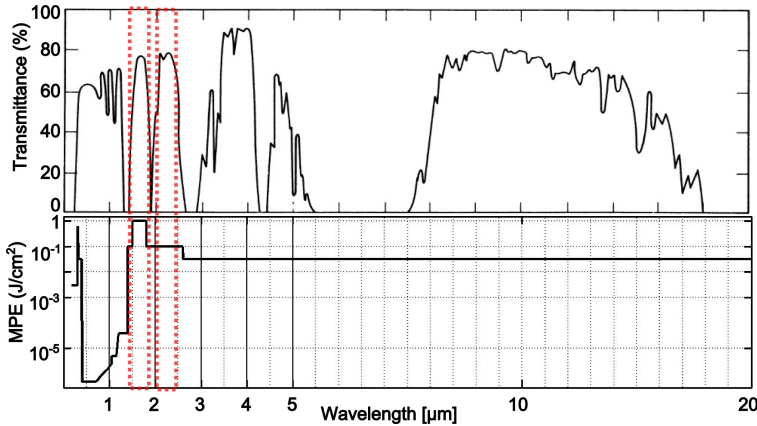


Fig. 4.16.: Choice of Lidar system wavelength, up) atmospheric transmittance [61], down) Maximum Permissible Exposure (MPE) for eye safety operation

multiplied with the emission limit for a single pulse (assume all pulses have the same pulse duration and are smaller $18\mu\text{s}$) [79].

$$AEL_{\text{pulse train}} = AEL_{\text{single pulse}} \cdot C_5 = AEL_{\text{single pulse}} \cdot N^{-0.25} \quad (4.18)$$

with N being the number of pulses in the considered time frame, such as 10s which leads to $N=10000$ gives an allowed single pulse energy of $8 \times 10^{-4} \text{J}$. In the future the suggested measurement technique might be combined with a laser scanning approach which would lead to different laser safety scenarios [55].

4.4. Summary and conclusion

In this chapter, theoretical basic of the Lidar system is discussed first of all. Those knowledges are the basis of the following Lidar system design. Then, based on the theoretical background the new concept of a cost efficient design by using a broad spectrum laser is introduced which is the unique point of the presented work. Then, following with the

requirements and limitations of the new Lidar concept are discussed. Table.4.1 concludes those parameter requirements for the new concept Lidar system.

Table 4.1.: Requirements of the cost efficient Lidar concept with broad spectrum laser sources

Parameters	Value
Minimum laser power	0.6 W
Laser spectrum width	Ca. 10 MHz for 10 m coherence length
LOS measurement distance	LOS 45 ~ 135m(Multi distance) Or LOS 70 m (Single distance)
Minimum measurement distance	50 m
Probe length	10 m, maximum 20 m
Number of measurement range	Single or 4
Scan scenario	2 dimensional scan
Beam separation or scan angle	26° (Half angle)

5. Simulation of the Doppler wind Lidar

In order to assist the Lidar system design and evaluate the system performance, a simulation model is developed. The simulation design is based on the Lidar equation which is described on Section 3.2.2. Fig.5.1 shows the flow chart of the simulation concept. In order to keep the flexibility, the simulator is designed into different modules:

1. Modelling and simulation of a Gaussian laser beam;
2. Low altitude tropospheric ($< 250\text{m}$) aerosol modelling and scattering;
3. Scattering signal collection and detection;
4. Signal processing and wind field estimation.

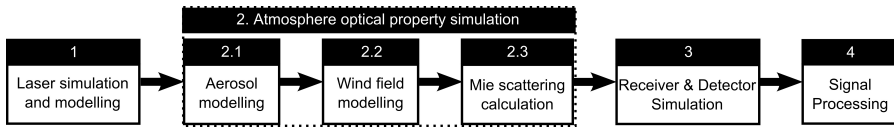


Fig. 5.1.: Chronological flow diagram of the simulator design

The simulator is designed as a slicing model of atmosphere which is called Feuillette model. It is developed for a time domain coherent Lidar simulation [152]. Fig.5.2 illustrates the concept of the atmosphere slicing method. The transceiver is located at $z=0$. At the distance z_m , a slice of atmosphere with a thickness of ΔZ locates on the LOS of the Lidar beam. Each slice contains a huge number of aerosols which are scattering the laser beam, and then propagates back to the receiver plane at $z=0$.

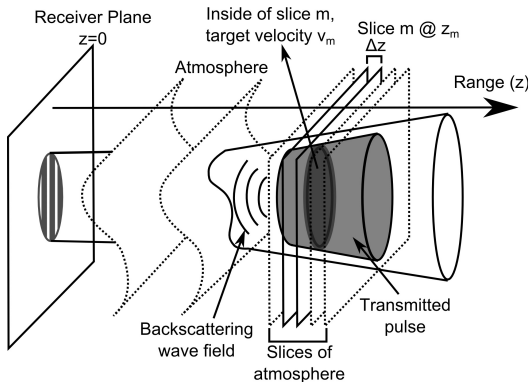


Fig. 5.2: Sketch of the Feuillette model with atmosphere slicing for heterodyne coherent Lidar system simulation [152]

In this chapter, a modified Feuillette simulation model for simulating the special designed Lidar system is discussed. Within the model, a broad spectrum laser module is simulated by adding random phase noise. Fig.5.3 illustrates the simulation process in steps.

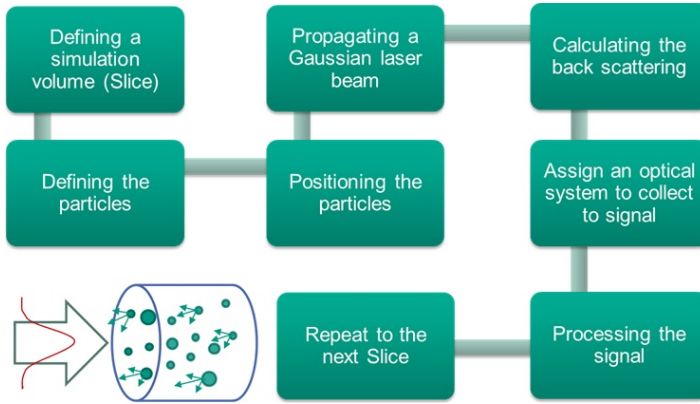


Fig. 5.3.: Schematic illustration of the process of the simulation design

Section 5.2 describes a single particle scattering with a cylindrical coordinate system to simulate the atmospheric scattering. Section 5.3 shows the laser source. Section 5.4 illustrates the receiver and sender system. Section 5.5 gives the full model and simulation results.

5.1. Atmospheric scattering simulation

The atmosphere model can be categorized as an aerosol model which describes the properties of aerosols (such as urban, continental, offshore, fog, rain, snow, ...), an aerosol optical property model which includes the particle scattering and absorption calculations, and a wind model interacts with the measured or simulated wind data. Aerosols are defined as a mixture of solid or liquid particles in gas, usually air [81]. Particles' size ranges from about $0.002\mu\text{m}$ to more than $100\mu\text{m}$ [81]. Aerosols at different locations and weather situations contain a mixture of different components [41]. These components mixed each other to form certain aerosol types without physical or chemical interaction between each other. A lognormal distribution is frequently used for the size distribution on each component [41, 78].

$$\frac{dN_i(r)}{dr} = \frac{N_i}{\sqrt{2\pi r \log \sigma_i} \ln 10} \cdot \exp\left(-\frac{1}{2} \left(\frac{\log r - \log r_{\text{mod } N_i}}{\log \sigma_i}\right)^2\right) \quad (5.1)$$

Where, $r_{\text{mod } N_i}$ is the mode radius, i denotes the different components, N_i is the total particle number density of component i ; σ_i describes the standard derivation of the distribution. To simulate the optical properties of the atmosphere, Mie theory is typically used as an analytical solution for the prediction of particle scattering phenomenon when the particles are assumed to be spherical in most case [89, 124]. The simulation algorithm is based on Maetzler's Matlab code [117] which originally documented by Bohren et.al. [15].

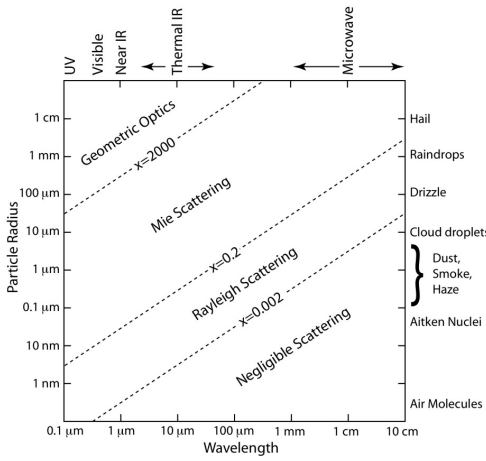


Fig. 5.4: Light scattering regimes depending on the particle size and wavelength [29]

Assuming $x = 2\pi r/\lambda$ is the size parameter of the scattering particles. Assuming $\lambda = 1.55 \mu\text{m}$, for big particles, $x \gg 1 \rightarrow r \gg 0.25\mu\text{m}$, geometrical optics method is used for the particle scattering simulation. For small particles, $x \ll 1 \rightarrow r \ll 0.25\mu\text{m}$, Rayleigh scattering theory is used. Mie scattering theory is introduced for analysis of particles which are in between. Fig.5.4 illustrates the different regimes for particle scatterings depending on the particle size and incident light wavelength.

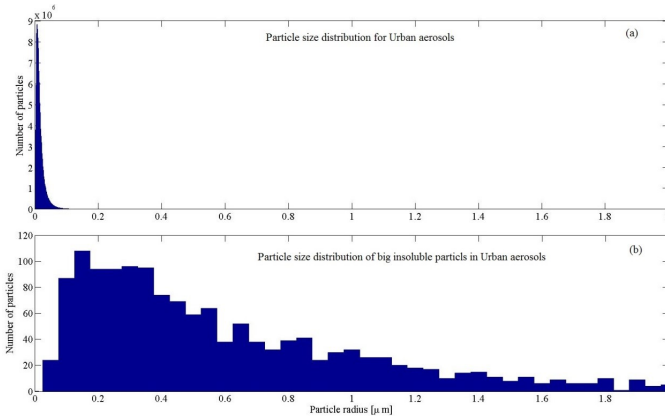


Fig. 5.5: Histogram plot of Urban aerosol particle size distribution

Fig.5.5 shows a histogram size distribution according the urban aerosol model that the parameters are described in [78]. In the simulation, the Mie scattering methods to these aerosols are applied. Fig.5.6 shows the backscattering coefficient for the same particle distribution. It can be seen that the particle sizes in the range between $0.15\mu\text{m}$ and $0.25\mu\text{m}$ contribute significantly to the backscattered signal, although the majority of the particles have less than $0.1\mu\text{m}$ radius. Fig.5.5 shows a closer look at the distribution of the bigger insoluble components in the urban aerosol model which are in this region of interest.

5. Simulation of the Doppler wind Lidar

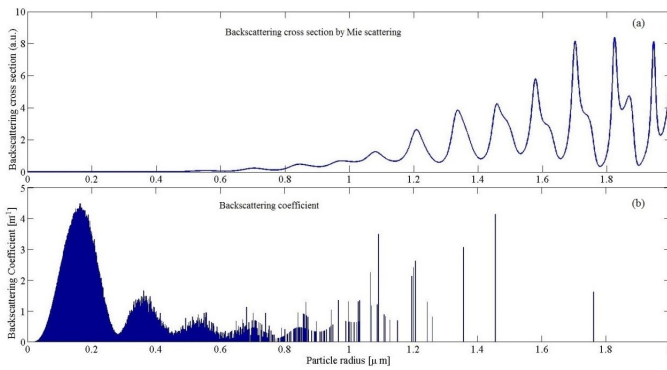


Fig. 5.6: Mie backscattering cross section and coefficient

Furthermore, a study of calculating the backscattering coefficient for individual components for different aerosol types is applied [BSFS14]. Fig.5.7 shows the calculation result of 4 different aerosol types.

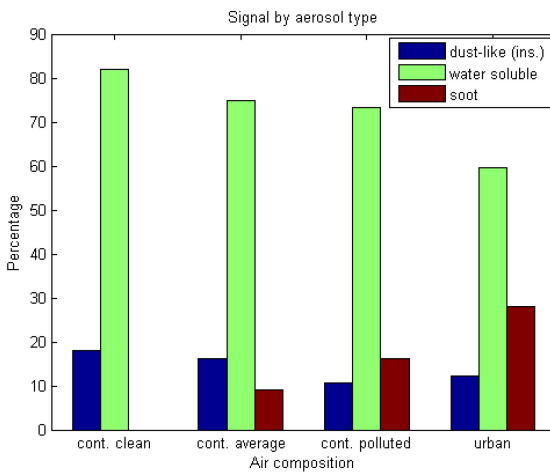


Fig. 5.7: Impact of the different components on the overall backscattering coefficient [BSFS14]

5.2. Modelling of lasers

5.2.1. Gaussian shape laser beam

The electrical wave field of laser can be described as a product of a time dependent function with a normalized space dependent function which is given as

$$U_T(\xi, z, t) = g_T(t)U_T(\xi, z) \quad (5.2)$$

Where $\int |U_T(\xi)|^2 d\xi = 1$, the time function of transmitter laser light is given as

$$g_T(t) = \tilde{g}_T(t) \exp(-j2\pi\nu_T t) \quad (5.3)$$

where $\tilde{g}_T(t) = \sqrt{T_T P_T} \exp(-j\varphi_T(t))$, P_T is the transmission beam power, φ_T is the phase function, T_T is the truncation factor due to the spatial filter. The phase function φ_T defines the spectrum shape and optical bandwidth of laser source. The time invariant electrical beam field in space domain on the transmitter plane ($z = 0$) is given as [5].

$$U_T(\xi, 0) = A_0 \cdot \exp\left(-\frac{\xi^2}{W_0^2}\right) \exp\left(\frac{ik\xi^2}{2F_0}\right) \quad (5.4)$$

Where $\xi = \sqrt{x^2 + y^2}$ is the radial position in polar coordinate, x and y are position in Cartesian coordinate. F_0 is the phase front radius. $F_0 = \infty$ identifies a collimated beam, $F_0 > 0$ is convergent beam, and $F_0 < 0$ shows the divergent beam. W_0 is the beam waist at the exit aperture; $k = \omega c$ is the optical wave number, ω is the spectrum, c is the speed of light in vacuum. At the distanced plane ($z = L$), the Gaussian beam wave is

$$U_T(\xi, L) = \frac{A_0}{\sqrt{\Theta_0^2 + \Lambda_0^2}} \cdot \exp\left(-\frac{\xi^2}{W_0^2}\right) \exp\left(ikL - i \tan^{-1} \frac{\Lambda_0}{\Theta_0} - \frac{ik\xi^2}{2F_0}\right) \quad (5.5)$$

Where, $A = A_0 / \sqrt{\Theta_0^2 + \Lambda_0^2}$ is the on-axis amplitude changes, $\Theta_0 = 1 - L/F_0$ shows the amplitude change due to the refraction, and $\Lambda_0 = 2L/kW_0^2$ is the amplitude change due to the diffraction; $\tan^{-1}(\Lambda_0/\Theta_0)$ describes the longitudinal phase shift.

5.2.2. Spectrum of Laser

5.2.2.1. Statical simulation approach

Within the statical simulation approach, a time invariant system is assumed. To simulate the coherence detection, the coherence function $\gamma(z)$ is used. $\gamma(z)$ is the inverse Fourier transform of the light source spectrum $S(\nu)$, which are defined as Eq.(5.6a) for a Gaussian shape spectrum, and Eq.(5.6b) for a Lorentzian shape spectrum.

$$\gamma(z) = \exp\left(-\frac{1}{\ln 2} \left(\frac{\pi z \Delta\nu_0}{2c}\right)^2\right) \xleftrightarrow{\mathcal{F}} S(\nu) = S_0 \exp\left(-4 \ln 2 \left[\frac{\nu - \nu_0}{\Delta\nu}\right]^2\right) \quad (5.6a)$$

$$\gamma(z) = \exp\left(-\frac{\pi \Delta\nu_0}{c} |z|\right) \xleftrightarrow{\mathcal{F}} S(\nu) = S_0 \cdot \frac{\Delta\nu_0^2}{4(\nu - \nu_0)^2 + \Delta\nu_0^2} \quad (5.6b)$$

Then, the simulated coherence signal power from each atmosphere slice is given as

$$P_{\text{out}} = \frac{P_{\text{ref}} + P_{\text{si}}}{2} + P_{\text{Nois}} + \gamma(\Delta z_i) \sqrt{P_{\text{ref}} \cdot P_{\text{si}}} \exp\left(-j\nu_{\text{Dopp},i}t + \frac{2\pi}{\lambda} \Delta z_i\right) \quad (5.7)$$

The signal amplitude from each slice can be described with the coherence function which depends on the light path difference of the measured slice and the desired delay path.

5.2.2.2. Dynamical simulation approach

The phase function $\phi_T(t)$ can be modelled as a winner levy process [129].

$$\phi_n = \phi_{n-1} + \Delta_n \quad (5.8)$$

Where Δ_n is the step size of the jump and zero mean Gaussian random variable. Its variance sets the speed of the process and equal to $s_\Delta^2 = 2pBT$. BT is referred as the phase noise rate and express the relative double sided bandwidth of the process. The phase function can be calculated as

$$\varphi_T(t) = \arg \left\{ F^{-1} \left\{ \exp \left[-2 \ln 2 \left(\frac{\nu}{\Delta\nu} \right)^2 \right] \exp [j\psi(\nu)] \right\} \right\} \quad (5.9)$$

Where $\psi(\nu)$ is an arbitrary real function. Then $\psi(\nu)$ can be calculated as

$$\psi(\nu) = \arg \left\{ F \left\{ \exp \left[2 \ln 2 \left(\frac{\nu}{\Delta\nu} \right)^2 \right] \exp [j\psi(\nu)] \right\} \right\} = \arg \{ F \{ \exp [j\psi(\nu)] \} \} \quad (5.10)$$

E. Brinkmeyer et.al show that repeating this process is able to lead to an acceptable approximation of the electrical field [22]. Piratically, a random phase jump method is applied into the laser field function to achieve this process in a Matlab based simulation. The number of phase jumps per time interval changes with the laser spectral bandwidth $\Delta\nu$. Fig.5.8 illustrates the simulation results with this phase jump method based on [22]. The discredited time is 1ns and 2^{14} data points are used for simulation.

5.3. Sending and receiving optics

A Doppler Lidar attempts to measure the speed of a volume of air at a given distance. A perfect device would therefore only deliver light to and collect light from a small volume of air at a specified position and nowhere else. Therefore, the return signal would only contain information from the desired mass of air. In reality, some portion of the return

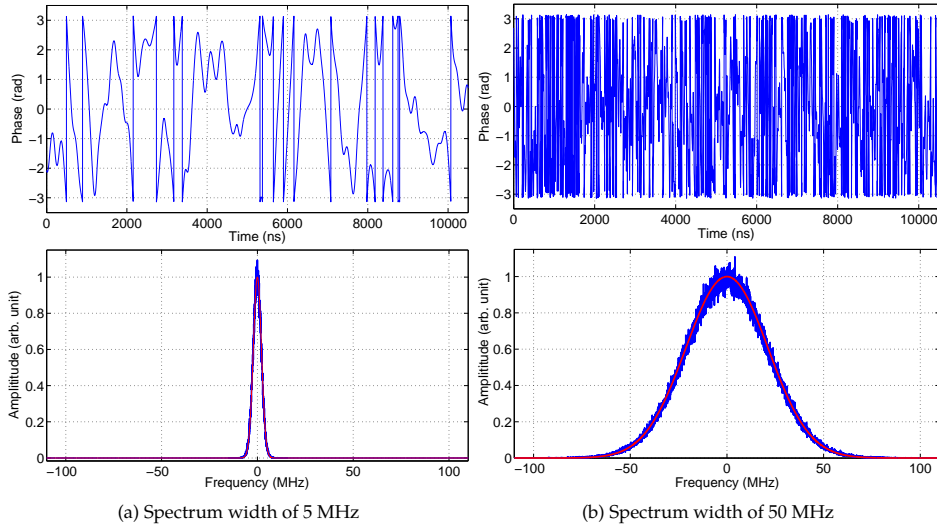


Fig. 5.8.: Simulated power spectrum with phase jump method

signal will undoubtedly come from elsewhere. A Spatial Collection Efficiency (SCE) is defined as Eq.(5.11) for further analysis.

$$\text{SCE} = \frac{\iiint_V P(\nu) d\nu}{\iiint_A P(\nu) d\nu} \quad (5.11)$$

where V is the volume of interest and A is all of the space. SCE is the ratio of the power collected from V divided by the overall power collected. Fig.5.9 shows a simple model of the receiver which consists essentially of a telescope lens, a spatial filter (field stop), and a collimator for collimating the scattering light into fiber. When light comes from off-axis, the focus on the spatial filter plane will shift from the center, therefore part of the light will be blocked and after a critical angle the light is no longer pass through the spatial filter.

5.3.1. A simplified spatial collection efficiency model

A system with mono-static configuration, where the transmitting and receiving beam share the same optical axis, has been considered. Assuming at distance z , the area illuminated by the incident Laser is $\pi w(z)^2$, where $w(z)$ is the beam waist radius at distance z (Fig.5.10). D_{Rec} is the effective receiver diameter, $2w(0)$ is the transmitted laser beam diameter at the focus position. Here, I separate the transmission and receiving beam in order to make a general concept. The confocal configuration is a special case with $2w(0) = D_{\text{Rec}}$.

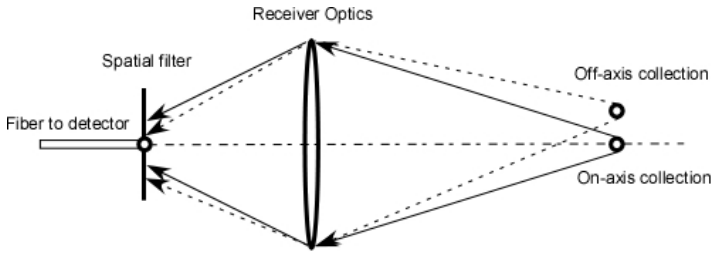


Fig. 5.9.: Simple model of the receiver setup, solid line shows the collection of on axis laser light only, dash line shows the off-axis collection

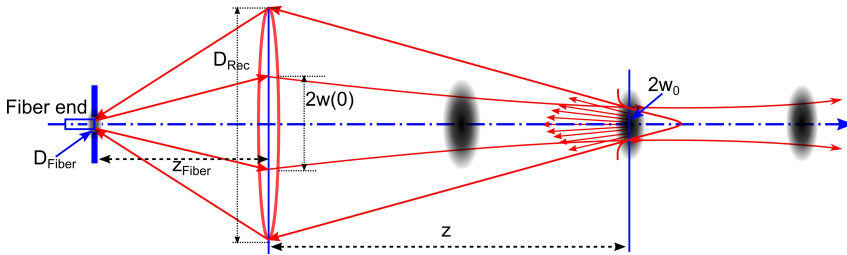


Fig. 5.10.: Illustration of the receiver model for analysis of the collection efficiency

Consider a Gaussian beam which is focused into a distance z_0 , at distance z the beam size $w(z)$ is given as

$$w(z) = w_0 \sqrt{1 + \left(\frac{\lambda(z - z_0)}{\pi w_0^2} \right)^2} \quad (5.12)$$

The beam waist radius at the focus point is given as

$$w_0 = M \cdot r_{\text{Fiber}} \quad (5.13)$$

here M_{Lens} is the magnification factor for a Gaussian beam propagating through a lens.

$$M_{\text{Lens}} = \frac{f_{\text{Trans}}}{\sqrt{(z_{\text{Fiber}} - f_{\text{Trans}})^2 + \left(\frac{\pi r_{\text{Fiber}}^2}{\lambda} \right)^2}} \quad (5.14)$$

where z_{Fiber} denotes the distance from fiber to the lens, f_{Trans} is the focal length of the transmitter lens, r_{Fiber} is the radius of the fiber core. For simplification, the beam waist at the focus point w_0 can be calculated as

$$w_0 = F \cdot \frac{2\lambda_0}{\pi n} \quad (5.15)$$

Where $F = z_F / D_{\text{Lens}}$ is the f-number of the system, z_F is the focused range, λ_0 is the laser wavelength, n is the refractive index of medium. Fig.5.11 shows the beam diameter with initial diameter of 20 mm at the telescope when focused at 50, 75, and 100 m. A Doppler Lidar obtains $z \gg f_{\text{Rec}}$, therefore $w_{\text{img}}(z) = \frac{f_{\text{Rec}}}{z} w(z)$. For simplification, the wave field distribution on distance z along the beam waist is uniform. Therefore, the beam area can be used to describe the intensity of wave field. For simplification, the SCE is defined as an ultimate thin slice in distance z .

$$\begin{cases} SCE(z) = \frac{A_{SF}}{A_{\text{img}}}, & A_{SF} < A_{\text{img}} \\ SCE(z) = 1, & A_{SF} \geq A_{\text{img}} \end{cases} \quad (5.16)$$

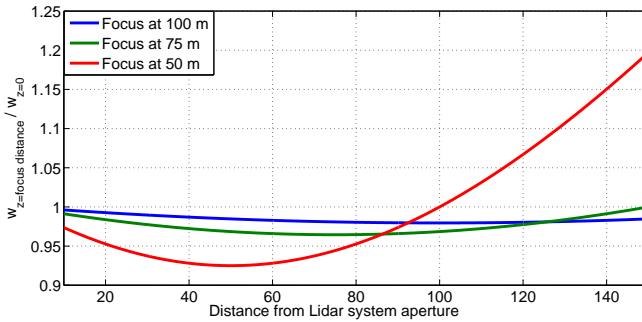


Fig. 5.11: Normalized beam diameter at different distance with a lens diameter of 20 mm

With a 250 μm spatial filter diameter, the calculated SCE is shown on Fig.5.12. After certain distance, all the backscattering light is collected by the receiver.

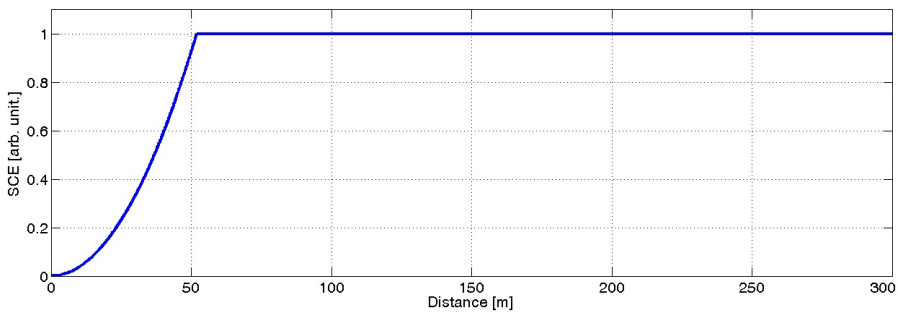


Fig. 5.12.: SCE from different distances

5.3.2. SCE model with a Gaussian field

A Gaussian beam field on the transmitter aperture plane ($z = 0$) is given as Eq.(5.17) [5].

$$U_0(r, 0) = A_0 \cdot \exp\left(-\frac{r^2}{w_0^2}\right) \exp\left(\frac{ikr^2}{2F_0}\right) \quad (5.17)$$

where $r = \sqrt{x^2 + y^2}$, x and y are the position in Cartesian coordinate; F_0 is the phase front radius, when $F_0 = \infty$ identifies a collimated beam, $F_0 > 0$ is convergent beam, $F_0 < 0$ is the divergent beam; $k = \omega/c$ is the optical wave number, ω is the angular frequency, c is the speed of light in vacuum. At distanced z , the Gaussian beam field is given as

$$U_0(r, z) = \frac{A_0}{\sqrt{\Theta_0^2 + \Lambda_0^2}} \cdot \exp\left(-\frac{r^2}{W_0^2}\right) \exp\left(ik(z - z_0) - i \tan^{-1} \frac{\Lambda_0}{\Theta_0} - \frac{ikr^2}{2F_0}\right) \quad (5.18)$$

where, $A(z) = A_0 / \sqrt{\Theta_0^2 + \Lambda_0^2}$ is the on axis amplitude, $\Theta_0 = 1 - z/F_0$ illustrate the change due to refraction, $\Lambda_0 = 2z/kw_0^2$ is the amplitude change due to diffraction; $\tan^{-1}(\Lambda_0/\Theta_0)$ describes the longitudinal phase shift. The Gaussian field received at spatial filter position is given as

$$u_{\text{img}}(z) = \frac{f_{\text{Rec}}}{z} U_0(r, z) \quad (5.19)$$

Therefore, the SCE for a Gaussian wave field is then given as the convolution of image field with a transmission function of a circular aperture which is given as

$$f(r) = \begin{cases} 1, & r < r_{\text{Aperture}} \\ 0, & r \geq r_{\text{Aperture}} \end{cases} \quad (5.20)$$

5.3.3. SCE model for an off-axis case

When considering an un-confocal system, the transmitter optics are often not the same as receiver. Therefore, the collimation uncertainties for transmission and receiving beam lead to a directional separation for the two beams. This separation makes the image field at the spatial plane away from center. Then the collection efficiency is reduced depends on the angle of separation. We introduce a function of overlapping which shows the area passing through the spatial filter, to describe this effect (Fig.5.13). The separation d is given as $d = z_{\text{SF}} \cdot \theta_{\text{OffAxis}}$, where z_{SF} is the distance of spatial filter from the collection lens, θ_{OffAxis} is the off-axis angle which is the angle between sending and receiving beam.

$$f_{\text{overlap}} = r^2 \cos^{-1}\left(\frac{d^2 + r^2 - R^2}{2dr}\right) + R^2 \cos^{-1}\left(\frac{d^2 + r^2 - R^2}{2dr}\right) - \frac{1}{2} \sqrt{(-d + r + R)(d + r - R)(d - r + R)(d + r + R)} \quad (5.21)$$

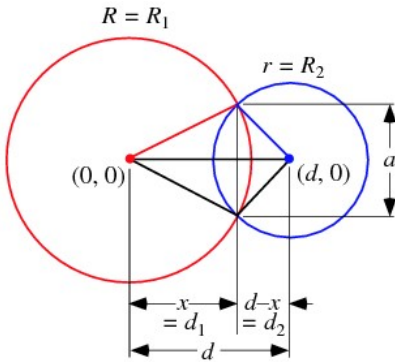


Fig. 5.13: Illustration of the circular overlapping, the overlapped part shows the light pass through the spatial filter, others are blocked

5.3.4. Simulation of range reduction factor

Assuming a monostatic Lidar system where the same telescope is used for the transmission and receiving. Fredlich et.al. [58] derived the reduction factor X for the detected signal as

$$X = \left[1 + \left(\frac{D}{2S_0} \right)^2 + \left(\frac{\pi D^2}{2\lambda R} \right)^2 \left(1 - \frac{R}{F} \right)^2 \right]^{-1} \quad (5.22)$$

Where, D is the telescope diameter, S_0 is the transverse coherence length of the return signal and F is the measurement range where the transmit/receive telescope focused.

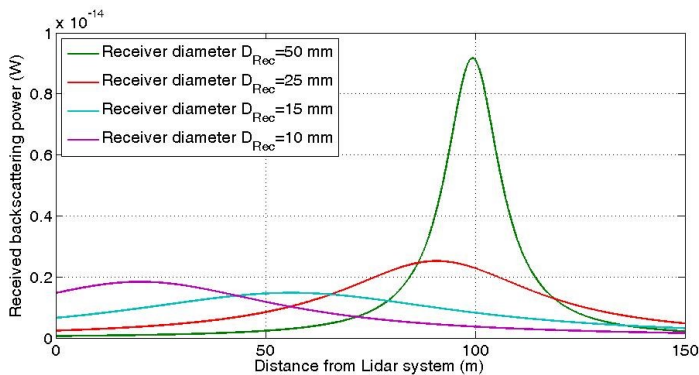


Fig. 5.14.: Range weighting factor with different receiver diameters when focused to 100 m

5.4. Full system simulation

5.4.1. Simplified cylindrical coordination concept

Due to the cylindrical symmetry along the optical axis with transmission and detection optical system, a new cylindrical polar coordinates concept is introduced to replace the Cartesian Coordinates which was used in our previous simulation work. As shown in Fig.5.15, the position of a point P is described as $P(r, \theta, z)$. Where $r = \sqrt{x^2 + y^2}$ is the distance from Z-axis to the point P, θ is the angle between the reference plane (XZ plane) and the plane of point P to Z-axis, z is the distance from point P to the XY plane.

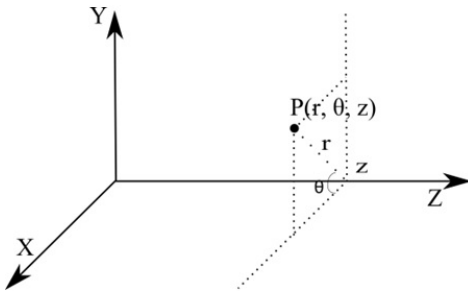


Fig. 5.15: Using a cylindrical coordinates to describe the position of a point P

Since the distance from detector to the target is far greater than the distance between different aerosols in the same target region, the scattering light from different particles can be treating as parallel. In the simulation, no spatial coherence between the scattering light from different aerosols is assumed. Therefore, the phase difference in the coherent detection due to the scattering light from different aerosols only depends on the light path difference. The light path from particle $P_i(r_i, \theta_i, z_i)$ to receiver can be described as Eq.(5.23) which only depends on the plane distance z and the Euclidean distance r from Z-axis to the point r , while θ information can be ignored.

$$LP_i = \sqrt{z_i^2 + r_i^2} \quad (5.23)$$

Within the new simulation concept, the particle position information is folded from 3D to 2D which makes the simulation easier and computation costs lower. Fig.5.16 graphically shows the folding transformation from a 2D plane $r_i, \theta_i|_{z=z_1}$ to a 1D line $r_i|_{z=z_1}$.

5.4.2. The modified Feuillete model

As briefly shown in Section 5.1, the slicing atmosphere Feuillete model is introduced for simulating the coherent Doppler Lidar system. Fig.5.17 illustrates the simulation process of the Feuillete model. Where the atmosphere is sliced into small elements, this small element consists numbers of aerosols. The backscattering cross section is calculated for individual

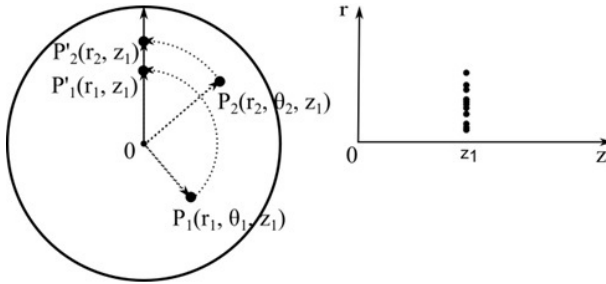


Fig. 5.16: A graphical description of particle position transformation, all aerosols on the plane z_1 will transform onto one line

particles then summed up over each elements to generate the backscattering signal. The signal power from element m is given as

$$P_m(t) = P_m \left(t - \frac{2z_R}{c} \right) \frac{\pi\beta\eta_0 D^2}{4R^2} \tag{5.24}$$

The power received from the slice m at distance z_m with a thickness of Δz is given as

$$P_m(t) = \int_{z_m}^{z_m+2\Delta z} P_m \left(t - \frac{2z}{c} \right) \frac{\pi\beta\eta_0 D^2}{4R^2} dz \tag{5.25}$$

The time variant simulation process is given as Fig.5.17 which can be divided into 4 different parts. The transmitter models the laser with a single wavelength and random phase with Winner process to model a Lorentzian shape power spectrum. The backscattering process uses the Feuillet atmospheric slicing model to model the backscattering. Then the backscattering and reference laser are transferred to the receiver to process the coherent detection. The simulated time signal is processed via FFT to get the power spectrum.

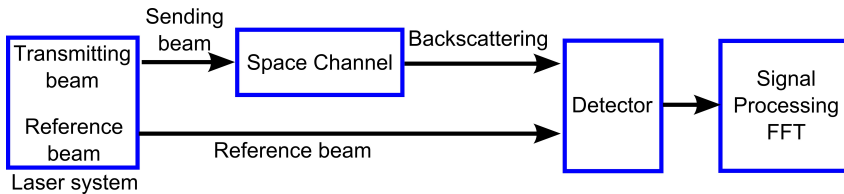


Fig. 5.17.: Block diagram of the simulation process

5.4.3. Full simulation results

5.4.3.1. Simulation results with the time invariant model

Time invariant model is simulated via Matlab, while time variant model is simulated via Simulink. Fig.5.18 shows the simulated power spectrum raw data with different wind speed 10 m/s, 20 m/s, and 30 m/s which corresponds to Doppler shift frequency of 13 MHz, 26 MHz, and 40 MHz.

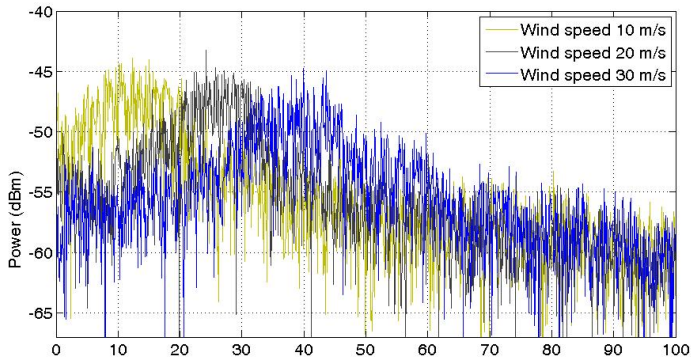


Fig. 5.18.: Simulated power spectrum signal with different wind speeds

Fig.5.19 illustrates the power spectrum graph with different linewidth. Graph shows that due to the higher phase noise of the broader spectrum lasers, a higher noise spectrum shows up on the simulation results. Meanwhile, the broader source spectrum makes the Doppler spectrum wider which leads a worse spectrum resolution.

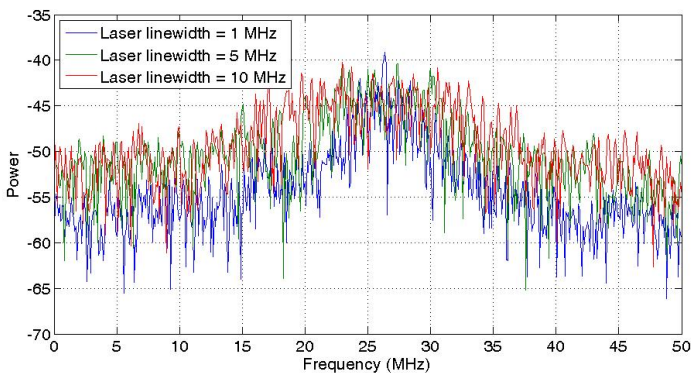


Fig. 5.19.: Simulated power spectrum signal with different laser linewidth

5.4.4. Simulation results with the dynamical simulation

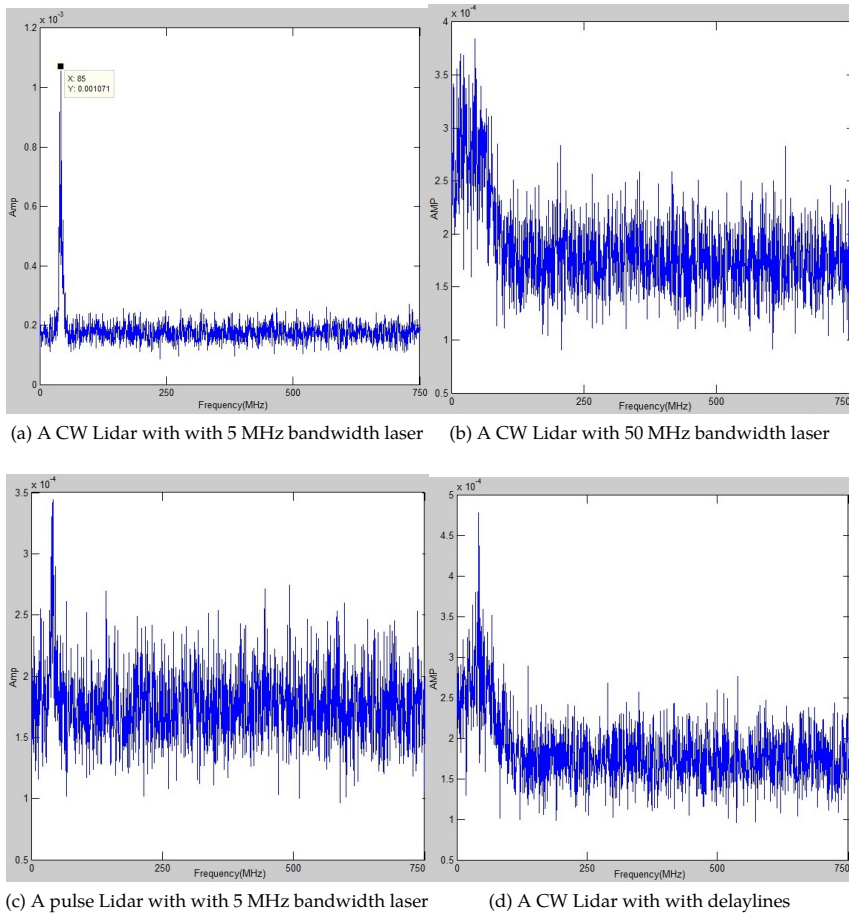


Fig. 5.20.: Spectrum analysis result from the dynamical model simulation

The full dynamical model simulation is carried on Simulink. The system parameters can be set up via the graphical user interface as shown on Fig.5.21.

Fig.5.20 shows a simulation result from the time variant simulation. Fig.5.20a is the result from the laser modelled with 5 MHz spectrum width, while Fig.5.20b shows the result with a 50 MHz laser spectrum width. Here with this simulation result, only the laser phase noise is considered, the detector noises, laser RIN, and other system noises are not considered. The simulations are carried from a CW Lidar scenario with 1800 ns laser pulse length, and a pulse Lidar scenario with 200 ns pulse length. Comparing Fig.5.20d which is associate with a delayline with the result from Fig.5.20a without delayline, the SNR with delayline is

5. Simulation of the Doppler wind Lidar

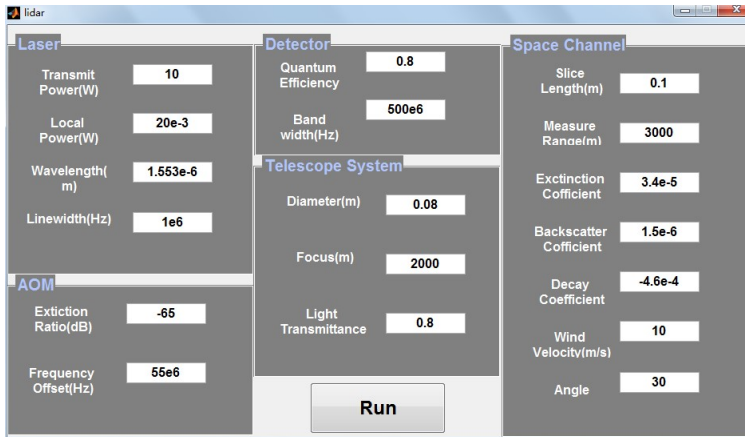


Fig. 5.21.: A GUI for setting of the simulator parameters

better. However, Fig.5.20d shows that even the measurement range are out of coherence length, it is still possible to obtain the Doppler signal, which need to be checked.

To check the effects of the phase noise to SNR, a time simulation was performed every half meters measurement distance. The SNR is defined as the maximum signal peak divided by the mean noise floor. Fig.fig:SimSNROverDistance shows the plotted result of such simulations. The simulated system carries a laser with 50 MHz linewidth which is around 2 meters coherence length. A fixed optical delay length of 10 meters is used to match the initial phase on a 5 meters measurement distance. The simulation results show a FWHM bandwidth of around 3 meters which is slightly longer than the calculated values, but matches with the experimental result showing on Chapter.6.

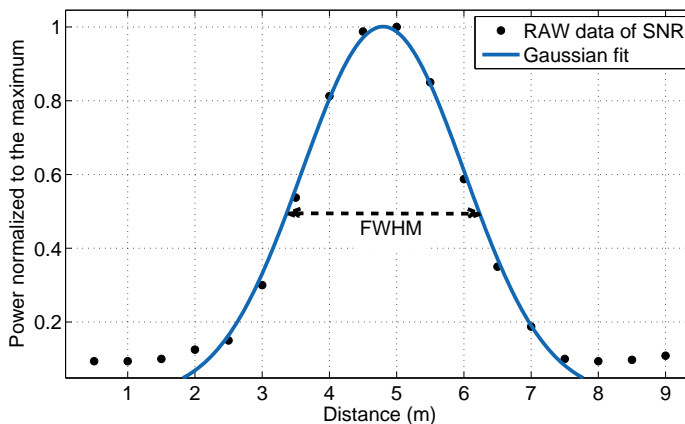


Fig. 5.22.: Simulated power spectrum signal with different laser linewidth

5.5. Summary and conclusion

In order to assist the design of the wind Doppler Lidar system, a complete simulation package is of interest. This also enables modelling the sensor system reaction for various weather scenarios and different hardware parameters. Unfortunately, there are no simulation packages which can be easily used as a testing tool for demonstrating the wind Lidar system reaction and helping the design of such a system. In this chapter, two different simulation approaches have been described, a time invariant system mainly used for simulating the signal received on the detector and a time variant system based on an atmospheric slicing Feuillete model for a running Lidar system simulation.

The time invariant model is focused on the simplified Mie scattering theory and temporal coherent Gaussian beam laser module. In order to optimize computation costs for calculating scattering from a huge amount of aerosols, a cylindrical coordinate system is used. Further simplification is achieved by dimension folding which leaves out the parameter from analysis. The simulation model also takes into account the changing components parameters as shown in previous section of the changes on the laser spectrum line width.

The time variant simulation with the atmosphere slicing model is based on the Feuillete Lidar which is modified to be able to use the broad spectrum laser sources. With this model, a CW and a pulse Lidar system have been simulated with a narrow band laser source which is imaging the model of ZephIR and WindCube Lidar systems. The differences of the presented Feuillete model Lidar simulation here is introducing the broad spectrum laser source with the Wiener-Khinchine method. A simulation was carried on different spectrum bandwidths have been performed which shows by matching of a time delay on reference beams can achieve a better detection performance. Furthermore, a simulation result was performed with different measurement distances shows a quite nice match of SNR changing over distance with the laser source coherence function.

To summarize this chapter, current work on the development of this simulator is based on keeping the model simple, while presenting arguments for ignoring the speckle effect due to spatial coherence (which was claimed to be an important effect for free space communication applications). While there is considerable research focus on models for partial spatial coherence effects on free space communication, there is very little reference to model which take into account backscatter. Going forward, a detailed analysis exploring the role of partial spatial coherence on backscatter is planned. Furthermore, along with the polarization effects on the scattering light detection, wind fluctuation module based on measurements and simulated data, different aerosol model for the adverse weather conditions, such as fog, rain, or snow.

6. Experimental realization of the Doppler Lidar feasibility

In order to evaluate the new concept, various experimental setups are designed and build up for testing. In this chapter, those designs are discussed and the experimental results are analyzed. The contents on this chapter are partially published on the author's following papers [SBF⁺14a, SBF⁺14b, SBB⁺13, SATF⁺14].

6.1. Wind tunnel design for wind flow measurements

In order to evaluate the new wind Lidar performance, a test environment with a stable reference wind flow is required. Therefore, a compact close loop wind tunnel is designed with the possibility to create a uniform wind flow and change the aerosol properties. Wind speed can be changed from 0.5 m/s to 10 m/s with a step size of 0.05 m/s. Fig.6.1 and 6.2 illustrate the designed wind tunnel.



Fig. 6.1: The designed close loop wind tunnel

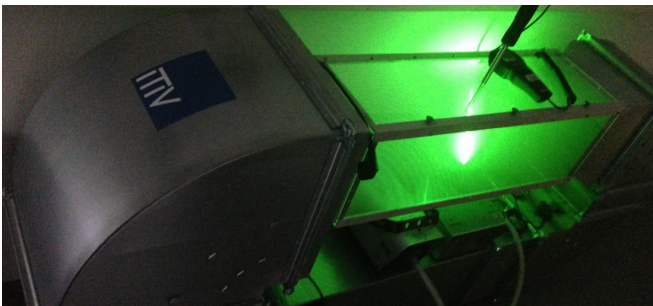


Fig. 6.2: Wind tunnel under operation as the target with a green laser Lidar system

6.2. Laser transmitter

The detectability of coherent detection relates to the optical path difference. To understand the coherence and other parameters of the laser sources is very important for evaluation of the Lidar performance. Table.6.1 gives the parameters of laser sources and Laser Diode Driver (LDD) which are used for the experiments.

Table 6.1.: Parameters of laser sources and laser diode driver for the experimental setup

	Model number	Max Power	Wavelength	Linewidth	L_{Coh}
Roithner	RLTMSL-532	50 mW	532 nm	< 1 pm	Ca. 50 m
Ondax	TO810-PLR170	170 mW	810 nm	50 MHz	←
Ondax	LD785-SE400	400 mW	785 nm	→	~2 m
Thorlabs	LD785-SE400	430 mW	785 nm	→	~2 m
ELOVIS, Dynalase					
Max. drive current		Modulation frequency		TEM Control Accuracy	
1600 mA		100 MHz		+/- 0.05°C	
Newport, Model 6000 with 6505 laser Diode driver					
Max. drive current		Modulation frequency		Drive current noise	
500 mA		DC to 350 kHz		< 8.0 μA	

6.2.1. Evaluation of laser coherence length

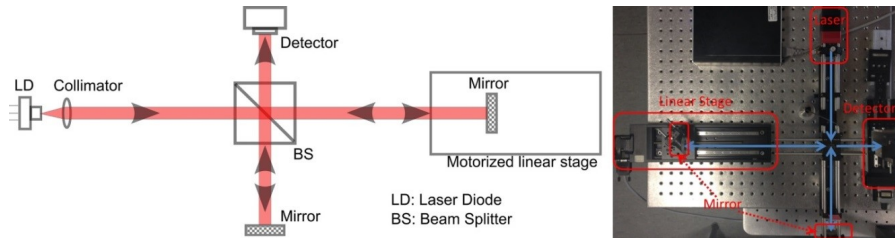


Fig. 6.3.: Michelson interferometer for measuring laser coherence length

The coherence function of the Laser diode (LD) is important for evaluating the Lidar performance. It can be measured by identifying the "contrast" of the interference as a function of the time shift between the two beams in a Michelson interferometer [136]. The measurement setup is illustrated at Fig.6.3, where a motorized linear stage is used to drive one mirror to continually change the position.

$$\text{Contrast} = \frac{I_{\text{max}} - I_{\text{min}}}{I_{\text{max}} + I_{\text{min}}} = |\gamma(z)| \quad (6.1)$$

Beam reflected from the fixed reference mirror has power P_{ref} , and the beam reflected from the moving signal mirror has power P_s , then the mixed signal power is

$$P_{\text{det}} = \frac{P_{\text{ref}} + P_s}{2} + \sqrt{P_s \cdot P_{\text{ref}}} \cdot \gamma(\Delta z) \cdot e^{\frac{2\pi}{\lambda} \Delta z} \quad (6.2)$$

Fig.6.4 shows the measurement with a 150 mm linear stage; the bottom two show the power of reference P_{ref} and signal P_s . Since the reference mirror is fixed, the beam power is unchanged. However, the linear stage moves the signal mirror, the reference beam power is changing with distance. Therefore, with the knowledge of $P_{\text{det}}(\Delta z)$, $P_{\text{ref}}(\Delta z)$, and $P_s(\Delta z)$, the coherence function $\gamma(\Delta z)$ can be calculated.

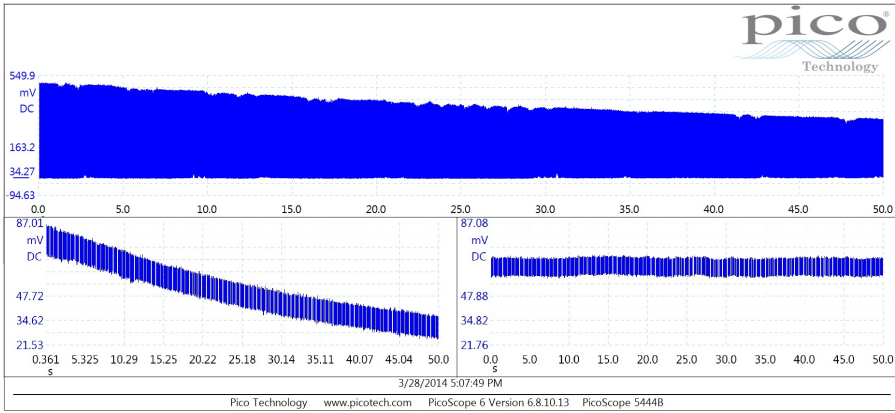


Fig. 6.4.: Up. Coherent length measurement through the whole linear stage range, Down. the signal beam power (left) and the reference beam power (right)

6.2.2. Evaluation of the laser diode intensity noise

Relative intensity noise is defined by the standard "DIN EN ISO 11554" [131].

$$\text{RIN}_t = \frac{\langle \Delta P(t)^2 \rangle}{P_0^2} \quad (6.3)$$

Where P_0 is the average optical power, $\Delta P(t)$ is the fluctuation of the overall optical power which includes the detector noise, laser shot noise and laser excess noise. The detector noise is specified by the photo detector as pW/\sqrt{Hz} which can be measured by switch off the laser. The laser shot noise is depend on the the DC current of the photo detector.

$$\Delta P = \Delta P_{\text{Detector}} + \Delta P_{\text{shot}} + \Delta P_{\text{excess}} \quad (6.4)$$

Table 6.2.: Parameters of detector and ESA for LD noise analysis setup

Photo detector	Menlosys FPD510	
Sensitivity @ 1550 nm	0.95	A/W
Gain	4E+4	V/W
3dB bandwidth	200	MHz
Dark state noise	-120	dBm
NEP	3	pW/vHz
Spectrum Analyser	HP 8591E	
Resolution BW	300	kHz
Frequency range	9 kHz to 1.8 GHz	

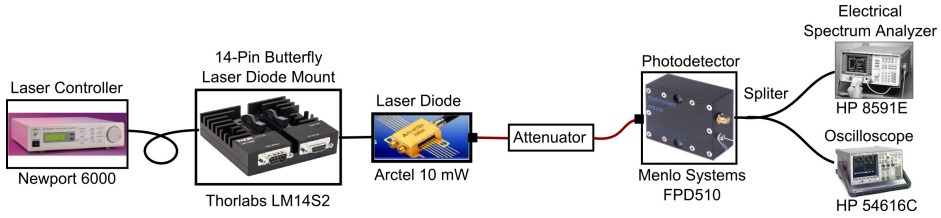


Fig. 6.5.: Laser RIN measurement system setup

Fig.6.5 shows the measurement setup for the laser RIN analysis. Table.6.2 gives the parameter of PD and Electrical spectrum analyzer (ESA) (Agilent 8591E). The LD drive current is controlled by the LD controller. The intensity noise are measuring the power fluctuation directly after the LD output. An attenuator is placed in between the LD and PD to bring down the laser power to the measurement range. The optical power fluctuation turns to the electrical power fluctuation via the PD and measured by an electrical spectrum analyser. By switching off the LD, the power fluctuation of the photo detector (detector noise), ΔP_{Det} can be measured. The shot noise power is given as

$$P_{\text{shot}} = \langle i_n^2 \rangle \cdot R_L = 2ei_{DC} \cdot R_L = 2e \cdot rP_0 \cdot R_L = 2e \cdot r \frac{U_0}{rG} \cdot R_L = 2e \cdot \frac{U_0}{G} \cdot R_L \quad (6.5)$$

Where, r is the responsibility of the detector, G is the detector gain, R_L is the load resistance. Since $i_t(t) = \frac{e\eta}{h\nu} P_{Op}(t)$, and $P_E(t) = i_t^2(t)R$, the electrical power is proportional to square of the optical power, $P_E(t) \propto P_{Op}^2(t)$, therefore the RIN equation is

$$RIN_t = \frac{\Delta P_E(t)}{P_E(t)} \quad (6.6)$$

ΔP_E is the noise power measured by an ESA, P_E is the average power measured by an oscilloscope. Detailed process of the RIN measurement is referred to Appendix.C.

Fig.6.6 illustrates the measured power spectrum of laser RIN and the noise from ESA and PD. From the graph a strong noise in comparison with the PD and ESA until 14 MHz can be observed, after 14 MHz the noise is relative low.

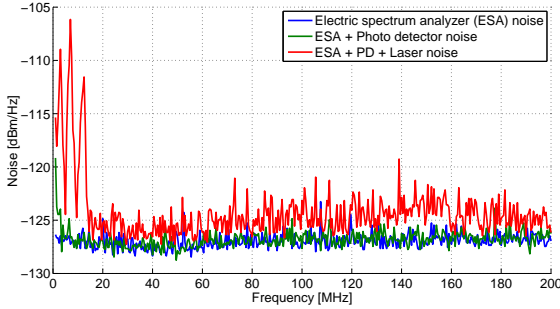


Fig. 6.6: Measured noise from ESA, PD, and laser RIN

Fig.6.7 illustrates the RIN at high frequency ($> 20\text{MHz}$), and right shows the RIN at low frequency ($< 20\text{MHz}$). For the CW operation, the Newport 6000 LDD gives a Root mean square (RMS) drive current noise of $< 2\mu\text{A}$ with the 6505 LDD module. Assuming the noise equally distributed to the entire bandwidth 200 MHz, the normalized LDD current noise is given as $2 \times 10^{-6}\text{A}/200\text{MHz} = 1 \times 10^{-14}\text{A}/\text{Hz}$. If the drive current is 100mA, the noise is $1 \times 10^{-15}\text{A}/\text{Hz}$. Since the optical power $P_{\text{Op}}(t) \propto I_{\text{LDD}}(t)$, the optical noise is given as $10 \times \log_{10}(1 \times 10^{-13}) = -30 \text{ dB}/\text{Hz}$ which is the same level as the measured RIN at 100mA.

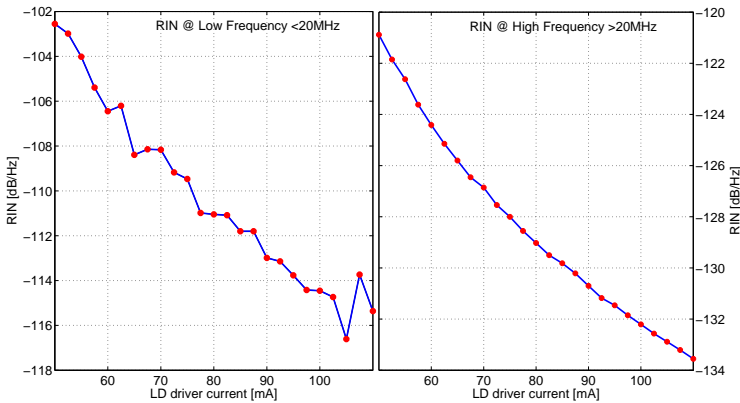


Fig. 6.7.: Measured laser RIN at different LD drive current

6.3. Sending and receiving optics design

6.3.1. Bi-static system with single photo detector

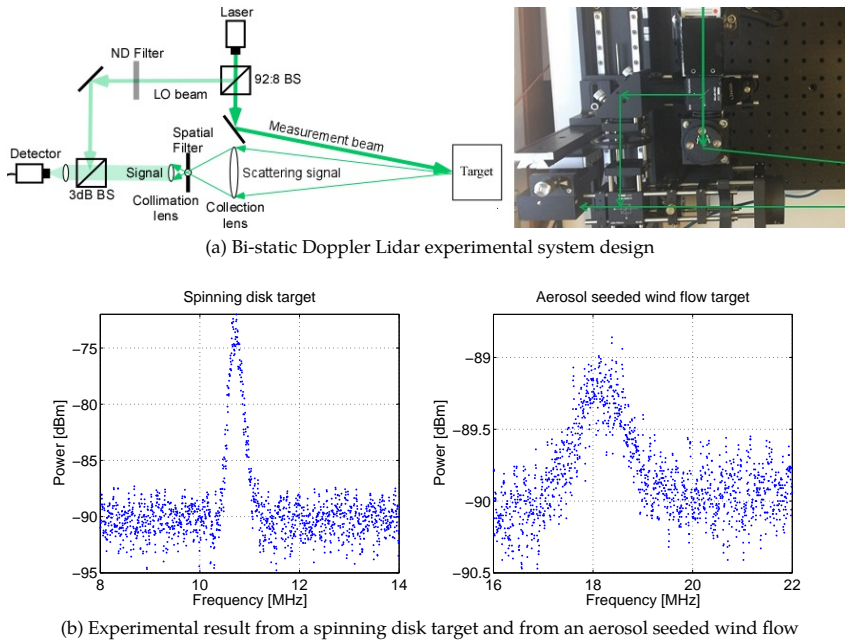


Fig. 6.8.: Free space bi-static Doppler Lidar experimental system with single photo detector

Fig.6.8a shows a system with 50 mW solid state CW laser with 532 nm wavelength single longitudinal mode and 50 m coherence length. A receiver is designed to collect the scattering light and collimated to a parallel beam. The reference beam splits from the laser by a 92:8 BS and passes into a 50:50 BS to mix with the signal beam. The mixed signal contains the beat frequency (Doppler frequency) signal. It is measured by the photo detector and digitized by a high speed digitizer (National Instruments PXI-5662). Digitized signals are acquired into the computer for further analysis.

Fig.6.8b shows the measurement results from the bi-static system with a spinning disk target. The LOS surface moving speed is 2.8 m/s which corresponds a Doppler frequency of 10.8 MHz (left) and from aerosols seeded wind flow with flow speed of 4.8 m/s corresponding with a Doppler frequency of 18 MHz(right). The target distance is 2 m in front of the telescope. Since the reflection power from a spinning disk surface has a much higher power than the backscattering from aerosols, Fig.6.8b shows a much higher SNR from spinning target (left) in comparing with the results from the wind flow (right). Furthermore, the signal width of the wind flow measurement is wider than the spinning disk. This is because the reflection from the spinning disk surface is from a fixed distance, however, the

backscattering from the wind flow are integrated over a range about 1 meter. Therefore, the derivation of the target speed is higher on the wind flow measurement.

6.3.2. Bi-static configuration with balanced photo detector

As discussed on Section.6.2.2, coherent Lidar system uses a strong reference beam power which brought a strong laser RIN into the detection. Therefore, such RIN noise decreases the SNR of the system. To reduce the effects from reference beam RIN, a balanced photo detector is used instead of the single detection in this section.

Within this design (Fig.6.9a) the single detector is substituted with a balanced detector to efficiently use the two output ports from the BS in order to reduce the laser RIN from the strong reference beam. It turns out that the balanced detector concept reveals a SNR gain of 5dB whereby the speed of a solid spinning target has been measured for both setups at the same speed (ca. 2.8 m/s, LOS) and distance (2 m) (Fig.6.9b). The higher noise power from the balanced detector is due to the allowance of higher reference beam power. The advantages of the balanced detector concept are a better SNR and also a higher beam power with regards to the reference beam. When changing the measurement distance, readjustment of the bi-static free space setups can be difficult.

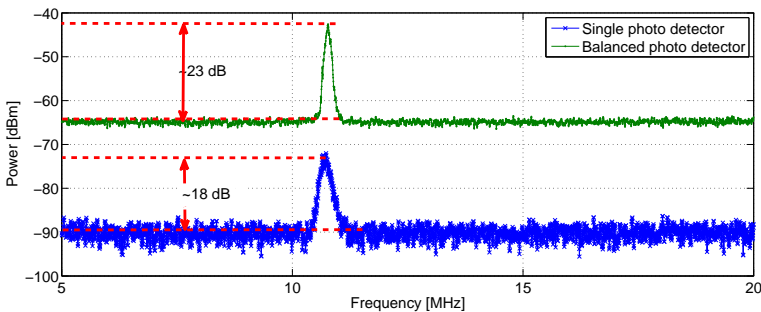
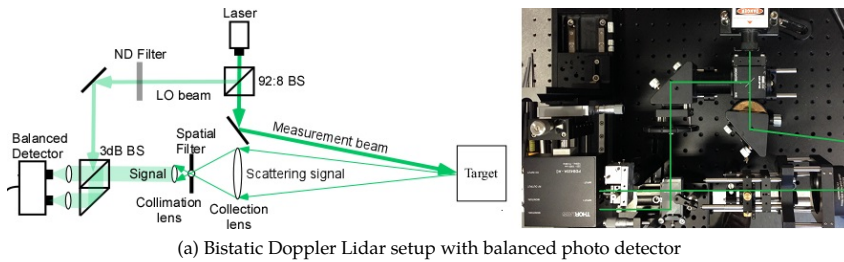
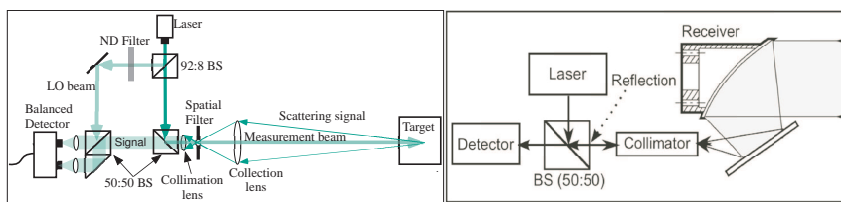


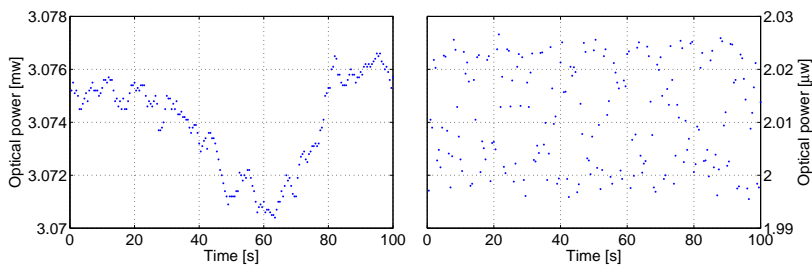
Fig. 6.9.: Free space bistatic Doppler Lidar setup with balanced photo detector

6.3.3. Monostatic configuration with 50:50 BS as a combiner

As a consequence of the problem to align the bistatic setup, a mono-static configuration that the transmitter and receiver setup aligned at the same axis has been designed (Fig.6.10a). Thus with this design, a 50:50 BS directs the beam to the target. With this changes, the measurement beam and the backscattered signal beam are on the same optical axis. However, due to the additional surface of the optical components a high noise is registered. The reflected power on each surface is about 0.7% of the incident laser power (Fig.6.10b). Therefore with this high noise power, coherent measurement could not be achieved.



(a) Monostatic configuration setup



(b) Measurement results of power transmitted to the collimator and reflected from surface

Fig. 6.10.: The monostatic configuration setup with standard beam splitter

6.3.4. Mono-static configuration with off-axis parabolic mirror

To avoid the phase noise caused by additional surface reflections from the optical components, in this design an off-axis parabolic mirror with a center hole (Thorlabs, MPD7621143-90-M01) substitutes the 50:50 BS (Fig.6.11). In this design, the sending beam passes through the center hole in the off-axis parabolic mirror and is collimated to infinity while the receiving mirror is focused to the measurement location. Due to no interaction between the sending and receiving beam, no noise comes from the sending beam into detection.

However, with off-axis parabolic mirror the off-axis light creates "Comma" which decreases the collection efficiency. Fig.6.12 illustrates the sketch of the beam focusing quality test setup. The focus quality evaluation of the off-axis parabolic mirror is carried on both via a

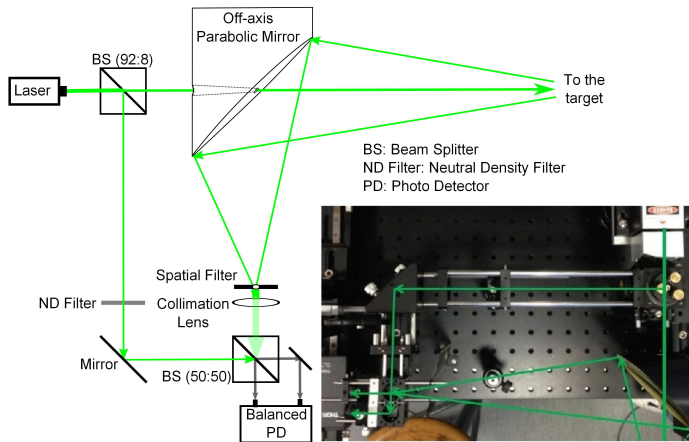


Fig. 6.11.: Monostatic configuration non-confocal system with off-axis parabolic mirror

Zemax simulation and with an actual measurement with a camera based beam profiler. Both simulation and experiments are following the same design as shown with Fig.6.12.

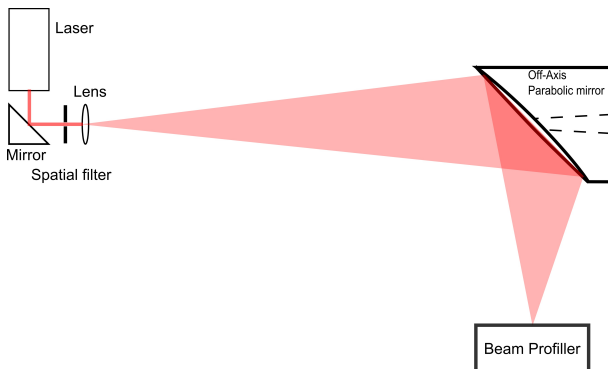


Fig. 6.12: Sketch of beam focusing quality by the off-axis parabolic mirror

Fig.6.13a and Fig.6.13b are the simulation and measurement result. The simulation uses a point laser source at 1 meter with 0.2 degree divergence, meanwhile the measurement result has an object distance of 18 meters. For the short distance, a strong comma appears. For a longer distance, the "comma" effect in the terms of scattering light collection is negligible.

Fig.6.14 and 6.15 show the results from a spinner disk target and the wind flow measurement. An SNR drop depending on the distance is observed, while the receiving power is proportional to $1/d^2$ with d as the distance. Assuming the reference power is stable, the beat signal power depends on the the signal power P_d and the coherence function $\gamma(d)$. Therefore, the beat signal amplitude can be describe with the equation $f(d) = a \cdot d^{-1} \cdot e^{-b \cdot d}$,

6. Experimental realization of the Doppler Lidar feasibility

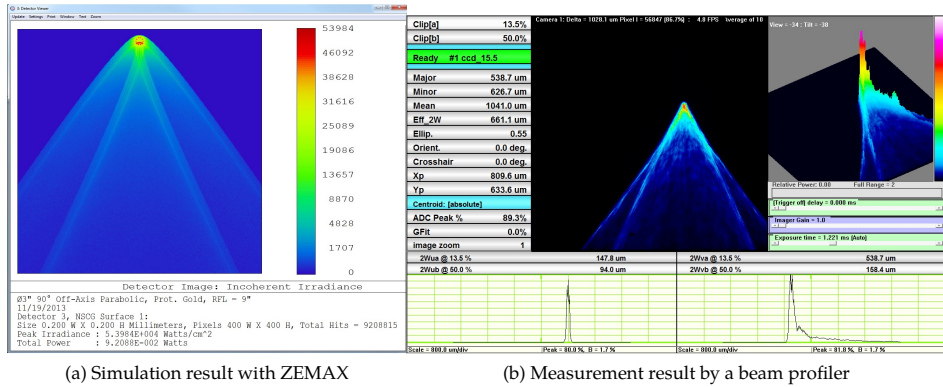


Fig. 6.13.: Focusing quality of the off-axis parabolic mirror

with d as the distance. Assuming the noise floor is the same for different distances, the SNR can be described as $SNR(d) = a \cdot d^{-1} \cdot e^{-b} \cdot d$.

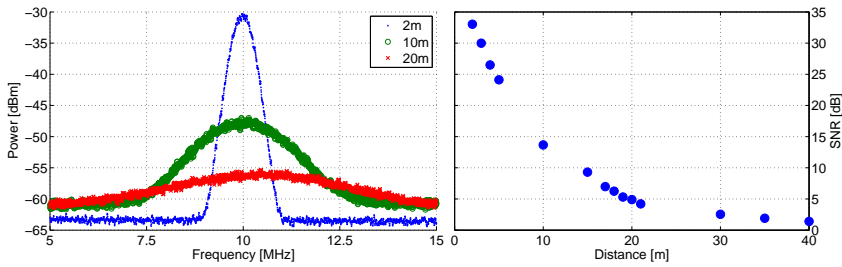


Fig. 6.14.: Experiment result for a solid target. Measurement result at different measurement distances(Left), SNR plot against measurement distances(right)

6.4. Variable length reference beam design

The laser sources with a measured coherence length of ca. 2 m are used. By adjusting the reference mirror position, measurement can only be achieved when light path difference between sample and reference beam is within the coherence length. Therefore, the laser coherence length defines the depth resolution. The theoretical background of this concept has been discussed on chapter 5. Fig.6.16 illustrates the work principle of such systems.

As discussed on Section 6.4.4, the off-axis parabolic mirror receiver design is used for the final system. The Ondax TO810-PLR170 laser diode with the operating wavelength of 810 nm, spectrum linewidth 50 MHz which corresponds to 2 m coherence length has been used.

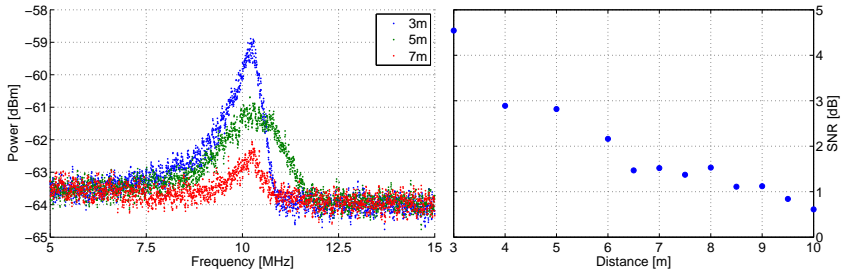


Fig. 6.15.: Experiment result for an air flow with the wind tunnel. Power Spectrum at different measurement distances(Left), SNR plot against measurement distances(right)

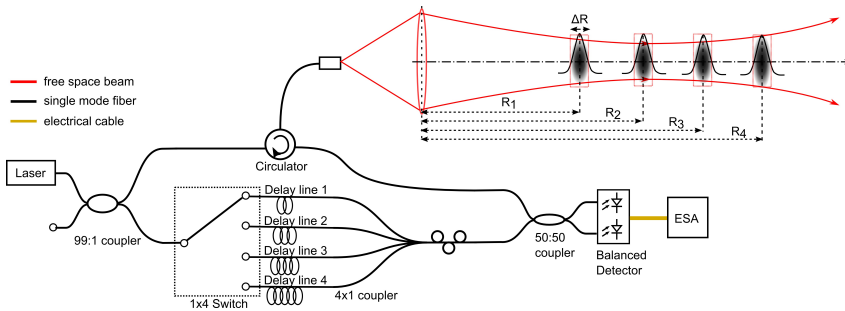


Fig. 6.16.: Illustration of CW Lidar concept with range independent probe length

Several single mode fiber delayline is used as the delayline on the reference beam to match the initial phase for different measurement distances. Fig.6.17 shows the measurement power spectrum results at a fixed distance with different fiber delaylines. The ideal length of the delayline fiber l_{fiber} can be calculated as $l_{\text{fiber}} = 2 \cdot d_{\text{meas}} / n_{\text{fiber}}$ with the measurement distance d_{meas} and the refraction index of the fiber core $n_{\text{fiber}} = 1.453$. For a 2 m target distance the ideal fiber delayline is $l_{\text{fiber}} = 2 \times 2 / 1.453 = 2.75\text{m}$. As shown on Fig.6.17, the highest SNR achieved with a fiber delayline length of 2 m, which is the closest to the ideal length of 2.75 m. Bigger the optical path difference leads to a smaller SNR value. The results show that with this 2 m coherence length laser, for a multiple length delayline concept the delayline length differences need to be ca. 10 m in order to avoid the influence from the other delaylines. Furthermore, the -3 dB width from the SNR peak is around 2 m which matches the coherence length of the laser diode.

Fig.6.18 shows the experimental results with a 7 m fixed fiber delayline and the SNR plot with different measurement distances. Fig.6.19 shows the curve fitting of the SNR measurement data against the distance. With 7 m fiber delaylines, the optimal measurement distance is $d_{\text{meas}} = l_{\text{fiber}} n_{\text{fiber}} / 2 = 4.8\text{m}$. As shown on Fig.6.19, the peak SNR position is more or less at the same position with the ideal delayline length "4.8 m". Therefore, with the delayline concept, the best measurement distance is matching with the fiber delayline length.

6. Experimental realization of the Doppler Lidar feasibility

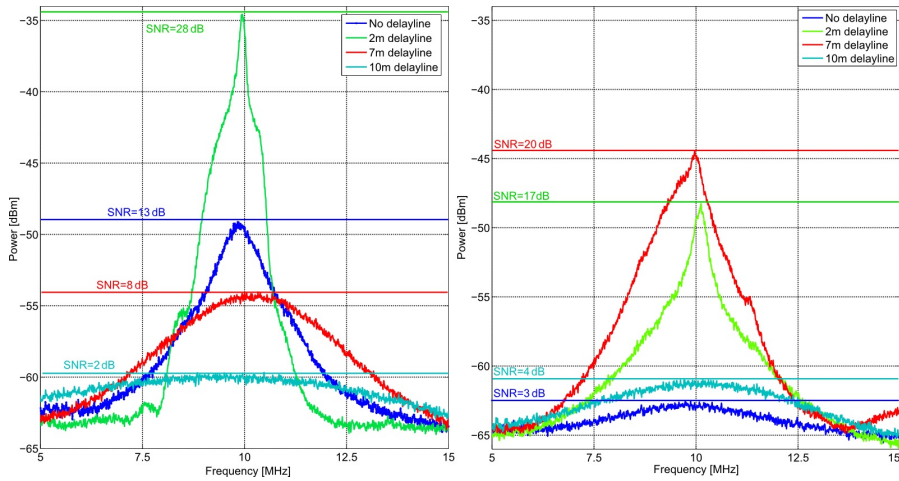


Fig. 6.17.: Measurement results with different fiber delayline length for a fixed target distance of 2 (left) and 4 m (right)

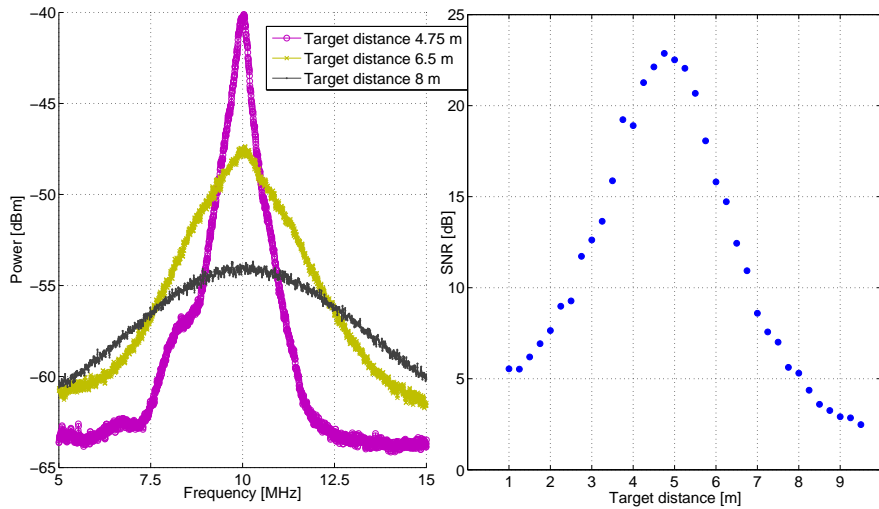


Fig. 6.18.: Measurement results with a fixed 7 m fiber delayline length at different measurement distance (left) and the SNR-Distance plot (right)

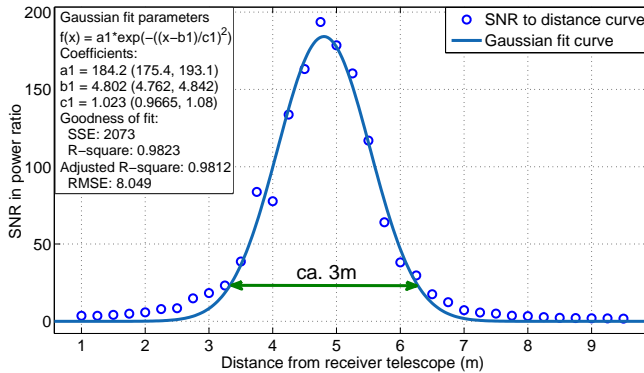


Fig. 6.19.: Gaussian curve fitting of the SNR against distance measurement results

6.5. Summary and conclusion

In this chapter, a detailed system design of the cost efficient Doppler wind Lidar system with broad spectrum laser has been discussed. The purpose of this chapter is to evaluate the feasibility of using the short coherence length lasers for the Doppler wind Lidar application. In Chapter.5, a simulation environment have been discussed for numerical simulation of the system design parameters. Here, an experimental environment is designed and build up for testing of different parts of the Lidar systems. The experimental system is based on laser diodes with short coherence length about 2m. A free space concept is used for the easy handling and optical components alignment.

With the experimental system, different sending and receiving optics have been designed and tested. Due to the weak backscattering signals, a very high requirement on the optical surface back reflections or cross talk have been realized. There, the concept of using an off-axis parabolic mirror with a center hole shows the best performance which is used as the final design in the experimental environments for testing of different lasers and evaluation of the delayline concept. However, due to the hardware limitations, the delayline concept is only tested up to 7m with different single mode fibers. Then, the final experimental setup ended up with a low powered single direction short distance measurement system. For further experimental tests, a prototype equipped with the components required from the analysis phase is desired. The evaluation for a long distance (up to 150 meters) measurements is the next steps of the Lidar system design in the near futures.

From the experimental results, it is very clearly to indicate that if the light path difference between reference and signal beam is longer than the coherence length, the SNR is reducing. If the light path difference is twice long as the coherence length, the SNR reduces 10dB. Therefore, when using different delayline length, keep the length difference more than twice of the coherence length can minimize the influence of scattering light from the other probe volumes.

Part III.

The “industry-friendly” Lidar assisted active pitch
control design

7. Wind turbine modelling

The wind turbine system consists wind character, aerodynamic, structural dynamics, hydrodynamics, mooring lines, electrical and control system, to simulate all those parts in one simulation is difficult and costs a lot computation power. There are a number of design tools available to model the HAWT in a fully coupled time domain dynamic analysis. A. Cordle et.al. reported different simulation tools for HAWT modelling in detail [34].

1. Fatigue, Aerodynamics, Structures, and Turbulence (FAST) by NREL is a public available HAWT simulation tool [97]
2. Automatic Dynamic Analysis of Mechanical Systems (ADAMS) by MSC. Software Corporation is a commercial general purpose multi-body dynamics simulation tool
3. Bladed by Garrad Hassan is a commercial simulation tool for modelling of onshore fixed-bottom wind turbines and extended for offshore wind turbine modelling
4. 3Dfloat by the Norwegian University of Life Sciences (UMB) for modelling of floating offshore wind turbines with full coupling between structural dynamics, aerodynamics, hydrodynamics and control systems.

Following in this thesis, the 5-MW wind turbine model designed by NREL is used as the reference [98]. Table.7.1 shows the main properties of the wind turbines. The full model parameters are given at Table.A.1 in Appendix.A.2.

Table 7.1.: Properties of the NREL 5-MW Baseline reference wind turbine [96]

Rated power	5 MW
Rotor orientation, configuration	Upwind, 3 Blades
Control mode	Variable speed, collective pitch
Rotor, Hub diameter	126 m, 3 m
Cut-in, rated, cut-out wind speed	3, 11.4, 25 m/s
Cut-in, rated rotor speed	6.9 rpm, 12.1 rpm
Rated tip speed	80 m/s
Rotor mass	110,000 kg
Nacelle mass	240,000 kg
Tower mass	347,460 kg

For the simulation purpose, a FAST nonlinear model with the selected Degree of Freedom (DOF) is used. Section.7.1 gives a general overview of this model. However, FAST model is too complex to integrate into the RHC controller design. Therefore, a simplified reduced DOF model is designed based on the study by C.L. Bottasso et.al. [19]. Following in Section.7.2 till Section.7.5 show the theoretical details and design of the numerical model for each DOF.

7.1. FAST wind turbine model

FAST is an open source aero-elastic HAWT simulation tool designed by NREL. Along with AeroDyn, FAST were determined suitable for the calculation of wind turbine loads for design and certification. There are over 1,000 possible output variables from a FAST model simulation, including motions of each blade, shaft, nacelle, yaw, and wind. FAST is written in FORTRAN 90, but a Dynamic Linked Library (DLL) is available to be used in MATLAB Simulink simulations as an S-function block. Fig.7.1 shows the process of FAST simulation.

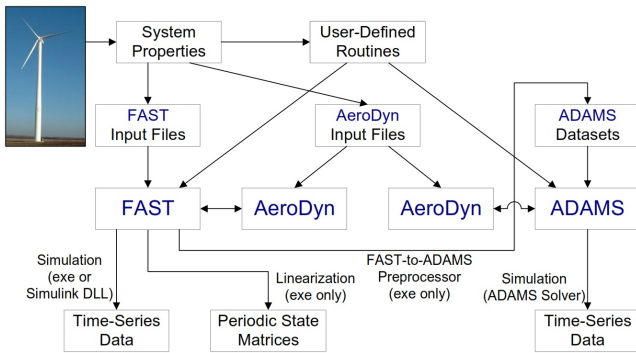


Fig. 7.1: Models of the FAST operation [99]

Generator model, Lidar measurement, pitch control, and yaw control are designed as separated modules within the same Simulink environment to accomplish a full simulation. Fig.7.2 shows the simulation block diagram which includes three main parts. Generator model simulates the process of generator, in this thesis a simple model converting rotor rotation to generator power is used. Pitch controller module is the main design part. Furthermore, for comparison, different pitch control approaches are tested.

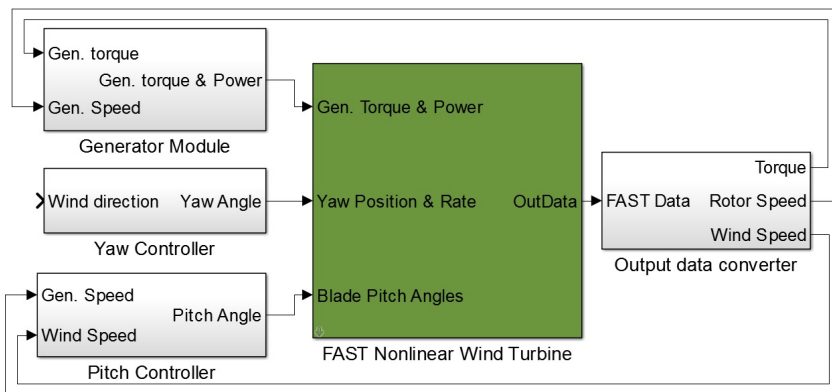


Fig. 7.2.: Simulation block diagram in a Simulink environment

FAST model has 24 DOFs for a three-blade wind turbine. 6 platform DOFs are used for offshore turbine simulations. The supported DOFs by FAST model are:

1. Generator model [1 DOF]
2. Drive train model [1 DOF]
3. 1st and 2nd blade flapwise model [2x3 (number of blades) DOFs]
4. 1st blade edgewise model [1x3 DOFs]
5. 1st and 2nd tower fore-aft model [2 DOFs]
6. 1st and 2nd tower side-to-side model [2 DOFs]
7. Yaw model [1 DOF]

A nominal model of wind turbine is designed for the new approach. For a better controller designing, the model with more DOFs benefits for the controller design. To reduce the system natural frequency is the objective of the controller design. Table.7.2 gives the full system natural frequencies from a simulation study by J.M. Jonkman [96]. The collective pitch control need to reduce the system behaviour around or below the rotation frequency of the rotor which is named "1-P frequency". With an individual pitch system, the loads on 3-P frequency for a three blades turbine or 2-P frequency for a two blades turbine can be further reduced [157]. However, the performance of individual pitch control is limited by the relatively slow pitch actuator in order to preserve the actuators and the blade bearings [31]. Therefore, the major pitch system on a commercial turbine is collective pitch. The rated rotor speed of this model is 12.1 rpm which corresponds 1-P frequency of 0.2017 Hz and 3-P frequency of 0.605 Hz.

Table 7.2.: System natural frequencies with FAST simulation [96]

Mode	Natural frequencies [Hz]
1 st Tower Fore-Aft	0.324
1 st Tower Side-to-Side	0.312
1 st Drive-train Torsion	0.6205
1 st Blade Collective Flap	0.6993

7.2. Aerodynamics model

For the RHC controller design, FAST model is too complex and not possible to integrate into the control loop. Therefore, a simplified reduced DOFs nominal model is designed based on the study by C.L. Bottasso et.al. [19]. The nominal model is divided into an aerodynamic model and a servo-elastic model. The aerodynamic model simulates the forces affected by the airflow around the turbine body. Details of the aerodynamics model is given on Appendix.A.1. The power extracted by a wind turbine is given as Eq.(7.1).

$$P_{\text{Extr}} = \frac{1}{2} \rho U_{\infty}^3 A_D C_P = \frac{1}{2} \rho \pi U_{\infty}^3 R_{\text{Rtr}}^2 C_P \quad (7.1)$$

Where ρ is the air density, A_D is the rotor swept area, R_{Rtr} is rotor radius, U_∞ is wind speed in far upstream side which is $U_\infty = \frac{U_{REWS}}{1-a}$, C_P is the power coefficient. Therefore, aerodynamic torque and thrust forces on the rotor are given as

$$\tau_{Rtr} = \frac{1}{2} \rho \pi R_{Rtr}^3 U_{rel}^2 C_Q(\lambda_{TSR}, \beta_{CP}) \quad (7.2a)$$

$$f_T = \frac{1}{2} \rho \pi R_{Rtr}^2 U_{rel}^2 C_T(\lambda_{TSR}, \beta_{CP}) \quad (7.2b)$$

Where $\lambda_{TSR} = \frac{\Omega_{Rtr} \cdot R_{Rtr}}{U_{wind}}$ is the tip-speed ratio, $C_Q = \frac{C_P}{\lambda_{TSR}}$ is the torque coefficient, C_T is the thrust force coefficient. When consider the tower fore-aft bending, the wind speed is given as the relative wind speed $U_{rel} = U_{REWS} - \dot{d}_{Twr}$, where d_{Twr} is the fore-aft displacement of the tower top, \dot{d}_{Twr} is the moving speed.

7.2.1. Linearisation of the aerodynamics model

Assuming a collective pitch system, since the rotor torque is a function of wind speed U , rotor speed Ω_{Rtr} , and pitch angle β_{CP} . Therefore, the rotor torque at the balance point is given as

$$\tau_{Rt,0} = \frac{1}{2} \rho \pi R_{Rtr}^3 U_0^2 C_Q(\lambda_{TSR,0}, \beta_{Pitch,0}) \quad (7.3)$$

with $\lambda_{TSR,0} = \frac{\Omega_{Rt,0} \cdot R_{Rtr}}{U_0}$, by the Taylor series expansion, the rotor torque is given as

$$\tau_{Rtr} = \tau_{Rt,0} + \frac{\delta \tau_{Rtr}}{\delta U} \Delta U + \frac{\delta \tau_{Rtr}}{\delta \Omega_{Rtr}} \Delta \Omega_{Rtr} + \frac{\delta \tau_{Rtr}}{\delta \beta_{CP}} \Delta \beta_{CP} + R_2 \quad (7.4)$$

Then, the incremental generator torque signal can be given as a state space model

$$\Delta \tau_{Rtr} \cong \left[\left. \frac{d\tau_{Rtr}}{dU} \right|_{U_0} \quad \left. \frac{d\tau_{Rtr}}{d\Omega_{Rtr}} \right|_{\Omega_{Rt,0}} \quad \left. \frac{d\tau_{Rtr}}{d\beta_{CP}} \right|_{\beta_{Pitch,0}} \right] \left[\Delta U \quad \Delta \Omega_{Rtr} \quad \Delta \beta_{CP} \right]^T + R_2 \quad (7.5)$$

Where the partial differential parts at equilibrium point are given as

$$\left. \frac{d\tau_{Rtr}}{dU} \right|_{U_0} = \rho \pi R_{Rtr}^3 U_0 C_{Q,0} - \frac{1}{2} \rho \pi R_{Rtr}^4 \Omega_{Rt,0} \left. \frac{\partial C_T}{\partial \lambda_{TSR}} \right|_{\lambda_{TSR,0}} \quad (7.6a)$$

$$\left. \frac{d\tau_{Rtr}}{d\Omega_{Rtr}} \right|_{\Omega_{Rt,0}} = \frac{1}{2} \rho \pi R_{Rtr}^4 U_0 \left. \frac{\partial C_Q}{\partial \lambda_{TSR}} \right|_{\lambda_{TSR,0}} \quad (7.6b)$$

$$\left. \frac{d\tau_{Rtr}}{d\beta_{CP}} \right|_{\beta_{Pitch,0}} = \frac{1}{2} \rho \pi R_{Rtr}^3 U_0^2 \left. \frac{\partial C_Q}{\partial \beta_{CP}} \right|_{\beta_{Pitch,0}} \quad (7.6c)$$

Applying the same linearisation approach for the thrust force, at the balance point, the thrust force can be represent as

$$f_{T,0} = \frac{1}{2} \rho \pi R_{Rtr}^2 U_0^2 C_T (\lambda_{TSR,0}, \beta_{Pitch,0}) \quad (7.7)$$

Therefore, by the Taylor series expansion, the thrust force is given as

$$f_T = f_{T,0} + \frac{df_T}{dU} \delta U + \frac{df_T}{d\Omega_{Rtr}} \delta \Omega_{Rtr} + \frac{df_T}{d\beta_{CP}} \delta \beta_{CP} + R_2 \quad (7.8)$$

Then writing as an incremental thrust force signal with a state space model as

$$df_T \cong \left[\left. \frac{df_T}{dU} \right|_{U_0} \quad \left. \frac{df_T}{d\Omega_{Rtr}} \right|_{\Omega_{Rt,0}} \quad \left. \frac{df_T}{d\beta_{CP}} \right|_{\beta_{Pitch,0}} \right] \begin{bmatrix} \Delta U & \Delta \Omega_{Rtr} & \Delta \beta_{CP} \end{bmatrix}^T + R_2 \quad (7.9)$$

Where the partial differential parts at equilibrium point are given as

$$\left. \frac{df_T}{dU} \right|_{U_0} = \rho \pi R_{Rtr}^2 U_0 C_{Q,0} - \frac{1}{2} \rho \pi R_{Rtr}^3 \Omega_{Rt,0} \left. \frac{\partial C_T}{\partial \lambda_{TSR}} \right|_{\lambda_{TSR,0}} \quad (7.10a)$$

$$\left. \frac{df_T}{d\Omega_{Rtr}} \right|_{\Omega_{Rt,0}} = \frac{1}{2} \rho \pi R_{Rtr}^3 U_0 \left. \frac{\partial C_T}{\partial \lambda_{TSR}} \right|_{\lambda_{TSR,0}} \quad (7.10b)$$

$$\left. \frac{df_T}{d\beta_{CP}} \right|_{\beta_{Pitch,0}} = \frac{1}{2} \rho \pi R_{Rtr}^2 U_0^2 \left. \frac{\partial C_T}{\partial \beta_{CP}} \right|_{\beta_{Pitch,0}} \quad (7.10c)$$

7.3. Wind turbine Servo-Elastic structure model

The servo-elastic dynamic model of HAWT can be separated into: drive-train, generator, tower, blades, pitch actuator, and torque actuator submodels. The dynamic model of each DOFs can be represented as an Equation of Motion (EoM) written as

$$M(q, u, t) \ddot{q} + f(q, \dot{q}, u, v, t) = 0 \quad (7.11)$$

Where M is the mass matrix, f is the force function, q is the states vector, \dot{q} and \ddot{q} are the first and second derivatives of state q, representing the speed and acceleration, u is control vector, v is wind input vector. For the design of MPC controller, a linearised model for each DOFs is applied by the help of FAST. Then, the 2nd order representation of EoM by FAST as an output of the linearisation process is given as

$$M \Delta \ddot{q} + C_{Damp} \Delta \dot{q} + K \Delta q = F \Delta u + F_d \Delta v \quad (7.12)$$

Where M , C , K are the mass, damping and stiffness matrices, F and F_d are the control and wind disturbance matrices, Δ represents the perturbations. The system states are $x = \begin{bmatrix} \Delta q \\ \Delta \dot{q} \end{bmatrix}$, the first order derivative, $\dot{x} = \begin{bmatrix} \Delta \dot{q} \\ \Delta \ddot{q} \end{bmatrix}$, can be written in a state space form as

$$\dot{x} = Ax + B\Delta u + \Gamma\Delta v \quad (7.13)$$

with

$$A = \begin{bmatrix} 0 & I \\ -M^{-1}K & -M^{-1}C_{\text{Damp}} \end{bmatrix}, B = \begin{bmatrix} 0 \\ -M^{-1}F \end{bmatrix}, \Gamma = \begin{bmatrix} 0 \\ -M^{-1}F_d \end{bmatrix} \quad (7.14)$$

7.3.1. Dynamic model of rotor

Assuming the azimuth angle of rotor and generator are Ω_{Rtr} , Ω_{Gen} , the rotational speed of rotor and generator are given as Ω_{Rtr} , Ω_{Gen} . the EoM of the rotor is given as Eq.(7.15).

$$J_{\text{Rtr}}\dot{\Omega}_{\text{Rtr}} = \tau_{\text{Rtr}} - \tau_{\text{DT}} \quad (7.15)$$

Here, τ_{DT} is the counter torque applied by the drive train low speed shaft, where $\tau_{\text{DT}} = k_{\text{DT}} \cdot \theta_{\text{DT}} + c_{\text{DT}} \cdot \Omega_{\text{DT}}$. Assuming the drive train is rigid, then the torque τ_{DT} is equal to the generator torque, $\tau_{\text{DT}} = N_{\text{Gear}}\tau_{\text{Gen}}$. On the steady operational condition, the aerodynamic torque on rotor is equal to the generator torque, $\tau_{\text{Rt},0} = N_{\text{Gear}}\tau_{\text{Gen}}$, therefore

$$J_{\text{Rtr}}\Delta\dot{\Omega}_{\text{Rtr}} - \frac{d\tau_{\text{Rtr}}}{d\Omega_{\text{Rtr}}}\Delta\Omega_{\text{Rtr}} = \frac{d\tau_{\text{Rtr}}}{d\beta_{\text{CP}}}\Delta\beta_{\text{CP}} + \frac{d\tau_{\text{Rtr}}}{dU}\Delta U \quad (7.16)$$

7.3.2. Dynamic model of generator

The generator is modelled at the end of low speed shaft directly within FAST model. Therefore, assuming the generator speed is Ω_{Gen} , the high speed shaft is given as $\Omega_{\text{HS}} = N_{\text{Gear}}\Omega_{\text{Gen}}$ which represents the generator speed. The EoM of generator is

$$N_{\text{Gear}}^2 J_{\text{Gen}}\dot{\Omega}_{\text{Gen}} = \tau_{\text{DT}} - N_{\text{Gear}}\tau_{\text{Gen}} \quad (7.17)$$

here τ_{DT} is the torque from low speed shaft. Combining the EoM of the rotor (Eq.(7.15)) into the generator, if the drive-train is perfectly rigid, $\theta_{\text{Rtr}} = \theta_{\text{Gen}}$, $\Omega_{\text{Rtr}} = \Omega_{\text{Gen}}$.

$$\left(J_{\text{Rtr}} + N_{\text{Gear}}^2 J_{\text{Gen}} \right) \dot{\Omega}_{\text{Gen}} = \tau_{\text{Rtr}} - N_{\text{Gear}}\tau_{\text{Gen}} \quad (7.18)$$

Let $J_{\text{Rtr}} + N_{\text{Gear}}^2 J_{\text{Gen}} = J_{\text{tot}}$ be the total rotational inertia and add into Eq.(7.18), then the equation can be rewritten as

$$J_{\text{tot}}\dot{\Omega}_{\text{Gen}} = \tau_{\text{Rtr}} - N_{\text{Gear}}\tau_{\text{Gen}} \quad (7.19)$$

Adding the linearized rotor aero torque into equation, we get

$$J_{\text{tot}} \Delta \dot{\Omega}_{\text{Gen}} - \frac{\delta \tau_{\text{Rtr}}}{\delta \Omega_{\text{Rtr}}} \Delta \Omega_{\text{Gen}} = \begin{bmatrix} \frac{\delta \tau_{\text{Rtr}}}{\delta \beta_{\text{CP}}} & -N_{\text{Gear}} \end{bmatrix} \begin{bmatrix} \Delta \beta_{\text{CP}} \\ \Delta \tau_{\text{Gen}} \end{bmatrix} + \frac{\delta \tau_{\text{Rtr}}}{\delta U} \Delta U \quad (7.20)$$

Defining the states as $x = \theta_{\text{Gen}}$, the EoM of generator model can be written with the state-space representation as Eq.(7.21).

$$\Delta \dot{x}_{\text{Gen}} = \frac{\delta \tau_{\text{Rtr}} / \delta \Omega_{\text{Rtr}}}{J_{\text{tot}}} \Delta x_{\text{Gen}} + \begin{bmatrix} \frac{\delta \tau_{\text{Rtr}} / \delta \beta_{\text{CP}}}{J_{\text{tot}}} & -\frac{N_{\text{Gear}}}{J_{\text{tot}}} \end{bmatrix} \Delta U + \frac{\delta \tau_{\text{Rtr}} / \delta U}{J_{\text{tot}}} \Delta v \quad (7.21)$$

The generator EoM parameters are given as Table.7.3. The output power of generator is

$$P_{\text{Gen}} = \Omega_{\text{Gen}} \tau_{\text{Gen}} \eta_{\text{Gen}} \quad (7.22)$$

Where η_{Gen} is generator efficiency, τ_{Gen} is the generator torque. The generator model is nonlinear which is linearised around the set point $P_{\text{Gen},0}$ with Eq.(7.23).

$$P_{\text{Gen}} = P_{\text{Gen},0} + \left. \frac{\partial P_{\text{Gen}}}{\partial \Omega_{\text{Gen}}} \right|_{\Omega_{\text{Gen},0}} \cdot \delta \Omega_{\text{Gen}} + \left. \frac{\partial P_{\text{Gen}}}{\partial \tau_{\text{Gen}}} \right|_{\tau_{\text{Gen},0}} \cdot \delta \tau_{\text{Rtr}} \quad (7.23)$$

Where,

$$\left. \frac{\partial P_{\text{Gen}}}{\partial \Omega_{\text{Gen}}} \right|_{\Omega_{\text{Gen},0}} = \eta_{\text{Gen}} \Omega_{\text{Gen},0}, \quad \left. \frac{\partial P_{\text{Gen}}}{\partial \tau_{\text{Gen}}} \right|_{\tau_{\text{Gen},0}} = \eta_{\text{Gen}} \tau_{\text{Gen},0} \quad (7.24)$$

Table 7.3.: Linearized generator EoM parameters by FAST

wind speed	Pitch angle	Generator speed	Mass matrix	Damping matrix	Disturbance matrix
U_{HubH}	β_{CP}	Ω_{Rtr}	$M _{OP}$	C	F_d
5 m/s	0°	7.51rpm	4.38e7	1.11e6	3.92e5
8 m/s	0°	9.16rpm	4.38e7	1.99e6	7.36e5
11.4 m/s	0°	12.1rpm	4.38e7	2.39e6	1.02e6
15 m/s	10.4°	12.1rpm	4.38e7	5.95e6	1.06e6
18 m/s	14.9°	12.1rpm	4.38e7	1.06e7	1.21e6
21 m/s	18.7°	12.1rpm	4.38e7	1.57e7	1.34e6
24 m/s	22.1°	12.1rpm	4.38e7	2.17e7	1.49e6

7.3.3. Tower first order fore-aft model

Wind flow creates the thrust force perpendicular to the rotor plane which affects the dynamics movement of turbine head (rotor and nacelle). The HAWT tower can be modelled

as a 1-mass damper-spring system as shown on Fig.7.3. Assuming no Yaw error during operation, the thrust force is only applying perpendicular to the rotor plane which results a fore-aft movement of the tower top. The tower fore-aft dynamics EoM is

$$m_{TWR}\ddot{d}_{TWR} + c_{TWR}\dot{d}_{TWR} + k_{TWR}d_{TWR} - f_T = 0 \quad (7.25)$$

Where, m_{TWR} is the modal mass of the tower, d_{TWR} , \dot{d}_{TWR} , \ddot{d}_{TWR} are the displacement, speed, and acceleration, k_{TWR} and c_{TWR} are spring and damping coefficient. Adding the linearized thrust force into the model, the EoM of the tower model is given as

$$\begin{aligned} m_{TWR}\Delta\ddot{d}_{TWR} + \left(c_{TWR} + \frac{\delta f_T}{\delta U}\right)\Delta\dot{d}_{TWR} + k_{TWR}\Delta d_{TWR} - \frac{\delta f_T}{\delta\Omega_{Rtr}}\Delta\Omega_{Gen} - \frac{\delta f_T}{\delta\Omega_{Rtr}}\Delta\Omega_{DT} \\ = \frac{\delta f_T}{\delta U}\Delta U + \frac{\delta f_T}{\delta\beta_{CP}}\Delta\beta_{CP} \end{aligned} \quad (7.26)$$

Let the states be defined as $x_{Tfa} = [d_{Tfa} \quad \dot{d}_{Tfa}]^T$, the EoM can be written as

$$\begin{aligned} \Delta\dot{x}_{Tfa} = \begin{bmatrix} 0 & 1 \\ -\frac{k_{TWR}}{M_{TWR}} & -\frac{c_{TWR} + \delta f_T / \delta U}{M_{TWR}} \end{bmatrix} \begin{bmatrix} d_{Tfa} \\ \dot{d}_{Tfa} \end{bmatrix} + \begin{bmatrix} 0 & 0 \\ \frac{\delta f_T / \delta\beta_{CP}}{M_{TWR}} & 0 \end{bmatrix} \begin{bmatrix} \Delta\beta_{CP} \\ \Delta\beta_{CP} \end{bmatrix} \\ + \begin{bmatrix} 0 \\ \frac{\delta f_T / \delta U}{M_{TWR}} \end{bmatrix} \Delta U + \begin{bmatrix} 0 \\ \frac{\delta f_T / \delta\Omega_{Rtr}}{M_{TWR}} \end{bmatrix} \Delta\Omega_{Gen} + \begin{bmatrix} 0 \\ \frac{\delta f_T / \delta\Omega_{Rtr}}{M_{TWR}} \end{bmatrix} \Delta\Omega_{DT} \end{aligned} \quad (7.27)$$

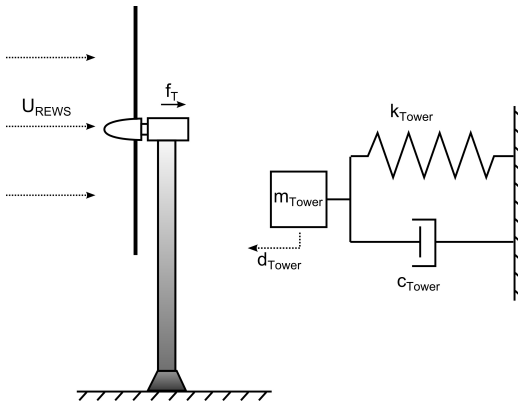


Fig. 7.3: The HAWT tower modelled as a 1-mass damper-spring system [92]

The linearized EoM parameters of tower model are given on Table.7.4.

Table 7.4.: Linear model parameters of tower by FAST

wind speed	Pitch angle	Rotor speed	Mass matrix	Damping matrix	Stiffness matrix	Disturbance matrix
U_{HubH}	β_{CP}	Ω_{Rtr}	$M _{OP}$	C	K	F_d
5 m/s	0°	7.51rpm	4.38e5	3.77e4	1.85e6	5.43e4
8 m/s	0°	9.16rpm	4.38e5	5.37e4	1.85e6	7.02e4
11.4 m/s	0°	12.1rpm	4.38e5	7.25e4	1.85e6	8.91e4
15 m/s	10.4°	12.1rpm	4.38e5	1.026e5	1.85e6	8.02e4
18 m/s	14.9°	12.1rpm	4.38e5	1.07e5	1.85e6	8.04e4
21 m/s	18.7°	12.1rpm	4.38e5	1.07e5	1.85e6	7.9e4
24 m/s	22.1°	12.1rpm	4.38e5	1.09e5	1.85e6	7.91e4

7.3.4. Drive-train model

Drive-train transfers the rotor torque to generator. It includes a low speed shaft connected to the rotor, a high speed shaft connected to generator, and a gearbox to convert the low rotor speed to high generator speed (Fig.7.4 Up). The drive-train properties are applied on low speed shaft within FAST [99]. It can be modelled as a 2-mass damper-spring model (Fig.7.4 down). The rotor and generator EoMs are given as

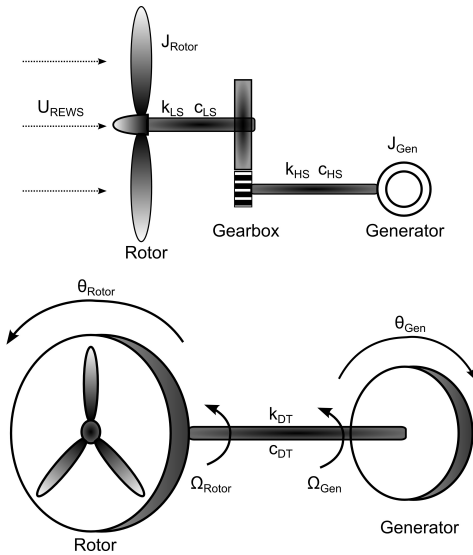


Fig. 7.4: Free body diagram of the HAWT drive-train (up), and the simplified 2-mass damper-spring model (Source: www.uwig.org)

$$J_{Rtr} \dot{\Omega}_{Rtr} = \tau_{Rtr} - k_{DT} \theta_{DT} - c_{DT} \Omega_{DT} \quad (7.28a)$$

$$N_{Gear}^2 J_{Gen} \dot{\Omega}_{Gen} = -N_{Gear} \tau_{Gen} + k_{DT} \cdot \theta_{DT} + c_{DT} \Omega_{DT} \quad (7.28b)$$

With $\dot{\Omega}_{Rtr} = \dot{\Omega}_{Gen} + \dot{\Omega}_{DT}$, $\Omega_{Rtr} = \Omega_{Gen} + \Omega_{DT}$. Where θ_{DT} , Ω_{DT} and $\dot{\Omega}_{DT}$ denotes the drive-train shaft torsion angle, angular speed, and acceleration. k and c are spring and damper coefficient, LS and HS represent the low speed shaft and high speed shaft. Therefore, the EoM of drive-train torsion is given as

$$\dot{\Omega}_{DT} + \left(\frac{c_{DT}}{J_{Rtr}} + \frac{c_{DT}}{N_{Gear}^2 J_{Gen}} \right) \Omega_{DT} + \left(\frac{k_{DT}}{J_{Rtr}} + \frac{k_{DT}}{N_{Gear}^2 J_{Gen}} \right) \theta_{DT} = \frac{\tau_{Rtr}}{J_{Rtr}} + \frac{\tau_{Gen}}{N_{Gear} J_{Gen}} \quad (7.29)$$

Adding the linearized rotor aerodynamic equation into the drive-train EoM, we get

$$\begin{aligned} \Delta \dot{\Omega}_{DT} + \left(\frac{c_{DT} - d\tau_{Rtr}/d\Omega_{Rtr}}{J_{Rtr}} + \frac{c_{DT}}{N_{Gear}^2 J_{Gen}} \right) \Delta \Omega_{DT} + \left(\frac{k_{DT}}{J_{Rtr}} + \frac{k_{DT}}{N_{Gear}^2 J_{Gen}} \right) \Delta \theta_{DT} \\ = \left[\frac{\delta\tau_{Rtr}/\delta\beta_{CP}}{J_{Rtr}} \quad -\frac{1}{N_{Gear} J_{Gen}} \right] \begin{bmatrix} \Delta\beta_{CP} \\ \Delta\tau_{Gen} \end{bmatrix} + \frac{\delta\tau_{Rtr}/\delta U}{J_{Rtr}} \Delta U + \frac{\delta\tau_{Rtr}/d\Omega_{Rtr}}{J_{Rtr}} \Delta \Omega_{Gen} \end{aligned} \quad (7.30)$$

Writing the equations into the state space representation as

$$\begin{aligned} \Delta \dot{x}_{DT} = & \begin{bmatrix} 0 & 1 \\ -\frac{k_{DT}}{J_{Rtr}} - \frac{k_{DT}}{N_{Gear}^2 J_{Gen}} & -\frac{c_{DT}}{J_{Rtr}} + \frac{\delta\tau_{Rtr}}{\delta\Omega_{Rtr}} \frac{1}{J_{Rtr}} - \frac{c_{DT}}{N_{Gear}^2 J_{Gen}} \end{bmatrix} \begin{bmatrix} \Delta\theta_{DT} \\ \Delta\Omega_{DT} \end{bmatrix} \\ & + \begin{bmatrix} 0 & 0 \\ \frac{d\tau_{Rtr}}{d\beta_{CP}} \frac{1}{J_{Rtr}} & 0 \end{bmatrix} \begin{bmatrix} \Delta\beta_{CP} \\ \Delta\beta_{Pitch} \end{bmatrix} + \begin{bmatrix} 0 \\ -\frac{1}{N_{Gear} J_{Gen}} \end{bmatrix} \Delta\tau_{Gen} + \begin{bmatrix} 0 \\ \frac{\delta\tau_{Rtr}/\delta U}{J_{Rtr}} \end{bmatrix} \Delta v \\ & + \begin{bmatrix} 0 \\ \frac{\delta\tau_{Rtr}/\delta\Omega_{Rtr}}{J_{Rtr}} \end{bmatrix} \Delta\Omega_{Gen} \end{aligned} \quad (7.31)$$

The drive-train parameters depending on different operation conditions (Table.7.5). The model is used for the design and analysis of the drive-train system of a wind turbine system with gearboxes. For a PMDD system without gearbox, due to the high stiffness, this model can be ignored.

Table 7.5.: Linearized EoM of drive-train model parameters by FAST

wind speed	Pitch angle	Rotor speed	Mass matrix	Damping matrix	Stiffness matrix	Disturbance matrix
U_{HubH}	β_{CP}	Ω_{Rtr}	$M _{OP}$	C	K	F_d
5 m/s	0°	7.51rpm	3.88e7	7.32e6	8.68e8	3.92e5
8 m/s	0°	9.16rpm	3.88e7	8.21e6	8.68e8	7.36e5
11.4 m/s	0°	12.1rpm	3.88e7	8.6e6	8.68e8	1.02e6
15 m/s	10.4°	12.1rpm	3.88e7	1.22e7	8.68e8	1.06e6
18 m/s	14.9°	12.1rpm	3.88e7	1.68e7	8.68e8	1.21e6
21 m/s	18.7°	12.1rpm	3.88e7	2.19e7	8.68e8	1.34e6
24 m/s	22.1°	12.1rpm	3.88e7	2.79e7	8.68e8	1.49e6

7.4. Wind turbine actuator model

7.4.1. Generator torque actuator model

Wind turbine generator uses electrical converters to control the torque as shown on Figure.7.5, two different generator systems are common used, DFIG and PMSG. In a grid connected WEC system, keeping the electrical power output stable is the motivation for the power control. The wind turbine converter uses electrical load as inputs to the generator. For simplification, assuming generator torque as a control input, therefore, the torque actuator model of the generator is modelled as a 1st order system

$$\dot{\tau}_{\text{Gen}} + \frac{1}{T_e} (\tau_{\text{ref}} - \tau_{\text{Gen}}) = 0 \quad (7.32)$$

Where τ_{ref} is the reference generator torque, T_e is the time constant for generator. In simulation, T_e is the torque command update rate. Let the generator torque state be $x_{\text{Gen}} = \tau_{\text{Gen}}$, write the EoM of generator torque actuator model in state space as

$$\Delta \dot{x}_{\text{Gen}} = \Delta \dot{\tau}_{\text{Gen}} = -\frac{1}{T_e} \Delta \tau_{\text{Gen}} + \frac{1}{T_e} \Delta \tau_{\text{ref}} \quad (7.33)$$

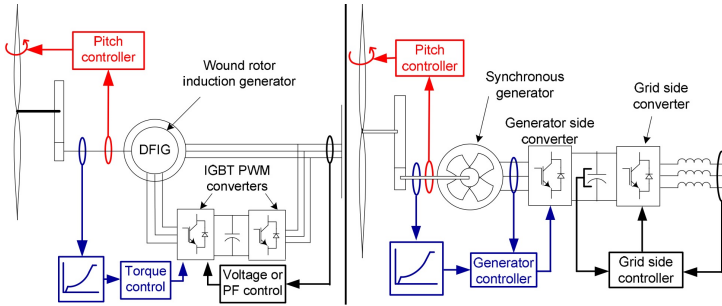


Fig. 7.5.: A DFIG generator system (left) and a PMSG generator system (right) [147]

7.4.2. Pitch actuator model

On a real VP-HAWT system, the blade pitch actuator system is either a hydraulic system or an electronic servo motors driven system. The dynamic motion of such system is relatively low and subject to some nonlinearity and constrains. The pitch actuator system can be modelled as a 2nd order dynamic system that the EoM can be written as

$$\ddot{\beta}_{\text{Pitch}} + 2\omega\zeta\dot{\beta}_{\text{CP}} + \omega^2 (\beta_{\text{CP}} - \beta_{\text{ref}}) = 0 \quad (7.34)$$

Where, ω is the undamped natural frequency, ζ is the damping factor of the pitch actuator, β_{ref} is the reference collective pitch angle. Let the collective pitch actuator states be $x_{\text{CP}} = [\beta_{\text{CP}} \ \dot{\beta}_{\text{CP}}]^T$, the EoM of pitch actuator model can be written in state space as

$$\Delta \dot{x}_{\text{CP}} = \begin{bmatrix} \Delta \dot{\beta}_{\text{CP}} \\ \Delta \ddot{\beta}_{\text{CP}} \end{bmatrix} = \begin{bmatrix} 0 & 1 \\ -\omega^2 & -2\zeta\omega \end{bmatrix} \begin{bmatrix} \Delta \beta_{\text{CP}} \\ \Delta \dot{\beta}_{\text{CP}} \end{bmatrix} + \begin{bmatrix} 0 & 0 \\ \omega^2 & 0 \end{bmatrix} \begin{bmatrix} \Delta \beta_{\text{ref}} \\ \Delta \tau_{\text{ref}} \end{bmatrix} \quad (7.35)$$

7.4.3. Dynamic wind model

The modelled wind fields have five parts: mean wind speed, turbulence, tower shadow, wind share and rotational sampling. Fig.7.6 shows the model block diagram [13].

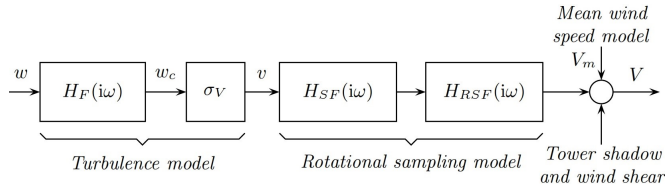


Fig. 7.6.: Block diagram of a TurbSim wind field model [13]

The mean wind speed is calculated in every time steps in medium and long term as

$$\bar{V}_m(t) = \sum_{i=1}^m A_i \cos(\omega_i t + \zeta_i) \quad (7.36)$$

Where ω_i is the discrete angular frequency, ζ_i is a stochastic variable uniformly distributed in $[-p, +p]$. A_i is the harmonic frequency amplitude which is given as

$$A_i = \frac{2}{p} \sqrt{\frac{1}{2} (S_V(\omega_i) + S_V(i+1)) (\omega_{i+1} - \omega_i)} \quad (7.37)$$

Where $S_V(\omega_i)$ is the power spectral density at ω_i . The large-band wind turbulence model is based on the Van der Hoven's model while von Karman's model is simulated for the short term component [43]. An example of the turbulence spectrum is given as

$$S_V(\omega_i) = \frac{k^2}{(1 + t_1^2 \omega_i^2)(1 + t_2^2 \omega_i^2)} \quad (7.38)$$

with k as the static gain which is given as

$$k \approx \sqrt{\frac{2p}{B \left(\frac{1}{2}, \frac{1}{3}\right)} \cdot \frac{\hat{T}_F}{T_s}} \quad (7.39)$$

Here T_s is the sampling period, B designates the beta function, T_F is the time constant of the shaping filter which is given as

$$\hat{T}_F = L/\bar{V}_m \tag{7.40}$$

Where L is the turbulence length scale, \bar{V}_m is the mean wind speed. t_1 and t_2 are the parameters as a function of mean wind speed. The wind turbulence model is described by the power spectrum which is characterized by the correlation length, turbulence intensity and the mean wind speed. The non-stationary turbulence component is modelled with a shaping filter with white noise. The transfer function of the shaping filter is given as Eq.(7.41) [13].

$$H_F(s) = \frac{k}{(1 + t_1s)(1 + t_2s)} \tag{7.41}$$

Fig.7.7 illustrates the parameters depends on the mean wind speed [67]. The rotational sampling model has two filters: a low pass filter gives a fictitious scalar wind speed for the entire rotor plane; an extra filter incorporated the rotation of the blades by amplifying the blades rotational frequency. Assuming e is the white noise, the turbulence wind can be described with a state space representation as Eq.(7.42) [67].

$$\begin{bmatrix} \dot{v} \\ \dot{\bar{v}} \end{bmatrix} = \begin{bmatrix} 0 & 1 \\ -\frac{1}{t_1t_2} & -\frac{t_1+t_2}{t_1t_2} \end{bmatrix} \begin{bmatrix} v \\ \bar{v} \end{bmatrix} + \begin{bmatrix} 0 \\ \frac{k}{t_1t_2} \end{bmatrix} e \tag{7.42}$$

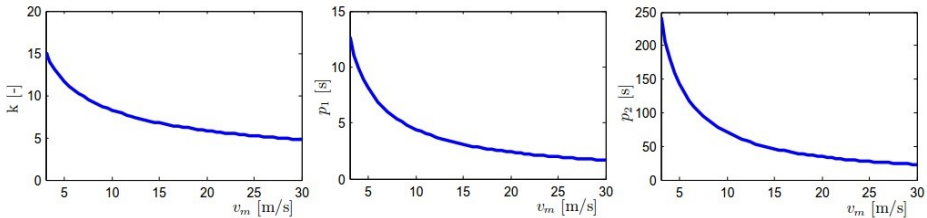


Fig. 7.7.: Parameters in the dynamic turbulence wind model ([67])

7.5. The combined reduced DOF numerical model of wind turbine

7.5.1. The nonlinear nominative model

The nonlinear system model can be represented as

$$\dot{x} = f(x, u, v) \tag{7.43}$$



Where $x \in R^N$ is the system states vector, $u \in R^M$ is the control inputs vector, $v \in R^O$ is the wind disturbance vector, $y \in R^P$ is the system outputs vector, $C \in R^{P \times N}$ is the state output matrix, \dot{x} is the deliverable of state x . Combining all different parts of turbine model to combine the full state model as Eq.(7.44).

$$J_{\text{tot}}\dot{\Omega}_{\text{Rtr}} + \tau_{\text{Gen}} - \tau_{\text{Rtr}} = 0 \quad (7.44a)$$

$$m_{\text{Twr}}\ddot{d}_{\text{Twr}} + c_{\text{Twr}}\dot{d}_{\text{Twr}} + k_{\text{Twr}}d_{\text{Twr}} - f_{\text{T}} = 0 \quad (7.44b)$$

$$N_{\text{Gear}}^2 J_{\text{Gen}}\dot{\Omega}_{\text{Gen}} + N_{\text{Gear}}\tau_{\text{Gen}} - k_{\text{DT}} \cdot \theta_{\text{DT}} - c_{\text{DT}}\Omega_{\text{DT}} = 0 \quad (7.44c)$$

$$\dot{\tau}_{\text{Gen}} + \frac{1}{T_e} (\tau_{\text{ref}} - \tau_{\text{Gen}}) = 0 \quad (7.44d)$$

$$\ddot{\beta}_{\text{CP}} + 2\zeta\omega\dot{\beta}_{\text{CP}} + \omega^2 (\beta_{\text{CP}} - \beta_{\text{ref}}) = 0 \quad (7.44e)$$

$$\dot{\theta}_{\text{Rtr}} - \Omega = 0 \quad (7.44f)$$

Where $\dot{\Omega}_{\text{Rtr}} = \dot{\Omega}_{\text{Gen}} + \dot{\Omega}_{\text{DT}}$, $\Omega_{\text{Rtr}} = \Omega_{\text{Gen}} + \Omega_{\text{DT}}$. Eq.(7.44a) is the second order equation for the rotational dynamics of rotor. Eq.(7.44b) represents the tower fore-aft dynamics. Eq.(7.44c) shows the drive-train torsion dynamics. Eq.(7.44d) and (7.44e) represent the generator and collective pitch actuator model. Define the control inputs vector as

$$u = [\beta_{\text{ref}} \quad \tau_{\text{ref}}]^T \quad (7.45)$$

The wind disturbance inputs vector is

$$v = [v_m + v_t] \quad (7.46)$$

Where, v_m and v_t are the mean and turbulent wind speed. Here a full state feedback is used for design of RHC controller. The system states are given as

$$z = x = [\Omega_{\text{Gen}} \quad \Delta\theta_{\text{DT}} \quad \Delta\dot{\theta}_{\text{DT}} \quad d_{\text{Bld}} \quad \dot{d}_{\text{Bld}} \quad d_{\text{Twr}} \quad \dot{d}_{\text{Twr}}]^T \quad (7.47)$$

Where the available states of the HAWT are rotor speed, drive-train torsion angular displacement and speed, 1st order blade flap-wise displacement and speed, and 1st order tower fore-aft displacement and speed. Considering the pitch actuator dynamics and electrical generator torque dynamic, the pitch angle and rates and generator torque are added into the model as controllable states which are

$$x_{\text{ctr}} = [\beta_{\text{CP}} \quad \dot{\beta}_{\text{CP}} \quad \tau_{\text{Gen}}]^T \quad (7.48)$$

7.5.2. Linear numerical model

The system model can be represented with a state space format as

$$\dot{x} = Ax + Bu + \Gamma u_D \quad (7.49)$$

Where $x \in R^N$ is the system states vector, $u \in R^M$ is the control inputs vector, $v \in R^O$ is the wind disturbance inputs vector, $y \in R^P$ is the system outputs vector, $A \in R^{N \times N}$ is the state parametric matrix, $B \in R^{N \times M}$ is the system control inputs gain matrix, $\Gamma \in R^{N \times O}$ is the disturbance inputs gain, $C \in R^{P \times N}$ is the state output matrix, \dot{x} is the deliverable of x .

The linearisation of the nonlinear model can be done by the FAST linearisation analysis which is useful for developing the full linear representation of the state matrices for the controller designs. The linearisation process consist two steps: computing a periodic steady state operating point condition for the DOFs and numerically linearised the FAST model at this operating point to form periodic state matrices. The output state matrices is averaged for non-periodic or time invariant controls development [99]. Fig.7.8, 7.9 show the linearisation parameters at different operation points: $\left. \frac{\delta \tau_{Rtr}}{\delta U} \right|_{U_0}$, $\left. \frac{\delta \tau_{Rtr}}{\delta \Omega_{Rtr}} \right|_{\Omega_{Rtr,0}}$, $\left. \frac{\delta \tau_{Rtr}}{\delta \beta_{CP}} \right|_{\beta_{Pitch,0}}$.

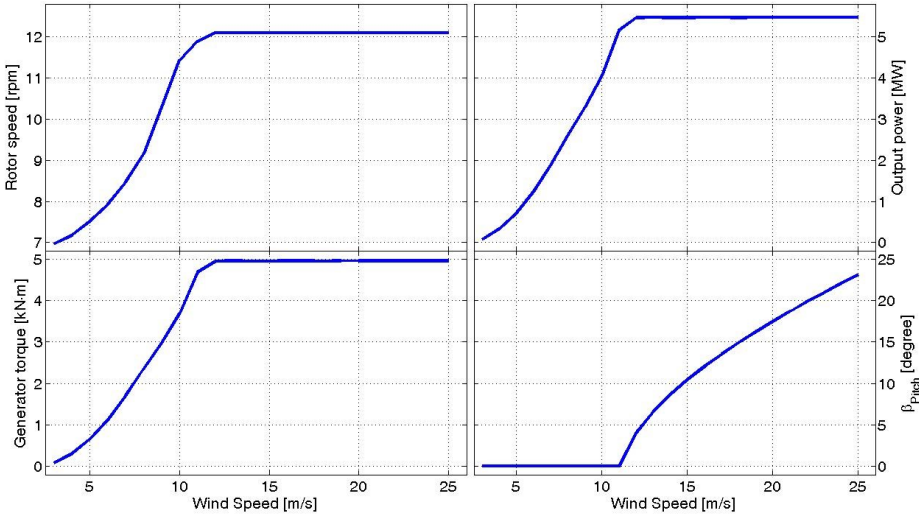


Fig. 7.8.: States output of a FAST wind turbine model with different wind speed inputs

Here, a 2-DOF linearized model with the tower fore-aft and rotor rotation states is discussed. The DOFs of blades are not added into the model since the collective pitch system does not benefit to reduce the loads on blades. For a PMDD wind turbine system, the drive-train dynamics can be ignored. However, when simulating a DFIG turbine with gearbox, the drive-train can be added into the model. The detailed model with adding drive-train and blade flapwise DOFs are discussed in Appendix A.3.4. The system states are defined as

$$\begin{aligned} \Delta x_{2DOF} &= \left[\Delta x_{Gen} \quad \Delta x_{Tfa} \quad \Delta x_{CP} \quad \Delta x_{GenTq} \right]^T \\ &= \left[\Delta \Omega_{Gen} \quad \Delta d_{Tfa} \quad \Delta \dot{d}_{Tfa} \quad \Delta \beta_{CP} \quad \Delta \dot{\beta}_{CP} \quad \Delta \tau_{Gen} \right]^T \end{aligned} \quad (7.50)$$

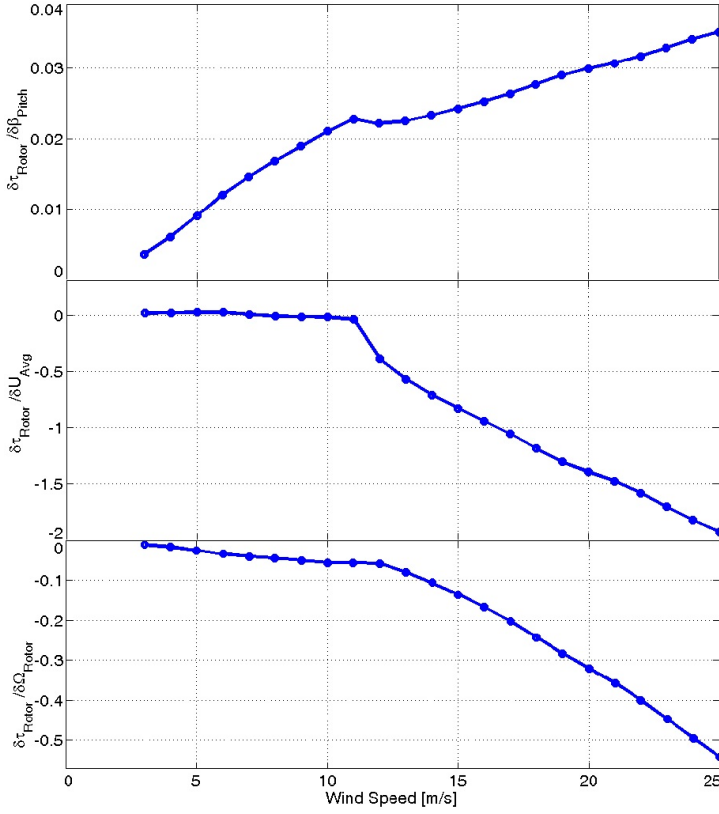


Fig. 7.9.: Different model parameters of wind turbine at different wind speeds

The tower fore-aft and generator dynamics model in state space format are given as

$$\Delta\dot{x}_{Tfa} = \begin{bmatrix} 0 & 1 \\ -\frac{k_{Twr}}{M_{Twr}} & -\frac{c_{Twr} + df_T/dU}{M_{Twr}} \end{bmatrix} \Delta x_{Tfa} + \begin{bmatrix} 0 & 0 \\ \frac{df_T/d\beta_{CP}}{M_{Twr}} & 0 \end{bmatrix} \begin{bmatrix} \Delta\beta_{CP} \\ \Delta\dot{\beta}_{CP} \end{bmatrix} \quad (7.51a)$$

$$+ \begin{bmatrix} 0 \\ \frac{df_T/dU}{M_{Twr}} \end{bmatrix} \Delta u_D + \begin{bmatrix} 0 \\ \frac{df_T/d\Omega_{Rtr}}{M_{Twr}} \end{bmatrix} \Delta\Omega_{Gen}$$

$$\Delta\dot{x}_{Gen} = \frac{d\tau_{Rtr}/d\Omega_{Rtr}}{J_{tot}} \Delta x_{Gen} + \frac{d\tau_{Rtr}/d\beta_{CP}}{J_{tot}} \Delta\beta_{CP} + \frac{d\tau_{Rtr}/dU}{J_{tot}} \Delta u_D - \frac{d\tau_{Rtr}/dU}{J_{tot}} \Delta\dot{x}_{Tfa} \quad (7.51b)$$

Then, the 2-DOF tower fore-aft/generator 6-state linearized model in state space is given as

$$\Delta\dot{x}_{2DOF} = A_{2DOF}\Delta x_{2DOF} + B_{2DOF}\Delta u + \Gamma_{2DOF}\Delta u_D \quad (7.52)$$

where,

$$A_{2\text{DOF}} = \begin{bmatrix} A_{\text{Rtr}} & A_{\text{Rtr-Tfa}} & A_{\text{Rtr-}\beta} & A_{\text{Rtr-}\tau} \\ A_{\text{Tfa-Gen}} & A_{\text{Tfa}} & A_{\text{Tfa-}\beta} & 0 \\ 0 & 0 & A_{\beta} & 0 \\ 0 & 0 & 0 & A_{\tau} \end{bmatrix} \quad (7.53a)$$

$$B_{2\text{DOF}} = \begin{bmatrix} 0 \\ 0 \\ B_{\beta} \\ B_{\tau} \end{bmatrix}, \Gamma_{2\text{DOF}} = \begin{bmatrix} \Gamma_{\text{Rtr}} \\ \Gamma_{\text{Tfa}} \\ 0 \\ 0 \end{bmatrix} \quad (7.53b)$$

with,

$$A_{\text{Rtr}} = \frac{d\tau_{\text{Rtr}}/d\Omega_{\text{Rtr}}}{J_{\text{tot}}}, A_{\text{Rtr-Tfa}} = \begin{bmatrix} 0 & \frac{d\tau_{\text{Rtr}}/d\beta_{\text{CP}}}{J_{\text{tot}}} \end{bmatrix} \quad (7.54a)$$

$$A_{\text{Rtr-}\beta} = \begin{bmatrix} \frac{d\tau_{\text{Rtr}}/d\beta_{\text{CP}}}{J_{\text{tot}}} & 0 \end{bmatrix}, A_{\text{Rtr-}\tau} = -\frac{1}{J_{\text{tot}}}, A_{\text{Tfa-Gen}} = \begin{bmatrix} 0 \\ \frac{\delta f_{\text{T}}/\delta\Omega_{\text{Rtr}}}{M_{\text{Twr}}} \end{bmatrix} \quad (7.54b)$$

$$A_{\text{Tfa}} = \begin{bmatrix} 0 & 1 \\ -\frac{k_{\text{Twr}}}{M_{\text{Twr}}} & -\frac{c_{\text{Twr}} + \delta\tau_{\text{T}}/\delta U}{M_{\text{Twr}}} \end{bmatrix}, A_{\text{Tfa-}\beta} = \begin{bmatrix} 0 & 0 \\ \frac{\delta f_{\text{T}}/\delta\beta_{\text{CP}}}{M_{\text{Twr}}} & 0 \end{bmatrix} \quad (7.54c)$$

$$A_{\beta} = \begin{bmatrix} 0 & 1 \\ -\omega^2 & -2\omega\zeta \end{bmatrix}, A_{\tau} = -\frac{1}{T_e}, B_{\beta} = \begin{bmatrix} 0 & 0 \\ \omega^2 & 0 \end{bmatrix} \quad (7.54d)$$

$$B_{\tau} = \begin{bmatrix} 0 & \frac{1}{T_e} \end{bmatrix}, \Gamma_{\text{Rtr}} = \frac{\delta\tau_{\text{Rtr}}/\delta U}{J_{\text{tot}}}, \Gamma_{\text{Tfa}} = \begin{bmatrix} 0 \\ \frac{\delta\tau_{\text{Rtr}}/\delta U}{J_{\text{Rtr}}} \end{bmatrix} \quad (7.54e)$$

7.5.3. Piecewise Linear (Affine) model

In the previous sections, linearized models have been discussed. However, due to the strong nonlinearity of the model, the linearized parameters are different at different set points. Therefore, to overcome the nonlinearity of turbine dynamics, a discrete time Piecewise Linear (system) (PWL) model which obtains multiple linear models depending on the wind conditions is used. Then the PWL model in state space is

$$\begin{cases} \Delta\dot{x} = A_i\Delta x + B_i\Delta u + \Gamma_i\Delta u_{\text{D}} \\ y = C_i\Delta x + D_i\Delta u + D_{d,i}\Delta u_{\text{D}} \end{cases}, \text{ iff } U_{\text{REW}}^* \in R_i \quad (7.55)$$

Where R_i represent the region i . In order to obtain an overview through the entire operation modes, an affine model is beneficial for the controller design. The formulation of a standard Piecewise Affine (system) (PWA) model is given as

$$\dot{x} = A_i x + B_i u + f_i, \text{ iff } (x, u) \in R_i \quad (7.56a)$$

$$y = C_i x + D_i u + g_i, \text{ iff } (x, u) \in R_i \quad (7.56b)$$

Since $\Delta \dot{x} = \dot{x} - \dot{x}^*$, $\Delta x = x - x^*$, $\Delta u = u - u^*$, $\Delta u_D = u_D - u_D^*$, $\Delta y = y - y^*$. Where $*$ denotes the set point where the linearization is applied. Therefore,

$$\begin{aligned} & \begin{cases} \Delta \dot{x} = A_i \Delta x + B_i \Delta u + \Gamma_i \Delta u_D \\ \Delta y = C_i \Delta x + D_i \Delta u + D_{d,i} \Delta u_D \end{cases} \\ \rightarrow & \begin{cases} \dot{x} - \dot{x}^* = A_i(x - x^*) + B_i(u - u^*) + \Gamma_i(u_D - u_D^*) \\ y - y^* = C_i(x - x^*) + D_i(u - u^*) + D_{d,i}(u_D - u_D^*) \end{cases} \end{aligned} \quad (7.57)$$

Which gives

$$\begin{cases} \dot{x} = A_i x + B_i u + \Gamma_i u_D + f_i \\ y = C_i x + D_i u + D_{d,i} u_D + g_i \end{cases}, \quad \text{iff } U_{\text{REW}}^* \in R_i \quad (7.58)$$

Where the affine terms are defined as the system dynamics function at the linearization points, $f_i = \dot{x}^* - A_i x^* - B_i u^* - \Gamma_i u_D^*$, $g_i = y^* - C_i x^* - D_i u^* - D_{d,i} u_D^*$. The PWA system can be modelled with Multi-Parametric Toolbox (MPT) or via modelling language YALMIP [115] or HYSDEL [176].

7.6. Wind filed modelling

A stochastic inflow turbulence simulation tool TurbSim developed by NREL is used for simulation. TurbSim numerically simulate time series of the three component wind vectors at points in a 2D vertical rectangular grid fixed in space to generate full space wind fields (Fig.7.10). The TurbSim output can be used as input into the AeroDyn based simulations.

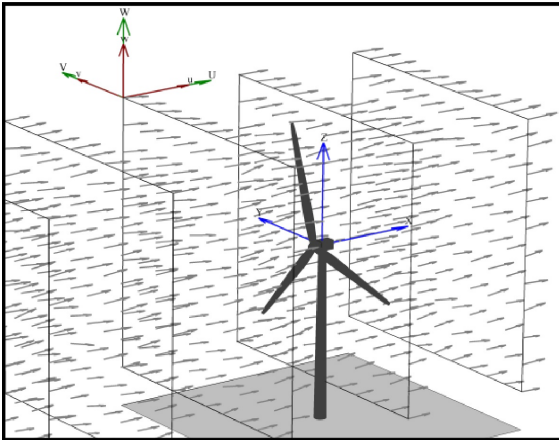


Fig. 7.10: Wind field simulation with TurbSim [95]

AeroDyn is an aerodynamics module for designing of HAWT, which interfaces with different dynamics analysis packages (such as FAST, ADAMS, SIMPACK, and FEDEM) for aero-elastic analysis of HAWT models. AeroDyn calculates aerodynamic lift drag, and pitching moment of airfoil sections along the turbine blades with the information from

input files on turbine geometry, as well as data from the aero-elastic simulator such as operating condition, turbine geometry, blade-element velocity, location and wind inflow, to calculate forces for each blades segment. It uses both BEM theory and generalized dynamic wake theory for calculating the effects of turbine wake. Detailed theory behind AeroDyn can be found in the AeroDyn theory guide [128]. Fig.7.11 illustrates the simulation process with TurbSim and AeroDyn.

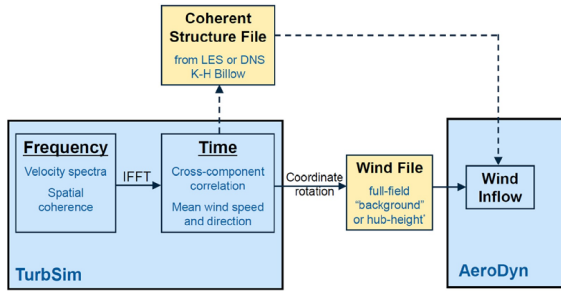


Fig. 7.11: Block diagram of TurbSim simulation, a frequency domain wind field is generated and transformed to time domain wind field compatible to AeroDyn [128]

7.6.1. Lidar measurement simulation

In chapter 4, a Lidar simulator for the Lidar system design purpose is discussed. To prepare the wind signal measured by a Lidar system to be used for the controller, Lidar measurement simulators have been designed by various researchers. In this thesis, the wind signal for pitch controller is generated by the Lidar simulator designed by E. Simley [160]. The Lidar simulator can simulate the commercial ZephIR CW Lidar for measuring at one single distance or the WindCube pulse Lidar for measuring up to 5 ranges simultaneously. Furthermore, the beam can be one beam or two beams focusing on a fixed position at the hub height or one or three beams which scans the field as the rotor rotation.

Lidar measures the LOS wind speed which is the combination of (u,v,w) wind speeds. The detected radial wind velocity is given as

$$U_{\text{LOS}} = u \cos \theta + v \sin \theta \sin \psi + w \sin \theta \cos \psi \quad (7.59)$$

Where θ is the angle between the Lidar beam and wind direction, ψ is the blade azimuth angle. Assuming $v = w = 0$, the estimated longitudinal wind velocity vector u is given as

$$\hat{u} = \frac{v_{\text{LOS}}}{\cos \theta} \quad (7.60)$$

Lidar measures the wind speed along the LOS of measurement beam with the weighting function $RWF(F, R)$ where F is the focus distance along LOS, R is the measurement range. Therefore, the wind speed measured at a distance F is determined as

$$v_{\text{LOS}}(F) = \int_0^{\infty} v_r(R) RWF(F, R) dR \quad (7.61)$$

Where $v_r(R)$ is the radial wind velocity at the range R along the LOS direction. For a CW Lidar the range weighting function is given as

$$\text{RWF}_{\text{CW}}(F, R) = \begin{cases} \frac{K_N}{R^2 + (1 - R/F)^2 R_R^2}, & \text{if } R \geq 0 \\ 0, & \text{else} \end{cases} \quad (7.62)$$

Where $R_R = \pi w_0^2 / \lambda$ is the Rayleigh range, w_0 is the beam waist radius at e^{-2} intensity, K_N is a normalizing constant. The weighting function of a pulsed Lidar system is given as

$$\text{RWF}_{\text{Pulse}}(F, R) = \frac{1}{2\Delta p} \left\{ \text{Erf} \left(\frac{R - F + \Delta p/2}{r_p} \right) - \text{Erf} \left(\frac{R - F - \Delta p/2}{r_p} \right) \right\} \quad (7.63)$$

Where, $\text{Erf}(\cdot)$ is the error function, Δp is the range gate, r_p is the e^{-1} half width of the pulse, $r_p = \Delta r/2\sqrt{\ln(2)}$, Δr is the full width at half maximum pulse width. Then, the range weighting function of our new approach is discussed at chapter 4 which is given as

$$\text{RWF}_{\text{New}}(F, R) = \frac{\pi^2 w_0^4}{\pi^2 w_0^4 + \lambda^2 (z - F)^2} \cdot \exp \left(-\frac{\pi \Delta v_0}{c} \cdot 2 |z - R| \right) \quad (7.64)$$

The Lidar simulator performs this range weighting average process. In the terms of turbulence wind, Lidar naturally capture the lower part of the frequency spectrum of the wind. To apply the Lidar measurement into control simulations, a so called "Taylor's frozen turbulence hypothesis" approach is applied [172]. Fig.7.12 shows the definition of "Taylor's hypothesis", that an eddy with a diameter of 100m has a temperature difference of 5°C between the front and back side (a). The same eddy 10 seconds later, is blown downwind at a wind speed of 10 m/s (b). Here, a wind speed turbulence structure is spatial domain is unchanging during the transportation of the eddy.

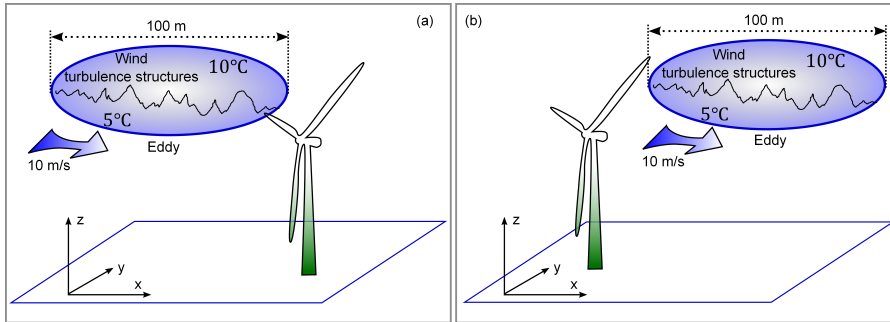


Fig. 7.12.: Taylor's hypothesis example

Applying this concept into Lidar simulation, the measured wind fields at measurement position after passing a distance z_{Range} to reach the wind turbine, wind filed remains

the same. Most of the Lidar simulators designed for the wind turbine preview control applications based on this Taylor's hypothesis. However, as discussed on previous chapters, the wind evolution effects inside of the upstream induction zone changes the mean wind speed and the turbulence characteristic. Driven by the needs of more accurate Lidar measurement simulation for preview controller design of wind turbines, recently some researches are focused on unfrozen the Taylor's hypothesis in a Lidar simulator design. L. Tasca summarized the unfrozen method on his master thesis [171]. The mathematical model for unfrozen the turbulence is described by Kirstensen theory [108] which provides a coherence value as a function of frequencies for determining the transition from one wind history to another. The coherence function is suggested by Pielke and Panofsky [141] to have a form as Eq.(7.65).

$$\text{coh}(f) = \exp\left(-a \frac{fD}{U_0}\right) \quad (7.65)$$

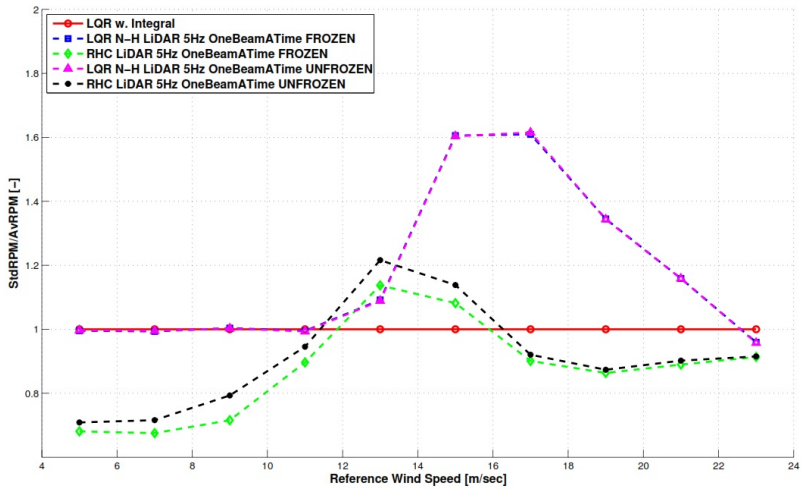
where f is the frequency, U_0 is the mean wind speed, D is the displacement between two points in space, a is a dimensionless 'decay parameter' of the order 10. As shown on the results (Fig.7.13) by L. Tasca, the Lidar assisted predictive control with unfrozen Lidar simulator does not show much advantages [171].

7.7. Summary and conclusion

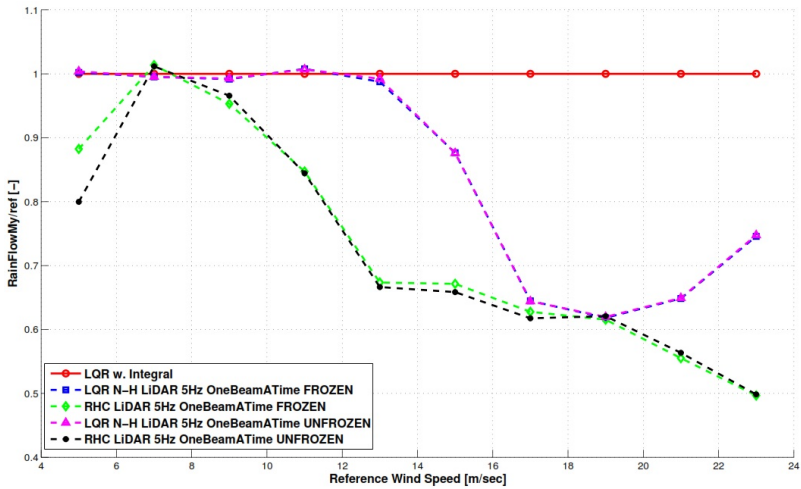
In this chapter, an introduction and theoretical background of wind turbine model are discussed. The turbine model used in this work is based on the NREL 5-MW reference wind turbine which is well documented by Jonkmann et.al. as a FAST model [98]. The FAST model is implemented into Simulink via an S-function link to simulate the reaction of a real wind turbine. The FAST model has 24 DOFs for a three-bladed wind turbine which can be activated or deactivated by users.

For the RHC controller design, the design of numerical nominative reduced models are documented. The main DOFs of the nominative model considered in this thesis are aerodynamics model (rotor rotation), the rotation dynamics model of generator, and tower fore-aft oscillation model. The drive-train torsion dynamics model, blade flapwise model, and pitch and generator torque models are discussed as well. Depending on the objective of controller design, those sub-models can be combined freely. For example with a PMDD wind turbine system, the drive-train model can be ignored due to the high stiffness of PMDD system drive-trains. For an individual pitch controller design, the dynamics model of pitch flapwise deflection, even the edgewise deflection can be added. However, with a collective pitch controller design, those information are not necessary normally.

In section.7.5 and Appendix.A.3, different model combinations and the linearized model parameter matrix are given in detail.



(a) Rotor rotational speed



(b) Generator torque

Fig. 7.13.: Simulation results of the standard deviation of rotor rotational speed and generator torque for predictive control with frozen and unfrozen Lidar simulator normalized to the LQR control method without Lidar [171]

8. Active pitch control system design

As briefly discussed in previous chapters, wind turbines are designed for 20 years lifetime under various environmental conditions. The wind shear and turbulence cause periodical torque fluctuations and bending moments on the turbine structures. Conventional turbine pitch controllers are operating above rated wind speed to minimize the rotation speed error of generator to the rated speed.

In this chapter, an optimal predictive control approach based on the 2-DOF FF/FB method is designed with the FF term designed as a RHC to take the wind preview information into account. The standard 2-DOF FF/FB control is based on model inverse FF design which is described in Section.3.4.2. However, this method cannot take system constraints into account. The full states feedback based RHC control is capable for considering the system constraints. However, due to the complex design, there are still difficulties for applying into industrial applications. The new 2-DOF RHC/FB control approach is based on a RHC method to design the FF term which is capable to take system constrain into account and it is an optimal based control (Fig.8.1).

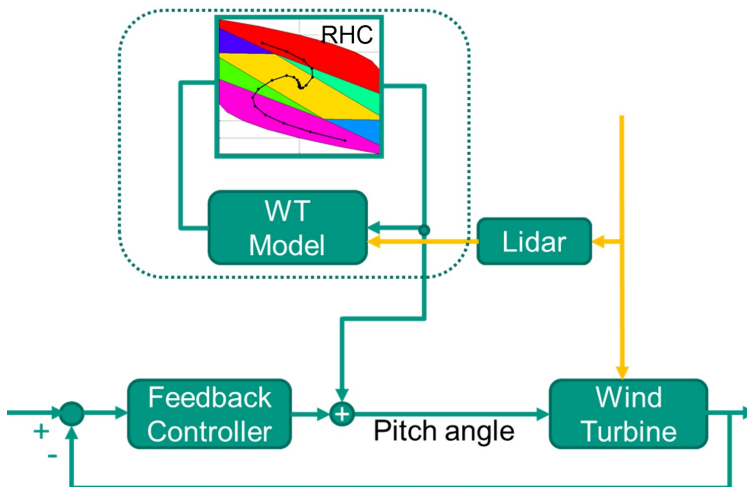


Fig. 8.1.: 2DOF RHC/FB preview control for wind turbine active pitch system

In this chapter, details of the wind turbine and wind field modelling, the 2-DOF RHC/FB controller design, and the evaluation based on Simulink simulation environment with a nonlinear wind turbine model designed by the FAST tool are discussed.

8.1. Benchmark control system design

For simplification, in this dissertation only the collective pitch control (CPC) based on the linear models (described at Section.7.5.2) is discussed. The designed controllers are 2-DOF RHC/FB with Lidar measurements as preview information. For the validation of controller, a PI FB controller based on the work by E.A. Bossanyi [17] and J.Jonkman [98] and a 2DOF model inversed FF/FB controller based on the work by F. Dunne [53], N.Wang [181] and D.Schlipf [155] are designed and applied.

The objectives of the active pitch controller are to maximize the energy capture, minimize the dynamic mechanical loads, and keep the power quality to comply with interconnection standards. Here the major objective is to reduce the mechanical loads, which lead to the fatigue damage on several components, in order to increase the WECS lifetime. However, keeping the maximization of energy capture during the design of controller is important. There are two different mechanical loads: static loads, which are caused by the interaction with the mean wind speed; and dynamic loads, which are induced by the spatial and temporal fluctuation of the wind field. Dynamic loads by the wind fluctuation are more important from the control point of view.

8.1.1. Collective pitch feedback control

PI(D) FB controllers are widely used for industrial wind turbine control applications. A classical PID controller can be written with the Laplace variable s as

$$u = \left(K_P + \frac{K_I}{s} + \frac{K_D s}{1 + st} \right) e \quad (8.1)$$

Where K_P , K_I , and K_D are the PID control gain, e is the system error input, t is time constant to prevent the derivative term from becoming large at high frequency. As shown on Fig.7.2, the controller is split into generator torque controller, blade pitch controller, and yaw controller. In this thesis, I assume the yaw angle is perfect aligned, therefore, yaw control is disabled. The industrial turbine controller uses torque control below rated wind speed, and the pitch control up the rated wind speed. The control objective of the torque controllers below the rated wind speed is to maximize the power coefficient C_P to keep the output power maximal.

$$\tau_{Gen} = \frac{\pi \rho R_{Rtr}^5 C_P}{2 \lambda^3 N_{Gear}^3} \Omega_{Gen}^2 \quad (8.2)$$

Where τ_{Gen} is the generator torque, ρ is the air density, λ is the tip speed ratio, N_{Gear} is the gear ratio, Ω_{Gen} is the generator rotation speed.

In practice, the generator torque control can be separated into 3 main regions and 2 transition regions (Fig.8.2). In region 1 below the cut-in wind speed, generator torque is zero. Region 1.5 is a transition between region 1 and 2, where torque changes from zero until the maximum C_P . In region 2, torque is tracking the optimal C_P curve. Region 2.5 is a transition region between region 2 and 3 to limit tip speed at rated power. In region 3, the blade pitch

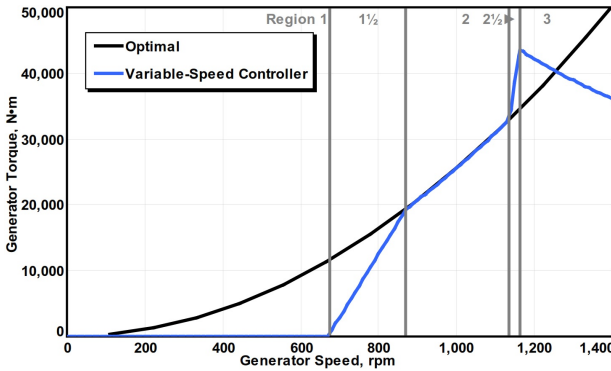


Fig. 8.2: Generator torque of variable speed wind turbines [98]

control system takes over to keep generator in a constant speed. As shown on Fig.8.3, the torque controller selects different operation regions for controlling the generator torques.

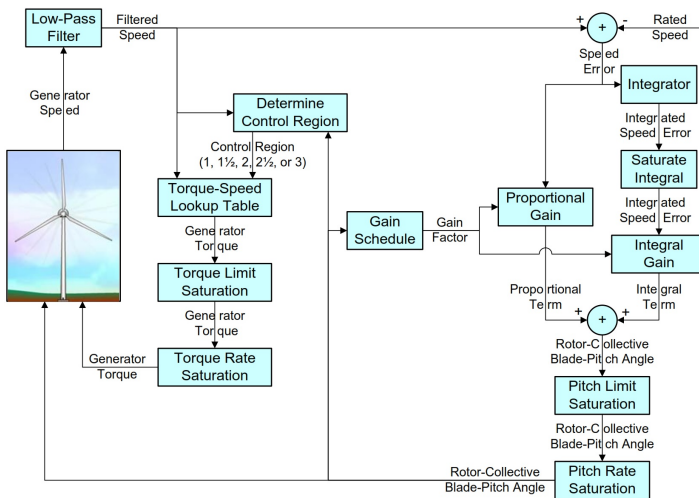


Fig. 8.3: A FB CP controller for wind turbine pitch system [98]

The pitch control is designed based on 1-DOF system for region 3 to keep the generator speed at the rated speed (1173.7 rpm). The EoM is given as

$$\tau_{Rt} - N_{Gear} \tau_{Gen} = \left(J_{Rt} + N_{Gear}^2 J_{Gen} \right) \frac{d}{dt} (\Omega_{Rt,0} + d\Omega_{Rt}) = J_{DT} \Delta \dot{\Omega}_{Rt} \quad (8.3)$$

Where the N_{Gear} is the gear ratio of the gearbox (for the PMDD the $N_{Gear} = 1$), τ_{Rt} is the aerodynamic torque of the low speed shaft, τ_{Gen} is the torque on high speed shaft, J_{Rt} is the rotor inertia, $\Omega_{Rt,0}$ is the low speed shaft reference speed, $d\Omega_{Rt}$ is the perturbation of

the low speed shaft, t is the time, $\Delta\dot{\Omega}_{\text{Rtr}}$ is the low-speed shaft rotational acceleration. In Region 3, the generator and rotor is working at the constant power condition,

$$\tau_{\text{Gen}} = \frac{P_0}{N_{\text{Gear}} \cdot \Omega_{\text{Rtr}}}, \quad \tau_{\text{Rtr}} = \frac{P(\beta_{\text{CP}} \Omega_{\text{Rtr},0})}{\Omega_{\text{Rtr},0}} \quad (8.4)$$

here P is mechanical power, P_0 is rated power, $\Omega_{\text{Rtr},0}$ is rated rotor speed at 12.1 r/min, β_{CP} is collective pitch angle. Then, expand the equation with Taylor series, we get

$$\tau_{\text{Gen}} \approx \frac{P_0}{N_{\text{Gear}} \cdot \Omega_{\text{Rtr},0}} + \frac{P_0}{N_{\text{Gear}} \cdot \Omega_{\text{Rtr},0}^2} \Delta\Omega_{\text{Rtr}} \quad (8.5a)$$

$$\tau_{\text{Rtr}} \approx \frac{P_0}{\Omega_{\text{Rtr},0}} + \frac{1}{\Omega_{\text{Rtr},0}} \left(\frac{\partial P}{\partial \beta} \right) \Delta\beta \quad (8.5b)$$

here $\Delta\beta$ is a small perturbation of the blade pitch angles. The PID pitch controller regulates the rotor speed, with the combination of the proportion and integration parts to get the perturbation of the pitch angle. The PI controller is given as:

$$\Delta\beta = K_P N_{\text{Gear}} \cdot \Delta\Omega_{\text{Rtr}} + K_I \int N_{\text{Gear}} \Delta\Omega_{\text{Rtr}} dt \quad (8.6)$$

We assume the azimuth angle of the rotor is φ , then

$$\dot{\varphi} = \Delta\Omega_{\text{Rtr}} \quad (8.7)$$

Therefore, the EoM for the rotor speed error can be written as

$$J_{\text{DT}} \ddot{\varphi} + \left(\frac{K_P N_{\text{Gear}}}{\Omega_{\text{Rtr},0}} \left(-\frac{\partial P}{\partial \beta} \right) - \frac{P_0}{\Omega_{\text{Rtr},0}^2} \right) \dot{\varphi} + \frac{N_{\text{Gear}} K_I}{\Omega_{\text{Rtr},0}} \left(-\frac{\partial P}{\partial \beta} \right) \varphi = 0 \quad (8.8)$$

Reforming the system with the damping ζ and natural frequency ω_n as

$$\ddot{\varphi} + 2\omega_n \zeta \dot{\varphi} + \omega_n^2 \varphi = 0 \quad (8.9)$$

Where

$$\omega_n = \sqrt{\frac{K}{J_{\text{DT}}}}, \quad \zeta = \frac{D}{2J_{\text{DT}}\omega_n} \quad (8.10)$$

With $D = \frac{K_P N_{\text{Gear}}}{\Omega_{\text{Rtr},0}} \left(-\frac{\partial P}{\partial \beta} \right) - \frac{P_0}{\Omega_{\text{Rtr},0}^2}$, $K = \frac{N_{\text{Gear}} K_I}{\Omega_{\text{Rtr},0}} \left(-\frac{\partial P}{\partial \beta} \right)$, where in an active pitch to feather HAWT, $\partial P / \partial \beta$ is negative in Region 3. Therefore, the control gain is positive. However, the $-P_0 / \Omega_{\text{Rtr},0}^2$ term introduces a negative damping. For pitch controller design, M. Hansen

et. al. suggested to neglect the negative damping factor to give the natural frequency and damping as $\omega_n = 0.6 \text{ rad/s}$, $\xi = 0.6 \sim 0.7$ [69].

$$K_P = \frac{2J_{DT}\Omega_{Rtr,0}\xi\omega_n}{N_{Gear}} \left(-\frac{\partial P}{\partial \beta} \right), \quad K_I = \frac{J_{DT}\Omega_{Rtr,0}\omega_n^2}{N_{Gear}} \left(-\frac{\partial P}{\partial \beta} \right) \quad (8.11)$$

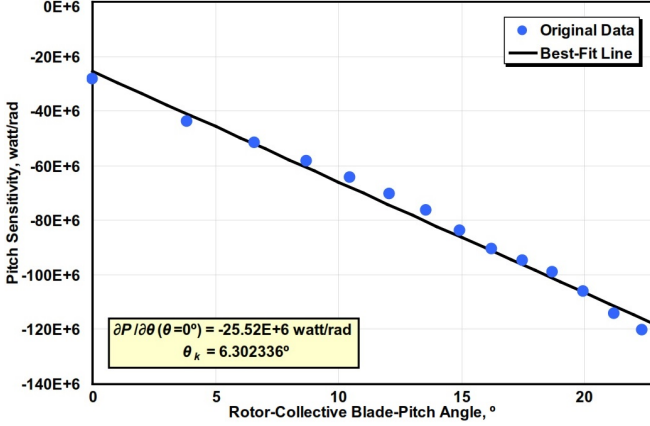


Fig. 8.4: Pitch sensitivity in Region 3 [98]

Therefore, the sensitivity of aerodynamic power to the rotor collective blade pitch $\partial P/\partial \beta$ is defining the PI gains. For the NREL 5-MW baseline offshore wind turbine, Fig.8.4 shows the pitch sensitivity which varies rather linearly depending on the pitch angle [98]. Applying the linear equation of the pitch sensitivity into the PI gain for the gain scheduling on blade pitch angle as

$$K_P(\beta) = \frac{2J_{DT}\Omega_{Rtr,0}\xi\omega_n}{N_{Gear}} \left[-\frac{\partial P}{\partial \beta}(\beta = 0) \right] GK(\beta) \quad (8.12a)$$

$$K_I(\beta) = \frac{J_{DT}\Omega_{Rtr,0}\omega_n^2}{N_{Gear}} \left[-\frac{\partial P}{\partial \beta}(\beta = 0) \right] GK(\beta) \quad (8.12b)$$

Where $GK(\beta)$ is the dimensionless gain-correction factor which is given as Eq.(8.13) [69].

$$GK(\beta) = \frac{1}{1 + \beta/\beta_K} \quad (8.13)$$

Gains are calculated as $K_P(\beta = 0^\circ) = 0.01882681$, $K_I(\beta = 0^\circ) = 0.008068634$ [69]. Fig.8.5 shows the PI gains at different pitch angle. Detail parameters of the baseline PI feedback controller (Table.A.1) are shown on Appendix.A.2. The PID gains can be tuned manually. Table.8.1 shows the effects when increasing a gain parameter indecently.

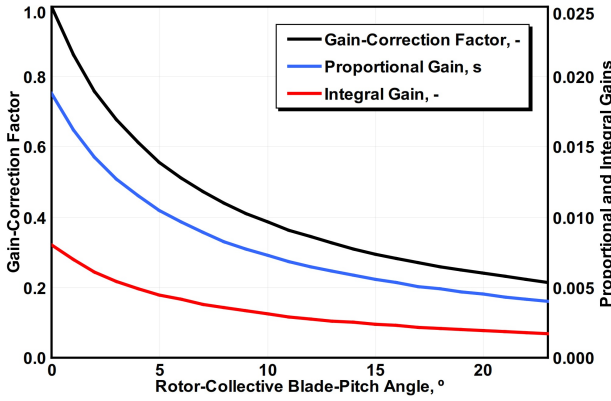


Fig. 8.5: PI gain and correction factor [98]

Table 8.1.: Effects of PID gain tuning by increasing a parameter independently

Parameters	Rise time	Overshoot	Setting time	State error	Stability
K_P	Decrease	Increase	Small change	Decrease	Degrade
K_I	Decrease	Increase	Increase	Eliminate	Degrade
K_D	Minor change	Decrease	Decrease	No effect	Improve if K_D small

8.1.2. Full-state feedback LQR controller

LQR is a linear model based controller. Basically, LQR is the unconstrained linear MPC [127]. Therefore, building-up the LQR controller is the first step to the MPC design. The LQR controller is based on the linearised model of Eq.(7.44) from Section.7.5. For simplification, the drivetrain torsion and the actuator DOFs are not implemented into the design.

$$J_{\text{tot}}\dot{\Omega}_{\text{Rt}} + \tau_{\text{Gen}} - \tau_{\text{Rt}} = 0 \quad (8.14a)$$

$$m_{\text{Twr}}\ddot{d}_{\text{Twr}} + c_{\text{Twr}}\dot{d}_{\text{Twr}} + k_{\text{Twr}}d_{\text{Twr}} - f_{\text{T}} = 0 \quad (8.14b)$$

$$\dot{\tau}_{\text{Gen}} + \frac{1}{T_e}(\tau_{\text{ref}} - \tau_{\text{Gen}}) = 0 \quad (8.14c)$$

$$\ddot{\beta}_{\text{Pitch}} + 2\zeta\omega\dot{\beta}_{\text{Pitch}} + \omega^2(\beta_{\text{Pitch}} - \beta_{\text{ref}}) = 0 \quad (8.14d)$$

$$\dot{\theta}_{\text{Rtr}} - \Omega = 0 \quad (8.14e)$$

where θ_{Rtr} is an integral state represented as the rotor azimuth angle ($\theta_{\text{Rtr}} = \int_{t-\Delta t}^t \Omega dt$). It is useful for reducing the steady error in the model mismatch [20]. The linear model is described in Section.7.5.2 and the parameters are given in Appendix.A.3. The cost function is given as Eq.(8.15) over the infinite time horizon.

$$J_{\text{LQR}} = \frac{1}{2} \int_0^{\infty} (\Delta x^T Q \Delta x + \Delta u^T R \Delta u) dt \quad (8.15)$$

where Q is positive semi-definite weighting matrix, R is positive definite weighting matrix. x is the n -dimension state variable, u is m -dimension input variables. According to the LQR control theory, the optimal control is given as Eq.(8.16).

$$u(t) = K_{\text{LQR}}x(t), \quad (8.16a)$$

$$K_{\text{LQR}} = -R^{-1}B^T P \quad (8.16b)$$

where K_{LQR} is the LQR controller gain matrix, R^{-1} is the inverse of R , B^T is the transpose of B in Eq.(8.16), P is given by solving the Algebraic Riccati Equation (ARE) (Eq.(8.17)). [110]

$$PA + A^T P - PBR^{-1}B^T P + Q = 0 \quad (8.17)$$

However, since the wind turbine system is a strong nonlinear system, the standard LQR control approach linearise the turbine system at an operation point (x^*, u^*, U_m^*) , where U_m^* denotes the measured wind speed for determine the operation point for linearisation. Based on the reduced model (Chapter7), the linear model may have errors for trimming the turbine via the broad operational conditions. As explained in [18], the control variables (pitch angle and torque) and the linear state parameters are functions of wind speed. The linearised wind turbine model is a Linear Parameter Varying System (LPV) with the wind speed U_m^* as the parameter.

However, the standard LQR design does not take the effects of wind disturbance input Δw into account. DAC is a control method to take the disturbance into the model and control loop [111]. The state-space system with the disturbance inputs is

$$\Delta \dot{x} = A\Delta x + B\Delta u + \Gamma\Delta w \quad (8.18a)$$

$$\Delta y = C_y\Delta x \quad (8.18b)$$

Here x is the system states, Δu is the predicted control input, Δw is the previously measured disturbance wind vector, y is the measured outputs. With the DAC approach, the disturbance input Δw is assumed to know the waveform model, but unknown of the amplitude. Then, DAC uses the state estimator to recreate the disturbance. These disturbances are used as part of the FB control to reduce (accommodate) any persistent effects [185]. The disturbance model in state-space form is

$$\dot{z}_d(t) = Fz_d(t) \quad (8.19a)$$

$$\underline{u}_d(t) = \Theta z_d(t) \quad (8.19b)$$

Therefore, the disturbance is added into the original LQR model. From the feedback law, the accommodated control is given as Eq.(8.20). Fig.8.6 shows the block diagram of such a DAC control with plant and disturbance state estimator [184].

$$u^*(t) = K_{\text{LQR}}x(t) + G_D \dot{z}_d(t) \quad (8.20)$$

Where G_D is the disturbance gain which can be designed to cancel or mitigate the wind speed disturbances by minimizing the norm $\|B \cdot K_{LQR} + \Gamma \cdot \Theta\|$. Then, the augmented state matrices are given as Eq.(8.21).

$$\bar{A} = \begin{bmatrix} A & \Gamma\Theta \\ 0 & F \end{bmatrix}, \quad \bar{B} = \begin{bmatrix} B \\ 0 \end{bmatrix}, \quad \bar{C} = [C \quad 0], \quad \bar{K} = [K_{LQR} \quad K_D] \quad (8.21)$$

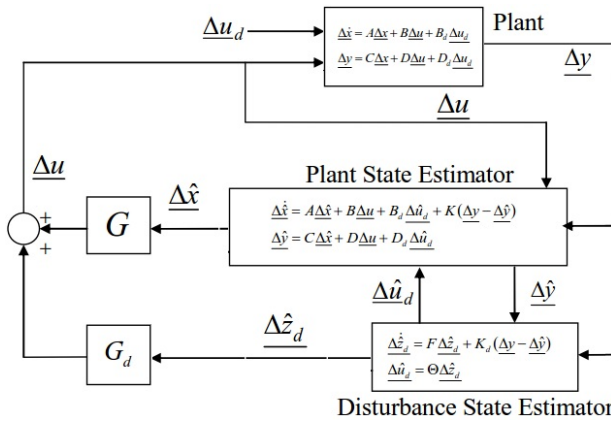


Fig. 8.6: Block diagram of DAC control method with state estimator [184]

Within the standard DAC design, an estimator is used to estimate the disturbances. Without additional sensors, DAC allows estimation of wind speed for minimization of the system disturbance [68, 167].

Due to the integration of Lidar preview wind measurement in the last decades, the wind disturbances can be actually measured. Therefore, the DAC controller is able to accommodate the Lidar measurement directly instead of the estimator. One of such method, Non-Homogeneous LQR (NHLQR), is applied by C.MD.Riboldi [149]. With this method, a cost function, Eq.(8.22) is minimized around a trim condition (x^*, u^*, V_m^*) described by Eq.(8.14).

$$J_{LQR} = \frac{1}{2} \int_t^{t-T_f} (\Delta x^T Q \Delta x + \Delta u^T R \Delta u) dt + \frac{1}{2} \Delta x^T (t - T_f) Q_f \Delta x (t - T_f) \quad (8.22)$$

where T_f is the finite prediction horizon. The perturbation control inputs are given as

$$J_{LQR} = -R^{-1} B^T P \Delta x(t) - R^{-1} B^T \int_0^\infty \left(e^{-\bar{A}^T (t - \tau)} P G \Delta w(\tau) \right) d\tau \quad (8.23)$$

where matrix P represents the solution of the steady state ARE, $\bar{A} = A - BR^{-1}B^TP$, Δw is the wind disturbance inputs. Therefore, the non-homogeneous components of the control commands generated by the Lidar preview wind disturbance is given as Eq.(8.24).

$$\Delta u_{NH} = -R^{-1}B^T\bar{A}^{-T}PG\Delta w \quad (8.24)$$

8.1.3. A comparison of LQR control with PI Feedback baseline control

Based on the controller described above, a comparison of LQR approach to the standard PI baseline feedback controller is given on Fig.8.7. The simulated controllers are the LQR control which is described in this section, and the standard industrial PI feedback baseline control described previously. The simulation is carried out with the FAST 5.0 MW three bladed horizontal axis reference wind turbine model designed by NREL.

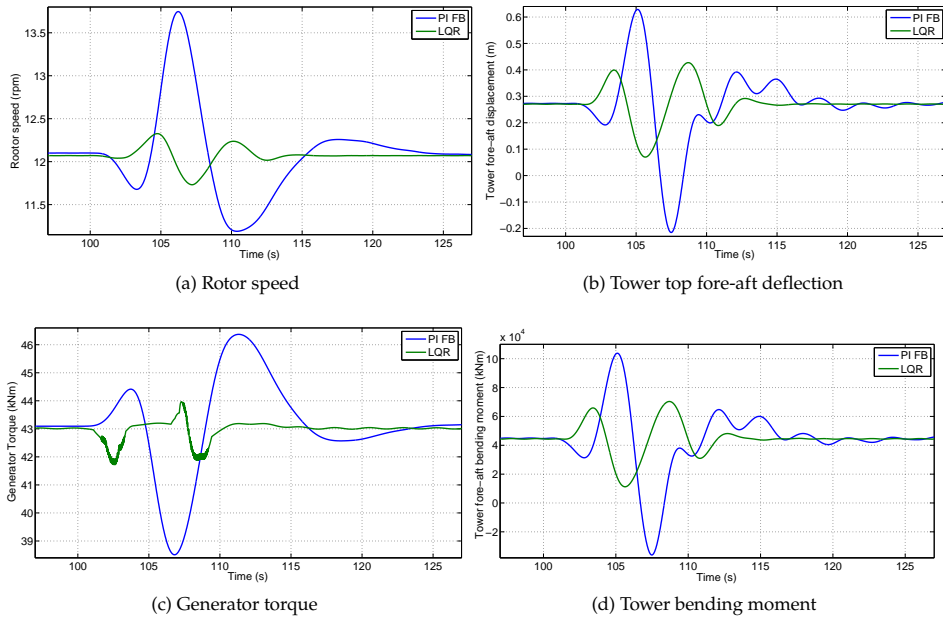


Fig. 8.7.: A time series simulation results comparison of LQR control with PI feedback control with an IEC EOG wind profile

The simulation results shown in this Section are performed with a EOG 1-year gust specified by IEC standard. The reference hub height wind speed is defined as 16 m/s. Since the FAST online Lidar signal simulation is not working with a simple user defined wind profile. A pre wind field determination is proceeded first by FAST simulation, then restored in a Matlab file to reload with the simulation.

Fig.8.7a and 8.7b illustrate the time histories of the rotor rotational speed Ω and the tower top fore-aft deflections. From this figure, it is clearly shown that the two LQR controller are much less fluctuation due to the consideration of the system model for different operation points. Fig.8.7c and 8.7d shows the generator torque and the tower bending moment. A great reduction of system torque can be observed with the LQR approach.

Fig.8.8 shows the simulation statistic result of standard deviation. Fig.8.8a and 8.8c show the LQR control in high wind speed region 3 has a better control performance on reducing the generator torque and keep generator on a stable rotation speed. However, on the lower wind speed of region 3 and region 2.5, LQR control lost their benefit in comparing with standard PI control design. One of the explanations is the model accuracy. Since the LQR design relies on the reduced model which consists the generator rotation and first order tower bending DOFs. However, the PI controller is designed based on the transfer function from generator rotational speed to the pitch angle but with all available DOFs activated. Therefore, the influences from the other DOFs to the transfer function has been considered. However, due to the more accurate model on different operation points, the overall performance of a wide range of LQR technique is better in comparing to the PI controller. Fig.8.8b and 8.8d show that the LQR controller has better performance over a wide operation range in comparing to the PI FB control.

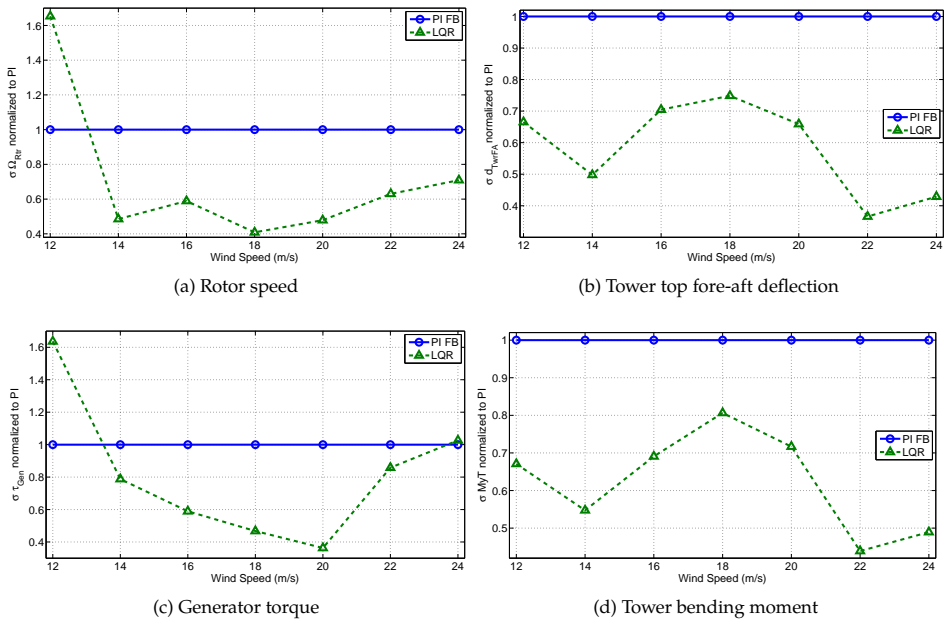


Fig. 8.8.: Standard deviation results comparison of LQR control with PI feedback control

8.1.4. 2-DOF Feedforward/Feedback Control

Theoretical background of the 2-DOF FF/FB controller has been briefly introduced in Section.3.4.2. For benchmarking of the new controller design, a 2-DOF controller based on model inverse ZPETC FF control is used. To design the model inverse FF control, a model linearisation is applied through the FAST tool. Therefore, with sampling time of 0.0125s, the linearised transfer functions $P_{\Omega\beta}$ and $P_{\Omega u}$ are given as Eq.(8.25) [53].

$$P_{\Omega\beta} = \frac{0.091923(z + 1.584)(z - 1.094)(z - 0.922)(z - 0.1628)}{(z - 0.9968)(z^2 - 1.932z + 0.9356)(z^2 - 1.951z + 0.9819)} \quad (8.25a)$$

$$P_{\Omega u} = \frac{0.0002991(z + 1.829)(z - 0.1577)(z^2 - 1.572z + 0.6193)}{(z - 0.9968)(z^2 - 1.932z + 0.9356)(z^2 - 1.951z + 0.9819)} \quad (8.25b)$$

Therefore, the FF controller is given as

$$FF = -P_{\Omega\beta}^{-1} \cdot P_{\Omega u} \quad (8.26)$$

By applying the ZPETC method to remove the non-minimum phase zeros, with sampling time of 0.0125 s, the ZPETC FF controller is given as Eq.(8.27) [53].

$$FF_{ZPETC} = \frac{0.09587(z + 1.829)(z + 0.6313)(z - 0.9142)(z - 0.1573)(z^2 - 1.572z + 0.6194)}{z^4(z - 0.922)(z - 0.1628)} \quad (8.27)$$

8.2. Design of the 2-DOF RHC/FB controller

8.2.1. Controller structure

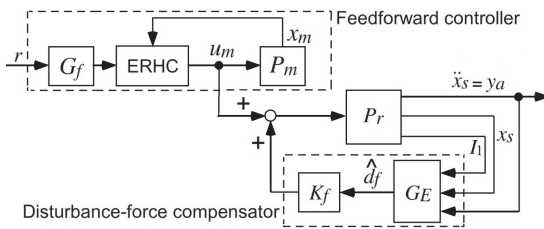


Fig. 8.9: Block diagram of the 2DOF electrodynamics shaker controller [177]

The 2-DOF RHC/FB control consists: a nominative model of wind turbine generates a states-output; a RHC controller calculates the pitch commands; the wind field is generated by TurbSim; the RHC controller takes the Lidar data to predict the future pitch commands; the FB controller generates the correcting pitch commands and add into the RHC commands for the FAST nonlinear turbine model. Reference signal can be the states at the linearisation set point or the output from the nominative model. This concept is introduced by T. Hatanaka

et.al. for controlling of an electrodynamic shaker (Fig.8.9) [177]. Where, P_m is the nominal model of plant, P_r is the real plant, K_f is disturbance-force compensator, \hat{d}_f is the estimated disturbance force, G_E is the disturbance estimator.

8.2.2. Receding horizons

Fig.8.10 illustrates the principle of the receding horizon control. RHC is based on iterative, finite horizon optimization of a plant model. At time k the plant state is sampled and an optimal predicted output is calculated for a fixed time horizon $[k, k + p]$ in the future. A corresponding control input for the plant is calculated, but only the selected steps of commands are implemented. Then this processes are repeated from the current states, yielding a new control and prediction. The prediction horizon is continuously shifted forward. For this reason MPC is also called RHC.

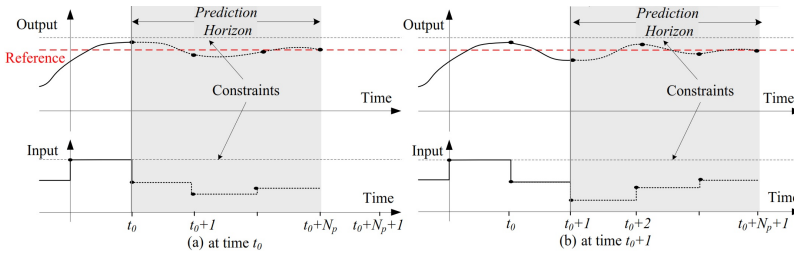


Fig. 8.10.: Illustration of the receding horizon of RHC methods [164]

8.2.3. Prediction model

A prediction model is the precondition and foundation of the MPC, according to this model the controller can predict the system output in the predictive horizon and calculate the optimal control output. The prediction model uses in this thesis is:

$$x(k + 1) = Ax(k) + B\Delta u(k) + \Gamma\Delta w(k - N_{pre}) \quad (8.28a)$$

$$y(k) = C_y x(k) \quad (8.28b)$$

Here x is the system states, Δu is the predicted control input, Δw is the disturbance wind input with preview measurement, assuming preview time is t_{pre} , then the preview step delay is $N_{pre} = t_{pre}/t_s$. y is the measured outputs.

8.2.4. Cost function

As briefly mentioned above, the RHC controller performs an optimization on the predicted output of the plant. Assume the time is k , $\Delta u(k + j|k)$ denotes the input of Δu at time $(k + j)$

in the future, so the same expressed of $\Delta x(k+j|k)$, $\Delta y(k+j|k)$. For the optimization, a cost function is defined where the different outputs and control inputs can be weighted to decide the objectives of the controller. It is given as a quadratic function Eq.(8.29) [93].

$$J_k[x(k), u] = \sum_{j=1}^N \|y(k+j|k) - y_r(k+j|k)\|_{Q(j)}^2 + \sum_{j=0}^{N_c-1} \|\Delta u(k+j|k)\|_{R(j)}^2 \quad (8.29)$$

Which subject to the system constraints given as

$$y_{\min} \leq y(k+j|k) \leq y_{\max}, j = 1, \dots, N \quad (8.30a)$$

$$\Delta u_{\min} \leq \Delta u(k+j|k) \leq \Delta u_{\max}, j = 0, \dots, N_{c-1} \quad (8.30b)$$

Here $\Delta y(k+j|k)$ is the predicted output from the plant, $\Delta y_r(k+j|k)$ is the reference output and $\Delta u(k+j|k)$ is the predicted control input. $[y(k+j|k) - y_r(k+j|k)]$ denotes the tracking error. The weights of the tracking error and control inputs are determined by the matrix Q and R which are tuning parameters. The Q matrix decides the priority of control objective focuses. For a multi-states system, choosing the Q matrix values is a trade-off. More weight on the state tracks more the reference and vice-versa [116]. The matrix R decides the priority of the input signals. The relative weights of Q and R determine the overall amount of control that is used to reach the set points. If R is small relative to Q the controller will more focus on tracking reference and if R is much larger than Q the controller will do more focus on controlling the variable of the input signal. The weight matrix are manually tuned to achieve the control objectives [77]. The weight matrices Q and R can be tuned from the starting point which is given as

$$Q_i = \frac{1}{(x_{i|\max})^2}, \quad R_i = \frac{1}{(u_{i|\max})^2}. \quad (8.31)$$

8.2.5. Solving the MPC optimization problem

The design process of the RHC method is detailed discussed on Section.B.1. The basic idea of the RHC control is to solve the Constrained finite time optimal control (CFTOC) problem over a finite prediction time of t_{Pre} . The optimization problem takes the predicted controlled output from the prediction model and finds the optimal input changes so the predicted output is driven towards the reference by minimize the quadratic cost function Eq.(8.29). Eq.(8.29) can be rewrite in a matrix form as Eq.(8.32).

$$\min_{\forall \{x, u\}} J_k, \quad \text{s.t. } J_k = \|y(k) - y_r(k)\|_Q^2 + \|\Delta U(k)\|_R^2 \quad (8.32)$$

Where

$$y(k) = \begin{bmatrix} y(k+1|k+N_{\text{Pre}}) \\ \vdots \\ y(k+N|k+N_{\text{Pre}}) \end{bmatrix}, Y_r(k) = \begin{bmatrix} y_r(k+1|k+N_{\text{Pre}}) \\ \vdots \\ y_r(k+N|k+N_{\text{Pre}}) \end{bmatrix} \quad (8.33a)$$

$$\Delta U(k) = \begin{bmatrix} \Delta u(k|k+N_{\text{Pre}}) \\ \vdots \\ \Delta u(k+N_c-1|k+N_{\text{Pre}}) \end{bmatrix} \quad (8.33b)$$

The weighting factor Q and R are given as

$$Q = \begin{bmatrix} Q(1) & 0 & \cdots & 0 \\ 0 & Q(2) & \cdots & 0 \\ \vdots & \vdots & \ddots & \vdots \\ 0 & 0 & \cdots & Q(N) \end{bmatrix}, R = \begin{bmatrix} R(1) & 0 & \cdots & 0 \\ 0 & R(2) & \cdots & 0 \\ \vdots & \vdots & \ddots & \vdots \\ 0 & 0 & \cdots & R(N_c-1) \end{bmatrix} \quad (8.34)$$

Defining the output states tracking error between the system response and reference as

$$E(k) = Y_r(k) - C_z P x(k) - C_z G_v \Delta V(k) \quad (8.35)$$

The output states are given as

$$y(k) = C_y P x(k) + C_y G_z \Delta U(k) + C_y G_v \Delta V(k) \quad (8.36)$$

Reformulating the cost function we get

$$\begin{aligned} J_k &= [C_z G_z \Delta U(k) - E(k)]_Q^2 + \Delta U(k)_R^2 \\ &= \left[\Delta U^T(k) (C_z G_z)^T - E^T(k) \right] Q [C_z G_z \Delta U(k) - E(k)] + \Delta U^T(k) R \Delta U(k) \\ &= \Delta U^T(k) \left[(C_z G_z)^T Q C_z G_z + R \right] \Delta U(k) - 2E^T(k) C_z G_z \Delta U(k) + E^T(k) Q E(k) \end{aligned} \quad (8.37)$$

Assuming $H = 2 \left[(C_z G_z)^T Q C_z G_z + R \right]$, $f = -2E^T(k) C_z G_z \Delta U(k)$, the cost function is

$$\min_{\forall \{x, u\}} J_k = \min_{\forall \{x, u\}} \left[\frac{1}{2} \Delta U^T(k) H \Delta U(k) + f^T \Delta U(k) \right] + \text{const.} \quad (8.38)$$

Subject to the constrain of

$$\begin{bmatrix} I \\ -I \\ C_z G_z \\ -C_z G_z \end{bmatrix} \Delta U(k) \leq - \begin{bmatrix} u_{\max} \\ u_{\min} \\ z_{\max} - C_z P x(k) - C_z G_v \Delta V(k) \\ z_{\min} + C_z P x(k) + C_z G_v \Delta V(k) \end{bmatrix} \quad (8.39)$$

8.3. Controller verification

The simulation presented here for analysing of the Design load case (DLC) is carried out with the IEC standard 61400-1 [85]. The fatigue loads analysis (according to DLC 1.2) is based on the Normal turbulence model (NTM) wind model. The extreme loads analysis is carried out with the Extreme turbulence model (ETM), Extreme coherent gust with direction change (ECD), and EOG wind models according to DLC 1.3, 1.4, and 2.3.

8.3.1. Fatigue and extreme loads

Fatigue is the weakening of a material caused by repeatedly applied loads. When the repeated cyclic loads are adding up above a certain threshold, metal fatigue occurs to localize a structural damage. The fatigue life N_f is defined as the number of stress cycles of a specified character before the material failure by American Society for Testing and Materials (ASTM). The fatigue life N_f is given as an S-N curve, also known as Woehler curve which is a curve of the magnitude of a cyclic stress amplitude (S_a) against the number of cycles to failure (N) [153].

$$N_i S_i^k = K \quad (8.40)$$

Where N_i is number of cycles to failure at a given stress S_i , k and K are the material parameters. The fractional damage of a material is given as

$$D_i = \frac{n_i S_i^k}{N_i S_i^k} = \frac{n_i}{N_i} \quad (8.41)$$

With N_i as the number of cycles at the stress amplitude S_i . The total stress can be calculated with the Palmgren-Miner rule as the sum of the individual fractional damages.

$$D = \sum_{i=1}^j \frac{n_i}{N_i} \quad (8.42)$$

Wind turbine consists different loads: static loads do not associate with rotation; steady loads associate with rotation; cyclic loads is due to wind shear, blade weight, yaw motions; impulsive loads are short duration loads, such as blades passing through tower shadow; stochastic loads are due to turbulence; transient loads are due to start and stop; then resonance induced loads are due to excitations near the natural frequency of the structure [169]. Those load spectrum has a constant range fluctuating around a constant mean value and frequency which describe as Damage Equivalent Load (DEL). DEL is used to compare different kinds of load spectrum. The short term DEL for each input time series is

$$DEL_j^{ST0} = \left(\frac{\sum_k (n_k (L_k^{R0})^m)}{n_j^{STeq}} \right)^{\frac{1}{m}} \quad (8.43)$$

Where, $n_j^{ST_{eq}}$ is the total equivalent fatigue number of cycles for time series j , with $n_j^{ST_{eq}} = f^{eq} \cdot T_j$, f^{eq} represents the frequency, T_j is the elapsed time. L_k^{R0} is the adjusted load ranges about a zero fixed-mean. Furthermore, a lifetime equivalent load is given as

$$DEL^{Life} = \left(\frac{\sum_j \sum_k \left(n_{jk}^{Life} (L_k^R)^m \right)}{n^{Life, eq}} \right)^{\frac{1}{m}} \quad (8.44)$$

Where, $n^{Life, eq} = \sum_j f_j^{Life} n_j^{ST_{eq}}$, $n_j^{ST_{eq}}$ is the short term equivalent count, f^{Life_j} is the lifetime count extrapolation factor. n^{Life_k} is the extrapolated cycle counts over the design lifetime. n^{Life_k} is the load range value. In practice, DEL can be obtained via the output option with FAST simulation. Damages and DELs can be analysed with the NREL post processing toolboxes Mcrunch and Mlife [75].

The indicator for the merit of performance can be categorized as following.

- RMS of the rotor power error Standard Deviation (SD) in rpm. Smaller is better.
- RMS of the generator power error SD. Smaller the error better the power quality.
- RMS of the blade pitch rates in degrees per second (deg/s). This is used to indicate the level of actuator usage. A high value means high blade pitch actuator usage, therefore, smaller is better for pitch actuator loads.
- The tower Fore-Aft (FA) and Side-Side (SS) bending fatigue DEL.
- The Low Speed Shaft (LSS) torsion fatigue DEL.
- The blade root flapwise and edgewise bending fatigue DEL.

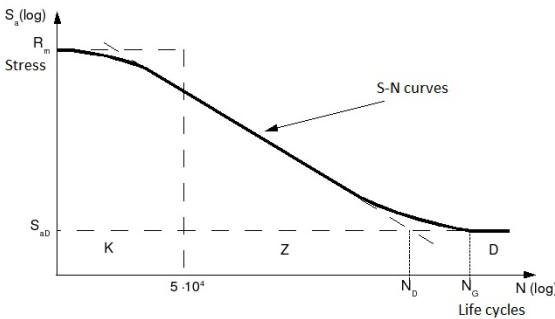


Fig. 8.11: Schematic SN curve of a material [153]

8.3.2. The simplest 1-state pitch controller

The 1-state pitch controller design was detailed described on the Master thesis by Mr.Xu [Xu13] and the article [SXBS14]. The 1-state linear model is based on the rotor rotation

dynamics described as Eq.(7.44a) in Section.7.3 which is linearised Eq.(7.44a) at the center operation point of Region 3 (18 m/s). The model is given as Eq.(8.45).

$$\dot{x}_1 = -0.75x_1 - 28.55\Delta\beta + 0.503\Delta v; \quad y = x_1 \quad (8.45)$$

which subjects to the system constrain of

$$0^\circ \leq \beta \leq 90^\circ \quad (8.46a)$$

$$-8^\circ \leq \Delta\beta \leq +8^\circ \quad (8.46b)$$

$$7(rpm) \leq \Omega_{Rt} \leq 13.1(rpm) \quad (8.46c)$$

The cost function Eq.(8.47) is to minimize the tracking error of rotor speed and pitch angle variable rates.

$$J_k = \|y(k+j|k) - y_r(k+j|k)\|_Q^2 + \|\Delta u(k+j|k)\|_R^2 \quad (8.47)$$

where $y_r(k+j|k)$ is the reference value of the controller, here is to minimize the tracking error $\|y(k+j|k) - y_r(k+j|k)\|$. $\|\Delta u(k+j|k)\|$ is the pitch rates. The MPC controller is designed by MPT with an explicit solution.

Apply this controller into an extreme operational gust (EOG) wind profile with an initial wind speed of 25 m/s. Assuming the wind speed is measured at the preview time which is the prediction time of the designed controller, here is ca. 2s.

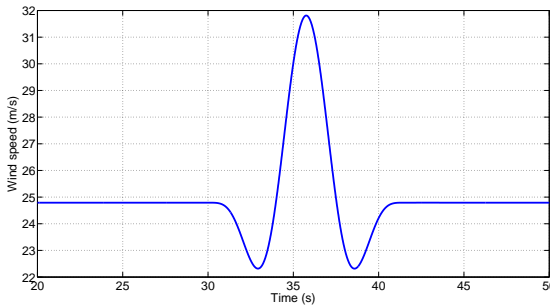


Fig. 8.12: A simple EOG-1-year gust wind profile with 25 m/s initial wind speed

Fig.8.13 shows a comparison of the time histories of the rotor speed and pitch position from a standard industry PI-FB controller and the new 2-DOF RHC/FB controller. Benefiting from the Lidar preview measurement, the 2-DOF RHC/FB controller pre rotate the pitch to fit with the incoming wind speed. A more constant rotor shaft speed was observed. The objective in this simulation is to eliminate the rotation speed error which can be observed from this simulation result.

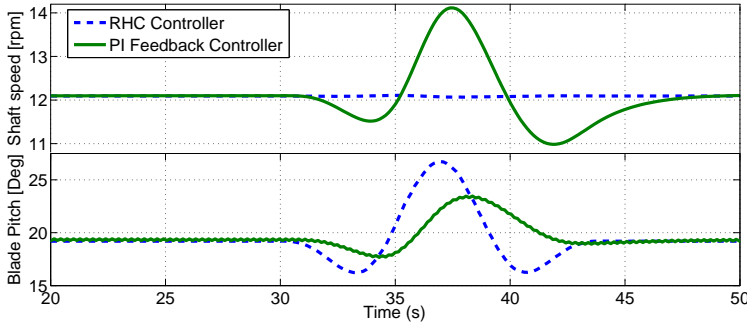


Fig. 8.13.: Simulation result of the rotor rotation speed and collective pitch angle with an IEC EOG wind profile at 25 m/s

8.3.3. 2-DOF RHC/FB control

The objective of pitch control with tower fore-aft model is to suppress the oscillations of tower top, keeping the generator speed constant, meanwhile to keep the pitch actuator movement as less as possible. The controller is optimizing the cost function of

$$J_k = \sum_{j=1}^N \|y(k+j|k) - z_r(k+j|k)\|_{Q(j)}^2 + \sum_{j=0}^{N_s-1} \|\Delta u(k+j|k)\|_{R(j)}^2 \quad (8.48)$$

Here Q is the weighting matrix for the full system states errors which includes the weight for generator speed Q_1 , and the weight for tower fore-aft displacement Q_2 and speed Q_3 . R is the weight for control inputs which includes the weight for pitch angle rates R_1 and generator torque rates R_2 . The system constrains are given as

$$\begin{bmatrix} 0.7 \text{ rad/s} \\ 0 \text{ m} \\ -0.2 \text{ m/s} \end{bmatrix} \leq \begin{bmatrix} \Omega_{Rtr} \\ d_{Tfa} \\ \dot{d}_{Tfa} \end{bmatrix} \leq \begin{bmatrix} 1.4 \text{ rad/s} \\ 1 \text{ m} \\ 0.2 \text{ m/s} \end{bmatrix} \quad (8.49a)$$

$$\begin{bmatrix} -0.02 \text{ rad} \\ -0.14 \text{ rad/s} \\ 0 \text{ kNm} \end{bmatrix} \leq \begin{bmatrix} \beta_{Pitch} \\ \dot{\beta}_{Pitch} \\ \tau_{Gen} \end{bmatrix} \leq \begin{bmatrix} 1.57 \text{ rad} \\ 0.14 \text{ rad/s} \\ 47.4 \text{ kNm} \end{bmatrix} \quad (8.49b)$$

$$\begin{bmatrix} -1.6 \text{ rad} \\ -0.28 \text{ rad/s} \\ -47.4 \text{ kNm} \end{bmatrix} \leq \begin{bmatrix} \Delta\beta_{Pitch} \\ \Delta\dot{\beta}_{Pitch} \\ \Delta\tau_{Gen} \end{bmatrix} \leq \begin{bmatrix} 1.6 \text{ rad} \\ 0.28 \text{ rad/s} \\ 47.4 \text{ kNm} \end{bmatrix} \quad (8.49c)$$

$$\begin{bmatrix} -0.02 \text{ rad} \\ 0 \text{ kNm/s} \end{bmatrix} \leq \begin{bmatrix} \beta_{ref} \\ \tau_{ref} \end{bmatrix} \leq \begin{bmatrix} 1.57 \text{ rad} \\ 47.4 \text{ kNm/s} \end{bmatrix} \quad (8.49d)$$

$$\begin{bmatrix} -1.6 \text{ rad} \\ -47.4 \text{ kNm/s} \end{bmatrix} \leq \begin{bmatrix} \Delta\beta_{ref} \\ \Delta\tau_{ref} \end{bmatrix} \leq \begin{bmatrix} 1.6 \text{ rad} \\ 47.4 \text{ kNm/s} \end{bmatrix} \quad (8.49e)$$

The penalty weights on states and inputs are given as

$$Q_{Gen} = \frac{1}{(\Delta\Omega_{Rt,max})^2} = 2, \quad Q_{d_{Tfa}} = \frac{1}{(\Delta d_{Tfa,max})^2} = 4, \quad Q_{i_{Tfa}} = 0 \quad (8.50a)$$

$$R_{Pitch} = \frac{1}{(\Delta\beta_{Pitch,max})^2} = 0.4, \quad R_{\tau_{Gen}} = \frac{1}{(\Delta\tau_{Gen,max})^2} = 0 \quad (8.50b)$$

The MPC controller is designed with the MPC toolbox and implemented into Simulink with the multiple MPC control toolbox and adaptive MPC toolbox. Two different RHC controllers have been designed, a simple linear MPC controller with a linearised model at set point 18 m/s, and a gain scheduling MPC which is designed based on a set of linear models linearised with every 1 m/s start from 3 m/s until 31 m/s.

8.3.4. Simulation with a step changes wind profile

The purpose of this section is to use a simple step changing of wind speed to test the step response of the designed 2-DOF RHC/FB controller. Fig.8.14 shows the simple step wind profile, a steady wind without shear and turbulence but increase 1 m/s every 25s.

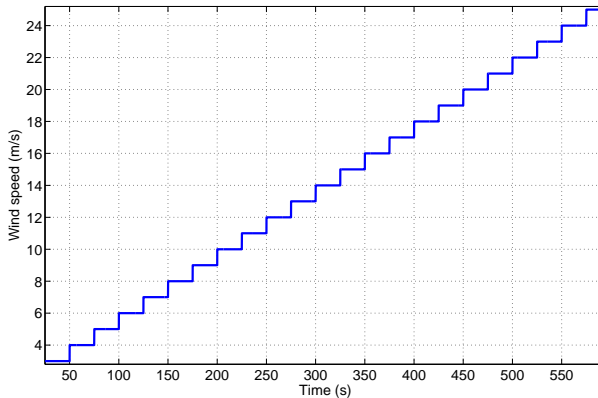


Fig. 8.14: Step increasing wind profile every 1 m/s from 3 m/s to 25 m/s

To verify the 2-DOF RHC/FB controller, results based on different control methods are compared. The controllers present here include: an industry standard gain scheduling FB controller developed by NREL which briefly described in Section.8.1.1; a gain scheduling LQR controller described on Section.8.1.2; and a 2-DOF FF/FB controller with Lidar measurement designed based on the nonlinear wind turbine model by D. Schlipf from Stuttgart University; and the new designed RHC controller based on a Full States Feedback (FSFB) MPC method with Lidar preview measurement detailed described at Section.8.2. The FSFB RHC controller includes a simple linear RHC controller and a gain scheduling RHC controller to deal with nonlinearity of the turbine model to increase the control performance.

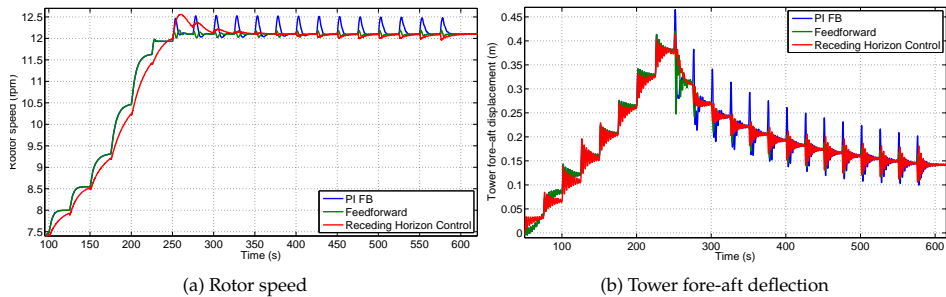


Fig. 8.15.: Time series simulation results with the simple step wind profile

The simulation results presented here were carried out with a simple reduced DOF nonlinear turbine model with rotor and generator rotation DOF, tower fore-aft deflection DOF, pitch and generator actuator DOFs. With the nonlinear nominative turbine model, a full states outputs are carried out for formatting a FSFB.

Fig.8.15 shows the time series data from the simulation over the entire operational wind speed region to give an overview of the controller response. The controllers tested here are only considered the pitch control. Below the rated wind speed in region 2, the pitch control is disabled in order to catch up the maximum possible wind power. Therefore, only the results in region 3 is discussed.

Fig.8.16a and 8.16b shows the closed up view of the rotor rotational speed response on region2.5 and region3. In region 3, the conventional industrial PI-FB control shows the worst performance, since no wind preview information is considered. The LQR controller shows a better performance than PI controller as well, even without the Lidar preview measurement. But the LQR controller uses a gain scheduling approach based on the REWS from any kind of wind sensors. Here in this simulation result a perfect knowledge of the REWS information is assumed. The gain scheduling RHC controller was supposed to deal with the nonlinearity of the turbine model in comparison of the linear controller to gain a better performance. However, it shows a worse result than the linear method. The reason for this bad performance could be considered on the tuning of parameters. Due to the complexity of the multiple inputs multiple outputs (MIMO) model and the wide operation region, a rather rough adjustment of tuning parameters have been used, therefore an optimal gain parameter was not yet settled. One of the possible future topic could be a brute force control parameters tuning or an analytical solutions on increasing of the controller performances. Nevertheless, the linear RHC controller shows a grate advantage in comparing with the PI controller due to the Lidar preview measurement information. The similar results can be observed from the 2-DOF FF/FB control methods.

Fig.8.17 shows the time series results of the rotor torque and tower fore-aft bending moment in region3. Both results from the rotor torque and tower fore-aft bending moment show the same trends. Due to the Lidar assisted preview controller keep the rotor rotating stable, the torque on the rotor is more constant. The tower bending moment is reduced as well by the preview controllers.

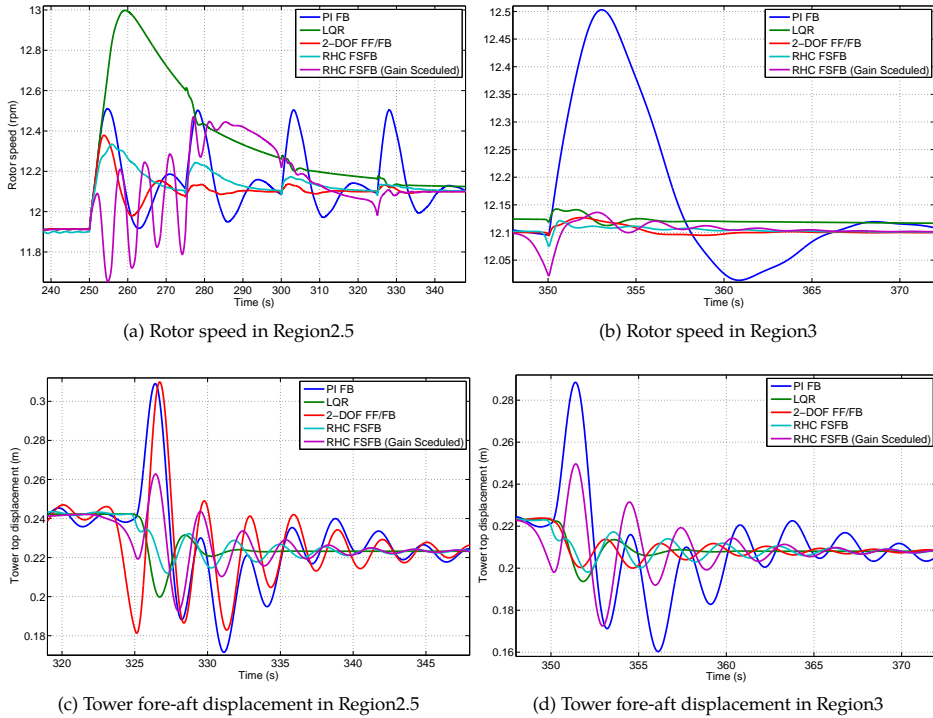


Fig. 8.16.: Time series rotor rotational speed and tower fore-aft deflection response with the simple step wind speed changes from 15 m/s to 16 m/s

Fig.8.18 shows a close up view of the actual pitch angle in region2.5 and 3. On region2.5, a strong fluctuation of the gain scheduling MPC can be observed. This is the reason for the unstable of rotor rotation and tower fore-aft deflections. Similarly the non Lidar preview controller gain scheduled LQR show a better performance which is quite close to the Lidar preview controller performance.

8.3.5. Simulation with a deterministic gust wind profile

The gust wind profile "EOGR+2" which is defined on DLC 2.3, 3.2, and 4.2 by the IEC standard [85] for an ultimate loads case analysis with the scenario of power production, start up and normal shut down case. The wind inputs are defined as the hub height wind speeds with $U_{\text{hub}} = U_{\text{Rated}} \pm 2\text{m/s}$, U_{Rated} , U_{in} , and U_{out} . Another type of the gust wind profile for the ultimate loads case analysis is ECD which is defined on the DLC 1.4 as the hub height wind speeds of $U_{\text{hub}} = U_{\text{Rated}} \pm 2\text{m/s}$, and U_{Rated} . In this section, only the EOG case was considered. The ECD case with extreme wind direction changes is not simulated.

8. Active pitch control system design

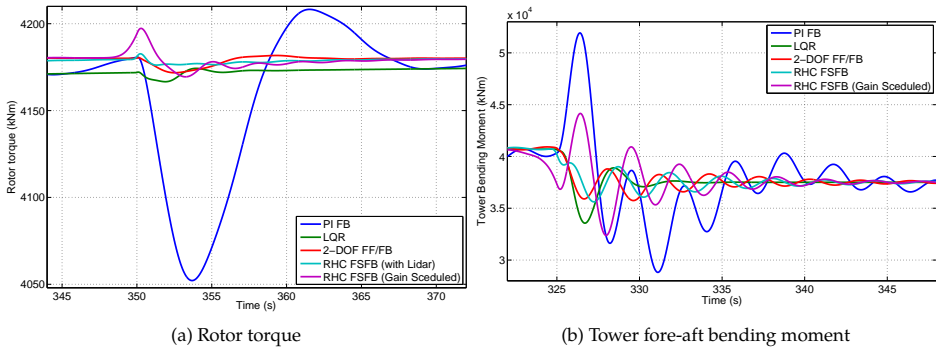


Fig. 8.17.: Time series from the simulation results with the simple step wind profile

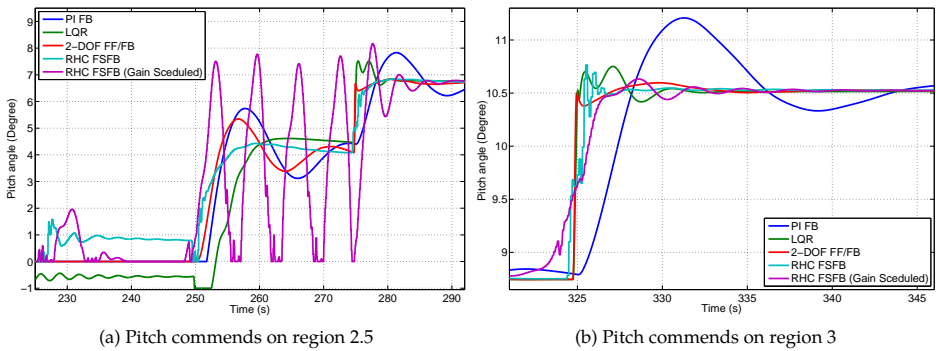


Fig. 8.18.: Time series from the simulation results with the simple step wind profile

The results presented in this section include the standard PI(D) FB CP controller, a 2-DOF FF/FB CP controller designed by D.Schlipf, a LQR controller based on work by C.E.D. Riboldi, then the 2-DOF RHC/FB controller which is designed on previous sections. The PI(D) controller uses the generator rotational speed as a control inputs to regulate the collective pitch angle. The other three controllers are taking the Lidar wind preview measurement data as an input to achieve a preview control strategy. The FF controller are designed with an inverse model method based on a reduced nonlinear wind turbine model. For the simulation and real application implementations, the FF control gain is generated offline as a look up table. Then the LQR controller and 2-DOF RHC/FB controller are designed with a full state feedback method. Worth to address here is that in a real wind turbine scenario, the full operational states are normally not fully observable. Therefore, a Kalman filter to estimate the missing state value are commonly used in a full state feedback controller. The 2-DOF RHC/FB controller presented here uses a reduced order nominative

model (can be nonlinear or linear, in this chapter, a LPV model is used) in the control loop to estimate the full system states.

The purpose of the comparison results presented in this section are to show the benefits of reducing the operation loads of wind turbine by consider the Lidar preview wind measurement with in a gust wind profile which causes the wind turbine stop working for prevents from the over loading on generator. Fig.8.12 illustrates the profile of a simple EOG-1-year gust wind profile with an initial wind speed of 18 m/s for the simulation.

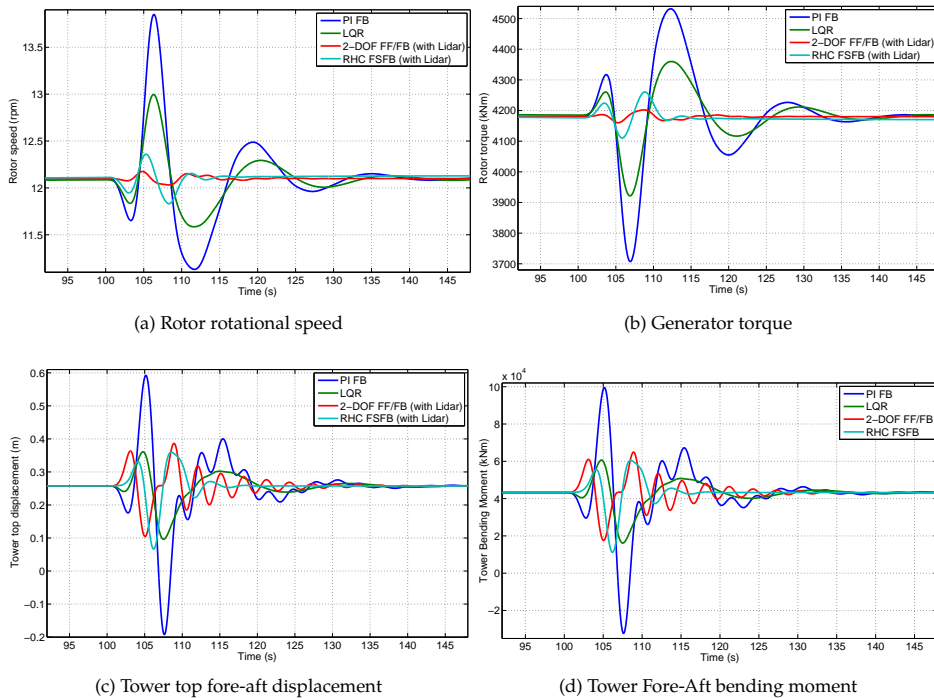


Fig. 8.19.: Time series results from an IEC gust profile “EOGR+2” with initial wind speed of 13.4 m/s with comparison between a PI, LQR, 2-DOF FF/FB and RHC controllers

Fig.8.19 shows the time series data of a PI(D) FB, LQR, 2-DOF FF/FB, and the 2-DOF RHC/FB controllers. The performance indicators are: the rotor rotational speed Fig.8.19a, the generator torque Fig.8.19b, the tower top fore-aft displacement Fig.8.19c, and the tower fore-aft bending moment Fig.8.19d. All the results with less fluctuation have better performance. The similar results can be observed from this study in comparison to the step up wind profiles. In this study, the LQR still shows advantages on reducing of the rotor rotation speed and torque fluctuations. Moreover, due to the consideration of tower fore-aft model in the design of LQR control the effect of reducing of tower fore-aft deflection and bending moment achieved a compatible result to the Lidar preview controller.

By activating the Lidar preview, controller has the incoming wind information in advance. This preview wind information is used by the controller to generate the pitch commands to control the pitch position fitting to the incoming wind field as shown with Fig.8.20, then the preview pitch controller can react faster than the PI controller.

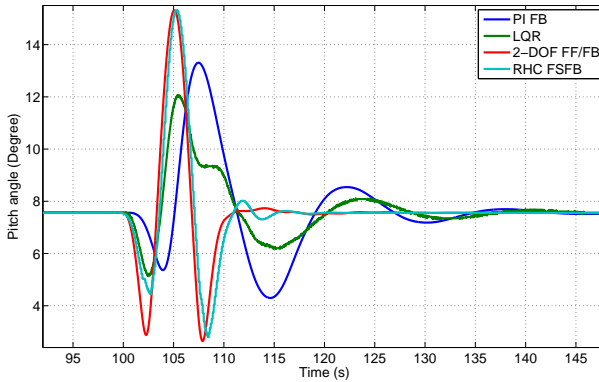


Fig. 8.20: Time series of the pitch command input

8.4. Simulation results with the non-linear FAST turbine model

8.4.1. Simulation results with a deterministic gust wind model

Following from the previous section, on Section.8.3.5, simulation with the “EOGR+2” wind profile is carried on with a nonlinear nominative model with the tower fore-aft deflection and generator rotation elastic-dynamics DOFs. The simulation scenario is based on DLC 2.3, 3.2, and 4.2 by the IEC 61400-1 standard [85] for the ultimate loads case analysis. The generated wind profile is a simple wind field consisting only the hub height wind information. Therefore, the simulation carried on in this section only considered the local wind speed information. In the real operational environment, a full field wind information which covers the entire rotor span is necessary. Fig.8.21 shows a time series plot from the FAST simulation for comparison of the PI baseline controller, LQR controller, 2-DOF FF/FB controller, and the RHC controller. The EOG wind field has an initial wind speed of 13.4 m/s which is the rated wind speed of turbine 11.4 m/s + 2 m/s. The IEC standard further specified EOGR (rated wind speed), EOGR-2 (rated wind speed - 2 m/s), EOGI (cut-in wind speed), and EOGO (cut-out wind speed) for the extreme load analysis.

With this simple hub height wind profile, the LQR control shows an excellent result in compare to the others. The 2-DOF FF/FB and 2-DOF RHC/FB controller could not show their excellences as the results (Fig.8.19) from the nominative model. Since with the FAST simulation, all the supported DOFs have been activated, however, the controller is designed based on the tower fore-aft deflection and generator rotation DOFs. Therefore, the control performance is not as good as the simulation with the tower and generator only nominative

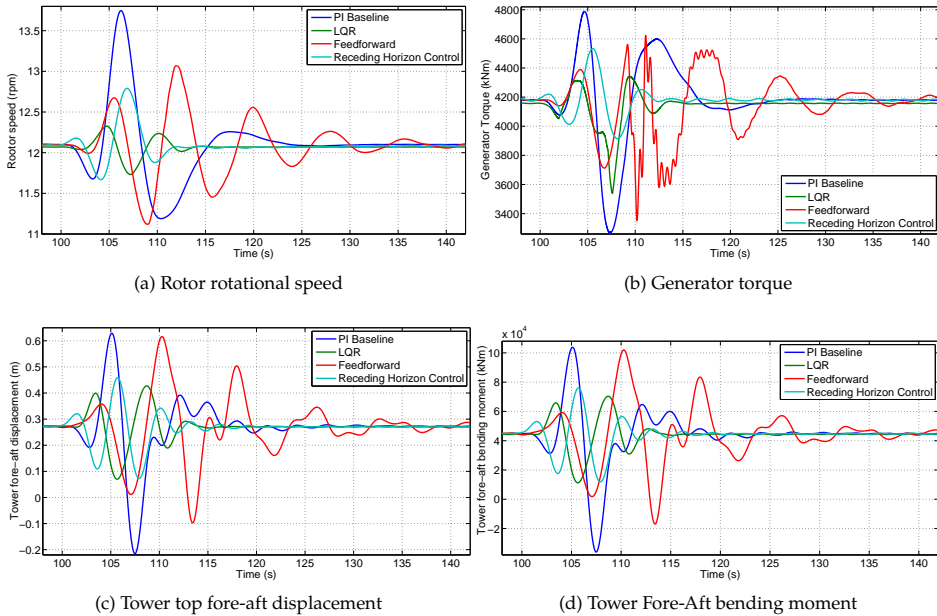


Fig. 8.21.: Time series plots from an IEC gust profile "EOGR+2" with initial wind speed of 13.4 m/s for comparing of a PI, LQR, 2-DOF FF/FB and RHC control

model. By introducing further elastic dynamics model into the controller design, the control performance would be better, however, the controller is becoming more heavy.

8.4.2. Simulation results with a normal turbulent wind model (NTM)

The NTM is defined by the IEC standard [85] on DLC1.2, DLC2.4, and DLC6.4 for fatigue loads analysis. The wind speed required by IEC standard are $U_{in} < U_{hub} < U_{out}$. In this sections, every 2 m/s steps start from 10 m/s until 24 m/s are simulated and analysed.

Fig.8.22a shows an IEC Class A turbulence wind speed time series. The blue curve shows the hub height wind speed, the brown curve illustrates the Lidar measurement from a fixed distance with a rotational scan. The scanning rate is 80 points per scan with a measurement time of 0.0125 s, which gives 1 revolution per second. Then the REWS is averaged every with 80 measurement data. Within the simulations in this section, the preview wind data is pre-measured and stored in a Matlab file to be recalled for the simulation. Fig.8.22b shows the direction changes. Here in this simulation, the yaw control is disabled, therefore the wind direction is not taking into account for the control.

From previous section, the preview controllers with the Lidar measurement result a better performance on the reduction of the rotor rotation and tower deflections with a simple gust

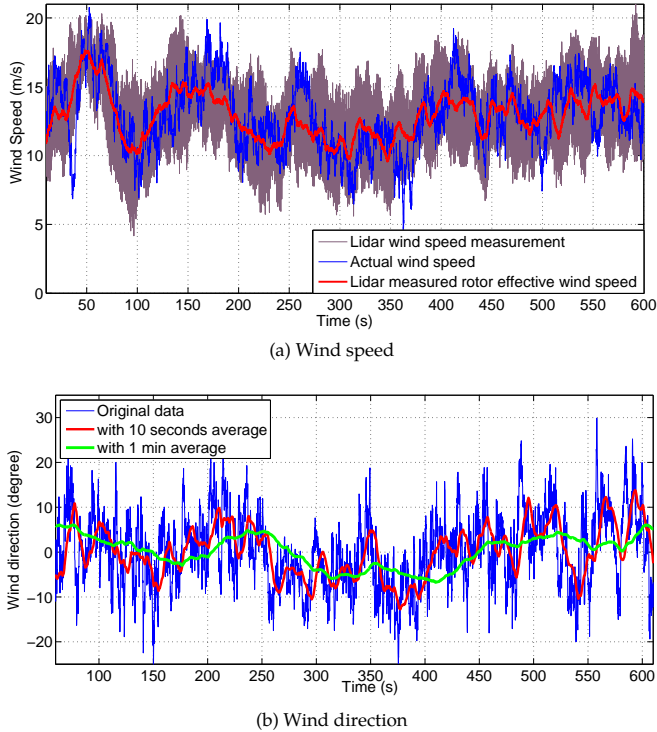


Fig. 8.22.: A wind speed (a) and direction (b) time series plot of an IEC ClassA turbulence wind profile with 13 m/s mean speed

wind condition. In this section, the simulation results obtained from the same controllers are compared with an operational turbulence wind condition. The parameters of the controller design are tuned based on the simple step and gust wind profile from previous sections. The simulations are carried on the FAST nonlinear wind turbine model operated within Simulink environment. Since the FAST model is not carrying an actuator model, an external actuator model is designed and implement into the model. The predictive horizon of the RHC controller is set to 3 s. The RHC controller is set to a 10 Hz control frequency therefore, the predictive horizon is 30 steps. The LPV model parameters and gain matrices are scheduled with the incoming wind speed which are averaged in 10 s.

Fig.8.23a and 8.23b show the standard deviation plots of the generator rotational speed and low speed shaft torque which are normalized with the mean value. Fig.8.23c and 8.23d show the standard deviation of the tower top displacement and tower bending moment normalized with the mean values. On the low speed part of Region III, the PI and FF controller which are not model based control show a better performance. This is due to the linearisation error of the model in the high nonlinearity region of the model. A more

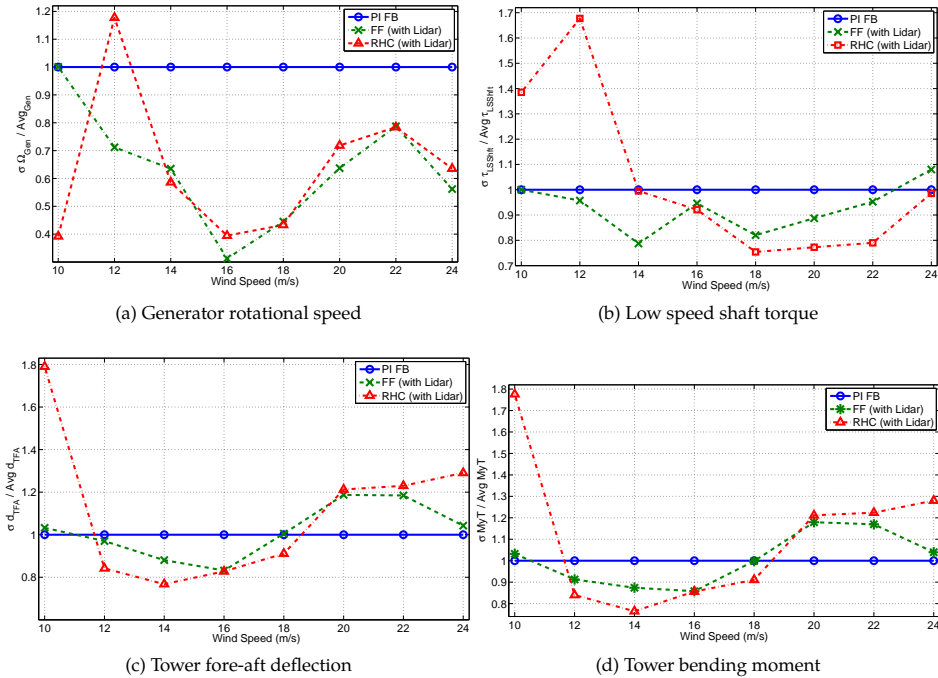


Fig. 8.23.: Normalized Standard deviation plots by the mean value for the generator rotation speed (a), generator torque (b), tower fore-aft deflection (c), and tower bending moment (d)

precise linear model in the region 2.5 and low speed region of region 3 are required to increase the control performance.

These results show that the FF controller with Lidar preview measurement have slightly benefits in compare with the standard PI feedback controller, however, the new 2-DOF RHC/FB control approach still need further tuning to get into a comparable performance.

Fig.8.24 shows the damage equivalent loads (DEL) on high speed shaft (generator side) torque and tower fore-aft bending moment. With the simulated result, it very clearly shows that the three controllers with Lidar preview measurements are able to reduce the shaft torque loads by previously know the incoming wind fields. The three preview controllers have similar performances, however, benefits from the linear parameter varies model based design, the NHLQR and 2-DOF RHC/FB control designs have slightly better result in compare with the 2-DOF FF/FB control.

8. Active pitch control system design

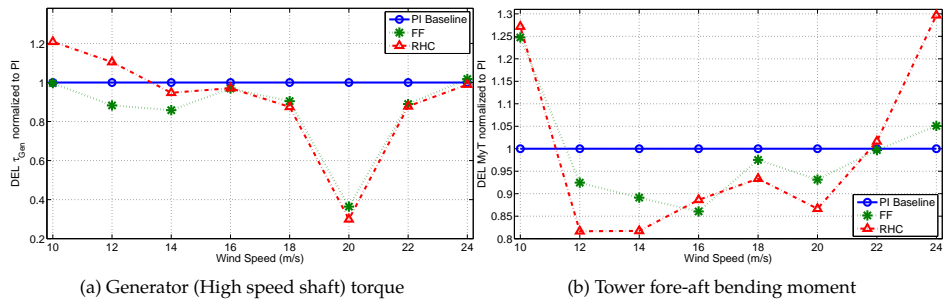


Fig. 8.24.: Damage equivalent loads (DEL) of high speed shaft (generator) torque (a) and tower fore-aft bending moment from simulation with IEC category A turbulent wind field

8.4.3. Simulation result with a hub height wind measurement only Lidar

The performance of the preview controller is strongly dependent on the parameter of the Lidar sensors. As discussed previously, the measurement quality from a Lidar system depends on the measurement ranges, probe lengths, and scanning scenarios. In this section, by the help of the Lidar simulator designed by E.Simley, a pulsed or CW Lidar signals can be simulated. The CW simulator can provide a single distance measurement, the probe length is defined by the range weighting factor of the Lidar optics. The pulse Lidar simulator can take the measurement up to 5 different distances, the probe length and measurement distances can be customized by the users. By default, the WindCube Lidar properties are predefined in the simulator with 30m probe length and 30m distance gab in between. Fig.8.25 shows the plots of the DEL of high speed shaft (generator) torque (Fig.8.25a) and tower fore-aft bending moment (Fig.8.25b) from simulation with a Hub height wind measurement only Lidar and a scanning Lidar. Both Lidar systems are measuring from the same distance (60m in front of the rotor plane). Both FF and RHC control results show that the hub height only measurement do not create advantages in reducing of the system loads. The reason for this results could be considered as the local wind speed measurement can not represent the effective wind speed over the whole turbine rotors. Therefore, for a pitch control application in order to reduce the system loads created by the in homogeneous wind field, a one or two beam hub height only measurement is not useful.

8.5. Summary and conclusion

Modern multi-mega watt wind turbines have a swept diameter over 150 m, the wind share both in horizontal and vertical domain as well as the wind turbulence in time domain create a periodic and stochastic loads on wind turbine structures, such as blades, tower, drivetrain, ect. The motivation in this chapter is to design and show the benefit of advanced control methods applying to wind turbine active pitch system.

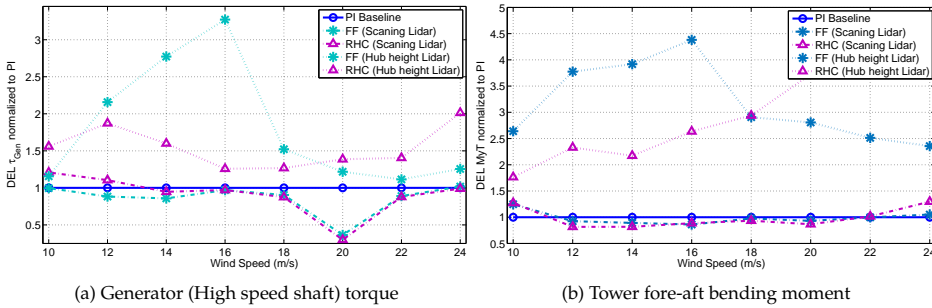


Fig. 8.25.: Damage equivalent loads (DEL) of high speed shaft (generator) torque (a) and tower fore-aft bending moment (b) from simulation with a Hub height wind measurement only Lidar and a scanning Lidar

Specifically, in this chapter, the design of the benchmark controllers, industrial PI-FB controller and 2-DOF FF/FB controller, were briefly discussed. Then, following with the detail of the new model based 2-DOF RHC/FB controller design namely 2-DOF RHC/FB control are presented. The RHC controller is designed based on the linear and the PWA model which are described in Chapter.7. To evaluate the designed controller, a comparison of a standard industrial PI-FB controller and a 2-DOF FF/FB controller based on a model inverse FF control design by other research group are presented.

The evaluations of the controllers were applied on a simple step increasing and decreasing of wind speed, deterministic gust wind profiles, and sets of IEC category A turbulence wind fields. The simple step wind profiles are used to tune the design parameters of the controller. The deterministic gust wind profiles are used to test of the designed controller. Then, the IEC category A turbulence wind profiles are used for analysing of the DEL of wind turbines. Based on the IEC standard [85], to perform a DEL analysis of wind turbine, a set of 6-18 different wind profiles with the same turbulence intensity and mean speed are required. Here in this thesis, 6 different turbulence wind fields were generated by TurbSim with different random seed for each wind speed and turbulence category. Then the simulation for each controller are simulated with these 6 wind profile every 2-3 m/s in region 3. The simulated data were analysed via MCrunch and Mlife for DEL.

Performing from the step wind profiles at each wind speed, a more stable generator rotation speed, and less tower fore-aft movement and bending moments can be observed from the NHLQR control design. However, due to the parameter tuning, the RHC design approach did not show advantages in comparison to the PI controller. Then from a deterministic gust wind profile, similar results can be observed. Even with the simplest single state model based controller design, due to the Lidar preview measurement, a prediction of the incoming gust helps controller eliminate the generator speed errors.

The results from the simulation with a IEC category A turbulent wind profile did not show such a clear different in comparison to the PI controller. Eventhough, the preview controllers show their benefits. Especially in middle to high wind speed in region 3. However, at

region 2.5 and low wind speed in region 3, only the well tuned FF/FB controller show the advantage against the PI controller.

In summary, the simplest PI FB controller still can show a good performance with an IEC category A turbulent wind field. The differences between the PI controller and the modern Lidar preview control methods are not so much.

Discussion and conclusions

9. Discussion and conclusion

9.1. Contributions of the presented work

The control of wind turbine based on Lidar preview measurement becomes state of the art for research and development in the near future wind energy applications. However, the commercial Lidar systems are commonly designed for multi-purposes usages. Those system equipped a ultra-narrow line-width lasers which are commonly fiber laser with some kilo-meters coherence length. Furthermore, such Lidar system usually has a measurement range of more than 200 meters. To measure such distances, a pulse energy of $10 \mu\text{J}$ is required. Such laser systems are in a high commercial price which leads to a high price of the Lidar system. Such high cost of Lidar system limits their application on the control systems for commercial wind turbines.

However, for pitch control applications, the optimal measurement distance is in between 50 and 120 meters. Therefore, for such shorter distances, the laser power requirement can be reduced to $1.5 \sim 4.5 \mu\text{J}$. For a CW Lidar system with $10 \mu\text{s}$ pulse duration, the optical power is about $200 \sim 500 \text{ mW}$. A narrow linewidth signal longitudinal mode semiconductor laser is commercially available in a low price.

Sofar, not yet a single product or research works focus on a Lidar system design which is specified for turbine control purpose. Therefore, to develop a Lidar system focused on wind turbine preview control purpose is very important. The presented work focused on the developing of a cost efficient Lidar system which is specified for the preview pitch control of wind turbine. Particularly, I have focused on the first step of the new Lidar system design and development, the feasibility study of the new approach. To evaluate the concept, a simulation environment and a laboratory based proof of concept setup is build and tested.

Furthermore, to specify the Lidar system, a unique approach of preview control of the active wind turbine pitch system is designed. The designed control system is a collective pitch controller which modified the state-of-the-art 2-DOF control approach with model inverse FF control to a model based RHC control which is named as a 2-DOF RHC/FB control. This approach takes the advantages from both 2-DOF design and RHC optimal control methods. In control theory, both methods are the states of the art since long time ago. However, by this combination, the better performance optimal RHC control methods are easier to be accepted by industry.

Within this thesis, I have focused on two aspects under the motivation of lower down the COE of wind energy. The "Industry-friendly model predictive controller" is designed to reducing the loads applied on the wind turbine system. To achieve this goal, the cost efficient Lidar system is proposed and evaluated via simulation and experiments. The proposed Lidar system introduces a broad spectrum semiconductor laser with a relative shorter coherence length into a coherent Doppler Lidar system.

9.2. Conclusion and discussions

State-of-the-art Doppler wind Lidar systems usually use fiber lasers with long coherence length in the range of kilo meters. The broad spectrum lasers are not used in a coherent Doppler Lidar system, due to the high phase noise. However, such lasers have a very strong cost advantages in compare with fiber lasers. The presented approach is first of all the design of a cost efficient Lidar system based on a low coherence lasers. With this approach, one hand, the price of laser source can be reduced as discussed on previous sections, a low cost semiconductor laser diode could be used on such Lidar systems. On the other hand, the coherence length of laser can be benefit to define a constant probe length of a CW Lidar system.

For designing such Lidar systems, first of all a systematic consideration of the system requirement has been discussed with in Chapter 4. From the controller design point of view, the requirement are different depending on the size of wind turbine and the control strategies. Within the presented work, the NREL 5MW reference wind turbine model based on the Senvion SE (former REpower SE) 6.2M126 wind turbine with 126 meter rotor diameter.

To achieve a better control performance with the Lidar previously measuring the incoming wind speed, a simulation based study shows a better performance with the Lidar measurement at $0.6 \sim 0.7$ diameter of the rotor. Therefore, a measurement distance of $70 \sim 80$ m in front of the rotor is optimal. With a scanning angle of 30° , the LOS distance is around $80 \sim 100$ m. With a normal urban aerosol condition, the efficiency of received scattering power is less than 1×10^{-10} in comparing to the transmitted laser power. As an example, a one watt CW laser transmitted to 100 m distance, only 100 pico-watt backscattering light will be received by the detector.

Detailed analysis of the Lidar system requirement have been done both from the sensor design point of view and the performance from the pitch control point of view in Chapter 4. The main questions of the design requirement are the maximum detection range, the probe length, and scan scenarios. The range and probe length defined the laser source parameters. With the simulation carried on Chapter.8, a hub height only Lidar measurement is not providing a useful information for the pitch preview control. Since the measurement is too localized, the hug height only wind speed can not represent the rotor effective wind speed. Fig.9.1 shows a comparison of the hub height only measurement and a full turbine rotor span scan measurement with a CW Lidar simulator. The bar plot shows how much reduction (negative value) or increasing (positive value) of the high speed shaft torque and tower fore-aft bending moment in comparison with PI baseline controller. The simulation results show that in most case with the scanning Lidar to measure the entire wind speed over the turbine rotor span can reduce the damage equivalent loads. However, with the hub height only measurement, the DEL increased comparing to the PI baseline controller.

Furthermore, since the RHC control is able to take a time set of the wind measurement data over the prediction horizon. A multiple distance measurement could be benefiting with the RHC controller. However, within the simulation presented in this dissertation, both the FAST simulation and Lidar simulation are based on the Taylor's hypothesis concept, which means the turbulences are not changing at different locations. Therefore, the impacts of the multiple distance measurement on the control performance is not checked. Table.9.1

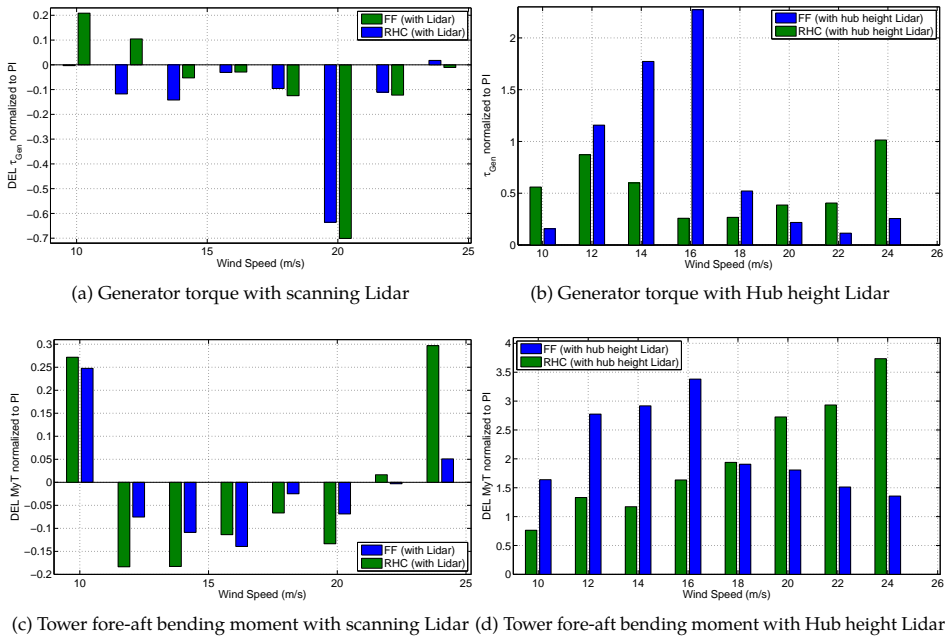


Fig. 9.1.: A comparison of the damage equivalent loads (DEL) of high speed shaft (generator) torque (up) and tower fore-aft bending moment (down) from a scanning Lidar (left) and hub height Lidar (right)

summarized the main required parameter of the Lidar system for pitch control applications.

To assist the proposed Lidar system design, in Chapter5, a simulator to model different parts of the Lidar components and the entire system reactions has been developed. The simulator has two different forms; a static simulation perform a calculation of receiving power and system signal to noise ratio. This simulation calculates the back-scattering for each particle and sums up the individual back-scattering to form the Lidar signal without considering the movement of particles and propagation time of lasers. A dynamic simulation is a modified Feuillette model which slices the atmosphere into small elements. Within each elements, assuming the optical properties and the moving speed of aerosols are the same. By propagating the laser beam to each atmosphere slices, the back-scattering signals with time delays are generated. With this model, a time domain full system simulation can be easily processed.

Finally the first step to design the Lidar system, a step wise experimental realization process is performed and the results have been discussed on Chapter.6. Within this process, various free space experimental setups are designed and build up to evaluate different parts of the new approach. The experimental setups are designed with free space optical components

Table 9.1.: Requirements of the cost efficient Lidar concept with broad spectrum laser sources

Minimum laser power	0.6 W (for 135 m LOS measurement distance)
Laser spectrum width	Ca. 10 MHz for 10 m coherence length
LOS measurement distance	LOS 45 ~ 135m(Multi distance) Or LOS 70 m (Single distance)
Minimum measurement distance	50 m
Probe length	10 m, maximum 20 m
Number of measurement range	Single or 4
Scan scenario	2 dimensional scan
Beam separation or scan angle	26° (Half angle)

in order to increase the operability. As a result from the free space experiments, with 50 mW solid state laser operating at 532 nm wavelength, a maximum wind flow measurement distance at 12 meters have been achieved with a probe length about 1 meters. The detector sensitivity of a 532 nm lasers is very low (< 0.45) in comparison to the detector operated at 1550 nm (ca. 0.95). To scale up to 135 meter measurement distance with 10 meters probe length at 1550 nm, a minimum laser power of 600 mW is required.

Then, the experimental results have been compared with the simulation as shown on Fig.9.2. Both simulation and experiment are carried on with a Lidar having a 50 MHz spectral linewidth. However, the simulated Laser spectrum has a Gaussian shape but the Laser used on the experiment has a Lorentzian spectral shape. This is one of the reason for the differences of the simulation and experiments. But never the less, both simulation and experiment show a similar results which approved the feasibility of the new Lidar concept with a short coherence length Laser.

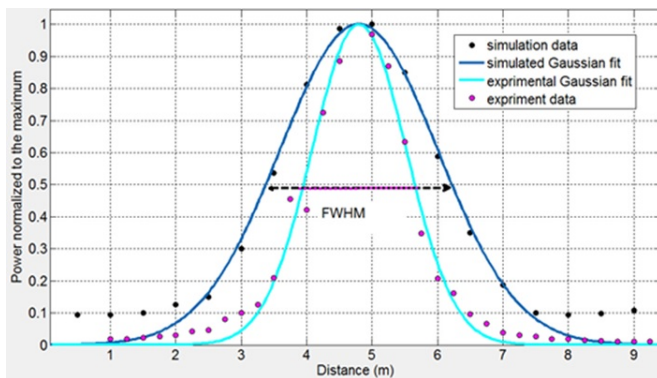


Fig. 9.2: A comparison plot of simulated and experimental data

Meanwhile, to apply such Lidar system into applications, an industry friendly pitch control approach named 2-DOF RHC/FB control is designed and detailed described in Chapter.8. The designed controller generates the pitch commands with the RHC method based on the Lidar preview wind measurements and adds to the original FB control loop without

modify the original controller. Therefore, even the predictive controller does not work properly, the original PI(D) FB controller still can control the system to be stable.

To design such controllers, first of all a reduced degree of freedom wind turbine model has been discussed and designed in Chapter 7. The model includes a nonlinear aerodynamics model, an elastic structure dynamics model, and a servo elastic actuator model. The nonlinear aerodynamics model is based on a look up table of C_p and C_t which is pre-calculated with FAST simulation tool at each operation points. The structure dynamics model includes the rotor, generator, blades, drivetrain, and towers. A free combination of the individual submodel can be done due to different objectives. Within the presented work, only the rotor/generator rotation DOF and tower first order fore-aft bending DOF have been taken into account.

For the proposed 2-DOF RHC/FB controller, the nominative model in the loop uses a LPV model instead of the nonlinear model to reduce the calculation and keep certain nonlinearities of the model.

For simulating of the controller performance, a FAST nonlinear wind turbine model designed by NREL is used within the Matlab Simulink environment via an S-Function interface. The reference wind turbine is a 5 MW 3 blades variable speed variable pitch HAWT system with a 126 m rotor diameter which is based on the Servion SE (former REpower SE) 6.2M126 wind turbine system. The FAST simulation is able to provide a reliable feedback for the controller performance analysis and capable for the IEC standard required turbine analysis.

To evaluate of the loads reduction effects, the designed controller is evaluated in comparing of the conventional industry PI baseline feedback controller, an model based LQR controller, and a 2-DOF FF/FB controller. The PI baseline controller is a gain scheduling feedback control which is designed by NREL. The 2-DOF FF/FB controller is designed by D. Schlipf for the NREL 5MW reference wind turbine. Then, the LQR controller is redesigned and tuned for the NREL 5MW reference wind turbine based on the work by Dr. C.Ed. Riboldi.

First step to evaluate the designed controller is carried out with simulations based on a nominative nonlinear reduced model with a first order tower fore-aft deflection dynamics, and generator rotational dynamics model. Moreover in order to provide a simulation more close to the real scenario a second order pitch actuator and first order generator torque actuator model is considered as well. This model is used for tuning of the controller parameter. On Section 8.1, a comparison of the designed LQR control with an argument state on the rotor rotation speed is performed against the conventional PI baseline feedback control. From the simulation results, the performance of the model based LQR control show an excellent result in comparison to the conventional industry PI baseline FB control.

Then the Lidar preview based predictive controllers considered in this dissertation include a 2-DOF feedforward/feedback (FF/FB) controller, a non-homogeneous LQR controller, and the receding horizon control (RHC). The feedforward controller is a model inverse controller. Then, the nhLQR control and RHC controller are designed with the same cost function as the LQR controller. However, due to the time constraints, only the results with the feedforward control and RHC is compared.

To simulate the predictive controller with Lidar preview measurement. A Lidar simulator which is designed by E. Simley is used for extracting of the wind field information generated by the TurbSim. The simulator can perform a rotation scan Lidar and a fixed position

stationary Lidar. To simulate a ZephIR CW Lidar, only one single distance measurement can be specified. Then, to simulate the pulsed Lidar which is based on the model of WindCube, maximum 5 distances could be simultaneously measured. The probe length, and the measurement distances between measurement points could be specified.

The performance of the designed controller was first analysed with a simple hub height only wind speed. These simple wind field includes a step increase on wind speed from cut-in speed 3 m/s until the cut-out speed 25 m/s, and a deterministic gust wind field which is specified by the IEC standard for extreme event analysis. The simulated EOG wind profile has the initial wind speed of 13.4 m/s which is the rated speed +2 m/s. Due to the time constrains, other wind speed specified by IEC standard are not performed. The result from such simple wind conditions show a clear advantages by taking Lidar preview measurement into account. However, due to the Linear model used for designing of the RHC controller, on region 2.5, a bad performance has been observed for the RHC controller. Therefore, a further gain tuning on low speed region is necessary.

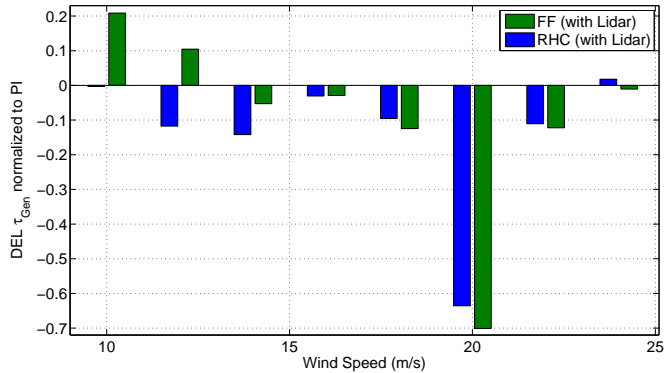
However, the simulation discussed for this nominative model is based on the assumption of the perfect knowledge of the Lidar preview measurement, and no other disturbances come from other submodels of the wind turbine, such as the drivetrain torsion, blade deflection, tower side-by-side deflections, and so on. Therefore, in a real wind turbine operational condition, these assumptions are not realistic.

Finally, on Section.8.4, further simulation have been performed based on the FAST non-linear model within the Simulink environments. The simulation is followed the DLCs about the fatigue loads analysis from the IEC standard. First of all, simulations with the deterministic gust wind model "EOGR+2" have been performed. Unlike the simulations with the reduced nominative model, due to the influences from other unmodelled DOFs, the performances is reduced. But, the Lidar preview measurement still provides benefits to the control performance. Another surprised result from this simulation is the performance of Argument-LQR controller. Even without the Lidar preview information, benefited with the perfect model scheduling, this controller shows an excellent performance, even better than the two Lidar assisted controller.

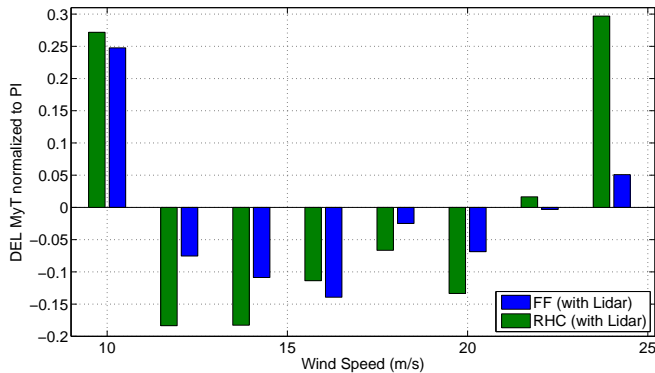
The NTM case is simulated for the DEL analysis with the tool "MCrunch". Based on the IEC standard [85], to perform a DEL analysis of wind turbine, a set of 6-18 different wind profiles with the same turbulence intensity and mean speed are required from the cut-in wind speed until cut-out wind speed. Here in this thesis, due to the limited time constrains, only the pitch control region from 10 to 24 m/s in every 2 m/s steps have been simulated. With each wind speed, 6 different turbulence wind fields were generated by TurbSim with different random seed but the same turbulence category. Then the simulation for each controller are simulated with the same 6 wind profiles in region 3. Therefore, each controller performed 48 simulations and those 48 results are used for analysis.

The presented result given on Section.8.4.2 are the combination with these 48 simulation results for each controller. The standard deviation plots are normalized to the PI baseline controller. Higher value than PI means a worse performance due to the high standard deviations. In contrast, a value less than 1 means a better performance. The results shows a better performance on keeping the rotation speed constant. This is due to a higher RHC controller weights are applied on generator rotation speed error. Since the controller is designed with a Linear model which is linearised at 16 m/s, an excellent performance can

be observed around this speed. But the performance on lower speed and high speed is a not as good as on the set point. Same results can be observed from the DEL plot as shown on Fig.9.3. Therefore, to gain a better performance over the wide operation range, a weight tuning linear RHC or rather a nonlinear RHC controller designed is advanced.



(a) DEL of Generator torque



(b) DEL of Tower fore-aft bending moment

Fig. 9.3.: Damage equivalent loads of generator torque and Tower fore-aft bending moment

9.3. Future works

The present work covered a novel Lidar system design and an industrial friendly collective pitch controller design. For the works on the Lidar system, as shown on Chapter3, there are curtain need for a specified Lidar system which is specialized for turbine control applications. However, current research and development on Lidar system design are not focused on this market. The presented work here, first of all is focused on design of such

Lidar system spatially for the wind turbine control applications. However, the work was stopped on the feasibility studies with simulation and experiments. With this studies, both simulations and experiments have shown the feasibility of designing such a cost efficient Lidar system with low cost broad spectrum laser sources.

However, the experimental test is limited on a diode laser with 810 nm and 532 nm. Then, due to the in lab experiments, a maximum measurement distance have been stopped on 10 meters range. To scale up the laboratory proof-of-concept setup into a prototype system, further challenges need to be considered. On Chapter 6, the sending and receiving optics design with the off-axis parabolic mirror with a center hole shows the best performances. Such system is working better with a shorter distance and a well collimated beam. When operating with a long detection range, such as couple ten meters or hundreds meters, the transmission beam diameter is getting too big which limited the system performance. Therefore, a different design approach need to be checked, such as a free space polarization based circulator could be tested for the performance to obtain a monostatic concept. Furthermore, in order to test the real system design for out door field testing, a prototype system with a 1550 nm laser source need to be designed and built. The laser safety and environment consideration have been briefly discussed on Chapter4, but for the daily operation these effects need to be checked and analysed in details.



Fig. 9.4: A following up setup for out door field testing

For the pitch controller design, the 2-DOF RHC/FB controller has been designed with a gain scheduling RHC with a LPV model. However due to the limited time, only the pitch control region, "Region 3" has been considered in this thesis. For designing of a controller which is suitable for the entire operation region, an extension of the controller to tune and test with the region 2 is needed.

The designed controller, within some working conditions, such as region 2.5 and low wind speed in region 3, the performances are not optimal. Therefore, a further parameter tuning is required. Furthermore, due to the high performance real time industrial control hardware, a nonlinear MPC might be possible to applied for achieving a better performance. The designed controller is based on a nominative model inside of the loop, therefore, the model error directly affects the control performance. A controller based on more DOF model might necessary to be checked for gaining a better performances.

A final goal to the presented work is to reduce of the cost of wind energy. Within this work, due to the limited time, the analysis could not cover the entire DLC cases specified by the IEC standard. In order to perform a whole IEC standard performance analysis, all the required design load cases need to be simulated and analysed.

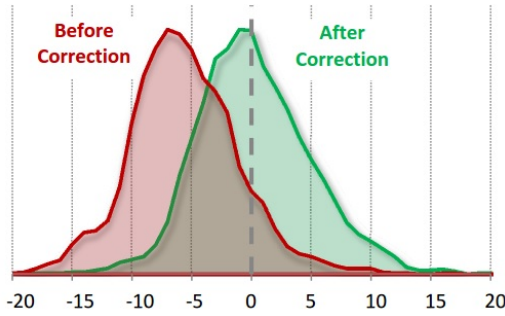


Fig. 9.5: istribution of the 10-minute average yaw error measured before and after correction [132]

Another side effects to be benefit from a Lidar preview is on the Yaw miss alignment. A study have been carried out from FirstWind about using the WindIris two beam Lidar to correct the misalignment of the yaw angle of wind turbines [132]. Based on this study, an average yaw error of 7 degrees during 30 days of observations as shown on Fig.9.5. By correcting of the yaw misalignment with Lidar system, an annual energy production (AEP) of the wind turbine could be increased by 1.8%, which is over 7,000 \$ annual benefit from a 2MW wind turbine. A further study on this economical effect could be worth to check.

Appendix

A. Information for wind turbine modelling

A.1. Aerodynamics of wind turbine

The work principle of HAWT can be described as the stream tube theory (Fig.A.1). The simplest model of the wind turbine is called actuator disc model where the turbine is replaced with a circular disc. The airstream flow with a velocity of U_∞ , air density of ρ , area of the cross-section of A_∞ passes through the disc. When the energy is extracted the wind speed slows down but only the mass of air which has passed through the rotor disc is affected. Assuming that the affected mass of air and the air does not pass through the rotor disc are separated, as shown in Fig.A.1, we use a boundary surface to show the affected air mass and this boundary surface can be extended to form a long stream-tube. No air exchange across the boundary, therefore, the mass flow rate of the air flowing along the stream-tube will be the same for all positions along the stream-tube. The kinetic energy of the air in the stream-tube decreased, therefore, the air slows down and the cross-sectional area will expand to accommodate the slower moving air [23]. Therefore,

$$\rho A_\infty U_\infty = \rho A_D U_D = \rho A_W U_W \quad (\text{A.1})$$

Where, A_D, U_D denotes the cross-sectional area and velocity at the disc position, W refers in the far wake position. Here we consider that the actuator disc induces a velocity variation which must be superimposed on the free stream velocity. We defined the variation of velocity as $-aU_\infty$, a is the axial flow induction factor. The wind velocity at disc is

$$U_D = U_\infty(1 - a) \quad (\text{A.2})$$

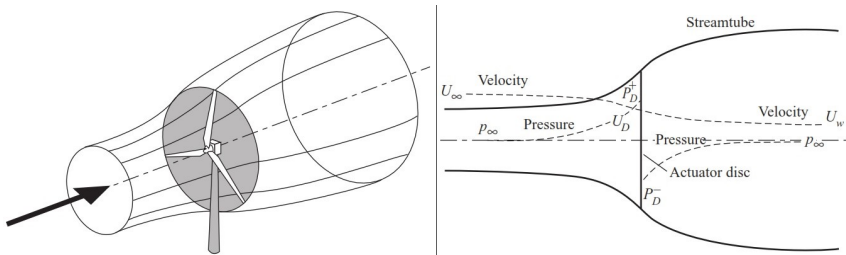


Fig. A.1.: Illustration of the actuator disc model and stream tube theory [59]

Assuming the air flow passing through the disk causes the velocity changes $U_\infty - U_W$. Then, the change of momentum by wind turbine equals to the velocity changes times the mass flow rate.

$$\text{Change of momentum} = (U_\infty - U_W)\rho A_D U_D \quad (\text{A.3})$$

Assuming the change of momentum is caused by the pressure differences through the disc only. For momentum conservation, the force exerted on the turbine is equal to the momentum change between the flow far upstream of the disc to the flow far downstream of the disc. Thus,

$$(P_D^+ - P_D^-)A_D = (U_\infty - U_W)\rho A_D U_\infty(1 - a) \quad (\text{A.4})$$

According to the Bernoulli's principle, for an inviscid flow, an increase in the speed of the flow occurs simultaneously with a decrease in pressure or in the potential energy [10].

$$\frac{1}{2}\rho U^2 + p + \rho gh = \text{const.} \quad (\text{A.5})$$

Therefore, apply the Bernoulli's equation for the airstream flow from upstream and downstream, the energy remains the same as the disk.

$$\frac{1}{2}\rho U_\infty^2 + p_\infty = \frac{1}{2}\rho U_D^2 + P_D^+ \quad (\text{A.6a})$$

$$\frac{1}{2}\rho U_W^2 + p_\infty = \frac{1}{2}\rho U_D^2 + P_D^- \quad (\text{A.6b})$$

Therefore, the pressure changes at the disc position is

$$(P_D^+ - P_D^-) = \frac{1}{2}\rho (U_\infty^2 - U_W^2) \quad (\text{A.7a})$$

$$\frac{1}{2}\rho (U_\infty^2 - U_W^2)A_D = (U_\infty - U_W)\rho A_D U_\infty(1 - a) \quad (\text{A.7b})$$

Therefore,

$$U_W = U_\infty(1 - 2a) \quad (\text{A.8})$$

The force on the air becomes

$$T = (P_D^+ - P_D^-)A_D = 2\rho A_D U_\infty^2 a(1 - a) \quad (\text{A.9})$$

Therefore, the power extracted from the air by the rotor disk is

$$P_{\text{Rtr}} = T U_D = 2\rho A_D U_\infty^3 a(1 - a)^2 \quad (\text{A.10})$$

Then, the power coefficient of wind turbine is given by the power captured by the rotor disc divide by the power available in the air flow. Thus,

$$C_p = \frac{P_{Rtr}}{P_{air\ flow}} = \frac{2\rho A_D U_\infty^3 a(1-a)^2}{\frac{1}{2}\rho A_D U_\infty^3} = 4a(1-a)^2 \quad (A.11)$$

The maximum power efficiency is given as $C_p = \frac{16}{27} \approx 59.3\%$ when $(a = \frac{1}{3})$ which is known as Lanchester-Betz limit [39, 40]. Furthermore, C_p is a nonlinear function of the turbine tip-speed ratio λ_{TSR} and blade pitch angle β (Figure.A.2).

$$\lambda_{TSR} = \frac{\omega_{Rtr} \cdot R_{Rtr}}{U_{Wind}} \quad (A.12)$$

Where, ω_{Rtr} is the rotor rotational speed, U_{wind} is the wind speed, R_{Rtr} is the radius of the rotor or the length of the blade.

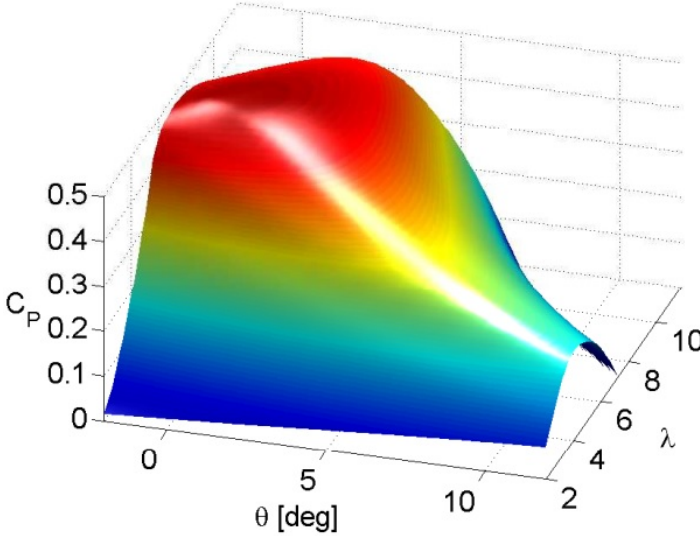


Fig. A.2.: Power coefficient as a function of tip speed ratio and pitch angle [76]

A.2. Properties of NREL 5-MW reference wind turbine

Table.A.1 shows the full properties of the NREL 5-MW baseline reference turbine which is used for the simulation in the presented work. This model is developed by NREL and widely used as a reference model for research and development of turbine control system.

A. Information for wind turbine modelling

Rated power	5 MW	
Rotor orientation, configuration	Upwind, 3 Blades	
Control mode	Variable speed, collective pitch	
Drivetrain mode	High speed, multi-stage gearbox	
Rotor, Hub diameter	126, 3	m
Cut-in, rated, cut-out wind speed	3, 11.4, 25	m/s
Cut-in, rated rotor speed	6.9, 12.1	rpm
Rated tip speed	80	m/s
Overhang, shaft tilt, pre-cone	5 m, 5°, 2.5°	
Rotor mass	110,000	kg
Nacelle mass	240,000	kg
Tower mass	347,460	kg
Drive-train property		
Rated Rotor Speed	12.1	rpm
Rated Generator Speed	1173.7	rpm
Gearbox Ratio	97:1	
Electrical Generator Efficiency	94.4	%
Equivalent Drive-Shaft Torsional-Spring Constant	867,637	kNm/rad
Equivalent Drive-Shaft Torsional-Damp Constant	6,215	kNm/(rad/s)
Fully-Deployed High-Speed Shaft Brake Torque	28,116.2	Nm
High-Speed Shaft Brake Time Constant	0.6	s
Generator inertia	534.116	kgm ²
Rotor inertia	38,768 k	kg · m ²
Total inertia	43,792 k	kg · m ²
Maximum generator torque	47402.97	Nm
Minimum generator torque	0	Nm
Maximum generator torque rate	15	kNm/s
Minimum generator torque rate	-15	kNm/s
Blade properties		
Length	61.5	m
Mass Scaling Factor	4.536 %	%
Overall (Integrated) Mass	17,740	kg
Second Mass Moment of Inertia (w.r.t. Root)	11,776 k	kg · m ²
First Mass Moment of Inertia (w.r.t. Root)	363,231	kgm
CM Location (w.r.t. Root along Preconed Axis)	20.475	m
Structural-Damping Ratio (All Modes)	0.477465	%
Tower		
Tower height above ground	87.6	m
CM Location (w.r.t. Ground along Tower Center-line)	38.234	m
Structural-Damping Ratio (All Modes)	1	%
Vertical Distance along Yaw Axis from Yaw Bearing to Shaft	1.96256	m
Distance along Shaft from Hub Center to Yaw Axis	5.01910	m

Distance along Shaft from Hub Center to Main Bearing	1.912	m
Hub Mass	56,780	kg
Hub Inertia about Low-Speed Shaft	115,926	kg · m ²
Nacelle Mass	240,000	kg
Nacelle Inertia about Yaw Axis	2,607,890	kg · m ²
Nacelle CM Location Downwind of Yaw Axis	1.9	m
Nacelle CM Location above Yaw Bearing	1.75	m
Equivalent Nacelle-Yaw-Actuator Linear-Spring Constant	9,028,320	kNm/rad
Equivalent Nacelle-Yaw-Actuator Linear-Damping Constant	19,160 k	Nm/(rad/s)
Nominal Nacelle-Yaw Rate	0.3	°/s
Natural frequency	0.88	rad/s
Damping factor	0.9	
Maximum blade pitch	90	deg
Minimum blade pitch	-1	deg
Maximum blade pitch	8	deg/s
Minimum blade pitch	-8	deg/s
Baseline control system properties		
Corner Frequency of Generator-Speed Low-Pass Filter	0.25	Hz
Peak Power Coefficient	0.482	
Tip-Speed Ratio at Peak Power Coefficient	7.55	
Rotor-Collective Blade-Pitch Angle at Peak Power Coefficient	0.0	°
Generator-Torque Constant in Region 2	0.0255764	Nm/rpm ²
Rated Mechanical Power	5.29661	MW
Rated Generator Torque	43,093.55	Nm
Transitional Generator Speed between Regions 1 and 1.5	670	rpm
Transitional Generator Speed between Regions 1.5 and 2	871	rpm
Transitional Generator Speed between Regions 2.5 and 3	1,161.963	rpm
Generator Slip Percentage in Region 2.5	10	%
Minimum Blade Pitch for Ensuring Region 3 Torque	1	°
Maximum Generator Torque	47,402.91	Nm
Maximum Generator Torque Rate	15	kNm/s
Proportional Gain at Minimum Blade-Pitch Setting	0.01882681	s
Integral Gain at Minimum Blade-Pitch Setting	0.008068634	
Blade-Pitch Angle at which the Rotor Power Has Doubled	6.302336	°
Minimum Blade-Pitch Setting	0	°



Maximum Blade-Pitch Setting	90	°
Maximum Absolute Blade Pitch Rate	8	°/s
Equivalent Blade-Pitch-Actuator Linear-Spring Constant	971,350	kNm/rad
Equivalent Blade-Pitch-Actuator Linear-Damping Constant	206	kNm/(rad/s)

Table A.1.: Overall properties of the NREL 5-MW baseline reference wind turbine [98]

A.3. Linear models of wind turbines

In chapter 7, a simplest 2-DOF wind turbine linear model has been discussed only taking the rotor rotation and tower fore-aft DOFs into account. However, the real wind turbine is more complex, in this section, complex model by adding drive-train, blade flapwise DOFs and the linearising parameters are shown.

A.3.1. 2-DOF linear model with tower Fore-Aft DOF

Detailed description of the 2-DOF linear model with tower fore-aft DOF has been discussed on Section.7.5.2. Here in this section, the detailed parameter of the model depending on operating wind speed is shown. The system states inputs are defined as

$$\begin{aligned} \Delta x_{2\text{DOF}} &= \begin{bmatrix} \Delta x_{\text{Gen}} & \Delta x_{\text{Tfa}} & \Delta x_{\text{Pitch}} & \Delta x_{\text{GenTq}} \end{bmatrix}^T \\ &= \begin{bmatrix} \Delta \Omega_{\text{Gen}} & \Delta d_{\text{Tfa}} & \Delta \dot{d}_{\text{Tfa}} & \Delta \beta_{\text{Pitch}} & \Delta \dot{\beta}_{\text{Pitch}} & \Delta t_{\text{Gen}} \end{bmatrix}^T \end{aligned} \quad (\text{A.13})$$

The tower fore-aft and generator dynamics model in state space format are given as

$$\begin{aligned} \Delta \dot{x}_{\text{Tfa}} &= \begin{bmatrix} \dot{d}_{\text{Tfa}} \\ \ddot{d}_{\text{Tfa}} \end{bmatrix} = \underbrace{\begin{bmatrix} 0 & 1 \\ -\frac{k_{\text{Twr}}}{M_{\text{Twr}}} & -\frac{c_{\text{Twr}} + \delta f_T / \delta U}{M_{\text{Twr}}} \end{bmatrix}}_{A_{\text{Tfa}}} \begin{bmatrix} d_{\text{Tfa}} \\ \dot{d}_{\text{Tfa}} \end{bmatrix} + \underbrace{\begin{bmatrix} 0 & 0 \\ \frac{\delta f_T / \delta \beta_{\text{Pitch}}}{M_{\text{Twr}}} & 0 \end{bmatrix}}_{A_{\text{Tfa-Pitch}}} \times \\ &\times \begin{bmatrix} \Delta \beta_{\text{Pitch}} \\ \Delta \dot{\beta}_{\text{Pitch}} \end{bmatrix} + \underbrace{\begin{bmatrix} 0 \\ \frac{\delta f_T / \delta U}{M_{\text{Twr}}} \end{bmatrix}}_{\Gamma_{\text{Tfa}}} \Delta v + \underbrace{\begin{bmatrix} 0 \\ \frac{\delta f_T / \delta \Omega_{\text{Rtr}}}{M_{\text{Twr}}} \end{bmatrix}}_{A_{\text{Tfa-Gen}}} \Delta \Omega_{\text{Gen}} \end{aligned} \quad (\text{A.14})$$

$$\begin{aligned} \Delta \dot{x}_{\text{Gen}} &= \underbrace{\frac{\delta \tau_{\text{Rtr}} / \delta \Omega_{\text{Rtr}}}{J_{\text{tot}}}}_{A_{\text{Rtr}}} \Delta x + \underbrace{\begin{bmatrix} \frac{\delta \tau_{\text{Rtr}} / \delta \beta_{\text{Pitch}}}{J_{\text{tot}}} & 0 \end{bmatrix}}_{A_{\text{Rotor-}\beta}} \Delta x_{\text{Pitch}} - \underbrace{\frac{1}{J_{\text{tot}}}}_{A_{\text{Rtr-GenTq}}} \delta \tau_{\text{Gen}} + \underbrace{\frac{\delta \tau_{\text{Rtr}} / \delta U}{J_{\text{tot}}}}_{\Gamma_{\text{Rtr}}} \Delta u_{\text{D}} \end{aligned} \quad (\text{A.15})$$

The 2-DOF tower fore-aft/generator 6-state linearized model in state space is given as

$$\Delta \dot{x}_{2\text{DOF}} = A_{2\text{DOF}} \Delta x_{2\text{DOF}} + B_{2\text{DOF}} \Delta u + \Gamma_{2\text{DOF}} \Delta u_D \quad (\text{A.16})$$

where,

$$A_{2\text{DOF}} = \begin{bmatrix} A_{\text{Rtr}} & 0 & A_{\text{Rtr}-\beta} & A_{\text{Rtr-GenTq}} \\ A_{\text{Tfa-Gen}} & A_{\text{Tfa}} & A_{\text{Tfa}-\beta} & 0 \\ 0 & 0 & A_{\text{Pitch}} & 0 \\ 0 & 0 & 0 & A_{\text{GenTq}} \end{bmatrix} \quad (\text{A.17a})$$

$$B_{2\text{DOF}} = \begin{bmatrix} 0 \\ 0 \\ B_{\text{Pitch}} \\ B_{\text{GenTor}} \end{bmatrix}, \Gamma_{2\text{DOF}} = \begin{bmatrix} \Gamma_{\text{Rtr}} \\ \Gamma_{\text{Tfa}} \\ 0 \\ 0 \end{bmatrix} \quad (\text{A.17b})$$

with,

$$A_{\text{Rtr}} = \frac{\delta \tau_{\text{Rtr}} / \delta \Omega_{\text{Rtr}}}{J_{\text{tot}}}, A_{\text{Rtr}-\beta} = \begin{bmatrix} \frac{\delta \tau_{\text{Rtr}} / \delta \beta_{\text{Pitch}}}{J_{\text{tot}}} & 0 \end{bmatrix} \quad (\text{A.18a})$$

$$A_{\text{Rtr-GenTq}} = -\frac{1}{J_{\text{tot}}}, A_{\text{Tfa-Gen}} = \begin{bmatrix} 0 \\ \frac{\delta f_T / \delta \Omega_{\text{Rtr}}}{M_{\text{Twr}}} \end{bmatrix} \quad (\text{A.18b})$$

$$A_{\text{Tfa}} = \begin{bmatrix} 0 & 1 \\ -\frac{k_{\text{Twr}}}{M_{\text{Twr}}} & -\frac{c_{\text{Twr}} + \delta \tau_T / \delta U}{M_{\text{Twr}}} \end{bmatrix}, A_{\text{Tfa}-\beta} = \begin{bmatrix} 0 & 0 \\ \frac{\delta f_T / \delta \beta_{\text{Pitch}}}{M_{\text{Twr}}} & 0 \end{bmatrix} \quad (\text{A.18c})$$

$$A_{\text{Pitch}} = \begin{bmatrix} 0 & 1 \\ -\omega^2 & -2\omega \zeta \end{bmatrix}, A_{\text{GenTq}} = -\frac{1}{T_e}, B_{\text{Pitch}} = \begin{bmatrix} 0 & 0 \\ \omega^2 & 0 \end{bmatrix} \quad (\text{A.18d})$$

$$B_{\text{GenTq}} = \begin{bmatrix} 0 & \frac{1}{T_e} \end{bmatrix}, \Gamma_{\text{Rtr}} = \frac{\delta \tau_{\text{Rtr}} / \delta U}{J_{\text{tot}}}, \Gamma_{\text{DT}} = \begin{bmatrix} 0 \\ \frac{\delta \tau_{\text{Rtr}} / \delta U}{J_{\text{Rtr}}} \end{bmatrix} \quad (\text{A.18e})$$

Depending on different set point for the linearization, the parameter matrix is varies. Linearized at the setting point with wind speed of 5 m/s, the pitch angle of $\beta_{\text{Pitch}} = 0$, rotor speed of $\Omega_{\text{Rtr}} = 7.51$ rpm. Then the parameter matrix of the model is

$$A|_{U_{\text{REW}}=5} = \begin{bmatrix} -0.0253 & 6.4898 \times 10^{-5} & -0.004 \\ 0 & 0 & 1 \\ 0.2213 & -4.2192 & -0.0861 \end{bmatrix} \quad (\text{A.19a})$$

$$B|_{U_{\text{REW}}=5} = \begin{bmatrix} 0.0246 & -2.2156 \times 10^{-6} \\ 0 & 0 \\ -1.8083 & 0 \end{bmatrix}, \Gamma|_{U_{\text{REWS}}=5} = \begin{bmatrix} 0.0089 \\ 0 \\ 0.124 \end{bmatrix} \quad (\text{A.19b})$$

A. Information for wind turbine modelling

Linearized at $U_{REWS} = 8$ m/s, $\beta_{Pitch} = 0^\circ$, $\Omega_{Rtr} = 9.16$ rpm, which gives the model parameter matrix as

$$A|_{U_{REWS}=8} = \begin{bmatrix} -0.0456 & 2.17 \times 10^{-4} & -0.0086 \\ 0 & 0 & 1 \\ 0.5378 & -4.2192 & -0.1227 \end{bmatrix} \quad (A.20a)$$

$$B|_{U_{REWS}=8} = \begin{bmatrix} -0.0116 & -2.2156 \times 10^{-6} \\ 0 & 0 \\ -3.3702 & 0 \end{bmatrix}, \Gamma|_{U_{REWS}=8} = \begin{bmatrix} 0.0168 \\ 0 \\ 0.1602 \end{bmatrix} \quad (A.20b)$$

Linearized at $U_{REWS} = 11.4$ m/s, $\beta_{Pitch} = 0^\circ$, $\Omega_{Rtr} = 12.1$ rpm, which gives the model parameter matrix as

$$A|_{U_{REWS}=11.4} = \begin{bmatrix} -0.0545 & -4.7197 \times 10^{-4} & -0.0133 \\ 0 & 0 & 1 \\ 0.9249 & -4.2237 & -0.1655 \end{bmatrix} \quad (A.21a)$$

$$B|_{U_{REWS}=11.4} = \begin{bmatrix} -0.0423 & -2.2156 \times 10^{-6} \\ 0 & 0 \\ -6.1452 & 0 \end{bmatrix}, \Gamma|_{U_{REWS}=11.4} = \begin{bmatrix} 0.0233 \\ 0 \\ 0.2036 \end{bmatrix} \quad (A.21b)$$

Linearized at $U_{REWS} = 15$ m/s, $\beta_{Pitch} = 10.44^\circ$, $\Omega_{Rtr} = 12.1$ rpm, which gives the model parameter matrix as

$$A|_{U_{REWS}=15} = \begin{bmatrix} -0.1358 & -5.975 \times 10^{-4} & -0.0226 \\ 0 & 0 & 1 \\ -0.5986 & -4.2215 & -0.2341 \end{bmatrix} \quad (A.22a)$$

$$B|_{U_{REWS}=15} = \begin{bmatrix} -0.8293 & -2.2156 \times 10^{-6} \\ 0 & 0 \\ -8.8124 & 0 \end{bmatrix}, \Gamma|_{U_{REWS}=15} = \begin{bmatrix} 0.0242 \\ 0 \\ 0.1831 \end{bmatrix} \quad (A.22b)$$

Linearized at $U_{REWS} = 18$ m/s, $\beta_{Pitch} = 14.9^\circ$, $\Omega_{Rtr} = 12.1$ rpm, which gives the model parameter matrix as

$$A|_{U_{REWS}=18} = \begin{bmatrix} -0.2424 & -8.518 \times 10^{-4} & -0.027 \\ 0 & 0 & 1 \\ -1.2942 & -4.2215 & -0.2445 \end{bmatrix} \quad (A.23a)$$

$$B|_{U_{REWS}=18} = \begin{bmatrix} -1.1831 & -2.2156 \times 10^{-6} \\ 0 & 0 \\ -9.5235 & 0 \end{bmatrix}, \Gamma|_{U_{REWS}=18} = \begin{bmatrix} 0.0277 \\ 0 \\ 0.1836 \end{bmatrix} \quad (A.23b)$$

Linearized at $U_{\text{REWS}} = 21 \text{ m/s}$, $\beta_{\text{Pitch}} = 18.66^\circ$, $\Omega_{\text{Rtr}} = 12.1 \text{ rpm}$, which gives the model parameter matrix as

$$A|_{U_{\text{REWS}}=21} = \begin{bmatrix} -0.3577 & -0.0012 & -0.0306 \\ 0 & 0 & 1 \\ -1.8198 & -4.2215 & -0.2442 \end{bmatrix} \quad (\text{A.24a})$$

$$B|_{U_{\text{REWS}}=21} = \begin{bmatrix} -1.4765 & -2.2156 \times 10^{-6} \\ 0 & 0 \\ -9.8362 & 0 \end{bmatrix}, \Gamma|_{U_{\text{REWS}}=21} = \begin{bmatrix} 0.0307 \\ 0 \\ 0.1804 \end{bmatrix} \quad (\text{A.24b})$$

Linearized at $U_{\text{REWS}} = 24 \text{ m/s}$, $\beta_{\text{Pitch}} = 22.05^\circ$, $\Omega_{\text{Rtr}} = 12.1 \text{ rpm}$, which gives the model parameter matrix as

$$A|_{U_{\text{REWS}}=24} = \begin{bmatrix} -0.495 & -0.0016 & -0.0343 \\ 0 & 0 & 1 \\ -2.3394 & -4.2224 & -0.2481 \end{bmatrix} \quad (\text{A.25a})$$

$$B|_{U_{\text{REWS}}=24} = \begin{bmatrix} -1.8211 & -2.2156 \times 10^{-6} \\ 0 & 0 \\ -10.457 & 0 \end{bmatrix}, \Gamma|_{U_{\text{REWS}}=24} = \begin{bmatrix} 0.0341 \\ 0 \\ 0.1805 \end{bmatrix} \quad (\text{A.25b})$$

A.3.2. 2-DOF linear model with drivetrain and rotor DOFs

Within this model, the turbine tower, blades are considered as rigid body, only the drivetrain subsystem is trade as flexible. The dynamic system states are defined as

$$\begin{aligned} \Delta x_{2\text{DOF_DT}} &= [\Delta x_{\text{GenDT}} \quad \Delta x_{\text{DT}} \quad \Delta x_{\text{Pitch}} \quad \Delta x_{\text{GenTq}}]^T \\ &= [\Delta \Omega_{\text{Gen}} \quad \Delta \theta_{\text{DT}} \quad \Delta \Omega_{\text{DT}} \quad \Delta \beta_{\text{Pitch}} \quad \Delta \dot{\beta}_{\text{Pitch}} \quad \Delta t_{\text{Gen}}]^T \end{aligned} \quad (\text{A.26})$$

The state space representation of the 2DOF linear model is given as

$$\Delta \dot{x}_{2\text{DOF_DT}} = A_{2\text{DOF_DT}} \Delta x_{2\text{DOF_DT}} + B_{2\text{DOF_DT}} \Delta u + \Gamma_{2\text{DOF_DT}} \Delta v \quad (\text{A.27})$$

Adding extended controllable system states, $x_{\text{ctr}} = [\beta_{\text{Pitch}} \quad \dot{\beta}_{\text{Pitch}} \quad \tau_{\text{Gen}}]^T$, into system

$$\Delta \dot{x} = \begin{bmatrix} A_{\text{Gen}} & B_{\text{Gen}} & 0 \\ 0 & A_{\text{Pitch}} & 0 \\ 0 & 0 & A_{\text{GenTq}} \end{bmatrix} \Delta x + \begin{bmatrix} 0 \\ B_{\text{Pitch}} \\ B_{\text{GenTor}} \end{bmatrix} \Delta u + \begin{bmatrix} \Gamma_{\text{Gen}} \\ 0 \\ 0 \end{bmatrix} \Delta v \quad (\text{A.28})$$

where,

$$A_{2DOF_DT} = \begin{bmatrix} 0 & A_{Gen-DT} & 0 & A_{Gen-GenTq} \\ A_{DT-Gen} & A_{DT} & A_{DT-Pitch} & A_{DT-GenTq} \\ 0 & 0 & A_{Pitch} & 0 \\ 0 & 0 & 0 & A_{GenTq} \end{bmatrix}, \quad (A.29a)$$

$$B_{2DOF_DT} = \begin{bmatrix} 0 \\ 0 \\ B_{Pitch} \\ B_{GenTq} \end{bmatrix}, \Gamma_{2DOF_DT} = \begin{bmatrix} 0 \\ \Gamma_{DT} \\ 0 \\ 0 \end{bmatrix} \quad (A.29b)$$

with

$$A_{Gen-DT} = \begin{bmatrix} \frac{k_{DT}}{N_{Gear}^2 J_{Gen}} & \frac{c_{DT}}{N_{Gear}^2 J_{Gen}} \end{bmatrix}, A_{Gen-GenTq} = -\frac{1}{N_{Gear} J_{Gen}} \quad (A.30a)$$

$$A_{DT} = \begin{bmatrix} 0 & 1 \\ -\left(\frac{k_{DT}}{J_{Rtr}} + \frac{k_{DT}}{N_{Gear}^2 J_{Gen}}\right) & -\left(\frac{c_{DT} - d_{T_{Rtr}}/d\Omega_{Rtr}}{J_{Rtr}} + \frac{c_{DT}}{N_{Gear}^2 J_{Gen}}\right) \end{bmatrix} \quad (A.30b)$$

$$A_{DT-Gen} = \begin{bmatrix} 0 \\ \frac{d_{T_{Rtr}}/d\Omega_{Rtr}}{J_{Rtr}} \end{bmatrix}, A_{DT-Pitch} = \begin{bmatrix} 0 & 0 \\ \frac{d_{T_{Rtr}}/d\beta_{Pitch}}{J_{Rtr}} & 0 \end{bmatrix} \quad (A.30c)$$

$$A_{DT-GenTq} = \begin{bmatrix} 0 \\ -\frac{1}{N_{Gear} J_{Gen}} \end{bmatrix}, A_{Pitch} = \begin{bmatrix} 0 & 1 \\ -\omega^2 & -2\omega\zeta \end{bmatrix}, A_{GenTq} = -\frac{1}{T_e} \quad (A.30d)$$

$$B_{Pitch} = \begin{bmatrix} 0 & 0 \\ \omega^2 & 0 \end{bmatrix}, B_{GenTq} = \begin{bmatrix} 0 & \frac{1}{T_e} \end{bmatrix}, \Gamma_{DT} = \begin{bmatrix} 0 \\ \frac{d_{T_{Rtr}}/dU}{J_{Rtr}} \end{bmatrix} \quad (A.30e)$$

Depending on different set point for the linearization, the parameter matrix is varies. Linearized at the setting point with wind speed of 5 m/s, the pitch angle of $\beta_{Pitch} = 0$, rotor speed of $\Omega_{Rtr} = 7.51$ rpm. The linearized states parameter matrix of the model is

$$A|_{U_{REWS}=5} = \begin{bmatrix} 0 & 172.83 & 1.238 & 0 & 0 & -1.93 \times 10^{-5} \\ 0 & 0 & 1 & 0 & 1 & 0 \\ -0.029 & -195 & -1.427 & 0.0278 & 0 & 1.93 \times 10^{-5} \\ 0 & 0 & 0 & 0 & 1 & 0 \\ 0 & 0 & 0 & -0.7744 & -1.584 & 0 \\ 0 & 0 & 0 & 0 & 0 & -10 \end{bmatrix} \quad (A.31a)$$

$$B|_{U_{REWS}=5} = \begin{bmatrix} 0 & 0 \\ 0 & 0 \\ 0 & 0 \\ 0 & 0 \\ 0.7744 & 0 \\ 0 & 10 \end{bmatrix}, \Gamma|_{U_{REWS}=5} = \begin{bmatrix} 0 \\ 0 \\ 0.0101 \\ 0 \\ 0 \\ 0 \end{bmatrix} \quad (A.31b)$$

Linearized at $U_{\text{REWS}} = 8 \text{ m/s}$, $\beta_{\text{Pitch}} = 0^\circ$, $\Omega_{\text{Rtr}} = 9.16 \text{ rpm}$, which gives the states parameter matrix as

$$A|_{U_{\text{REWS}}=8} = \begin{bmatrix} 0 & 172.83 & 1.238 & 0 & 0 & -1.93 \times 10^{-5} \\ 0 & 0 & 1 & 0 & 1 & 0 \\ -0.0517 & -195 & -1.45 & -0.0131 & 0 & 1.93 \times 10^{-5} \\ 0 & 0 & 0 & 0 & 1 & 0 \\ 0 & 0 & 0 & -0.7744 & -1.584 & 0 \\ 0 & 0 & 0 & 0 & 0 & -10 \end{bmatrix}, \quad (\text{A.32a})$$

$$B|_{U_{\text{REWS}}=8} = \begin{bmatrix} 0 & 0 \\ 0 & 0 \\ 0 & 0 \\ 0 & 0 \\ 0.7744 & 0 \\ 0 & 10 \end{bmatrix}, \quad \Gamma|_{U_{\text{REWS}}=8} = \begin{bmatrix} 0 \\ 0 \\ 0.019 \\ 0 \\ 0 \\ 0 \end{bmatrix} \quad (\text{A.32b})$$

Linearized at $U_{\text{REWS}} = 11.4 \text{ m/s}$, $\beta_{\text{Pitch}} = 0^\circ$, $\Omega_{\text{Rtr}} = 12.1 \text{ rpm}$ which gives the states parameter matrix as

$$A|_{U_{\text{REWS}}=11.4} = \begin{bmatrix} 0 & 172.83 & 1.238 & 0 & 0 & -1.93 \times 10^{-5} \\ 0 & 0 & 1 & 0 & 0 & 0 \\ -0.0617 & -195.21 & -1.46 & -0.0477 & 0 & 1.93 \times 10^{-5} \\ 0 & 0 & 0 & 0 & 1 & 0 \\ 0 & 0 & 0 & -0.7744 & -1.584 & 0 \\ 0 & 0 & 0 & 0 & 0 & -10 \end{bmatrix}, \quad (\text{A.33a})$$

$$B|_{U_{\text{REWS}}=11.4} = \begin{bmatrix} 0 & 0 \\ 0 & 0 \\ 0 & 0 \\ 0 & 0 \\ 0.7744 & 0 \\ 0 & 10 \end{bmatrix}, \quad \Gamma|_{U_{\text{REWS}}=11.4} = \begin{bmatrix} 0 \\ 0 \\ 0.0263 \\ 0 \\ 0 \\ 0 \end{bmatrix} \quad (\text{A.33b})$$

A. Information for wind turbine modelling

Linearized at $U_{REWS} = 15 \text{ m/s}$, $\beta_{Pitch} = 10.44^\circ$, $\Omega_{Rtr} = 12.1 \text{ rpm}$ which gives the states parameter matrix as

$$A|_{U_{REWS}=15} = \begin{bmatrix} 0 & 172.83 & 1.2378 & 0 & 0 & -1.93 \times 10^{-5} \\ 0 & 0 & 1 & 0 & 0 & 0 \\ -0.1535 & -195.21 & -1.5515 & -0.9367 & 0 & 1.93 \times 10^{-5} \\ 0 & 0 & 0 & 0 & 1 & 0 \\ 0 & 0 & 0 & -0.7744 & -1.584 & 0 \\ 0 & 0 & 0 & 0 & 0 & -10 \end{bmatrix}, \quad (A.34a)$$

$$B|_{U_{REWS}=15} = \begin{bmatrix} 0 & 0 \\ 0 & 0 \\ 0 & 0 \\ 0 & 0 \\ 0.7744 & 0 \\ 0 & 10 \end{bmatrix}, \quad \Gamma|_{U_{REWS}=15} = \begin{bmatrix} 0 \\ 0 \\ 0.0273 \\ 0 \\ 0 \\ 0 \end{bmatrix} \quad (A.34b)$$

Linearized at $U = 18 \text{ m/s}$, $\beta_{Pitch} = 14.9^\circ$, $\Omega_{Rtr} = 12.1 \text{ rpm}$ which gives the states parameter matrix as

$$A|_{U_{REWS}=18} = \begin{bmatrix} 0 & 172.83 & 1.2382 & 0 & 0 & -1.93 \times 10^{-5} \\ 0 & 0 & 1 & 0 & 0 & 0 \\ -0.2742 & -195.21 & -1.6724 & -1.3364 & 0 & 1.93 \times 10^{-5} \\ 0 & 0 & 0 & 0 & 1 & 0 \\ 0 & 0 & 0 & -0.7744 & -1.584 & 0 \\ 0 & 0 & 0 & 0 & 0 & -10 \end{bmatrix} \quad (A.35a)$$

$$B|_{U_{REWS}=18} = \begin{bmatrix} 0 & 0 \\ 0 & 0 \\ 0 & 0 \\ 0 & 0 \\ 0.7744 & 0 \\ 0 & 10 \end{bmatrix}, \quad \Gamma|_{U_{REWS}=18} = \begin{bmatrix} 0 \\ 0 \\ 0.0313 \\ 0 \\ 0 \\ 0 \end{bmatrix} \quad (A.35b)$$

Linearized at $U_{REWS} = 21$ m/s, $\beta_{Pitch} = 18.66^\circ$, $\Omega_{Rtr} = 12.1$ rpm which gives the states parameter matrix as

$$A|_{U_{REWS}=21} = \begin{bmatrix} 0 & 172.83 & 1.2377 & 0 & 0 & -1.93 \times 10^{-5} \\ 0 & 0 & 1 & 0 & 0 & 0 \\ -0.4042 & -195.21 & -1.8021 & -1.6678 & 0 & 1.93 \times 10^{-5} \\ 0 & 0 & 0 & 0 & 1 & 0 \\ 0 & 0 & 0 & -0.7744 & -1.584 & 0 \\ 0 & 0 & 0 & 0 & 0 & -10 \end{bmatrix} \quad (A.36a)$$

$$B|_{U_{REWS}=21} = \begin{bmatrix} 0 & 0 \\ 0 & 0 \\ 0 & 0 \\ 0 & 0 \\ 0.7744 & 0 \\ 0 & 10 \end{bmatrix}, \Gamma|_{U_{REWS}=21} = \begin{bmatrix} 0 \\ 0 \\ 0.0347 \\ 0 \\ 0 \\ 0 \end{bmatrix} \quad (A.36b)$$

Linearized at $U_{REWS} = 24$ m/s, $\beta_{Pitch} = 22.05^\circ$, $\Omega_{Rtr} = 12.1$ rpm which gives the states parameter matrix as

$$A|_{U_{REWS}=24} = \begin{bmatrix} 0 & 172.83 & 1.238 & 0 & 0 & -1.93 \times 10^{-5} \\ 0 & 0 & 1 & 0 & 0 & 0 \\ -0.5591 & -195.21 & -1.9573 & -2.057 & 0 & 1.93 \times 10^{-5} \\ 0 & 0 & 0 & 0 & 1 & 0 \\ 0 & 0 & 0 & -0.7744 & -1.584 & 0 \\ 0 & 0 & 0 & 0 & 0 & -10 \end{bmatrix}, \quad (A.37a)$$

$$B|_{U_{REWS}=24} = \begin{bmatrix} 0 & 0 \\ 0 & 0 \\ 0 & 0 \\ 0 & 0 \\ 0.7744 & 0 \\ 0 & 10 \end{bmatrix}, \Gamma|_{U_{REWS}=24} = \begin{bmatrix} 0 \\ 0 \\ 0.0385 \\ 0 \\ 0 \\ 0 \end{bmatrix} \quad (A.37b)$$

A.3.3. 3DOF linear model with tower fore-aft, drivetrain and rotor DOFs

Assuming the blades are rigid, in addition to the flexible tower, the drive train is considered as flexible. The dynamic system states are defined as

$$\begin{aligned} \Delta x_{3DOF} &= [\Delta x_{GenDT} \quad \Delta x_{Tfa} \quad \Delta x_{DT} \quad \Delta x_{Pitch} \quad \Delta x_{GenTq}]^T \\ &= [\Delta \Omega_{Gen} \quad \Delta x_{Tfa} \quad \Delta d_{Tfa} \quad \Delta \dot{d}_{Tfa} \quad \Delta \Omega_{DT} \quad \Delta \beta_{Pitch} \quad \Delta \dot{\beta}_{Pitch} \quad \Delta \tau_{Gen}]^T \end{aligned} \quad (A.38)$$

The state space representation of drivetrain shaft dynamics is given as

$$\begin{aligned}
\Delta \dot{x}_{DT} = \begin{bmatrix} \Delta \dot{\theta}_{DT} \\ \Delta \dot{\Omega}_{DT} \end{bmatrix} &= \underbrace{\begin{bmatrix} 0 & 1 \\ -\left(\frac{k_{DT}}{J_{Rtr}} + \frac{k_{DT}}{N_{Gear}^2 J_{Gen}}\right) & -\left(\frac{c_{DT} - \delta \tau_{Rtr} / \delta \Omega_{Rtr}}{J_{Rtr}} + \frac{c_{DT}}{N_{Gear}^2 J_{Gen}}\right) \end{bmatrix}}_{A_{DT}} \times \\
&\times \begin{bmatrix} \Delta \theta_{DT} \\ \Delta \Omega_{DT} \end{bmatrix} + \underbrace{\begin{bmatrix} 0 & 0 \\ \frac{\delta \tau_{Rtr} / \delta \beta_{Pitch}}{J_{Rtr}} & 0 \end{bmatrix}}_{A_{DT-Pitch}} \begin{bmatrix} \Delta \beta_{Pitch} \\ \Delta \dot{\beta}_{Pitch} \end{bmatrix} + \underbrace{\begin{bmatrix} 0 \\ -\frac{1}{N_{Gear} J_{Gen}} \end{bmatrix}}_{A_{DT-GenTq}} \Delta \tau_{Gen} \\
&+ \underbrace{\begin{bmatrix} 0 \\ \frac{\delta \tau_{Rtr} / \delta U}{J_{Rtr}} \end{bmatrix}}_{\Gamma_{DT}} \Delta v + \underbrace{\begin{bmatrix} 0 \\ \frac{\delta \tau_{Rtr} / \delta \Omega_{Rtr}}{J_{Rtr}} \end{bmatrix}}_{A_{DT-Gen}} \Delta \Omega_{Gen}
\end{aligned} \tag{A.39}$$

The linearised EoM of the generator with flexible drivetrain can be written as

$$\Delta \dot{x}_{GenDT} = \delta \dot{\Omega}_{Gen} = \underbrace{-\frac{1}{N_{Gear} J_{Gen}}}_{A_{Gen-GenTq}} \Delta \tau_{Gen} + \underbrace{\begin{bmatrix} \frac{k_{DT}}{N_{Gear}^2 J_{Gen}} & \frac{c_{DT}}{N_{Gear}^2 J_{Gen}} \end{bmatrix}}_{A_{Gen-DT}} \begin{bmatrix} \Delta \theta_{DT} \\ \Delta \Omega_{DT} \end{bmatrix} \tag{A.40}$$

Therefore, the state space representation of the 2DOF linear model is given as

$$\Delta \dot{x}_{3DOF} = A_{3DOF} \Delta x_{3DOF} + B_{3DOF} \Delta u + \Gamma_{3DOF} \Delta v \tag{A.41}$$

where,

$$A_{3DOF} = \begin{bmatrix} 0 & A_{Gen-DT} & 0 & A_{Gen-GenTq} \\ A_{DT-Gen} & A_{DT} & A_{DT-Pitch} & A_{DT-GenTq} \\ 0 & 0 & A_{Pitch} & 0 \\ 0 & 0 & 0 & A_{GenTq} \end{bmatrix} \tag{A.42a}$$

$$B_{3DOF} = \begin{bmatrix} 0 \\ 0 \\ B_{Pitch} \\ B_{GenTq} \end{bmatrix}, \quad \Gamma_{3DOF} = \begin{bmatrix} 0 \\ \Gamma_{DT} \\ 0 \\ 0 \end{bmatrix} \tag{A.42b}$$

with,

$$A_{\text{Gen-DT}} = \begin{bmatrix} \frac{k_{\text{DT}}}{N_{\text{Gear}}^2 J_{\text{Gen}}} & \frac{c_{\text{DT}}}{N_{\text{Gear}}^2 J_{\text{Gen}}} \end{bmatrix}, A_{\text{Gen-GenTq}} = -\frac{1}{N_{\text{Gear}} J_{\text{Gen}}} \quad (\text{A.43a})$$

$$A_{\text{DT}} = \begin{bmatrix} 0 & 1 \\ -\left(\frac{k_{\text{DT}}}{J_{\text{Rtr}}} + \frac{k_{\text{DT}}}{N_{\text{Gear}}^2 J_{\text{Gen}}}\right) & -\left(\frac{c_{\text{DT}} - \delta \tau_{\text{Rtr}} / \delta \Omega_{\text{Rtr}}}{J_{\text{Rtr}}} + \frac{c_{\text{DT}}}{N_{\text{Gear}}^2 J_{\text{Gen}}}\right) \end{bmatrix} \quad (\text{A.43b})$$

$$A_{\text{DT-Gen}} = \begin{bmatrix} 0 \\ \frac{\delta \tau_{\text{Rtr}} / \delta \Omega_{\text{Rtr}}}{J_{\text{Rtr}}} \end{bmatrix}, A_{\text{DT-Pitch}} = \begin{bmatrix} 0 & 0 \\ \frac{\delta \tau_{\text{Rtr}} / \delta \beta_{\text{Pitch}}}{J_{\text{Rtr}}} & 0 \end{bmatrix} \quad (\text{A.43c})$$

$$A_{\text{DT-GenTq}} = \begin{bmatrix} 0 \\ -\frac{1}{N_{\text{Gear}} J_{\text{Gen}}} \end{bmatrix}, A_{\text{Pitch}} = \begin{bmatrix} 0 & 1 \\ -\omega^2 & -2\omega \zeta \end{bmatrix}, A_{\text{GenTq}} = -\frac{1}{T_e} \quad (\text{A.43d})$$

$$B_{\text{Pitch}} = \begin{bmatrix} 0 & 0 \\ \omega^2 & 0 \end{bmatrix}, B_{\text{GenTor}} = \begin{bmatrix} 0 & \frac{1}{T_e} \end{bmatrix}, \Gamma_{\text{DT}} = \begin{bmatrix} 0 \\ \frac{\delta \tau_{\text{Rtr}} / \delta U}{J_{\text{Rtr}}} \end{bmatrix} \quad (\text{A.43e})$$

Depending on different operation points for processing the linearisation, the parameter matrix are various. Since the actuator models are independent on the DOF of system structure models. To make system simple, following in this section, only the parameters of the 3DOF structure models are discussed. Linearized at the setting point with wind speed of 5 m/s, the pitch angle of $\beta_{\text{Pitch}} = 0$, rotor speed of $\Omega_{\text{Rtr}} = 7.51$ rpm. Then the parameter matrix of the model is

$$A|_{U_{\text{REWS}}=5} = \begin{bmatrix} 3.65 \times 10^{-4} & 0 & 0 & 172.83 & 1.238 \\ 0 & 0 & 1 & 0 & 0 \\ 0.22 & -4.22 & -0.086 & -1.33 \times 10^{-6} & 0.22 \\ 0 & 0 & 0 & 0 & 1 \\ -0.029 & -7.33 \times 10^{-5} & -0.0045 & -195.21 & -1.427 \end{bmatrix}, \quad (\text{A.44a})$$

$$B|_{U_{\text{REWS}}=5} = \begin{bmatrix} -1.93 \times 10^{-5} & -5.5334 \times 10^{-6} \\ 0 & 0 \\ 0 & -1.81 \\ 0 & 0 \\ 1.93 \times 10^{-5} & 0.0278 \end{bmatrix}, \Gamma|_{U_{\text{REWS}}=5} = \begin{bmatrix} 0 \\ 0 \\ 0.124 \\ 0 \\ 0.0101 \end{bmatrix} \quad (\text{A.44b})$$

Linearized at $U_{REWS} = 8 \text{ m/s}$, $\beta_{Pitch} = 0^\circ$, $\Omega_{Rtr} = 9.16 \text{ rpm}$, which gives the model status parameter matrix as

$$A|_{U_{REWS}=8} = \begin{bmatrix} -2.27 \times 10^{-4} & 0 & 0 & 172.83 & 1.238 \\ 0 & 0 & 1 & 0 & 0 \\ 0.5378 & -4.2192 & -0.1227 & -1.5561 \times 10^{-5} & 0.5378 \\ 0 & 0 & 0 & 0 & 1 \\ -0.0517 & -2.45 \times 10^{-4} & -0.0098 & -195.2126 & -1.4499 \end{bmatrix}, \quad (\text{A.45a})$$

$$B|_{U_{REWS}=8} = \begin{bmatrix} -1.93 \times 10^{-5} & -5.53 \times 10^{-7} \\ 0 & 0 \\ 0 & -3.37 \\ 0 & 0 \\ 1.93 \times 10^{-5} & -0.0131 \end{bmatrix}, \quad \Gamma|_{U_{REWS}=8} = \begin{bmatrix} 0.0 \\ 0 \\ 0.16 \\ 0 \\ 0.19 \end{bmatrix} \quad (\text{A.45b})$$

Linearizing at $U_{REWS} = 11.4 \text{ m/s}$, $\beta_{Pitch} = 0^\circ$, $\Omega_{Rtr} = 12.1 \text{ rpm}$, which gives the linearised model status parameter matrix as

$$A|_{U_{REWS}=11.4} = \begin{bmatrix} -1.22 \times 10^{-4} & 0 & 0 & 172.83 & 1.238 \\ 0 & 0 & 1 & 0 & 0 \\ 0.9249 & -4.2237 & -0.1655 & 2.6 \times 10^{-5} & 0.9249 \\ 0 & 0 & 0 & 0 & 1 \\ -0.0617 & -5.331 \times 10^{-4} & -0.0151 & -195.2126 & -1.46 \end{bmatrix} \quad (\text{A.46a})$$

$$B|_{U_{REWS}=11.4} = \begin{bmatrix} -1.93 \times 10^{-5} & 0 \\ 0 & 0 \\ 0 & -6.1452 \\ 0 & 0 \\ 1.93 \times 10^{-5} & -0.0477 \end{bmatrix}, \quad \Gamma|_{U_{REWS}=11.4} = \begin{bmatrix} 0 \\ 0 \\ 0.2036 \\ 0 \\ 0.0263 \end{bmatrix} \quad (\text{A.46b})$$

Linearizing at $U_{REWS} = 13 \text{ m/s}$, $\beta_{Pitch} = 6.615^\circ$, $\Omega_{Rtr} = 12.1 \text{ rpm}$, which gives the linearised model status parameter matrix as

$$A|_{U_{REWS}=13} = \begin{bmatrix} -9.96 \times 10^{-5} & 0 & 0 & 172.83 & 1.238 \\ 0 & 0 & 1 & 0 & 0 \\ -0.0207 & -4.2215 & -0.2216 & 3.09 \times 10^{-5} & -0.0207 \\ 0 & 0 & 0 & 0 & 1 \\ -0.0903 & -5.4 \times 10^{-4} & -0.022 & -195.2126 & -1.4886 \end{bmatrix} \quad (\text{A.47a})$$

$$B|_{U_{REWS}=13} = \begin{bmatrix} -1.93 \times 10^{-5} & 0 \\ 0 & 0 \\ 0 & -8.2203 \\ 0 & 0 \\ 1.93 \times 10^{-5} & -0.6437 \end{bmatrix}, \quad \Gamma|_{U_{REWS}=13} = \begin{bmatrix} 0 \\ 0 \\ 0.1859 \\ 0 \\ 0.0254 \end{bmatrix} \quad (\text{A.47b})$$

Linearising at $U_{REWS} = 15$ m/s, $\beta_{Pitch} = 10.44^\circ$, $\Omega_{Rtr} = 12.1$ rpm, which gives the linearised model status parameter matrix as

$$A|_{U_{REWS}=15} = \begin{bmatrix} 9.96 \times 10^{-5} & 0 & 0 & 172.83 & 1.238 \\ 0 & 0 & 1 & 0 & 0 \\ 0.5986 & -4.2215 & -0.2341 & -4.86 \times 10^{-6} & -0.5986 \\ 0 & 0 & 0 & 0 & 1 \\ -0.1535 & -6.75 \times 10^{-4} & -0.0256 & -195.2126 & -1.5515 \end{bmatrix} \quad (A.48a)$$

$$B|_{U_{REWS}=15} = \begin{bmatrix} -1.93 \times 10^{-5} & 0 \\ 0 & 0 \\ 0 & -8.8124 \\ 0 & 0 \\ 1.93 \times 10^{-5} & -0.9367 \end{bmatrix}, \Gamma|_{U_{REWS}=15} = \begin{bmatrix} 0 \\ 0 \\ 0.1831 \\ 0 \\ 0.0273 \end{bmatrix} \quad (A.48b)$$

Linearising at $U_{REWS} = 18$ m/s, $\beta_{Pitch} = 14.9^\circ$, $\Omega_{Rtr} = 12.1$ rpm, which gives the linearised model status parameter matrix as

$$A|_{U_{REWS}=18} = \begin{bmatrix} 3.32 \times 10^{-4} & 0 & 0 & 172.8287 & 1.2382 \\ 0 & 0 & 1 & 0 & 0 \\ -1.2942 & -4.2215 & -0.2445 & 1.75 \times 10^{-6} & -1.2942 \\ 0 & 0 & 0 & 0 & 1 \\ -0.2742 & -9.62 \times 10^{-4} & -0.0305 & -195.2126 & -1.6724 \end{bmatrix} \quad (A.49a)$$

$$B|_{U_{REWS}=18} = \begin{bmatrix} -1.93 \times 10^{-5} & 0 \\ 0 & 0 \\ 0 & -9.5236 \\ 0 & 0 \\ 1.93 \times 10^{-5} & -1.3364 \end{bmatrix}, \Gamma|_{U_{REWS}=18} = \begin{bmatrix} 0 \\ 0 \\ 0.1836 \\ 0 \\ 0.0313 \end{bmatrix} \quad (A.49b)$$

Linearizing at $U_{REWS} = 21$ m/s, $\beta_{Pitch} = 18.66^\circ$, $\Omega_{Rtr} = 12.1$ rpm, which gives the linearised model status parameter matrix as

$$A|_{U_{REWS}=21} = \begin{bmatrix} 1.66 \times 10^{-4} & 0 & 0 & 172.8287 & 1.2377 \\ 0 & 0 & 1 & 0 & 0 \\ -1.8198 & -4.2215 & -0.2442 & -7.26 \times 10^{-6} & -1.8198 \\ 0 & 0 & 0 & 0 & 1 \\ -0.4042 & -0.0013 & -0.0345 & -195.2126 & -1.8021 \end{bmatrix} \quad (A.50a)$$

$$B|_{U_{REWS}=21} = \begin{bmatrix} -1.93 \times 10^{-5} & 5.5334 \times 10^{-5} \\ 0 & 0 \\ 0 & -9.8362 \\ 0 & 0 \\ 1.93 \times 10^{-5} & -1.6678 \end{bmatrix}, \Gamma|_{U_{REWS}=21} = \begin{bmatrix} 0 \\ 0 \\ 0.1804 \\ 0 \\ 0.0347 \end{bmatrix} \quad (A.50b)$$

Linearising at $U_{REWS} = 24$ m/s, $\beta_{Pitch} = 22.05^\circ$, $\Omega_{Rtr} = 12.1$ rpm, which gives the linearised model status parameter matrix as

$$A|_{U_{REWS}=24} = \begin{bmatrix} 0 & 0 & 0 & 172.8287 & 1.2379 \\ 0 & 0 & 1 & 0 & 0 \\ -2.3394 & -4.2224 & -0.2481 & -1.66 \times 10^{-5} & -2.3394 \\ 0 & 0 & 0 & 0 & 1 \\ -0.5591 & -0.0018 & -0.0388 & -195.2163 & -1.9573 \end{bmatrix} \quad (A.51a)$$

$$B|_{U_{REWS}=24} = \begin{bmatrix} -1.93 \times 10^{-5} & 0 \\ 0 & 0 \\ 0 & -10.457 \\ 0 & 0 \\ 1.93 \times 10^{-5} & -2.057 \end{bmatrix}, \Gamma|_{U_{REWS}=24} = \begin{bmatrix} 0 \\ 0 \\ 0.1805 \\ 0 \\ 0.0385 \end{bmatrix} \quad (A.51b)$$

A.3.4. Linear 4DOF model by adding collective pitch flapwise DOF

Individual sub-models have been discussed, here combining those sub-model together to formulate the full states model, which states vector are defined as

$$\begin{aligned} x &= [x_{Tfa} \quad x_{Gen} \quad x_{DT} \quad x_{Bfl} \quad x_{Pitch} \quad x_{GenTq}]^T \\ &= [d_{Tfa} \quad \dot{d}_{Tfa} \quad \Omega_{Gen} \quad \theta_{DT} \quad \dot{\theta}_{DT} \quad d_{Bfl} \quad \dot{d}_{Bfl} \quad \beta_{Pitch} \quad \dot{\beta}_{Pitch} \quad t_{Gen}]^T \end{aligned} \quad (A.52)$$

The input vector is defined as

$$u = [\beta_{ref} \quad t_{ref}]^T \quad (A.53)$$

The linearised 4DOF full states model of wind turbine system is given as

$$\Delta \dot{x} = A(x^*, u^*, U_{rel}^*) \Delta x + B(x^*, u^*, U_{rel}^*) \Delta u + \Gamma(x^*, u^*, U_{rel}^*) \Delta v \quad (A.54)$$

Where $U_{rel}^* = U^* - \dot{d}_{Twr} - \dot{d}_{Bfl}$. Where,

$$A = \begin{bmatrix} A_{Tfa} & A_{Tfa-Gen} & 0 & 0 & A_{Tfa-Pitch} & 0 \\ 0 & 0 & A_{Gen-DT} & 0 & 0 & A_{Gen-GenTq} \\ 0 & A_{DT-Gen} & A_{DT} & 0 & A_{DT-Pitch} & A_{DT-GenTq} \\ 0 & A_{Bfl-Gen} & 0 & A_{Bfl} & A_{Bfl-Pitch} & 0 \\ 0 & 0 & 0 & 0 & A_{Pitch} & 0 \\ 0 & 0 & 0 & 0 & 0 & A_{GenTq} \end{bmatrix} \quad (A.55a)$$

$$B = \begin{bmatrix} 0 \\ 0 \\ 0 \\ 0 \\ B_{Pitch} \\ B_{GenTor} \end{bmatrix}, \Gamma = \begin{bmatrix} \Gamma_{Tfa} \\ 0 \\ \Gamma_{DT} \\ \Gamma_{Bfl} \\ 0 \\ 0 \end{bmatrix} \quad (A.55b)$$

With,

$$A_{\text{Tfa}} = \begin{bmatrix} 0 & 1 \\ -\frac{k_{\text{Twr}}}{M_{\text{Twr}}} & -\frac{c_{\text{Tower}} + \delta f_T / \delta U}{M_{\text{Twr}}} \end{bmatrix}, A_{\text{Tfa-Gen}} = \begin{bmatrix} 0 \\ \frac{\delta f_T / \delta \Omega_{\text{Rtr}}}{M_{\text{Twr}}} \end{bmatrix} \quad (\text{A.56a})$$

$$A_{\text{Tfa-Pitch}} = \begin{bmatrix} 0 & 0 \\ \frac{\delta f_T / \delta \beta_{\text{Pitch}}}{M_{\text{Twr}}} & 0 \end{bmatrix}, A_{\text{Gen-DT}} = \begin{bmatrix} \frac{k_{\text{DT}}}{N_{\text{Gear}}^2 J_{\text{Gen}}} & \frac{c_{\text{DT}}}{N_{\text{Gear}}^2 J_{\text{Gen}}} \end{bmatrix} \quad (\text{A.56b})$$

$$A_{\text{Gen-GenTq}} = -\frac{1}{N_{\text{Gear}} J_{\text{Gen}}} \quad (\text{A.56c})$$

$$A_{\text{DT}} = \begin{bmatrix} 0 & 1 \\ -\left(\frac{k_{\text{DT}}}{J_{\text{Rtr}}} + \frac{k_{\text{DT}}}{N_{\text{Gear}}^2 J_{\text{Gen}}}\right) & -\left(\frac{c_{\text{DT}} - \delta \tau_{\text{Rtr}} / \delta \Omega_{\text{Rtr}}}{J_{\text{Rtr}}} + \frac{c_{\text{DT}}}{N_{\text{Gear}}^2 J_{\text{Gen}}}\right) \end{bmatrix} \quad (\text{A.56d})$$

$$A_{\text{DT-Gen}} = \begin{bmatrix} 0 \\ \frac{\delta \tau_{\text{Rtr}} / \delta \Omega_{\text{Rtr}}}{J_{\text{Rtr}}} \end{bmatrix}, A_{\text{DT-Pitch}} = \begin{bmatrix} 0 & 0 \\ \frac{\delta \tau_{\text{Rtr}} / \delta \beta_{\text{Pitch}}}{J_{\text{Rtr}}} & 0 \end{bmatrix} \quad (\text{A.56e})$$

$$A_{\text{DT-GenTq}} = \begin{bmatrix} 0 \\ -\frac{1}{N_{\text{Gear}} J_{\text{Gen}}} \end{bmatrix}, A_{\text{Bfl-Gen}} = \begin{bmatrix} 0 \\ \frac{\delta f_T / \delta \Omega_{\text{Rtr}}}{M_{\text{Blade}}} \end{bmatrix} \quad (\text{A.56f})$$

$$A_{\text{Bfl}} = \begin{bmatrix} 0 & 1 \\ -\frac{k_{\text{Blade}}}{M_{\text{Blade}}} & -\frac{c_{\text{Blade}} + \delta f_T / \delta U}{M_{\text{Blade}}} \end{bmatrix}, A_{\text{Bfl-Pitch}} = \begin{bmatrix} 0 & 0 & 0 \\ \frac{\delta f_T / \delta \beta_{\text{Pitch}}}{M_{\text{Blade}}} & 0 & 0 \end{bmatrix} \quad (\text{A.56g})$$

$$A_{\text{Pitch}} = \begin{bmatrix} 0 & 1 \\ -\omega^2 & -2\omega \zeta \end{bmatrix}, A_{\text{GenTq}} = -\frac{1}{T_e}, B_{\text{Pitch}} = \begin{bmatrix} 0 & 0 \\ \omega^2 & 0 \end{bmatrix} \quad (\text{A.56h})$$

$$B_{\text{GenTor}} = \begin{bmatrix} 0 & \frac{1}{T_e} \end{bmatrix}, \Gamma_{\text{Rtr}} = \frac{\delta \tau_{\text{Rtr}} / \delta U}{J_{\text{tot}}}, \Gamma_{\text{DT}} = \begin{bmatrix} 0 \\ \frac{\delta \tau_{\text{Rtr}} / \delta U}{J_{\text{Rtr}}} \end{bmatrix} \quad (\text{A.56i})$$

Same linearisation process approach as before has done at different operation point. Linearising at the processing points with wind speed of 5 m/s, the pitch angle of $\beta_{Pitch} = 0$, rotor speed of $\Omega_{Rtr} = 7.51$ rpm. The linearised model parameter matrix is given as

$$A = \begin{bmatrix} 3.65 \times 10^{-4} & 0 & 0 & 0 & 0 & 173 & 1.238 \\ 0 & 0 & 1 & 0 & 0 & 0 & 0 \\ -0.2602 & -4.437 & -0.03 & 0.1037 & 0.0023 & -5.9422 & -0.3028 \\ 0 & 0 & 0 & 0 & 1 & 0 & 0 \\ 33.2853 & 11.07 & -2.795 & -19.425 & -1.687 & 385.5 & 36.0468 \\ 0 & 0 & 0 & 0 & 0 & 0 & 1 \\ -0.0684 & -0.0132 & -0.0012 & 0.0079 & 0 & -195.67 & -1.4696 \end{bmatrix} \quad (A.57a)$$

$$B = \begin{bmatrix} 0 & -1.9323 \times 10^{-4} \\ 0 & 0 \\ 0.1923 & 0 \\ 0 & 0 \\ -133 & 0 \\ 0 & 0 \\ -0.0522 & 1.9332 \times 10^{-4} \end{bmatrix}, \Gamma = \begin{bmatrix} 0 \\ 0 \\ 0.0206 \\ 0 \\ 6.8244 \\ 0 \\ 0.002 \end{bmatrix} \quad (A.57b)$$

Linearizing at $U_{REWS} = 8$ m/s, $\beta_{Pitch} = 0^\circ$, $\Omega_{Rtr} = 9.16$ rpm, which gives the linearised model status parameter matrix as

$$A = \begin{bmatrix} 2.27 \times 10^{-4} & 0 & 0 & 0 & 0 & 173 & 1.238 \\ 0 & 0 & 1 & 0 & 0 & 0 & 0 \\ -0.2888 & -4.4356 & -0.0429 & 0.1066 & 0.0022 & -5.9422 & -0.3314 \\ 0 & 0 & 0 & 0 & 1 & 0 & 0 \\ 56.2106 & 11.0052 & -3.9149 & -19.92 & -2.1384 & 385.5 & 58.9718 \\ 0 & 0 & 0 & 0 & 0 & 0 & 1 \\ -0.1182 & -0.0133 & -0.0051 & 0.0082 & -5.28 \times 10^{-4} & -195.67 & -1.5197 \end{bmatrix} \quad (A.58a)$$

$$B = \begin{bmatrix} 0 & -1.9323 \times 10^{-5} \\ 0 & 0 \\ 0.1195 & 0 \\ 0 & 0 \\ -224.47 & 0 \\ 0 & 0 \\ -0.2141 & 1.9332 \times 10^{-5} \end{bmatrix}, \Gamma = \begin{bmatrix} 0 \\ 0 \\ 0.0288 \\ 0 \\ 8.5904 \\ 0 \\ 0.0088 \end{bmatrix} \quad (A.58b)$$

Linearizing at $U_{REWS} = 11.4$ m/s, $\beta_{Pitch} = 0^\circ$, $\Omega_{Rtr} = 12.1$ rpm, which gives the linearised model status parameter matrix as

$$A = \begin{bmatrix} 1.27 \times 10^{-4} & 0 & 0 & 0 & 0 & 173 & 1.238 \\ 0 & 0 & 1 & 0 & 0 & 0 & 0 \\ -0.3624 & -4.437 & -0.0509 & 0.1131 & 0.003 & -5.9422 & -0.405 \\ 0 & 0 & 0 & 0 & 1 & 0 & 0 \\ 88.748 & 10.896 & -5.5241 & -21.077 & -2.8592 & 385.5 & 91.51 \\ 0 & 0 & 0 & 0 & 0 & 0 & 1 \\ -0.1668 & -0.0134 & -0.0085 & 0.0087 & -8.9 \times 10^{-4} & -195.67 & -1.568 \end{bmatrix} \quad (A.59a)$$

$$B = \begin{bmatrix} 0 & -1.9323 \times 10^{-5} \\ 0 & 0 \\ 0.2139 & 0 \\ 0 & 0 \\ -393.675 & 0 \\ 0 & 0 \\ -0.4513 & 1.9332 \times 10^{-5} \end{bmatrix}, \Gamma = \begin{bmatrix} 0 \\ 0 \\ 0.0379 \\ 0 \\ 10.5518 \\ 0 \\ 0.0139 \end{bmatrix} \quad (A.59b)$$

Linearizing at $U_{REWS} = 15$ m/s, $\beta_{Pitch} = 10.44^\circ$, $\Omega_{Rtr} = 12.1$ rpm, which gives the linearised model status parameter matrix as

$$A = \begin{bmatrix} 9.96 \times 10^{-5} & 0 & 0 & 0 & 0 & 173 & 1.238 \\ 0 & 0 & 1 & 0 & 0 & 0 & 0 \\ -0.3053 & -4.4271 & -0.0569 & 0.1145 & 0.006 & -12.77 & -0.3968 \\ 0 & 0 & 0 & 0 & 1 & 0 & 0 \\ -20.717 & 11.1055 & -8.8543 & -21.364 & -4.9235 & 870.56 & -14.482 \\ 0 & 0 & 0 & 0 & 0 & 0 & 1 \\ -0.1018 & -0.0284 & -0.0035 & 0.0194 & 9.9 \times 10^{-4} & -197.38 & -1.5154 \end{bmatrix} \quad (A.60a)$$

$$B = \begin{bmatrix} 0 & -1.9323 \times 10^{-5} \\ 0 & 0 \\ -0.0826 & 0 \\ 0 & 0 \\ -583.19 & 0 \\ 0 & 0 \\ 0.1024 & 1.9332 \times 10^{-5} \end{bmatrix}, \Gamma = \begin{bmatrix} 0 \\ 0 \\ 0.0482 \\ 0 \\ 9.3596 \\ 0 \\ 0.004 \end{bmatrix} \quad (A.60b)$$

Linearizing at $U_{REWS} = 18 \text{ m/s}$, $\beta_{Pitch} = 14.9^\circ$, $\Omega_{Rtr} = 12.1 \text{ rpm}$, which gives the linearised model status parameter matrix as

$$A = \begin{bmatrix} 3.32 \times 10^{-4} & 0 & 0 & 0 & 0 & 173 & 1.238 \\ 0 & 0 & 1 & 0 & 0 & 0 & 0 \\ -0.23 & -4.4237 & -0.0596 & 0.1153 & 0.0067 & -15.7189 & -0.3426 \\ 0 & 0 & 0 & 0 & 1 & 0 & 0 \\ -76.7057 & 11.1847 & -9.5126 & -21.57 & -5.5436 & 1106.6 & -68.777 \\ 0 & 0 & 0 & 0 & 0 & 0 & 1 \\ -0.0416 & -0.0349 & -0.0017 & 0.0245 & 0.002 & -198.5676 & -1.4639 \end{bmatrix} \quad (A.61a)$$

$$B = \begin{bmatrix} 0 & -1.9323 \times 10^{-5} \\ 0 & 0 \\ -0.1704 & 0 \\ 0 & 0 \\ -651 & 0 \\ 0 & 0 \\ 0.3661 & 1.9332 \times 10^{-5} \end{bmatrix}, \Gamma = \begin{bmatrix} 0 \\ 0 \\ 0.0498 \\ 0 \\ 9.5835 \\ 0 \\ 0.0022 \end{bmatrix} \quad (A.61b)$$

Linearizing at $U_{REWS} = 21 \text{ m/s}$, $\beta_{Pitch} = 18.66^\circ$, $\Omega_{Rtr} = 12.1 \text{ rpm}$, which gives the linearised model status parameter matrix as

$$A = \begin{bmatrix} 1.66 \times 10^{-4} & 0 & 0 & 0 & 0 & 173 & 1.238 \\ 0 & 0 & 1 & 0 & 0 & 0 & 0 \\ -0.2165 & -4.4182 & -0.0662 & 0.1163 & 0.006 & -18.213 & -0.3469 \\ 0 & 0 & 0 & 0 & 1 & 0 & 0 \\ -118.795 & 11.2908 & -9.4424 & -21.82 & -5.4412 & 1325.4 & -109.3 \\ 0 & 0 & 0 & 0 & 0 & 0 & 1 \\ 0.0081 & -0.0405 & -0.0018 & 0.0292 & 0.0025 & -199.81 & -1.4227 \end{bmatrix} \quad (A.62a)$$

$$B = \begin{bmatrix} 0 & -1.9323 \times 10^{-5} \\ 0 & 0 \\ -0.5716 & 0 \\ 0 & 0 \\ -670 & 0 \\ 0 & 0 \\ 0.4951 & 1.9332 \times 10^{-5} \end{bmatrix}, \Gamma = \begin{bmatrix} 0 \\ 0 \\ 0.0545 \\ 0 \\ 9.293 \\ 0 \\ 0.0024 \end{bmatrix} \quad (A.62b)$$



Linearized at $U_{REWS} = 24 \text{ m/s}$, $\beta_{Pitch} = 22.05^\circ$, $\Omega_{Rtr} = 12.1 \text{ rpm}$, which gives the model status parameter matrix as

$$A = \begin{bmatrix} 0 & 0 & 0 & 0 & 0 & 173 & 1.238 \\ 0 & 0 & 1 & 0 & 0 & 0 & 0 \\ -0.123 & -4.4126 & -0.0654 & 0.1171 & 0.0071 & -20.4655 & -0.2696 \\ 0 & 0 & 0 & 0 & 1 & 0 & 0 \\ -170.26 & 11.3358 & -9.9992 & -22.06 & -6.0683 & 1541.9 & -159.219 \\ 0 & 0 & 0 & 0 & 0 & 0 & 1 \\ 0.0971 & -0.0455 & -2.2 \times 10^{-4} & 0.0338 & 0.0035 & -201.158 & -1.3437 \end{bmatrix} \quad (\text{A.63a})$$

$$B = \begin{bmatrix} 0 & -1.9323 \times 10^{-5} \\ 0 & 0 \\ -0.482 & 0 \\ 0 & 0 \\ -756.4 & 0 \\ 0 & 0 \\ 0.7876 & 1.9323 \times 10^{-5} \end{bmatrix}, \Gamma = \begin{bmatrix} 0 \\ 0 \\ 0.053 \\ 0 \\ 9.7515 \\ 0 \\ 9.7 \times 10^{-4} \end{bmatrix} \quad (\text{A.63b})$$

B. Design of the RHC controller

B.1. Linear RHC controller design

The RHC controller uses the linear model to predict the plant states and output over the prediction horizon. So the state estimation for the prediction model is

$$x(k+1|k) = Ax(k) + B\Delta u(k|k) + \Gamma\Delta v(k - N_{pre}|k) \quad (\text{B.1})$$

where $\Delta u(k|k)$ denotes the calculated controllable input at time k. $\Delta v(k|k)$ denotes the measured wind input at time k. When predicting the states by propagating the model over the prediction horizon, the second step states can be estimated as

$$\begin{aligned} x(k+2|k) &= Ax(k+1) + B\Delta u(k+1|k) + \Gamma\Delta v(k+1 - N_{pre}|k) \\ &= A^2x(k) + AB\Delta u(k|k) + B\Delta u(k+1|k) \\ &\quad + A\Gamma\Delta v(k - N_{pre}|k) + \Gamma\Delta v(k+1 - N_{pre}|k) \end{aligned} \quad (\text{B.2})$$

The third step can be estimated as

$$\begin{aligned} x(k+3|k) &= Ax(k+2) + B\Delta u(k+2|k) + \Gamma\Delta v(k+2|k) \\ &= A^3x(k) + A^2B\Delta u(k|k) + AB\Delta u(k+1|k) + B\Delta u(k+2|k) \\ &\quad + A^2\Gamma\Delta v(k - N_{pre}|k) + A\Gamma\Delta v(k+1 - N_{pre}|k) \\ &\quad + \Gamma\Delta v(k+2 - N_{pre}|k) \end{aligned} \quad (\text{B.3})$$

Therefore, at the end of control horizon, if $j \leq N_c$, the estimated system state is

$$\begin{aligned} x(k+N_c|k) &= Ax(k+N_c-1) + B\Delta u(k+N_c-1|k) + \Gamma\Delta v(k+N_c-1 - N_{pre}|k) \\ &= A^{N_c}x(k) + A^{N_c-1}B\Delta u(k|k) + \dots + B\Delta u(k+N_c-1|k) \\ &\quad + A^{N_c-1}\Gamma\Delta v(k|k) + \dots + \Gamma\Delta v(k+N_c-1 - N_{pre}|k) \end{aligned} \quad (\text{B.4})$$

When $N_c \leq j \leq N$, the estimated system state is

$$\begin{aligned} x(k+N_c+1|k) &= Ax(k+N_c) + B\Delta u(k+N_c|k) + \Gamma\Delta v(k+N_c - N_{pre}|k) \\ &= A^{N_c+1}x(k) + A_c^N B\Delta u(k|k) + \dots + B\Delta u(k+N_c|k) \\ &\quad + A_c^N \Gamma\Delta v(k - N_{pre}|k) + \Delta + \Gamma\Delta v(k+N_c - N_{pre}|k) \end{aligned} \quad (\text{B.5})$$

Therefore, until the end of the prediction horizon

$$\begin{aligned}
 x(k+N|k) &= Ax(k+N-1) + B\Delta u(k+N-1|k) + \Gamma\Delta v(k+N-1-N_{pre}|k) \\
 &= A^N x(k) + A^{N-1}B\Delta u(k|k) + \dots + A^{N-N_c}B\Delta u(k+N_c-1|k) \\
 &\quad + A^{N-1}\Gamma\Delta v(k-N_{pre}|k) + \Delta + \Gamma\Delta v(k+N-1-N_{pre}|k)
 \end{aligned} \tag{B.6}$$

If $N_{pre} \leq N-1$, the preview information is obtaining inside of the prediction model. If $N_{pre} > N-1$ the preview data cannot be considered during single prediction horizon. Therefore, extent the prediction horizon until N_{pre} , the extended prediction equation is given as

$$\begin{aligned}
 x(k+N+1|k) &= Ax(k+N) + B\Delta u(k+N|k) + \Gamma\Delta v(k+N-N_{pre}|k) \\
 &= A^{N+1}x(k) + A^N B\Delta u(k|k) + \dots + A^{N-N_c+1}B\Delta u(k+N_c|k) \\
 &\quad + A^N \Gamma\Delta v(k-N_{pre}+1|k) + \dots + \Gamma\Delta v(k+N-N_{pre}|k) \\
 x(k+N_{pre}|k) &= Ax(k+N_{pre}-1) + B\Delta u(k+N_{pre}-1|k) + \Gamma\Delta v(k|k) \\
 &= A^{N_{pre}}x(k) + A^{N_{pre}-1}B\Delta u(k|k) + \dots + A^{N_{pre}-N_c}B\Delta u(k+N_c-1|k) \\
 &\quad + A^{N_{pre}-1}\Gamma\Delta v(k-N_{pre}|k) + \dots + \Gamma\Delta v(k+N_{pre}-1|k)
 \end{aligned} \tag{B.7}$$

Therefore, the overall steps of predicted system states are given as eq.(B.9).

In order to keep the problem simple, instead of creating an extended prediction model, we update the measurement disturbance. After N_{pre} steps, the prediction model is given as (B.10). Therefore,

$$X(k) = Px(k) + G_z\Delta U(k) + G_v\Delta V(k) \tag{B.8}$$



$$\begin{aligned}
 & \underbrace{\begin{bmatrix} x(k+1|k+N_{Pre}) \\ \vdots \\ x(k+N_c|k+N_{Pre}) \\ \vdots \\ x(k+N|k+N_{Pre}) \end{bmatrix}}_{x(k)} = \underbrace{\begin{bmatrix} A & \vdots & \vdots \\ \vdots & A^{N_c} & \vdots \\ A^{N_c+1} & \vdots & \vdots \\ \vdots & \vdots & \vdots \\ A^N & \vdots & \vdots \end{bmatrix}}_P x(k) + \underbrace{\begin{bmatrix} B & \cdots & 0 \\ AB & \cdots & 0 \\ \vdots & \ddots & \vdots \\ A^{N_c-1}B & \cdots & B \\ A^{N_c}B & \cdots & AB \\ \vdots & \ddots & \vdots \\ A^{N-1}B & \cdots & A^{N-N_c}B \end{bmatrix}}_{G_z} \underbrace{\begin{bmatrix} \Delta u(k|k+N_{Pre}) \\ \vdots \\ \Delta u(k+N_c-1|k+N_{Pre}) \end{bmatrix}}_{\Delta u(k)} \\
 & + \underbrace{\begin{bmatrix} \Gamma & 0 & \cdots & \cdots & \cdots & 0 \\ A\Gamma & \Gamma & \cdots & \cdots & \cdots & 0 \\ \vdots & \vdots & \ddots & \ddots & \ddots & \vdots \\ A^{N_c-1}\Gamma & A^{N_c-2}\Gamma & \cdots & \Gamma & 0 & \cdots \\ \vdots & \vdots & \vdots & \vdots & \vdots & \vdots \\ A^{N_c}\Gamma & A^{N_c-1}\Gamma & \cdots & \Gamma & \cdots & \vdots \\ \vdots & \vdots & \vdots & \vdots & \vdots & \vdots \\ A^{N-1}\Gamma & A^{N-2}\Gamma & \cdots & \cdots & A\Gamma & \Gamma \end{bmatrix}}_{G_v} \underbrace{\begin{bmatrix} \Delta v(k|k+N_{Pre}) \\ \vdots \\ \Delta v(k+N-1|k+N_{Pre}) \end{bmatrix}}_{\Delta v(k)}
 \end{aligned} \tag{B.10}$$

C. Evaluation of the laser noise

The ESA is set to a resolution bandwidth of 1MHz and displays the power data with log-envelope scale. The measurement of the electrical power caused by the laser RIN takes the following steps.

1. Switch off the laser and take the measurement of detector noise with spectrum analyzer, then record the power data $\Delta P_{Det}(v)$.
2. Switch on the laser and take the measurement, and record the power data $\Delta P_{total}(v)$.
3. Subtracting the detector noise $\Delta P_{Det}(v)$ from the overall electrical power $\Delta P_{total}(v)$ to get the laser noise by $\Delta P_{Laser}(v) = \Delta P_{total}(v) - \Delta P_{Det}(v)$.
4. Calculate the shot noise from the measured DC voltage and subtracting from the laser noise, $\Delta P_{excess}(v) = \Delta P_{Laser}(v) - \Delta P_{shot}$.
5. Since log shaping tends to amplify noise peaks less than the rest of the noise signal, the detected signal is smaller than its true RMS value. This correction combined with the detector characteristics gives a total correction of 2.5dB, which should be added to any measured noise in the log display mode. We add the 2.5dB correction to the power $\Delta P_{total}(v)$. This correction factor is according to the HP spectrum analyzer data sheet [2].
6. The power given by the ESA is over a certain bandwidth Resolution Band Width (RBW) of ESA. We need normalize the power to 1Hz by subtract the correction factor $10 \cdot \log \frac{RBW}{1Hz}$.
7. Read out the average voltage U_E via oscilloscope, and calculate the power $P_E \text{mW} = \frac{(U_E \times 10^{-3})^2}{R} \text{W} = \frac{(U_E)^2}{R} \times 10^{-3} \text{mW}$, transfer to dBm with equation $P_E \text{dBm} = 10 \cdot \log(P_E \text{mW}) = 20 \log(U_E) - 47$, where $R = 50\Omega$ is the oscilloscope impedance.
8. Summarize the above factors and put them together, we get the equation for calculate the RIN noise based on measurement data as

$$RIN(v)|_{dBc/Hz} = \Delta P_{excess}(v) + 2.51 - 10 \cdot \log \frac{RBW}{1Hz} - (20 \cdot \log(U_E) - 47) \quad (C.1)$$

D. Atmospheric scattering theory

D.1. Rayleigh scattering (Molecular)

Rayleigh scattering is used to describe scattering from molecules, clusters and small particles, whose circumference is much less than the wavelength of the illumination light.

$$x = \frac{2\pi r}{\lambda} \ll 1 \quad (\text{D.1})$$

Where r is the radius of the particle, λ is the wavelength of the incident light and x is a value used to describe the size of the particle comparing with the wavelength λ .

The differential scattering cross section of the particle is given by Eq.(D.2).

$$\frac{\partial \sigma_{ss}}{\partial \Omega} = \frac{\pi^2 \alpha^2}{\epsilon_0^2 \lambda^4} \sin^2 \varphi \quad (\text{D.2})$$

Where α is the Polaris ability, φ is the angle of observation with respect to the dipole vector and ϵ_0 is the dielectric constant in vacuum [35].

As to the back scattering condition, φ equals $-\frac{\pi}{2}$ because light is transverse wave and the electric field vector is perpendicular to the propagation direction. Therefore, the backscatter coefficient $\beta(R)$ at distance R can be written as

$$\beta(R, \lambda) = \sum_j N_j \frac{\partial \sigma_{j,ss}}{\partial \Omega} = \sum_j N_j \frac{\pi^2 a_j^2}{\epsilon_0^2 \lambda^4} \quad (\text{D.3})$$

Where subscript j indicates different particle component, N_j and a_j are the number and Polaris ability of the component j .

From function (D.3), it is clear that $\beta(R)$ is inversely proportional to the fourth power of the wavelength. The backscattering intensity is prone to the shorter wavelength.

D.2. Mie scattering (Aerosol)

In the circumstance of bigger particles, where $x = \frac{2\pi r}{\lambda} \gg 1$, Mie scattering theory is applied instead of the Rayleigh scattering theory. Then the scattering cross section is changed to

$$\sigma_{\text{Mie}} = \frac{2\pi}{k^2} \sum_{n=1}^{\infty} (2n+1) (|a_n|^2 + |b_n|^2) \quad (\text{D.4})$$

Where $x = \frac{2\pi n_a r}{\lambda} = ka$, $m = \frac{n_p}{n_a}$, n_p and n_a are the refractive indexes of the sphere and the medium respectively, Ψ_n and ζ_n are complicated Bessel function and Hankel function [98].

In our case, the purpose is to measure the offshore wind speed over the sea level, where exists several aerosols with relatively big size [96]. The radius of these components varies from $0.01\mu\text{m}$ to $10\mu\text{m}$. That means the maximum $x = \frac{2\pi n_a r}{\lambda} \cong 125$ if the wavelength of the incident light is $0.532\mu\text{m}$. Thus, the backscattering signal from air over the ocean combines both of the Rayleigh backscattering from the molecular and the Mie backscattering from the aerosols. As discussed in the Reference [96], the derivation of the Rayleigh scattering theory and Mie scattering theory is evident once x is larger than 10. Therefore, Mie scattering theory is fit for the situation better than Rayleigh scattering.

As presented in functions (D.3) and (D.4), the calculation of backscattering coefficient is quite complex, so the measured values by experiment are used instead in practice. Clearly, the two functions indicate that the backscattering signal intensity favors short wavelength. It seems that the short wavelength is a better choice for the measuring system. However, in contrast, the CNR and the Transmission coefficient are enhanced at the longer wavelength. What is more, the incident light with longer wavelength benefits for the heterodyne efficiency and Eye-safety [99]. So the wavelength of the laser should be considered synthetically. A typical spectral diagram of the backscattering signal in air is given in Fig.D.1.

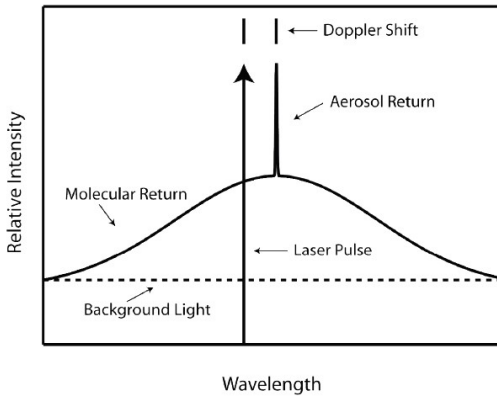


Fig. D.1: Compositions of the backscattering signal in air

D.3. Aerosol parameters

Table.D.1 shows a list of the properties of different type of aerosol components. Table.Tab:AerosolComposition shows the particle number concentration N_i for different aerosol type [78].

Table D.1.: Microphysical properties of different aerosol components [3,78]

Component	σ	$r_{\text{mod N}}$	r_{min}	r_{max}	ρ	Refractive Index 1.5 μm
Unit	-	μm	μm	μm	gcm^{-3}	
Insoluble	2.51	0.47	0.005	20.0	2.0	$1.41 + 1 \times 10^{-3}j$
Water-soluble	2.24	0.0212	0.005	20.0	1.8	$1.42 + 0.29j$
Soot	2.00	0.0118	0.005	20.0	1.0	$2.16 + 0.46j$
Sea salt (acc. mode)	2.03	0.209	0.005	20.0	2.2	$1.36 + 1.07 \times 10^{-3}j$
Sea salt (coa. mode)	2.03	1.75	0.005	60.0	2.2	
Sulfate droplets	2.03	0.0695	0.005	20.0	1.7	$1.321 + 1.12 \times 10^{-4}j$
Mineral (nuc. mode)	1.95	0.07	0.005	20	2.6	$1.42 + 1.4 \times 10^{-3}j$
Mineral (acc. mode)	2.00	0.39	0.005	20	2.6	
Mineral (coa. mode)	2.15	1.90	0.005	60	2.6	
Mineral-transported	2.20	0.50	0.02	5	2.6	

Table D.2.: Composition of components for different aerosol type [78]

Aerosol types	Components	$N_i \text{ cm}^{-3}$	Number mixing ratio n_j
Maritime clean	water soluble	1,500	0.987
	sea salt (acc.)	20	0.0132
	sea salt (coa.)	3.2×10^{-3}	2.11×10^{-6}
Maritime polluted	water soluble	3,800	0.422
	sea salt (acc.)	20	2.22×10^{-3}
	sea salt (coa.)	3.2×10^{-3}	3.56×10^{-7}
	soot	5180	0.576
Maritime tropical	water soluble	590	0.983
	sea salt (acc.)	10	0.0167
	sea salt (coa.)	1.3×10^{-3}	2.17×10^{-6}
Continental clean	water soluble	2,600	1.0
	insoluble	0.15	5.77×10^{-5}
Continental average	water soluble	7000	0.458
	insoluble	0.4	2.61×10^{-5}
	soot	8300	0.542
Continental polluted	water soluble	15,700	0.314
	insoluble	0.4	1.2×10^{-5}
	soot	8,300	0.686
Desert	water soluble	2000	0.87
	mineral (nuc.)	269.5	0.117
	mineral (acc.)	30.5	0.0133
	mineral (coa.)	0.142	6.17×10^{-5}
Urban	water soluble	28,000	0.177
	insoluble	1.5	9.49×10^{-6}
	soot	130,000	0.823
Antarctic	sulfate	42.9	0.998
	sea salt (acc.)	0.047	0.00109
	mineral (tra.)	0.0053	0.123e-3
Arctic	water soluble	1300	0.197
	insoluble	0.01	1.52×10^{-6}
	sea salt (acc.)	1.9	2.88×10^{-4}
	soot	5300	0.803

List of Figures

1	Sketch of the general idea of Lidar assisted wind turbine pitch control system	x
2	Illustration of CW Lidar concept with range independent probe length	xi
3	2DOF RHC/FB preview control for wind turbine active pitch system	xi
4	Sketch of the general idea of Lidar assisted wind turbine pitch control system	xiii
5	Illustration of CW Lidar concept with range independent probe length	xv
6	2DOF RHC/FB preview control for wind turbine active pitch system	xv
1.1	Illustration of environmental challenges for the modern offshore wind turbines	3
1.2	The growth of wind turbine size	4
1.3	Components of a standard HAWT system	5
1.4	Schematic S-N diagram for various fatigue critical structures	6
1.5	Generator rotation torque response	7
	(a) Cost of wind turbine components [45]	7
	(b) Cause of failures of wind turbines [150]	7
1.6	Damages and failure examples on the drive-train of a wind turbine	7
	(a) Damages on the gearbox bearing (Source: NOAA)	7
	(b) Generator failure by over speed (Source: BBC)	7
1.7	Tower mass scaling with swept area of rotor	8
1.8	Blades mass scaling with swept area of rotor	8
1.9	Sketch of the general idea of Lidar assisted wind turbine pitch control system	10
1.10	Sketch diagram of the thesis structure	10
2.1	Primary energy world consumption	11
2.2	Global cumulative installed wind capacity	12
2.3	A prediction of the LCOE of different renewable energy in Germany	13
2.4	Illustration of actuator disc model and stream tube theory	14
2.5	Illustration of the forces on a wind turbine blade element	15
2.6	Power curve of a wind turbine	16
2.7	Illustration of different incident angle to the blade	17
2.8	A bistatic wind Lidar concept	18
2.9	Lidar geometry	19
2.10	Sketch of coherence detection for the Doppler wind Lidar system	21
2.11	Model of the backscattering from different particles	21
2.12	CNR for a coherent Doppler Lidar	25
2.13	Balanced coherent detection	26
2.14	Logarithmic wind share	27



2.15	An example of extreme operating gust	29
2.16	Wind speed changes in upstream induction zone	30
2.17	Coherence function of measured wind and BEW speed	31
3.1	Ultrasonic anemometer and it's working principle	34
3.2	A Sodar system and the antenna array	34
3.3	WindCube pulse Lidar system	36
3.4	Block diagram of the WindCube Lidar system	36
3.5	A polarization circulator setup	37
3.6	Sketch of WindCube for retrieving wind speed	39
3.7	Propagation of a laser pulse and the receiving of backscattering light with a time gate	40
3.8	LOS velocity resolution for different CNR and average length	41
3.9	Avent Wind iris turbine mounted Lidar system	42
3.10	Optical head structure of the Wind iris 2 beam Lidar system	43
3.11	Illustration of wind speed and direction calculation with wind iris	44
3.12	Illustration of a tilted and rolled Lidar beam with wind iris	44
3.13	Wind speed measurement uncertainties	45
3.14	The CW ZephIR Doppler wind Lidar	46
3.15	ZephIR Lidar work principle	47
3.16	Transmission and receiving optics design of a CW and Pulsed Lidar	48
3.17	Illustration of CW and pulse Lidar measuring at different heights	48
3.18	Calculated signal collection efficiency when focused different ranges and the probe length and volume	49
3.19	Illustration of the conical scan of ZephIR Lidar	50
3.20	Windar Photonics Wind Eye Lidar system	53
3.21	System structure of WindEye Lidar	54
3.22	Galion Lidar system G250 and G4000	56
3.23	Halo Photonics Stream Line Lidar series	56
3.24	Mitsubishi Electric Lidar system lineups	57
3.25	Mitsubishi Nacelle Lidars	57
3.26	WindTracer Lidar system	58
3.27	Ocean University of China incoherent Doppler wind Lidar	58
3.28	Design concept of low coherence CW-Lidar system TU-Hamburg-Harburg	60
3.29	A PI FB controller for wind turbine pitch system	62
3.30	General working principle of a feedback control	63
3.31	Combined FB and FF 2-DOF control for the wind turbine pitch system	63
3.32	A 2DOF pitch controller with ZPETC FF term	64
3.33	A 2DOF pitch controller with FX-RLS adaptive FF term	65
3.34	A full states feedback model predictive control block diagram	66
4.1	A modified OCT system setup for paper quality measurement	72
	(a) Working principle	72
	(b) A setup for proof of the working principle	72
4.2	Laser coherence function and power spectrum function	73
4.3	Illustration of CW Lidar concept with range independent probe length	74
4.4	Range weighting function as a function of distance	75



4.5	Calculated backscattering power at different distances for different aerosols	76
4.6	CNR at different measurement distance and aerosols	76
4.7	A simulation result of wind turbulences within the induction zone	77
4.8	Calculated wind speed measurement uncertainty from the tilt	78
4.9	Time delay of measured wind speed	78
4.10	Wind speed weighting factor along the blade span	79
4.11	Single distance Lidar measurement scenario	80
4.12	Wind turbulence measurement (simulated) for different probe length	81
4.13	Multiple distance and position measurement scenario	82
4.14	Lidar system with three beam measurements at a fixed distance	83
4.15	Vertical share of wind speed and rotor effective wind speed	84
	(a) Vertical share of wind speed [9]	84
	(b) Turbine rotor span divided into 9 zones [139]	84
4.16	Choice of Lidar system wavelength	85
5.1	Chronological flow diagram of the simulator design	87
5.2	Sketch of the Feuillete model with atmosphere slicing for heterodyne coherent Lidar system simulation	87
5.3	Schematic illustration of the process of the simulation design	88
5.4	Light scattering regimes depending on the particle size and wavelength	89
5.5	Histogram plot of Urban aerosol particle size distribution	89
5.6	Mie back-scattering cross section and coefficient	90
5.7	Impact of the different components on the overall backscattering coefficient	90
5.8	Simulated power spectrum with phase jump method	93
	(a) Spectrum width of 5 MHz	93
	(b) Spectrum width of 50 MHz	93
5.9	Simple model of the receiver setup	94
5.10	Illustration of the receiver model for analysis of the collection efficiency	94
5.11	Normalized beam diameter at different distance with a lens diameter of 20 mm	95
5.12	SCE from different distances	95
5.13	Illustration of the circular overlapping	97
5.14	Range weighting factor with different receiver diameters when focused to 100 m	97
5.15	Using a cylindrical coordinates to describe the position of a point P	98
5.16	A graphical description of particle position transformation	99
5.17	Block diagram of the simulation process	99
5.18	Simulated power spectrum signal with different wind speeds	100
5.19	Simulated power spectrum signal with different laser linewidth	100
5.20	Spectrum analysis result from the dynamical model simulation	101
	(a) A CW Lidar with with 5 MHz bandwidth laser	101
	(b) A CW Lidar with 50 MHz bandwidth laser	101
	(c) A pulse Lidar with with 5 MHz bandwidth laser	101
	(d) A CW Lidar with with delaylines	101
5.21	A GUI for setting of the simulator parameters	102
5.22	Simulated power spectrum signal with different laser linewidth	102

6.1	The designed close loop wind tunnel	105
6.2	Wind tunnel under operation as the target with a green laser Lidar system .	105
6.3	Michelson interferometer for measuring laser coherence length	106
6.4	Coherent length measurement	107
6.5	Laser RIN measurement system setup	108
6.6	Measured noise from ESA, PD, and laser RIN	109
6.7	Measured laser RIN at different LD drive current	109
6.8	Free space bi-static Doppler Lidar experimental system with single photo detector	110
	(a) Bi-static Doppler Lidar experimental system design	110
	(b) Experimental result from a spinning disk target and from an aerosol seeded wind flow	110
6.9	Free space bistatic Doppler Lidar setup with balanced photo detector	111
	(a) Bistatic Doppler Lidar setup with balanced photo detector	111
	(b) Experimental results	111
6.10	The monostatic configuration setup with standard beam splitter	112
	(a) Monostatic configuration setup	112
	(b) Measurement results of power transmitted to the collimator and reflected from surface	112
6.11	Monostatic configuration non-confocal system with off-axis parabolic mirror	113
6.12	Sketch of beam focusing quality checking for the off-axis parabolic mirror .	113
6.13	Focusing quality of the off-axis parabolic mirror	114
	(a) Simulation result with ZEMAX	114
	(b) Measurement result by a beam profiler	114
6.14	Experiment result for a solid target. Measurement result at different measurement distances(Left), SNR plot against measurement distances(right)	114
6.15	Experiment result for an air flow with the wind tunnel. Power Spectrum at different measurement distances(Left), SNR plot against measurement distances(right)	115
6.16	Illustration of CW Lidar concept with range independent probe length . . .	115
6.17	Measurement results with different fiber delayline length for a fixed target distance of 2 (left) and 4 m (right)	116
6.18	Measurement results with a fixed 7 m fiber delayline length at different measurement distance (left) and the SNR-Distance plot (right)	116
6.19	Gaussian curve fitting of the SNR against distance measurement results . .	117
7.1	Models of the FAST operation	122
7.2	Simulation block diagram in a Simulink environment	122
7.3	The tower model as a 1-mass damper-spring system	128
7.4	Free body diagram of the HAWT drive train and the simplified 2-mass damper-spring model	129
7.5	The pitch and torque control within a DFIG and PMSG generator system . .	131
7.6	Block diagram of a TurbSim wind field model	132
7.7	Parameters in the dynamic turbulence wind model	133
7.8	States output of a FAST wind turbine model with different wind speed inputs	135
7.9	Different model parameters of wind turbine at different wind speeds	136



7.10	Wind field simulation with TurbSim	138
7.11	Block diagram of TurbSim simulation	139
7.12	Taylor's hypothesis example	140
7.13	Simulation result of predictive control with frozen and unfrozen Lidar simulator	142
	(a) Rotor rotational speed	142
	(b) Generator torque	142
8.1	2DOF RHC/FB preview control for wind turbine active pitch system	143
8.2	Generator torque of variable speed wind turbines	145
8.3	A PI feedback controller for wind turbine pitch system	145
8.4	Pitch sensitivity in Region 3	147
8.5	PI gain and correction factor	148
8.6	Block diagram of DAC control method with state estimator	150
8.7	A time series simulation results comparison of LQR control with PI feedback control	151
	(a) Rotor speed	151
	(b) Tower top fore-aft deflection	151
	(c) Generator torque	151
	(d) Tower bending moment	151
8.8	Standard deviation results comparison of LQR control with PI feedback control	152
	(a) Rotor speed	152
	(b) Tower top fore-aft deflection	152
	(c) Generator torque	152
	(d) Tower bending moment	152
8.9	Block diagram of the 2DOF electrodynamic shaker controller	153
8.10	Illustration of the receding horizon of RHC methods	154
8.11	Skemetic S-N curve of a material	158
8.12	A simple EOG-1-year gust wind profile	159
8.13	Simulation result of the rotor speed and collective pitch position	160
8.14	A simple step wind profile	161
8.15	Time series results with the simple step wind profile	162
	(a) Rotor speed	162
	(b) Tower fore-aft deflection	162
8.16	Time series rotor rotational speed and tower fore-aft deflection response with the simple step wind profile	163
	(a) Rotor speed in Region2.5	163
	(b) Rotor speed in Region3	163
	(c) Tower fore-aft displacement in Region2.5	163
	(d) Tower fore-aft displacement in Region3	163
8.17	Time series from the simulation results with the simple step wind profile	164
	(a) Rotor torque	164
	(b) Tower fore-aft bending moment	164
8.18	Time series from the simulation results with the simple step wind profile	164
	(a) Pitch commends on region 2.5	164
	(b) Pitch commends on region 3	164

8.19	Time series results from an IEC gust profile	165
	(a) Rotor rotational speed	165
	(b) Generator torque	165
	(c) Tower top fore-aft displacement	165
	(d) Tower Fore-Aft bending moment	165
8.20	Time series of the pitch command input	166
8.21	Time series results from an IEC gust profile with FAST simulation	167
	(a) Rotor rotational speed	167
	(b) Generator torque	167
	(c) Tower top fore-aft displacement	167
	(d) Tower Fore-Aft bending moment	167
8.22	Time series plot of IEC Class A turbulence wind profile	168
	(a) Wind speed	168
	(b) Wind direction	168
8.23	Normalized Standard deviation plots by the mean value	169
	(a) Generator rotational speed	169
	(b) Low speed shaft torque	169
	(c) Tower fore-aft deflection	169
	(d) Tower bending moment	169
8.24	Damage equivalent loads for simulated with IEC category A turbulent wind field	170
	(a) Generator (High speed shaft) torque	170
	(b) Tower fore-aft bending moment	170
8.25	Damage equivalent loads from a hub height Lidar	171
	(a) Generator (High speed shaft) torque	171
	(b) Tower fore-aft bending moment	171
9.1	A comparison of the damage equivalent loads from a scanning Lidar and hub height Lidar	177
	(a) Generator torque with scanning Lidar	177
	(b) Generator torque with Hub height Lidar	177
	(c) Tower fore-aft bending moment with scanning Lidar	177
	(d) Tower fore-aft bending moment with Hub height Lidar	177
9.2	A comparison plot of simulated and experimental data	178
9.3	Damage equivalent loads of generator torquen and Tower fore-aft bending moment	181
	(a) DEL of Generator torque	181
	(b) DEL of Tower fore-aft bending moment	181
9.4	A following up setup for out door field testing	182
9.5	Distribution of the 10-minute average yaw error measured before and after correction	183
A.1	Illustration of the actuator disc model and stream tube theory	187
A.2	Power coefficient	189
D.1	Compositions of the backscattering signal in air	218



List of Tables

2.1	Summary of backscattering coefficient values	20
2.2	Parameters for wind turbine classes	28
3.1	A comparison of Sodar and Lidar	35
3.2	Commercial Lidar for wind energy applications	36
3.3	Specification of WindCube Lidar system	37
3.4	Specification data of Wind iris Lidar system	42
3.5	Specification of ZephIR Lidar	47
3.6	Specification of Windar Photonics WindEye Lidar system	53
3.7	A comparison of the parameters of different Lidar system	55
3.8	Specification of the Ocean University of China incoherent Lidar	59
3.9	The main differences between CW and pulsed Lidar systems	61
4.1	Requirements of the cost efficient Lidar with broad spectrum laser sources	86
6.1	Parameters of laser sources and laser diode driver for the experimental setup	106
6.2	Parameters of detector and ESA for LD noise analysis setup	108
7.1	Properties of the NREL 5-MW Baseline reference wind turbine	121
7.2	System natural frequencies with FAST simulation	123
7.3	Linearized generator EoM parameters by FAST	127
7.4	Linearized tower model parameters by FAST	129
7.5	Linearized EoM of drive-train model parameters	130
8.1	Effects of PID gain tuning by increasing a parameter independently	148
9.1	Requirements of the cost efficient Lidar with broad spectrum laser sources	178
A.1	Overall properties of the NREL 5-MW baseline reference wind turbine	192
D.1	Microphysical properties of different aerosol components	219
D.2	Composition of components for different aerosol type	220

Glossary

A_D	Area of the stream tube cross section at actuator disk position. 13
A_{Rec}	Area of receiver telescope. 40
A_{ref}	Reference laser electrical field amplitude. 21
A_∞	Area of the stream tube cross section at infinity. 13
A_{zi}	The azimuth wind direction angle. 50
B	Signal bandwidth. 23
C_D	Drag coefficient. 15
C_L	Lift coefficient. 15
$C_P(r)$	Radially dependent power coefficient of rotor blade. 30
C_P	Power coefficient. 14
C_t	Torque coefficient. 179
D_{Rec}	Diameter of receiver telescope. 53
D_W	Far wake position. 13
E_L	Energy of the laser pulse. 40
F_0	The phase front radius. 91
G_D	The disturbance controller gain. 150
G_E	The disturbance estimator. 154
H_{hub}	The hub height. 45
H_{pre}	The prefilter. 79
I_0	The laser light intensity overall spectrum. 72
K_D	The derivative gain. 62
K_I	The integral gain. 62
K_P	The proportional gain. 62
K_f	The disturbance-force compensator. 154
L_u	Turbulence scale length. 28
M_{Lens}	The magnification factor for a Gaussian beam propagating through a lens. 94
$N_D(\nu)$	The dark noise. 50
N_f	The fatigue life defined as the number of stress cycles. 157
N_i	The number of cycles to failure at a given stress. 157
$N_j(R)$	Particle concentration. 19
P_{Air}	Mechanical power of the air flow. 14
P_{Air}	Power available in the air flow. 14
P_L	Laser power. 19
P_{Rtr}	Power captured with the rotor disc. 14
P_S	Signal beam power. 107
P_m	The nominal model of plant. 153
P_{rec}	Detector receiving power. 20

P_{ref}	Reference beam power. 24
P_r	The real plant model. 154
Q	Positive semi-definite state weighting matrix. 149
R	Positive definite input weighting matrix. 149
R_{Load}	Load register of photo detector. 23
R_L	The transmittance of the photo detector. 40
R_{PD}	Responsibility of the photo diode. 40
R_{Rtr}	Radius of the rotor. 14
$S(\nu)$	The laser source spectrum. 72
S_i	The stress level. 157
T	Temperature. 23
U_D	Air flow velocity at actuator disk position. 13
U_{LOS}	The radial wind velocity. 46
U_W	Wind speed at far wake position. 13
U_l	Wind speed measured from left Lidar beam. 43
U_{rel}	Relative wind speed. 14
U_r	Wind speed measured from right Lidar beam. 43
U_{wind}	Wind speed. 14
U_{∞}	Air flow velocity at infinity. 13
V_{CM}	Common mode voltage. 26
Z	Distance in the Lidar geometry. 40
Z_{range}	The measurement distance. 78
ΔR	Scattering volume. 20
ΔZ	The probe length of Lidar. 51
$\Delta \nu$	Frequency fluctuations. 51
Δu	Perturbation system input. 149
Δw	The wind disturbance. 149
Ω_{rr}	Tangential blade element speed. 14
Ω_{sf}	Spatial frequency. 28
α_{Lidar}	The scanning cone angle. 43
α_{ext}	Extinction coefficient. 19
α_{ext}	Atmospheric extinction ratio. 40
α_{inc}	Thrust force. 15
α_{shear}	The exponential wind shear. 51
α_u	Turbulence intensity. 28
β_{Pitch}	Blade pitch angle. 14
β_{aer}	The backscattering from aerosol. 19
β_{mol}	The back-scattering from molecular. 19
β_{π}	Backscattering coefficient. 19
$\delta P(t)$	Optical power fluctuations. 23
η	Quantum efficiency of detector. 22
η_{H}	Heterodyne efficiency. 40
η_{Lidar}	Lidar efficiency. 40
η_{coll}	Collection efficiency. 20
η_{sys}	System efficiency. 20
$\gamma(\Delta z)$	The coherence function of the laser source. 75

$\gamma(\tau)$	The coherence function. 72
$\gamma(z)$	The inverse Fourier transform of the light source spectrum. 72
$\gamma_{w_i w_m}^2(f)$	Coherence function of measured wind speed and BEWS. 31
γ_{Yaw}	The yaw direction or the wind direction. 43
\hat{d}_f	The estimated disturbance force. 154
λ_0	The laser light wavelength. 20
ν	Laser light frequency. 72
ν_{Dopp}	Doppler frequency. 18
ν_{Inc}	Incident light frequency. 18
ν_{mod}	Model frequency. 51
ν_{p}	Backscattering laser light frequency. 18
ν_{ref}	Reference laser light frequency. 21
ν_{t}	Received backscattering laser light frequency at receiver. 18
ν_{x}	Transmission laser light frequency. 18
ν_i	Backscattering light frequency from particle i . 22
ω_{Rtr}	Rotor speed. 14
\overline{U}	The mean wind speed. 78
$\overline{\nu_{\text{Dopp}}}$	Doppler frequency shift. 51
ϕ	The angle between the flow direction and the rotor plane. 15
$\phi_T(t)$	The phase function modeled as a winner levy process. 92
ϕ_{TR}	Angle between the transmitter and receiver. 18
ϕ_{r}	Angle between the receiver and air flow. 18
ϕ_{x}	Angle between the transmitter and air flow. 18
ρ	Air density. 13
σ_{abs}	Particle absorption cross section. 19
σ_{ext}	Particle extinction cross section. 19
σ_{sca}	Particle scattering cross section. 19
σ_i	The standard derivation of particle distributions. 88
σ_{ν}	Standard deviation of the measured frequency. 51
τ_{Pulse}	Laser pulse length. 19
τ_{Rtr}	Rotor rotational torque. 15
τ_{c}	The laser coherence time. 73
θ_{las}	The scanning cone angle. 39
φ_T	The phase function. 91
a	Power law coefficient. 27
a_{Ind}	Axial flow induction factor. 13
c	The speed of light. 40
d_{FF}	The phase delay by implementation of the FF controller. 78
d_{LPF}	The time delay due to the low-pass filtering. 78

d_{Pitch}	The time delay due to applying the pitch commands to drive the pitch. 78
d_r	The time delay due to the REWS estimation. 78
d_s	The time delay delays due to the scan. 78
e	The elementary charge. 40
f	Frequency. 24
f^{Life_j}	The lifetime count extrapolation factor. 158
f_D	Drag force. 15
f_L	Lift force. 15
f_R	Drag force. 15
f_{Trans}	The focal length of the transmitter lens. 94
f_T	Drag force. 15
$g^{(1)}(\tau)$	The correlation function. 72
h	Planck's constant. 22
$h\nu$	The light quantum energy. 50
h_{ref}	Reference height. 27
i_{det}	Detector photo current. 22
k_b	Boltzmann's constant. 40
l_c	The laser coherence length. 73
n_j^{STeq}	The total equivalent fatigue number of cycles for time series j . 158
n^{Life_k}	The extrapolated cycle counts over the design lifetime. 158
r_{Fiber}	The radius of the fiber core. 94
$r_{\text{mod } N,i}$	The mode radius. 88
t_{Pre}	The preview time at the range i . 155
u	The m -dimension input variables. 149
u_{BEWS}	Blade effective wind speed. 30
u_{Wind}	The longitudinal wind speed. 50
u_g	Gust longitudinal linear velocity. 28
u_{ref}	Reference wind speed. 27
$w(z)$	The beam waist radius at distance z . 93
w_0	The beam waist radius at the focused position. 74
w_{Wind}	The tangential wind speed. 50
x	The n -dimension state variable. 149
z_{Fiber}	The distance from fiber to the lens. 94
z_{Foc}	The focused distance of the telescope. 74
z_F	The focus range of the system. 95
z_{ref}	Optical path distance of the reference beam. 21
z_i	Particle i position from receiver. 21

Acronyms

2-DOF	Two Degree of Freedom. 2
2-DOF FF/FB	2-DOF Feedforward/Feedback. 7
2-DOF RHC/FB	2-DOF Receding Horizon/Feedback Control. 7
ABL	Atmospheric boundary layer. 26
ADAMS	Automatic Dynamic Analysis of Mechanical Systems. 121
ADC	Analogue to Digital Converter. 38
AEL	Accessible Emission Limit. 85
AOM	Acousto-Optic Modulator. 37
ARE	Algebraic Riccati Equation. 149
ASTM	American Society for Testing and Materials. 157
BEWS	Blade Effective Wind Speed. 30
BLH	boundary layer height. 27
BS	Beam Splitter. 43
CDL	coherent Doppler Lidar. 3
CFD	Computational Fluid Dynamics. 29
CFTOC	Constrained finite time optimal control. 155
CMRR	Common-Mode Rejection Ratio. 26
CNR	Carrier to noise ratio. 24
COE	Cost of energy. 61
CP	Collective Pitch. 62
CRLB	Cramer Rao lower bound. 41
CW	Continue wave. 35
DAC	Disturbance accommodating control. 30
DEL	Damage Equivalent Load. 158
DFB	Distributed Feedback. 47
DFIG	Doubly fed induction generator. 17
DLC	Design load case. 157
DLL	Dynamic Linked Library. 122
DOF	Degree of Freedom. 121
DSP	Digital Signal Processing. 38
ECD	Extreme coherent gust with direction change. 157
EDFA	Erbium Doped Fiber Amplifier. 47
EKF	Extended Kalman filter. 30
EOG	Extreme operating gust. 28
EoM	Equation of Motion. 125

ESA	Electrical spectrum analyzer. 108
ETM	Extreme turbulence model. 157
EU	European Union. 11
EWEA	European Wind Energy Association. 12
FA	Fore-Aft. 158
FAST	Fatigue, Aerodynamics, Structures, and Turbulence. 121
FB	Feedback. xiii
FF	Feedforward. xiii
FFT	Fast Fourier Transform. 49
FIR	Finite Impulse Response. 65
FP	Fixed-Pitch. 15
FPGA	Field Programmable Gate Array. 49
FS	Fixed-Speed. 15
FSFB	Full States Feedback. 161
FWHM	Full Width at Half Maximum. 40
FX-RLS	Filtered-X Recursive Least Square. 63
GE	General Electric. 62
HAWT	Horizontal axis wind turbine. 3
I&I	Immersion and invariance. 30
IEA	International Energy Agency. 12
IPC	Individual Pitch Control. 62
LCOE	Levelized cost of energy. 12
LD	Laser diode. 106
LDD	Laser Diode Driver. 106
LES	large eddy simulation. 29
Lidar	Light Detection And Ranging. 2
LOS	Line-of-Sight. 18
LPV	Linear Parameter Varying System. 149
LQG	Linear-Quadratic-Gaussian. 67
LQR	Linear-Quadratic Regulator. 67
LSS	Low Speed Shaft. 158
MIMO	multiple inputs multiple outputs. 143
MLE	maximum likelihood estimator. 38
MO	Master Oscillator. 36
MOPA	Master oscillator power amplifier. 36
MPC	Model Predictive Control. 2
MPE	Maximum Permissible Exposure. 85
MPT	Multi-Parametric Toolbox. 138
NHLQR	Non-Homogeneous LQR. 150

NREL	National renewable energy laboratory. 29
NTM	Normal turbulence model. 157
O&M	Operations and Maintenance. 11
OADS	Optical Air Data Systems. 38
OCT	Optical Coherence Tomography. 6
PD	Photo detector/diode. 53
PI(D)	Proportional-Integral-Derivative. xiv
PMDD	Permanent magnet direct-drive. 4
PMSG	permanent magnet synchronized generator. 18
PRF	Pulse Reputation Frequency. 41
PSD	Rower spectral density. 23
PV	photovoltaic. 12
PWA	Piecewise Affine (system). 137
PWL	Piecewise Linear (system). 137
RBW	Resolution Band Width. 215
REWS	Rotor Effective Wind Speed. 82
RHC	Receding horizon control. 7
RIN	Relative intensity noise. 23
RMS	Root mean square. 109
RPS	Revolutions per seconds. 49
RWF	Range weighting function. 40
S-N	Cyclic Stress to Number to Failure. 4
SBL	Surface Boundary Layer. 27
SCE	Spatial Collection Efficiency. 93
SCIG	Squirrel-Cage Induction Generators. 16
SD	Standard Deviation. 158
SL	Semiconductor Laser. 54
SNR	Signal to noise ratio. 49
Sodar	Sound detection and ranging. 33
SOWFA	Simulator fOr Wind Farm Applications. 29
SS	Side-Side. 158
TI	Turbulence Intensity. 29
TSR	Tip Speed Ratio. 14
UIO	Unknown input observer. 30
VAD	Velocity-Azimuth Display. 50
VP	Variable-Pitch. 15
VS	Variable-Speed. 16
WECS	Wind energy conversion system. 1

ZPETC

Zero-Phase-Error Tracking Control. 63

References

- [1] ACKERMANN, T. and L. SOEDER: *Wind energy technology and current status: a review*. Renewable and Sustainable Energy Reviews, 4(4):315–374, 2000.
- [2] AGILENT: *Spectrum Analysis: Noise Measurements - Application Note 150-4*. Techn. Rep., Agilent, 1974.
- [3] AIAA: *Guide to Global Aerosol Models (GAM)*, 1999.
- [4] ANDO, T. and ET AL.: *All-fiber coherent Doppler LIDAR technologies at Mitsubishi Electric Corporation*. IOP Conference Series: Earth and Environmental Science, 1(1):012011, 2008.
- [5] ANDREWS, L. C.: *Field Guide to Atmospheric Optics*. SPIE Press, 2004.
- [6] ANTONIOU, I., H. EJSING JOERGENSEN and S. BRADLEY: *On the theory of SODAR measurement techniques*. Techn. Rep. 87-550-3217-6, Denmark. Forskningscenter Risoe, 2003. Denmark. Forskningscenter Risoe. Riso-R.
- [7] ASSOCIATION, E.: *UpWind - Design limits and solutions for very large turbines*. Techn. Rep., Ewea, 2011.
- [8] BANAKH, V. A., I. N. SMALIKHO, F. KOEPP and C. WERNER: *Representativeness of wind measurements with a cw Doppler lidar in the atmospheric boundary layer*. Appl. Opt., 34(12):2055–2067, 1995.
- [9] BATCHVAROVA, E., S.-E. GRYNING, R. FLOORS, C. VINCENT, A. PEÑA and T. MIKKELSEN: *Measurements and Modeling of the Wind Profile Up to 600 meters at a Flat Coastal Site*. In STEYN, D. G., P. J. BUILTJES and R. M. TIMMERMANS (eds.): *Air Pollution Modeling and its Application XXII*, NATO Science for Peace and Security Series C: Environmental Security, pp. 565–569. Springer Netherlands, 2014.
- [10] BERNOULLI, D.: *Hydrodynamics*. Dover, 1968.
- [11] BETZ, A.: *Das maximum der theoretisch moeglichen ausnutzung des windes durch windmotoren*. Zeitschrift fuer das Gesamte Turbinewesen, 20:3, 1920.
- [12] BETZ, A.: *Introduction to the theory of flow machines*. Pergamon Press, 1966.
- [13] BIANCHI, F., H. DE BATTISTA and R. MANTZ: *Wind Turbine Control Systems: Principles, Modelling and Gain Scheduling Design*. Springer, 2007.
- [14] BILBRO, J. W., C. DIMARZIO, D. FITZJARRALD, S. JOHNSON and W. JONES: *Airborne Doppler lidar measurements*. Applied Optics, 25(21):3952–3960, 1986.
- [15] BOHREN, C. F. and D. HUFFMAN: *Absorption and scattering of light by small particles*. Wiley, 1983.
- [16] BOQUET, M., R. PARMENTIER, L. SAUVAGE, J.-P. CARIOU and A. ALBERGEL: *Theoretical, CFD Analysis and Correction Methodology of Lidar Wind Profile Measurement in Complex Terrain*. In *European Wind Energy Conference and Exhibition (EWEA)*. EWEA, 2010.

- [17] BOSSANYI, E. A.: *The Design of closed loop controllers for wind turbines*. Wind Energy, 3(3):149–163, 2000.
- [18] BOTTASSO, C., A. CROCE, Y. NAM and C. RIBOLDI: *Power curve tracking in the presence of a tip speed constraint*. Renewable Energy, 40(1):1 – 12, 2012.
- [19] BOTTASSO, C., A. CROCE, B. SAVINI, W. SIRCHI and L. TRAINELLI: *Aero-servo-elastic modeling and control of wind turbines using finite-element multibody procedures*. Multibody System Dynamics, 16(3):291–308, 2006.
- [20] BOTTASSO, C., P. PIZZINELLI, C. RIBOLDI and L. TASCIA: *LiDAR-enabled model predictive control of wind turbines with real-time capabilities*. Renewable Energy, 71(0):442 – 452, 2014.
- [21] BP: *Statistical Review of World Energy 2013*. Techn. Rep., BP, June 2013 2013.
- [22] BRINKMEYER, E. and T. WATERHOLTER: *Continuous wave synthetic low-coherence wind sensing Lidar: motionless measurement system with subsequent numerical range scanning*. Optics Express, 21(2):1872–1897, 2013.
- [23] BURTON, T., D. SHARPE, N. JENKINS and E. BOSSANYI: *Wind Energy Handbook*. John Wiley & Sons, 2001.
- [24] BUTZBACH, M.: *Hochauflösende optische Kohärenztomographie mit einem Superkontinuuum-laser*. PhD thesis, KIT, 2012. Karlsruhe, KIT, Diss., 2011.
- [25] BUTZBACH, M., A. MALZ and W. STORK: *Optical Coherence Tomography for the Assessment of Paper Quality*. In *Advanced Photonics & Renewable Energy*, OSA Technical Digest (CD), p. SWD4. Optical Society of America, 2010.
- [26] CARIOU, J.-P.: *Pulsed Lidars in "Remote Sensing for Wind Energy"*. Techn. Rep., DTU, 2013.
- [27] CARIOU, J.-P., B. AUGERE and M. VALLA: *Laser source requirements for coherent lidars based on fiber technology*. Comptes Rendus Physique, 7(2):213–223, 2006.
- [28] CARIOU, J. P. and M. BOQUET: *Leosphere Pulsed Lidar Principles. Contribution to UpWind WP6 on Remote Sensing Devices*. Techn. Rep., UpWind WP6 report on Remote Sensing Devices, 2010.
- [29] CARN, S. A.: *Lecture note: GE4250 - Fundamentals of Remote Sensing*, 2013.
- [30] CARRIER and CARLSON: *A true air speed indicator*. Techn. Rep., Cruft Laboratories, Harvard University, 1944.
- [31] CASTAIGNET, D., I. COUCHMAN, N. K. POULSEN, T. BUHL and J. J. WEDEL-HEINEN: *Frequency-Weighted Model Predictive Control of Trailing Edge Flaps on a Wind Turbine Blade*. Control Systems Technology, IEEE Transactions on, 21(4):1105–1116, 2013.
- [32] CATTIN, R., S. BOURGEOIS, S. DIERER, M. MUELLER and S. KOLLER: *Wind Forecasts in complex terrain Experiences with SODAR and LIDAR*. In *Ice And Rocks III*, 2010.
- [33] COMMISSION, E.: *Energy 2020: A strategy for competitive, sustainable and secure energy*. Techn. Rep., European commission, 2010.

- [34] CORDLE, A., J. M. JONKMAN and G. G. HASSAN: *State of the art in floating wind turbine design tools*. In *21st International Offshore and Polar Engineering Conference*. National Renewable Energy Laboratory, 2011.
- [35] CORRADINI, S. and M. CERVINO: *Aerosol extinction coefficient profile retrieval in the oxygen A-band considering multiple scattering atmosphere. Test case: SCIAMACHY nadir simulated measurements*. *Journal of Quantitative Spectroscopy and Radiative Transfer*, 97(3):354–380, 2006.
- [36] COURTNEY, M.: *Calibrating nacelle Lidars*. Techn. Rep., DTU Wind Energy, 2013.
- [37] COURTNEY, M., R. WAGNER and P. LINDELOEW: *Commercial LIDAR profilers for wind energy. A comparative guide*. In *EWEC 2008*, p. 9. EWEC, 2008. Wind Energy Department, RisÅ, National Laboratory for Sustainable Energy, Technical University of Denmark, P.O. 49, DK-4000 Roskilde, Denmark.
- [38] CREMEAN, L., T. FOOTE, J. GILLULA, G. HINES, D. KOGAN, K. KRIECHBAUM, J. LAMB, J. LEIBS, L. LINDZEY, C. RASMUSSEN, A. STEWART, J. BURDICK and R. MURRAY: *Alice: An Information-Rich Autonomous Vehicle for High-Speed Desert Navigation*, vol. 36 of *Springer Tracts in Advanced Robotics*, chap. 14, pp. 437–482. Springer Berlin Heidelberg, 2007.
- [39] CUERVA, A. and A. SANZ-ANDRAS: *On sonic anemometer measurement theory*. *Journal of Wind Engineering and Industrial Aerodynamics*, 88(1):25–55, 2000.
- [40] DANG, D. Q., Y. WANG and W. CAI: *Nonlinear Model Predictive control (NMPC) of fixed pitch variable speed wind turbine*. In *Sustainable Energy Technologies, 2008. ICSET 2008. IEEE International Conference on*, pp. 29–33, 2008.
- [41] DEEPAK, A. and H. GERBER: *Report of the Experts Meeting on Aerosols and Their Climatic Effects*. Techn. Rep., World Meteorological Organization, 28-30 March 1983 1983.
- [42] DEGIORGIO, V.: *Phase shift between the transmitted and the reflected optical fields of a semireflecting lossless mirror is $\pi/2$* . *American Journal of Physics*, 48(1):81–81, 1980.
- [43] EKELUND, T.: *Modeling and linear quadratic optimal control of wind turbines*. PhD thesis, Chalmers University of Technology, 1997.
- [44] ENERGY, G.: *2.5MW Wind Turbine Series Brochure*, 2010.
- [45] ENERGY, U. D. OF: *Wind Power Today - 2004 Wind Energy Research Highlights*. Techn. Rep., US Department of Energy, 2005.
- [46] ENERGY, U. D. OF: *Wind Power Today 2010 - Advancing large wind turbine technoWind*. Techn. Rep., US Department of Energy, 2010.
- [47] ERIC, S., D. FIONA, J. H. LAKS and P. LUCY: *Lidars and wind turbine control in "Remote Sensing for Wind Energy"*. Techn. Rep., DTU, 2013.
- [48] ERIC, S. and P. LUCY: *Correlation between Rotating Lidar Measurements and Blade Effective Wind Speed*. In *51st AIAA Aerospace Sciences Meeting including the New Horizons Forum and Aerospace Exposition, Aerospace Sciences Meetings*. American Institute of Aeronautics and Astronautics, 2013. doi:10.2514/6.2013-749.
- [49] EWEA: *Wind Energy Factsheets*. Techn. Rep., EWEA, 2010.

- [50] EWEA: *EU Energy Policy to 2050: Achieving 80-95reductions*. Techn. Rep., the European wind association, 2011.
- [51] EWEA: *2030: the next steps for EU climate and energy policy*. Techn. Rep., EWEA, 2013.
- [52] FINGERSH, L., M. HAND and A. LAXSON: *Wind Turbine Design Cost and Scaling Model*. Research Report TP-500-40566, NREL, 2006.
- [53] FIONA, D., P. LUCY, W. ALAN, J. BONNIE and K. NEIL: *Combining Standard Feedback Controllers with Feedforward Blade Pitch Control for Load Mitigation in Wind Turbines*. In *48th AIAA Aerospace Sciences Meeting Including the New Horizons Forum and Aerospace Exposition*, Aerospace Sciences Meetings. American Institute of Aeronautics and Astronautics, 2010. doi:10.2514/6.2010-250.
- [54] FIONA, D., P. LUCY, W. ALAN, J. BONNIE, K. NEIL and S. ERIC: *Adding Feedforward Blade Pitch Control for Load Mitigation in Wind Turbines: Non-Causal Series Expansion, Preview Control, and Optimized FIR Filter Methods*. In *49th AIAA Aerospace Sciences Meeting including the New Horizons Forum and Aerospace Exposition*, Aerospace Sciences Meetings. American Institute of Aeronautics and Astronautics, 2011. doi:10.2514/6.2011-819.
- [55] FREDERIKSEN, A., R. FIESS, W. STORK, S. BOGATSCHER and N. HEUSSNER: *Eye safety for scanning laser projection systems*. *Biomedical Engineering / Biomedizinische Technik*, 57(3):175, 2012.
- [56] FREHLICH, R.: *Effects of Wind Turbulence on Coherent Doppler Lidar Performance*. *Journal of Atmospheric and Oceanic Technology*, 14(1):54–75, 1997.
- [57] FREHLICH, R., S. HANNON and S. HENDERSON: *Performance of a 2- μ m Coherent Doppler Lidar for Wind Measurements*. *Journal of Atmospheric and Oceanic Technology*, 11(6):1517–1528, 1994.
- [58] FREHLICH, R. G. and M. J. KAVAYA: *Coherent laser radar performance for general atmospheric refractive turbulence*. *Applied Optics*, 30(36):5325–5352, 1991.
- [59] FRERIS, L.: *Wind energy conversion systems*. Prentice Hall, 1990.
- [60] FRISCH, U. and A. KOLMOGOROV: *Turbulence: The Legacy of A. N. Kolmogorov*. Cambridge University Press, 1995.
- [61] FROSZ, M., M. JUHL and M. LANG: *Optical Coherence Tomography: System Design and Noise Analysis*. National Laboratory Riso, 2001.
- [62] FUJII, T. and T. FUKUCHI: *Laser Remote Sensing*. Taylor & Francis, 2005.
- [63] GAMLIEL, A. and G. P. AGRAWAL: *Spectrum-enhanced spreading of partially coherent beams*. *Optics Communications*, 78(3-4):203–207, 1990.
- [64] GOODMAN, J.: *Statistical Optics*. Wiley, 1985.
- [65] GRAS, J. L. and W. D. JONES: *Australian aerosol backscatter survey*. *Applied Optics*, 28(5):852–856, 1989.
- [66] GWEC: *Global wind statistics 2013*. Techn. Rep., Global wind energy council, 05.02.2014 2014.
- [67] HAMMERUM, K.: *A fatigue approach to wind turbine control*. PhD thesis, Technical University of Denmark, DTU, 2006.

- [68] HAND, M. M.: *Mitigation of Wind Turbine/Vortex Interaction Using Disturbance Accommodating Control*. Research Report TP-500-35172, NREL, 2003.
- [69] HANSEN, M. H., A. D. HANSEN, T. J. LARSEN, S. OEYE, P. SOERENSEN and P. FUGLSANG: *Control design for a pitch-regulated, variable speed wind turbine*. Techn. Rep., DTU, 2005.
- [70] HARRIS, M.: *Lidar for Turbine Control*. National Renewable Energy Laboratory (U.S.), 10:55, 2005.
- [71] HARRIS, M., G. CONSTANT and C. WARD: *Continuous-Wave Bistatic Laser Doppler Wind Sensor*. Appl. Opt., 40(9):1501–1506, 2001.
- [72] HARRIS, M. and D. A. SMITH: *Wind turbine control having a lidar wind speed measurement apparatus*, Oct. 2007. US Patent 7,281,891.
- [73] HATANAKA, T., T. YAMADA, M. FUJITA, S. MORIMOTO and M. OKAMOTO: *Explicit Receding Horizon Control of Automobiles with Continuously Variable Transmissions*, vol. 384 of *Lecture Notes in Control and Information Sciences*, chap. 46, pp. 561–569. Springer Berlin Heidelberg, 2009.
- [74] HAWLEY, J. G., R. TARG, S. W. HENDERSON, C. P. HALE, M. J. KAVAYA and D. MOERDER: *Coherent launch-site atmospheric wind sounder: theory and experiment*. Applied Optics, 32(24):4557–4568, 1993.
- [75] HAYMAN, G.: *NWTC Design Codes (MLife by Greg Hayman)*. <http://wind.nrel.gov/designcodes/postprocessors/MLife/>, 22-Oct. 2012 2012.
- [76] HENRIKSEN, L. C.: *Model Predictive Control of Wind Turbines*. IMM-PHD-2010-244. Technical University of Denmark (DTU), 2011.
- [77] HESPANHA, J. P.: *Lecture notes on LQG/LQR controller design*. Techn. Rep., University of California, 2007.
- [78] HESS, M., P. KOEPKE and I. SCHULT: *Optical Properties of Aerosols and Clouds: The Software Package OPAC*. Bulletin of the American Meteorological Society, 79(5):831–844, 1998.
- [79] HEUSSNER, N., S. BOGATSCHER and W. STORK: *Optimizing flying-spot display designs based on the upcoming edition of the laser safety standard*. Journal of the Society for Information Display, 22(1):9, January 2014.
- [80] HILL, C. and M. HARRIS: *QinetiQ Lidar Measurement Report*. Techn. Rep., QinetiQ, 2010.
- [81] HINDS, W.: *Aerosol Technology: Properties, Behavior, and Measurement of Airborne Particles*. Wiley, 2012.
- [82] HOOFT, E. VAN DER and T. VAN ENGELEN: *Estimated wind speed feed forward control for wind turbine operation optimisation*. In *Proceedings of European Wind Energy Conference*, London, UK, 2004.
- [83] HUFFAKER, R. M. and R. M. HARDESTY: *Remote sensing of atmospheric wind velocities using solid-state and CO₂ coherent laser systems*. Proceedings of the IEEE, 84(2):181–204, 1996.
- [84] IEA: *Renewable energy medium-term market report 2013*. Market report, International Energy Agency, 2013.

- [85] IEC: *Wind turbines - Part 1: Design requirements*, 2005.
- [86] IEC: *Wind Turbines: Power performance measurements of electricity producing wind turbines*, 2005.
- [87] IEC: *Safety of laser products - Part 1: equipment classification and requirements*, 2007.
- [88] IZATT, J. A. and M. A. CHOMA: *Theory of Optical Coherence Tomography*, pp. 47–72. Biological and Medical Physics, Biomedical Engineering. Springer Berlin Heidelberg, 2008.
- [89] JACKEL, D. and B. WALTER: *Modeling and Rendering of the Atmosphere Using Mie-Scattering*. Computer Graphics Forum, 16(4):201–210, 1997.
- [90] JAMES, J.: *A Student's Guide to Fourier Transforms: With Applications in Physics and Engineering*. Cambridge University Press, 2011.
- [91] JAYNES, D. W., J. F. MANWELL, J. G. MCGOWAN, W. M. STEIN and A. L. ROGERS: *MTC Final Progress Report: LIDAR*. Progress Report, Renewable Energy Research Laboratory, July 19 2007.
- [92] JESPERSEN, L. and M. W. KROGEN: *Model Predictive LIDAR Control of Wind Turbines for Load Mitigation*. PhD thesis, Aalborg University, 2011.
- [93] JING, Y.: *Study on model predictive control of the double-fed wind turbine*. PhD thesis, Shenyang University of Technology, June 2011.
- [94] JOHNSON, C. D.: *Disturbance-Accommodating Control; An Overview*. In *American Control Conference, 1986*, pp. 526–536, 1986.
- [95] JONKMAN, B. and L. KILCHER: *TurbSim User's Guide*. Techn. Rep., National Renewable Energy Laboratory, September 19, 2012 2012.
- [96] JONKMAN, J.: *Dynamics Modeling and Loads Analysis of an Offshore Floating Wind Turbine*. PhD thesis, University of Colorado, 2007.
- [97] JONKMAN, J.: *NWTC Computer-Aided Engineering Tools (FAST by Jason Jonkman, Ph.D.)*, 2-July-2014 2014.
- [98] JONKMAN, J. M., S. BUTTERFIELD, W. MUSIAL and G. SCOTT: *Definition of a 5-MW reference wind turbine for offshore system development*. Techn. Rep., National Renewable Energy Laboratory Golden, CO, 2009.
- [99] JONKMAN, J. M. and M. L. B. JR.: *FAST Users's Guide*. Techn. Rep. DE-AC36-99-GO10337, National Renewable Energy Laboratory, 2005.
- [100] JORANT, C.: *The implications of Fukushima: The European perspective*. Bulletin of the Atomic Scientists, 67(4):14–17, 2011.
- [101] JOSHI, A., X. WANG, D. MOHR, D. BECKER and C. WREE: *Balanced photoreceivers for analog and digital fiber optic communications*. In PIRICH, A. R., M. J. HAYDUK, E. J. DONKOR, P. J. DELFYETT and JR (eds.): *Enabling Photonics Technologies for Defense, Security, and Aerospace Applications*, vol. 5814, pp. 39–50. SPIE, 2005.
- [102] KANE, T. J., B. ZHOU and R. L. BYER: *Potential for coherent Doppler wind velocity lidar using neodymium lasers*. Applied Optics, 23(15):2477–2481, 1984.

- [103] KARLSSON, C. J., A. OLSSON, FREDRIK, D. LETALICK and M. HARRIS: *All-Fiber Multifunction Continuous-Wave Coherent Laser Radar at 1.55 μm for Range, Speed, Vibration, and Wind Measurements*. *Appl. Opt.*, 39(21):3716–3726, 2000.
- [104] KENT, G. S., G. K. YUE, U. O. FARRUKH and A. DEEPAK: *Modeling atmospheric aerosol backscatter at CO₂ laser wavelengths. 1: Aerosol properties, modeling techniques, and associated problems*. *Applied Optics*, 22(11):1655–1665, 1983.
- [105] KIKUCHI, K.: *Coherent Optical Communications: Historical Perspectives and Future Directions*, vol. 6 of *Optical and Fiber Communications Reports*, pp. 11–49. Springer Berlin Heidelberg, 2010.
- [106] KNUDSEN, T., T. BAK and M. SOLTANI: *Prediction models for wind speed at turbine locations in a wind farm*. *Wind Energy*, 14(7):877–894, 2011.
- [107] KOST, C.: *Levelized Cost of Electricity- Renewable Energy Technologies*. Techn. Rep., Fraunhofer ISE, 2013.
- [108] KRISTENSEN, L.: *On longitudinal spectral coherence*. *Boundary-Layer Meteorology*, 16(2):145–153, 1979.
- [109] KRISTENSEN, L.: *The perennial cup anemometer*. *Wind Energy*, 2(1):59–75, 1999.
- [110] KWAKERNAAK, H. and R. SIVAN: *Linear optimal control systems*. Wiley-Interscience publication. Wiley Interscience, 1972.
- [111] LEE, M. J. B. Y. J. and L. KENDALL: *Disturbance tracking control theory with application to horizontal axis wind turbines*. In *1998 ASME Wind Energy Symposium*. American Institute of Aeronautics and Astronautics, 1998.
- [112] LIEPMANN, H. W.: *On the Application of Statistical Concepts to the Buffeting Problem*. *Journal of the Aeronautical Sciences*, 19(12):793–800, 1952.
- [113] LINDELOEW, P.: *Fiber Based Coherent Lidars for Remote Wind Sensing*. PhD thesis, DTU, 2007.
- [114] LIU, Z.-S., B.-Y. LIU, S.-H. WU, Z.-G. LI and Z.-J. WANG: *High spatial and temporal resolution mobile incoherent Doppler lidar for sea surface wind measurements*. *Optics Letters*, 33(13):1485, July 2008.
- [115] LOFBERG, J.: *YALMIP : a toolbox for modeling and optimization in MATLAB*. In *Computer Aided Control Systems Design, 2004 IEEE International Symposium on*, pp. 284–289, 2013.
- [116] MACIEJOWSKI, J.: *Predictive Control: With Constraints*. Pearson Education. Prentice Hall, 2002.
- [117] MAEZLER, C.: *MATLAB Functions for Mie Scattering and Absorption*. Techn. Rep. 2002-11, Institut fuer Angewandte Physik, 2002.
- [118] McGRATH, A. J.: *An erbium:glass coherent laser radar for remote sensing of wind velocity*. PhD thesis, The Flinders University of South Australia, 1998.
- [119] McKAY, J. A.: *Fabry-Perot Etalon Aperture Requirements for Direct Detection Doppler Wind Lidar from Earth Orbit*. *Applied Optics*, 38(27):5859–5866, 1999.
- [120] McLAUGHLIN, D.: *Wind shear and its effect on wind turbine noise assessment*. Techn. Rep., Sgurr Energy, 2012.

- [121] MENZIES, R. T.: *Doppler lidar atmospheric wind sensors: a comparative performance evaluation for global measurement applications from earth orbit*. Applied Optics, 25(15):2546–2553, 1986.
- [122] MENZIES, R. T., M. J. KAVAYA, P. H. FLAMANT and D. A. HANER: *Atmospheric aerosol backscatter measurements using a tunable coherent CO2 lidar*. Applied Optics, 23(15):2510–2517, 1984.
- [123] MIDDLETON, W.: *Invention of the meteorological instruments*. Johns Hopkins Press, 1969.
- [124] MIE, G.: *Beitraege zur Optik trueber Medien, speziell kolloidaler Metalloesungen*. Annalen der Physik, 330(3):377–445, 1908.
- [125] MIKKELSEN, T., J. MANN, M. COURTNEY and M. SJOEHOLM: *Windscanner: 3-D wind and turbulence measurements from three steerable doppler lidars*. IOP Conference Series: Earth and Environmental Science, 1(1):012018, 2008.
- [126] MILONNI, P. W.: *Lidar. Range-Resolved Optical Remote Sensing of the Atmosphere*, vol. 102 of *Optical Sciences*. Springer, 2009.
- [127] MORARI, M. and J. H. LEE: *Model predictive control: past, present and future*. Computers and Chemical Engineering, 23(4-5):667 – 682, 1999.
- [128] MORIARTY, P. J. and A. C. HANSEN: *AeroDyn Theory Manual*. Technical report, National Renewable Energy Laboratory, 2005.
- [129] MUNIER, F., E. ALPMAN, T. ERIKSSON, A. SVENSSON and H. ZIRATH: *Estimation of phase noise for QPSK modulation over AWGN channels*. In *Proc. Giga Hertz 2003 Symp*, pp. 4–5, 2003.
- [130] NIELS, T., Z. FREDERIK, R. PIERRE-ÉLOUAN and S. NIELS: *Comparison of the wake of different types of wind turbine CFD models*. In *50th AIAA Aerospace Sciences Meeting including the New Horizons Forum and Aerospace Exposition*, Aerospace Sciences Meetings. American Institute of Aeronautics and Astronautics, 2012. doi:10.2514/6.2012-237.
- [131] NORMUNG, D. D. I. FUER: *Optics and photonics - Lasers and laser-related equipment - Test methods for laser beam power, energy and temporal characteristics*, 2008.
- [132] NRGSYSTEMS and FIRSTWIND: *Yaw Misalignment Correction Case Study*. Techn. Rep., Renewable NRG Systems, 2013.
- [133] ODGAARD, P. F., C. DAMGAARD and R. NIELSEN: *Unknown input observer based estimation of wind speed for wind turbines control*. In *World Congress*, vol. 18, pp. 1698–1703, 2011.
- [134] OESTERGAARD, K. Z., P. BRATH and J. STOUSTRUP: *Estimation of effective wind speed*. Journal of Physics: Conference Series, 75(1):012082, 2007.
- [135] ORTEGA, R., F. MANCILLA-DAVID and F. JARAMILLO: *A globally convergent wind speed estimator for wind turbine systems*. International Journal of Adaptive Control and Signal Processing, 27(5):413–425, 2013.
- [136] PASCHOTTA, R.: *Encyclopedia of laser physics and technology*, vol. 1. Wiley-VCH, 2008.
- [137] PATTERSON, J.: *The Cup Anemometer*. Royal Society of Canada, 1926.
- [138] PEDERSEN, C. and R. HANSEN: *Coherent lidar system based on a semiconductor laser and amplifier*, Nov. 2010. US Patent App. 12/679,685.

- [139] PENA, A., C. BAY HASAGER and J. LANGE: *Remote sensing for wind energy*. Techn. Rep., DTU Wind Energy, 2013.
- [140] PENA, A., T. MIKKELSEN, S.-E. GRYNING, C. B. HASAGER, A. N. HAHMANN, M. BADGER, I. KARAGALI and M. COURTNEY: *Offshore Vertical Wind Shear*. Techn. Rep. TREN-PP7EN-219048, DTU Wind Energy, Technical University of Denmark, 2012.
- [141] PIELKE, R. and H. PANOFSKY: *Turbulence characteristics along several towers*. Boundary-Layer Meteorology, 1(2):115–130, 1970.
- [142] PINEDA, I., S. AZAU, J. MOCCIA and J. WILKES: *Wind in power 2013 European statistics*. Techn. Rep., THE EUROPEAN WIND ENERGY ASSOCIATION, 2014.
- [143] POLINDER, H., S. W. DE HAAN, M. R. DUBOIS and J. G. SLOOTWEG: *Basic operation principles and electrical conversion systems of wind turbines*. EPE JOURNAL, 15(4):43, 2005.
- [144] POST, M. J.: *Aerosol backscattering profiles at CO₂ wavelengths: the NOAA data base*. Applied Optics, 23(15):2507–2509, 1984.
- [145] POST, M. J., F. F. HALL, R. A. RICHTER and T. R. LAWRENCE: *Aerosol backscattering profiles at $\lambda = 10.6\mu\text{m}$* . Applied Optics, 21(13):2442–2446, 1982.
- [146] QIN, S. J. and T. A. BADGWELL: *A survey of industrial model predictive control technology*. Control Engineering Practice, 11(7):733–764, 2003.
- [147] RAMTHARAN, G., N. CHRIS and B. ERVIN: *Importance of advanced simulations of electrical transients in wind turbines*. In *European Wind Energy Conference*, 2010.
- [148] RIBEIRO, L. and R. LUIS: *Sonic Anemometer and Atmospheric Flows Over Complex Terrain*. LAP Lambert Academic Publishing, 2012.
- [149] RIBOLDI, C. E.: *Advanced Control Laws for Variable-Speed Wind Turbines and Supporting Enabling Technologies*. PhD thesis, Politecnico di Milano, 2012.
- [150] RIBRANT, J. and L. BERTLING: *Survey of Failures in Wind Power Systems With Focus on Swedish Wind Power Plants During 1997 - 2005*. Energy Conversion, IEEE Transactions on, 22(1):167–173, March 2007.
- [151] ROTHERMEL, J. and W. D. JONES: *Ground-based measurements of atmospheric backscatter and absorption using coherent CO₂ lidar*. Applied Optics, 24(21):3487–3496, 1985.
- [152] SALAMITOU, P., A. DABAS and P. H. FLAMANT: *Simulation in the time domain for heterodyne coherent laser radar*. Applied Optics, 34(3):499–506, 1995.
- [153] SCHIJVE, J.: *Fatigue of Structures and Materials*. Springer, 2008.
- [154] SCHLIPF, D.: *Lidars and Wind Turbine Control II in "Remote Sensing for Wind Energy"*. DTU, 2013.
- [155] SCHLIPF, D. and P. W. CHENG: *Adaptive Feed Forward Control for Wind Turbines*. AT-AUTOMATISIERUNGSTECHNIK, 61(5):329–338, 2013.
- [156] SCHLIPF, D., P. W. CHENG and J. MANN: *Model of the Correlation between Lidar Systems and Wind Turbines for Lidar-Assisted Control*. Journal of Atmospheric and Oceanic Technology, 30(10):2233–2240, 2013.

- [157] SCHLIPF, D., D. J. SCHLIPF and M. KÜHN: *Nonlinear model predictive control of wind turbines using Lidar*. *Wind Energy*, 16(7):1107–1129, 2013.
- [158] SCHOLBROCK, A., P. FLEMING, L. FINGERSH, A. WRIGHT, D. SCHLIPF, F. HAIZMANN and F. BELEN: *Field testing LIDAR based feed-forward controls on the NREL controls advanced research turbine*. In *Proc. 51st AIAA Aerospace Sciences Meeting Including the New Horizons Forum and Aerospace Exposition*, pp. 2013–0818, 2013.
- [159] SIMLEY, E. and L. Y. PAO: *Design and evaluation of a wind speed estimator for hub-height and shear components*. In *European Academy of Wind Energy 9th PhD Seminar on Wind Energy in Europe*, 2013.
- [160] SIMLEY, E., L. Y. PAO, R. FREHLICH, B. JONKMAN and N. KELLEY: *Analysis of light detection and ranging wind speed measurements for wind turbine control*. *Wind Energy*, 17(3):413–433, 2014.
- [161] SJOEHOLM, M., E. DELLWIK, Q. HU, J. MANN, C. PEDERSEN and P. J. RODRIGO: *Field test of an all-semiconductor laser-based coherent continuous-wave doppler lidar for wind energy applications*. In *ISARS2014*, 2014.
- [162] SLINGER, C. and M. HARRIS: *Introduction to continuous-wave Doppler lidar*, chap. 4. DTU wind energy, Roskilde, 2012.
- [163] SMALIKHO, I. N. and V. A. BANAKH: *Accuracy of estimation of the turbulent energy dissipation rate from wind measurements with a conically scanning pulsed coherent Doppler lidar. Part I. Algorithm of data processing*. *Atmospheric and Oceanic Optics*, 26(5):404–410, 2013.
- [164] SOLIMAN, M., O. P. MALIK and D. T. WESTWICK: *Multiple Model Predictive Control for Wind Turbines With Doubly Fed Induction Generators*. *Sustainable Energy, IEEE Transactions on*, 2(3):215–225, 2011.
- [165] SOLTANI, M. N., T. KNUDSEN, M. SVENSTRUP, R. WISNIEWSKI, P. BRATH, R. ORTEGA and K. JOHNSON: *Estimation of Rotor Effective Wind Speed: A Comparison*. *Control Systems Technology, IEEE Transactions on*, 21(4):1155–1167, 2013.
- [166] SORENSEN, P., D. A. HANSEN, F. LOV, F. BLAABJERG and H. F. DONOVAN: *Wind farm models and control strategies*. Risoe National Laboratory, 2005.
- [167] STOL, K. A.: *Dynamics modeling and periodic control of horizontal-axis wind turbines*. PhD thesis, University of Colorado at Boulder, 2001.
- [168] STOTSKY, A. and B. EGARDT: *Model-based control of wind turbines: look-ahead approach*. *Proceedings of the Institution of Mechanical Engineers, Part I: Journal of Systems and Control Engineering*, 226(8):1029–1038, 2012.
- [169] SUTHERLAND, H. J.: *A summary of the fatigue properties of wind turbine materials*. *Wind Energy*, 3(1):1–34, 2000.
- [170] TARG, R., M. J. KAVAYA, R. M. HUFFAKER and R. L. BOWLES: *Coherent lidar airborne windshear sensor: performance evaluation*. *Applied Optics*, 30(15):2013–2026, 1991.
- [171] TASCA, L.: *LiDAR technology with unfrozen turbulence for wind turbine predictive control*. Master's thesis, Politecnico di Milano, 2013.

- [172] TAYLOR, G. I.: *The spectrum of turbulence*. Proceedings of the Royal Society of London. Series A-Mathematical and Physical Sciences, 164(919):476–490, 1938.
- [173] TAYLOR, J. R.: *An introduction to error analysis: the study of uncertainties in physical measurements*. University science books, 1997.
- [174] THOMSEN, S. C. and S. C. THOMSEN: *Wind turbine control and model predictive control for uncertain systems*. IMM-PHD-2010-229. Technical University of Denmark (DTU), 2010.
- [175] TOMIZUKA, M.: *Zero Phase Error Tracking Algorithm for Digital Control*. Journal of Dynamic Systems, Measurement, and Control, 109(1):65–68, 1987. 10.1115/1.3143822.
- [176] TORRISI, F. D. and A. BEMPORAD: *HYSDEL-a tool for generating computational hybrid models for analysis and synthesis problems*. Control Systems Technology, IEEE Transactions on, 12(2):235–249, 2004.
- [177] UCHIYAMA, Y., T. HATANAKA and M. FUJITA: *2DOF control of an electrodynamic shaker using explicit receding horizon control for feedforward term*. In *Control Applications (CCA), 2010 IEEE International Conference on*, pp. 596–601, 2010.
- [178] VAUGHAN, J. M. and P. A. FORRESTER: *Laser Doppler velocimetry applied to the measurement of local and global wind*. Wind Engineering, 13(1):15, 1989.
- [179] WAGNER, R., R. L. RIVERA, I. ANTONIOU, S. DAVOUST, T. FRIIS PEDERSEN, M. COURTNEY and B. DIZNABI: *Procedure for wind turbine power performance measurement with a two-beam nacelle lidar*. Techn. Rep., DTU Wind Energy, 2013.
- [180] WAGNER, R., R. L. RIVERA, I. ANTONIOU, S. DAVOUST, T. F. PEDERSEN, M. COURTNEY and B. DIZNABI: *Power curve measurement using a two -beam nacelle mounted lidar*. Techn. Rep., DTU, 2013.
- [181] WANG, N.: *LIDAR-assisted feedforward and feedback control design for wind turbine tower load mitigation and power capture enhancement*. PhD Thesis, Colorado School of Mines, 2013.
- [182] WINDPOWER: *Close up - GE's new 4.1MW turbine and its return to offshore*. Website, March 2011.
- [183] WOLF, E.: *Invariance of the Spectrum of Light on Propagation*. Physical Review Letters, 56(13):1370–1372, 1986. PRL.
- [184] WRIGHT, A. and L. FINGERSH: *Advanced control design for wind turbines*. Techn. Rep., NREL, 2008.
- [185] WRIGHT, A. D.: *Modern control design for flexible wind turbines*. Techn. Rep., National Renewable Energy Laboratory, 2004.
- [186] YUEN, H. P. and V. W. S. CHAN: *Noise in homodyne and heterodyne detection*. Opt. Lett., 8(3):177–179, 1983.
- [187] ZAK, J. A.: *Atmospheric Boundary layer sensors for application in a wake vortex advisory system*. Techn. Rep., NASA, 2003.

Supervised Student Research

- [AA10] AYUK, ROLAND ASHU and NAZIA AKBAR ALI: *Optical system setup for Doppler Wind Lidar systems*. Research Project, Karlsruhe Institute of Technology, 2010.
- [Ale10] ALEXANDER, DRISS: *Laboratory setup and experiments of Doppler Wind Lidar system*. Bachelor thesis, Karlsruhe Institute of Technology, 2010.
- [AT14] ASCHE-TAUSCHER, JULIAN: *Experimental evaluation of a short coherence length laser with a fiber delay-line for Doppler wind Lidar systems*. Master's thesis, Karlsruhe Institute of Technology, 2014.
- [Boe14] BOETTIGER, JAMES: *Interferometric laser coherence length measurement*. Research Project, Karlsruhe Institute of Technology, 2014.
- [Bru12] BRUNET, MARC-ETIENNE: *Performance Simulation of a Doppler LIDAR*. Research Project, McGill University, 2012.
- [Cha13] CHATTOPADHYAY, ABHIROOP: *Particles Backscattering with COMSOL multiphysics*. Research Project, Illinois Institute of Technology, 2013.
- [Ene14] ENE, ANCA: *Numerical simulation of the induction zone wind speed changes of a NREL 5-MW turbine using a LES method*. Research Project, Karlsruhe Institute of Technology, 2014.
- [Gal12] GALKOVSKAYA, ANASTASIA: *Atmospheric scattering and absorption simulator design with Matlab/Labview*. Bachelor thesis, Karlsruhe Institute of Technology, 2012.
- [Lea13] LEAL, SOFIA: *Introduce the Feed-Forward control into wind turbine pitch control system based on Matlab Simulink*. Research Project, University of Porto, 2013.
- [Mus12] MUSTAHSIN, ADIB: *Optical scattering Simulation with COMSOL*. Research Project, Karlsruhe Institute of Technology, 2012.
- [Ros12] ROSKORSCH, MICHAEL MARTIN: *Wind tunnel design for lab test of laser Doppler wind sensor*. Bachelor thesis, Karlsruhe Institute of Technology, 2012.
- [She11] SHEBBO, ALI: *Lab Test Setup of Laser Doppler Wind Remote Sensor*. Bachelor thesis, University of Applied Sciences Karlsruhe, 2011.
- [Säm10] SÄMANN, STEFAN UDO: *Laboratory setup and experiments of Doppler Wind Lidar system*. Bachelor thesis, Karlsruhe Institute of Technology, 2010.
- [Wan14] WANG, FENGYING: *Design of a laser Doppler Lidar simulator for testing of a wavelet domain denoising method to improve the Lidar signal SNR*. Master's thesis, Karlsruhe University of Applied Science, 2014.
- [WN12] WANG, ZHE and NGUYEN NHAN: *Coherent Laser Doppler Lidar system for speed measurement*. Research Project, Karlsruhe Institute of Technology, 2012.

- [Xu13] XU, SHENGYAO: *Model Predictive Control with LIDAR System for the Active Wind Turbine Pitch Control System*. Master's thesis, Karlsruhe University of Applied Science, 2013.
- [ZZL12] ZHANG, JINGYI, LU ZHOU and MING LIN: *Optical based particle concentration measurement for air pollution*. Research Project, Karlsruhe Institute of Technology, 2012.

Publications included in this Dissertation

Conference & Journal Papers

- [BDB⁺15] BEUTH, THORSTEN, SVETLANA DANILOVA, HARSHA UMESH BABU, SIEGWART BOGATSCHER, LEILEI SHINOHARA and NICO HEUSSNER: *Revision of an Optical Engineering Lecture Based on Students Evaluation of University Teaching*. International Journal of Information and Education Technology, 5(12):6, Dec 2015.
- [BGB⁺12] BOGATSCHER, S., C. GIESEL, T. BEUTH, H. UMESH-BABU, L. SHINOHARA, N. HEUSSNER, A. STRECK and W. STORK: *Fast scan-fail device for class 1 operation of scanning micromirrors at a high laser power in the near-infrared region*. Proc. SPIE 85120E, 85120E:-85120E, 2012. 10.1117/12.929717.
- [BSFS14] BEUTH, THORSTEN, LEILEI SHINOHARA, MAIK FOX and WILHELM STORK: *Calculation of Backscatter Coefficients for Lidar systems by Mie-Scattering Theory and Atmospheric Properties*. In DGaO, 2014.
- [SATF⁺14] SHINOHARA, LEILEI, JULIAN ASCHE-TAUSCHER, MAIK FOX, THORSTEN BEUTH and WILHELM STORK: *Design and evaluation of a short coherence length laser based Doppler wind Lidar system for wind energy applications*. In SPIE Photonics Europe - Optical Sensing and Detection, volume 9141, page 59, 2014.
- [SBB⁺13] SHINOHARA, L., T. BEUTH, S. BOGATSCHER, N. HEUSSNER, H. UMESH-BABU, S. DANILOVA, T. TRAN and W. STORK: *A Simulation Environment for assisting system design of Coherent Laser Doppler Wind Sensor for Active Wind Turbine Pitch Control*. Proc. SPIE, 8789:8789-32, 2013. 10.1117/12.908759.
- [SBF⁺14a] SHINOHARA, L., T. BEUTH, M. FOX, J. ASCHE-TAUSCHER and W. STORK: *Multi-length Fiber Delay Line for the Wind Turbine Pitch Control with a Doppler Wind Lidar System*. In DGaO, 2014.
- [SBF⁺14b] SHINOHARA, L., T. BEUTH, M. FOX, N. HEUSSNER, H. UMESH-BABU and W. STORK: *System Design of a Coherent Laser Doppler Wind Profiler for the Predictive Control of Wind Turbine System (WTS)*. In Int. Conf. Optics-photonics design & fabrication (ODF14), Tokyo, 2014.
- [SBH⁺12] SHINOHARA, L., S. BOGATSCHER, N. HEUSSNER, H. UMESH-BABU, M. BRUNET and W. STORK: *A coherent laser Doppler wind profiler for the active control of wind turbines*. Proc. SPIE 823519, 8235:823519-12, 2012.
- [STB⁺14] SHINOHARA, LEILEI, JULIAN ASCHE TAUSCHER, THORSTEN BEUTH, NICO HEUSSNER, MAIK FOX, HARSHA UMESH BABU and WILHELM STORK: *Optical system design and experimental evaluation of a coherent Doppler wind Lidar system for the predictive control of wind turbine*. Optical Review, 21(5):698-704, 2014.

- [SXBS14] SHINOHARA, LEILEI, SHENYAO XU, THORSTEN BEUTH and WILHELM STORK: *Receding horizon control (RHC) on a Lidar based preview controller design for the active wind turbine pitch system*. In *Jahrestagung KIT-Zentrum Energie*. KIT Scientific Publishing, 2014.